Journal of Engineering

ISSN 1726-4073

A Scientific Refereed Journal
Published by College of Engineering University of Baghdad

May
201 3

Number 5

Volume 19

ISSN 1726-4073

مجلة الهندسة

مجلة علمية محكمة تصدرها
كلية الهندسة ـ جامعة بغداد

أيار
2013

العدد 5
المجلد 19

ENGINEERING

College of Engineering Baghdad University Baghdad

List of Contents

English Section: Page

Bearing Capacity of Shallow Footing on Compacted Filling Dune Sand Over Reinforced Gypseous Soil

Assist. Prof. Dr. Bushra Sahal. Al-busoda
Email: albusoda@yahoo.com
Rusol Salman (M.Sc. Student)
Email: Salamrusel@yahoo.com

ABSTRACT:

Existence of these soils, sometimes with high gypsum content, caused difficult problems to the buildings and strategic projects due to dissolution and leaching of gypsum by the action of water flow through soil mass. In this research, a new technique is adopted to investigate the performance of replacement and geosynthetic reinforcement materials to improve the gypseous soil behavior through experimential set up manufactured loaclally specially for this work. A series of tests were carried out using steel container (600*600*500) mm. A square footing (100*100) mm was placed at the center of the top surface of the bed soil. The results showed that the most effective thickness for the dune sand layer with geotextile at the interface, within the tested range, was found to be almost equal to the width of foundation. Therefore, under this depth, the soil was reinforced with geogrid and geotextile. It can be shown that (Collapse Settlement Reduction Factor) increases to (72%) when using two layers of geogrid and one layer of geotextile under depth of replacement equal to the width of footing. In addition, the results showed that the bearing capacity increases to (1.5-2.0) time under concentric loads and (2.5-3) under eccentric loads after replacement and reinforcement of gypseous soil.

Key Word: Gypseous Soil, Dune Sand, Bearing Capacity, Reinfrocement Materials, Collapse Settlement.

الخلاصة

ان وجود هذه الترب بنسب عاليه في بعض المواقع قد سبب عدة مشاكل معقدة للمباني والمشاريع الستراتيجية بسبب ذوبان الجبس بتأثير جريان الماء خلال كتلة التربة. في هذا البحث اقترحت تقنية جديدة شملت فحص تبديل التربة والتسليح بمواد نسيجية ومشبكات لتحسين تصرف التربة من خلال موديل مختبري صنع محليا لهذا الغرض. سلسلة من الفحوصات لنماذج جافة واخرى مغمورة في صندوق حديدي أبعاده (600*600*500) ملم وأساس مربع الشكل بأبعاد (100*100) ملم وضع في وسط نموذج التربة المفروشة في صندوق الفحص. بينت النتائج أن أفضل عمق مؤثر لتبديل التربة الجبسية بكثبان رملية هو العمق الذي يساوي عرض الأساس بعد استخدام المواد النسيجية والمشبكات وقد لوحظ أن (Collapse Settlement Reduction Factor, CSRF) تزداد الى (72%) عندما نستخدم طبقتين من جيوكرد وطبقة من الجيوتكستيل تحت عمق تبديل يساوي عرض الأساس. وأن قابلية التحمل تزداد بنسبة (1.5-2.0) في حالة التحميل المركزي و (2.5-3.0) في حالة التحميل اللامركزي.

الكلمات الرئيسية :التربة الجبسية، الكثبان الرملية، قابلية التحمل، مواد التسليح، هطول الانهيار.

INTRODUCTION

Gypseous soil is that soil which contains enough gypsum ($CaSO_4.2H_2O$) that affect the behaviour of soil. Gypsum has specific gravity of (2.32) and its solubility of gypsum in water is (2gm/liter) at 20 C°, but the amount of dissolved gypsum can be much greater if water contains some salts (**Hesse, 1971 and Khan, 2005**). In Iraq gypseous soils concentrated in Mousal, Baiji, Tikrit, Sammera, North West of Baghdad, Anna, Heet, Ramadi, Falloja and they may be presented in other regions (**Al-Jananbi, 2002**).Gypseous soils are classified as collapsing soils. This is due to the fact that gypsum present in the soil provides an apparent cementation when the soil is dry but the intrusion of the water causes dissolution and softening leading generally to serious structural collapse (**Razouki, et al, 1994**).

Upon wetting, most of soils show settlement. The amount of settlement varies from soil to another and is dependent on load-induced stresses. But such settlement will eventually cease after a certain period of time. However, under certain conditions and for specific types of soils, subsequent wetting may cause additional settlement. This type of settlement is termed (Collapse) (**Casagrande, 1932**).

Many major projects suffered from several problems related to construction on or by gypseous soils, such as cracks, tilting, collapse, and leaching the soil. These problems could happen due to percolation of water into these soils causing dissolution of gypsum, which provides the cementing bonds between the soil particles. This process leads to collapse of soil structure and progressive compression, and the problem becomes more complicated if flow occurred causing continuous loss of soil mass and formation of serious cavities. For the construction of any kind of structure resting on problematic soils such as gypseous soils, there are many available methods to improve the behaviour of soil. Using Geosynthetic materials (Geotextile and Geogrid) as reinforcement, to increase bearing capacity and to decrease settlement for foundation was investigated by many researchers such as (**Das, 1988, Raymond, 1992, and Soliman** and **Hanna, 2010**). The designers have suggested partially replacing the collapsible soil with cohesionless material and using reinforcement materials and study their effects on the reduction of collapse settlement of collapsible soils when inundation was occur.

EXPERMENTAL WORK

1. Classification Tests:

The material used in this study was distributed gypseous soil brought from Tikrit, Salah Al-Deen Governorate and dune sand used in replacement of gypseous soil was obtained from Baiji, Salah Al-Deen Governorate. A series of tests was performed on the gypeous soil and dune sand according to ASTM procedures. Gypseous soil can be classified as (SC) and dune sand can be classified as (SP) according to the Unified Soil Classification System. The minimum unit weight of gypseous soil was determined according to the test described by (**Head, 1984**). It is widely accepted as standard test for sandy soils and the maximum unit weight of gypseous soil was determined according to ASTM D-64T (**Bowles, 1988**). Field unit weight of gypseous soil was determined by a field test (Sand Cone Method). This test was performed according to (**ASTM D1556-00**). The results of the maximum and minimum unit weights of gypseous soil are (14.10) kN/m^3 and (10.75) kN/m^3 respectively. **Table** (1), (2), (3), and (4) show the physical and chemical properties of gypseous soil and dune sand, respectively.

2. Test Box:

The soil beds were prepared in a steel box with inside dimensions (600*600) mm and (500) mm in height. The sides and bottom were made of (5) mm thickness plate;the purpose of the thickness is to give rigidity against pressure which may generate during loading of the soil. One face of the steel box is made from Plexiglass with dimensions (300*300) mm. The box placed over (800) mm width and (1000) mm length of strong steel base, which is connected to a stiff loading frame. The frame consists of two columns of steel channels, which is in turn bolted to a loading platform. This platform allowed to slide along the columns and can be fixed at any desired height by means of slotting spindles and holes provided at different intervals along the columns. The footing was made of steel plate of a thickness of (3) mm. . The footing was connected to suitable steel wings to facilitate the measurement of settlement. Ahydraulic jack was used to apply an axial loading on footing. The load on the footing was measured using proving ring of (20) kN capacity, while the settlement was measured by two dial gauges (0.01) mm fixed on the footing by two magnetic holders. Ageneral view of the

manufactured testing equipment is shown in **Figure** (1).

A sketch for the test box showing some of the studied parameters is shown in **Figure** (2). The detailed description of the model is explained in the following paragraphs.

The reinforcement used is polymer geomesh (Geogrid and Geotextile). **Table** (5) shows the properties of geogrid, and **Table** (6) shows the properties of geotextile, as supplied by Building Research Center (Iraq). **Figure** (3) shows the geogrid and geotextile used in this work.

TEST PROCEDURE FOR MODEL LOADING

1. Collapse Test Procedure:

1.Using raining technique, gypseous soil is placed in the steel box at field density (12.9) kN/m^3 and in situ moisture content (3.2%). The surface was leveled and checked by a bubble ruler (Balance).
2.When reaching the desired depth of soil in the steel box, sqaure footing was placed at the center of the test box.
3.For the tests on replaced gypseous soils, geotextile sheet was placed above the gypseous soil. Dune sand was placed in the steel box above the geotextile by raining technique to reach a relative density of (75%) and a unit weight of (16) kN/m^3.
4.For testing using geogrid within the dune sand layer, the geogrid was placed at different depths.
5.The base of the proving ring is made just in touch with the footing. The zero (initial) reading was recorded. Two magnetic holders with dial gauges were connected to the edges of the box.
6.Load increments are applied until settlement readings are less than (0.01) mm.
7. When reaching the inundation stress then another increment is applied, water is added to soil in the steel box, while the applied load was kept constant. The soil becomes fully saturated. Loads and settlements are recorded for the following (24) hours.

2. Bearing Capacity Test Procedure:

The test was conducted by using non repetitive static plate load test method according to the procedures of **ASTM D1194-94**. The bearing capacity was determined for various thicknesses of gypseous soil beds. In each test, the gypseous soil was placed in layers (5) cm thick. The placement density was controlled using raining technique.The gypseous soil was carefully spreaded in two perpendicular directions to ensure uniform density. When the final layer was layed, the surface was carefully leveled with the aid of straight edge. Then, the foundation was fixed in the center of test box in x and y direction in concentric loading and at determined eccentricity in case of eccentric loading and then the two magnetic holders with dial gauges in the edge of the box was connected. The load was continuously applied through the hydraulic jack. The applied load was recorded from the proving ring reading while the settlement was measured by the dial gauges. When soaking is conducted, the steel box is left for (24) hours to ensure that all soil was completely soaked. On the second day, the test was began . The application of load was continued up to failure. The failure was indicated by the increase of settlement at a constant magnitude of load intensity. When the test is done by replacing gypseous soil with dune sand, dune sand was placed in certain depth in the steel box by using raining technique and using geotextile at interface between gypseous soil and dune sand. Dune sand was carefully spreaded in two perpendicular directions to ensure uniform density. In reinforced condition, the gypseous soil was placed in the steel box by using raining technique. Before the construction of the next layer, the geotextile was placed above collapse soil and geogrid was placed in two layers through dune sand layer. The for mentioned procedure was followed for concentric and eccentric loading conditions.

RESULTS AND ANALYSIS

Tests carried out in this research are divided into the following series: (tests on gypseous soil under different inundation stresses (100,150,200) kPa, and tests on replaced gypseous soil with dune sand with the inclusion of geotextile at the interface at different depths of the gypseous soil layer (10,15,20) cm, in addition to geogrid with dune sand at dg/ds=(0.3B, 0.7B, and two layers).The behaviour of collapse settlement ratio (Δ_h/B) ratio of gypseous soil is governed by studying the following factors:
1.Effect of inundation stress on collapse strain.
2.Effect of depth of gypseous soil.
3.Effect of geogrid and geotextile on collapse settlement.

Where:
B=width of shallow footing.
dg= depth of geogrid in the dune sand layer.
ds= depth of dune sand.

The effect of inundation stress on collapse settlement of square shallow footing resting on gypseous soil was studied. The relationship between inundation stress and collapse settlement ratio was drawn in **Figure** (4). It is obvious from figure that the collapse settlement ratio increases linearly with increase of inundation stress and this behaviour was expected, where the increase in load would increase the rate of solution and cause softening of the soil resulting in loss of shear strength and increase in collapse settlement. Therefore, when comparing the results of collapse settlement at different inundation stresses, greater value of collapse settlement at (200) kPa were observed. **Table** (7) shows the relationship between inundation stress , collapse settlement ratio and collapse strain.

Figure (5) shows the relationship between inundation stress and collapse strain. From figure, it can be noticed that figure the collapse strain increases due to an increase of inundation stress in gypseous soil. Also, the maximum of collapse strain was (10.3%) under inundation stress at (200) kPa.

The collapse strain can be determined by equation follows:

$$\text{Collapse Strain}=\frac{\Delta_h}{h_\circ}*100$$

Where:

Δ_h = change in height of sample due to soaking.

$h_\circ$ = original height of sample.

After studying the effect of stress level on collapse strain, it is observed that a stress level (200) kPa, has greater collapse strain. Therefore, this stress level was chosed for studying the improvement of gypseous soil. Six tests were carried out by replacing the gypseous soil with dune sand at depth of (10, 15, and 20) cm before and after placement of geotextile. **Figure** (6) shows that collapse settlement ratio increases with the increase of depth of gypseous soil before placement of geotextile. This behaviour was expected due to increase in dissolution of gypsum, while **Figure** (7) shows that collapse settlement ratio with depths of dune sand after placement of geotextile. The optimum replacement thickness ratio (ds/B) is equal to (1). The increase in settlement with increasing soil replacement depth can be explained as the sand layer acted as a surcharge on the surface of the collapsible soil causing increase in the collapse settlement, which overcame the reduction of the collapse settlement which results from the decrease of the collapsible soil depth. Therefore, this depth will be used to improve the soil with geogrid within replaced layer in addition to the use of geotextile at the interface between dune sand and gypseous soil. Three tests were carried out on gypseous soil replaced with dune sand with inclusion of geotextile at the interface in addition to geogrid within dune sand at different depths of geogrid during soaking. The settlement collapse also decreased by the presence of the geotextile, in addition, the depth of geogrid layers appear to have a profound effect on the settlement collapse ratio during soaking. The relationship between the collapse settlement ratio and depths of geogrid, was presented in **Table** (8). From the inspection of results, it is observed that best reduction in collapse settlement ratio was noticed when using two layers of geogrid. While, less reduction was noticed at depth of (0.7B).

To evaluate the improvement in soil behaviour due to sand replacement and soil reinforcement, a collapse settlement reduction factor (CSRF) is introduced as follows:

$$CSRF=\frac{\Delta_h-\Delta}{\Delta_h}$$

Where:

$CSRF$ =collapse settlement reduction factor

Δ_h=collapse settlement of homogeneous collapsible soil

Δ=collapse settlement of reinforced partially replaced collapsible soil

From the results, it can be noticed that when using geogrid within dune sand layer in addition to the geotextile layer at the interface do not give a noticeable difference reduction in the collapse settlement of the footing (CSRF equal to (71%) for one layer and (72%) for two layers) than the case of using geotextile alone (CSRF equal to (68%)).This behavior may be attributed to the geogrid and geotextile work as tension

materials to resist the stress transmitted from foundation.

A series of model loading tests were carried out on gypseous soil improved by replacement with dune sand and reinforced with geosynthetics materials under concentered load. **Figure** (8) exhibits the relationship between the applied pressure and settlement of the gypseous soil in dry and soaked state. **Figure** (8) shows that the mode of failure can be described as a general shear failure. When gypseous soil is soaked for (24) hours and then loaded to failure, large draw down in bearing capacity was observed and a trend of behavior similar to that of local shear failure. This behaviour may be attributed to the breaking of bonds due to soaking. The test of soil at soaked state may be considered as a reference to measure the magnitude of improvement. **Figure** (8) illustrates the tests results at soaking state. From this Figure, it can be observed that the ultimate bearing capacity was (205) kPa; this denotes a high decreasing in bearing capacity after soaking if compared with the dry state. This is probably referred to the high dissolution rate of gypsum and generating voids which lead to reduce the friction areas between soil particles and then reduces the shear strength, in addition to increasing the ability of soil structure to roll slide, and deform to a new structure.

Dune sand was used at dense state to get the benefit of additional frictional resistance and it was placed in steel box by raining technique. This technique is simple and easily prepared to achieve desired density of dune sand.

Dune sand was placed at a depth of (B) and geotextile layer was used at the interface between dune sand and gypseous soil. From the results of collapse tests shown in **Figure** (6), it can be noticd that the best depth which gives minimum collapse settlement is (ds=B). Therefore, this depth is used in calculating bearing capacity after replacement. The test results are shown in **Figure** (9). It can be noticed that bearing capacity increases when replacing the gypseous soil with dune sand.

The reinforcement with geotextile was used at the interface between collapsible soil and dune sand, while, the geogrid was used on two layers (at depth of 0.3B and 0.7B) within the dune sand layer, in addition to the insertion of geotextile layer at the interface. **Figure** (10) shows the relationship between the bearing pressure and settlement for gypseous soil before and after reinforcement. From **Figure** (10), it can be noticed that after reinforcement, there is a high growing in bearing capacity and reduction in settlement when compared with the unreinforced gypseous soil during soaking.

Specific ratio was employed in the tests to investigate the limit of improvement in bearing capacity. This limit represents the ratio between ultimate bearing capacity of gypseous soil replaced by dune sand to the bearing capacity of collapsible soil without replacement. The term was calculated for both reinforced and unreinforced soil.

BCR) (Layered)= qult (Layered) /qult

Where:

BCR) (Layered) =bearing capacity ratio after replacing gypseous soil with dune sand at soaked state.

BCR) (Reinforced)= qult (Reinforced) / qult (Unreinforced)

Where:

BCR) (Reinforced) =bearing capacity ratio after replacing gypseous soil and reinforcing sand at soaked state.

The value of (BCR) when replacing the gypseous soil with dune sand was (1.7), while it was (2.0) when using reinforcement materials. From the results, it can be shown that the bearing capacity increases and that the settlement was reduced as compared with unreinforced tests during soaking.

A series of model loading tests was conducted on gypseous soil improved by replacement with dune sand and using geogrid and geotextile under different values of eccentricities under condition of soaking.

Figure (11) illustrates the load - settlement at edge and center curves for dry gypseous soil under different eccentricity values (e=0.05 B, 0.1 B, 0.15 B, 0.2 B), respectivelly. These results show that the behaviour of load – settlement curves seem to be like the general shear failure curve. This behaviour was expected because soil was in dense state.

The main problem of gypseous soil appeared during soaking because of the dissolution of gypsum. Therefore, many tests are conducted on gypseous soil during soaking under different values of eccentricity. From **Figure** (12), it can be observed that there is a high decrease in bearing capacity after soaking if compared with dry state.

The maximum load carrying increased with the decrease of eccentricity (e=0.05 B), and decreased when (e=0.2 B).

For small value of eccentricity, the difference in settlement between edge and center dial guage is a small value. But, this difference increased with the increase in eccentricity vslue. Therefore, the settlement decreases in dial guage reading at center increase in dial guage reading at edge with increasing the eccentricity value.

Tables (9) and (10) show the values of experimental and theroetical bearing capacity under dry and soaked states at different values of eccentricities.

An attempt was introduced to improve the bearing capacity of collapsible soil upon wetting by partially replacing the soil by dune sand. The geogrid and geotextile have proved in effectiveness in improving the bearing capacity, and reducing the settlement value. **Figure** (13) represents load – settlement at edge and center curves after replacing gypseous soil with dune sand under depth equal to (ds=B) in a soaked state under different values of ecentricities. From examining the figures, it can be observed that the bearing capacity increases after replacement. Also, it is noticed that the gypseous soil shows less settlement.

Figure (14) illustrates bearing pressure-settlement at edge and center curves for gypseous soil after replacing and reinforcing with geogrid and geotextile at different values of eccentricity during soaking. It can be seen that the maximum bearing capacity under soaking is at (e=0.05 B). This behaviour may be attributed to the stiffening effect created by reinforcement. This stiffening refers to the frictional interaction which take place within the mass of reinforced soil with increasing the number of geogrid layers. In addition, geotextile also causes more bond between soil and reinforcement and result in more stable mass structure.

CONCLUSION

1.Dune sand appeared successful in improvement of collapsible soil together with geogrid and geotextile.
2.The behaviour of collapsible soil is governed by its collapse strain, depth of the collapsible soil layer, and the inundation stresses. From the results, it can be conclded the collapse settlement increases with increasing collapse strain, depth of collapsible soil layer, and inundation stresses.
3.Collapse settlement increases due to an increase of the inundation stress and depth of the gypseous soil layer and decreases due to the insertion of the reinforcement material.
4. From the reuslts, using the geogrid within dune sand in two layers in addition to the geotextile layer at the interface gives lower values in collapse settlement than the case of using one layer of geogrid.
5. For concentric loads, the value of (BCR) when repacing the gypseous soil with dune sand was (1.7) time increase in ultimate bearing capacity, while (2) time when using reinforcement materials.
6. For eccentric loads, the load carrying capacity decreases with increase of eccentricity value.
7. At high values of eccentricity (e=0.2 B) high value obtained of (BCR), that equal to (2.8) time when using gysonthetics materials on replaced soil.

REFERENCES

Al-Janabi, F. H., (2002) "Assessment of Non-Linear Behavior of Fuel Oil Treated Reinforced Gypseous Soils", M.Sc. Thesis, Building and Construction Engineering Department, University of Technology, Baghdad.

Annual Book of ASTM Standard, Vol.04.08, (2000).

Bowles, J. E., (1988) "Foundation Analysis and Design", Fourth Edition, McGraw-hill, New York.

Casagrande, A. (1932) "The structure of clay and its importance in foundation engineering." *J. Boston Society of Civ. Engrs*., 19(4), 168-209.

Das, B. M. (1988) "Shallow foundation on sand underlain by soft clay with geotextile interface." *Geotechnical Special Publication* 18: 112-126.

Head, K. H., (1984-1986) "Manual of Soil Laboratory Testing" Volume 1,2, and 3. Prentch Press, London.

Hesse, P.R. (1971) "A text book of soil chemical analysis ".*Chemical Publishing Co*., Int., New York.

Khan, M.A.J., (2005) "Effect of compaction on the behavior of Kirkuk gypseous Soil" M.Sc. Thesis, Civil Engineering Department, University of Baghdad.

Razouki, S. S., Al-Omari, R. R., Nashat, I. H., Razouki, H. F. and Khalid, S. (1994) "The problems of gypsiferous soils in Iraq." *Symposium on gypsiferous soils and their effect on structures*, NCCL, Baghdad.

Raymond, G. P. (1992) "Reinforced sand behavior overlying compressible subgrades." *Journal of Geotechnical Engineering*, ASCE 118(11): 1663-1680.

Soliman, S. and Hanna, A. (2010) "Performance of reinforced collapsible soil." *Advances in* analysis, *Modeling and Design Proceedings of the Geoflorida Conference*, ASCE.

Table (1) physical properties of gypseous soil

w_c , (%)	3.2
γ_{field} , (kn/m^3)	12.9
g_s	2.41
l.l, (%)	36
p.l, (%)	22
k, (cm/sec), (variable head)	$2.358*10^{-5}$
cofficient of uniformity, c_u	2.12
cofficient of curvity, c_c	1.46

Table (2) chemical properties of gypseous soil

chemical composition	Percentage, (%)
SO_3	20.86
cl	0.053
gypsum content	45
T.S.S	47.4
$CaCO_3$	13.30
organic content	0.44
pH	8.8-9.2

Table (3) physical properties of dune sand

$\gamma_{used, (kn/m^3)}$	16.2
g_s	2.71
k, (cm/sec)	$3.452*10^{-4}$
cofficient of uniformity, c_u	1.67
cofficient of curvity, c_c	0.979

Table (4) chemical properties of dune sand

chemical composition	percentage, (%)
SO_3	0.055
cl	0.053
gypsum content	0.24
T.S.S	0.33
organic content	0.13
pH	8.75

Figure (1) general view of testing equipment

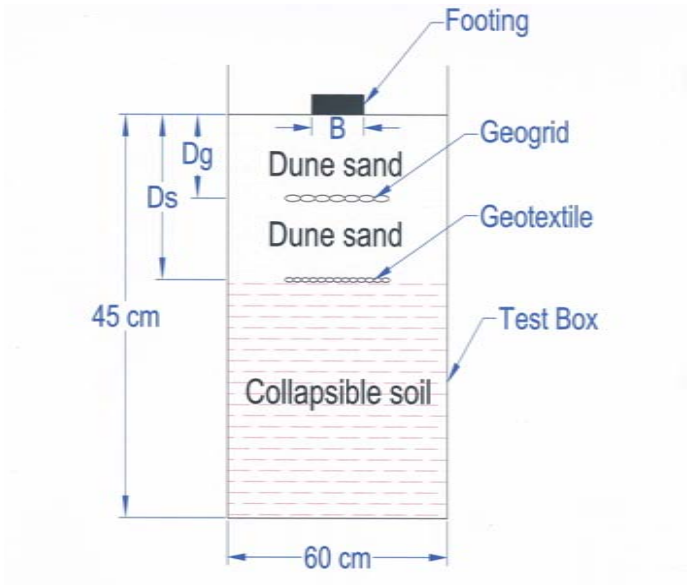

Figure (2) sketech for the test box illustrates some of the studied parameters

Table (5) properties of geogrid used, as supplied by building research center (iraq)

grid dimension, (mm)	8*6
thickness, (mm)	3.3
grid weight, (kg/m^2)	0.73
tensile strength (kn/m)	7.68

Table (6) properties of geotextile used, as supplied by building research center (iraq)

width of meshes, (mm)	0.10
thickness, (m)	$2.26*10^{-3}$
weight, (gr/m^2)	729
tensile strength warp, (n/5cm)	10870
tensile strength weft, (n/5cm)	2020

]

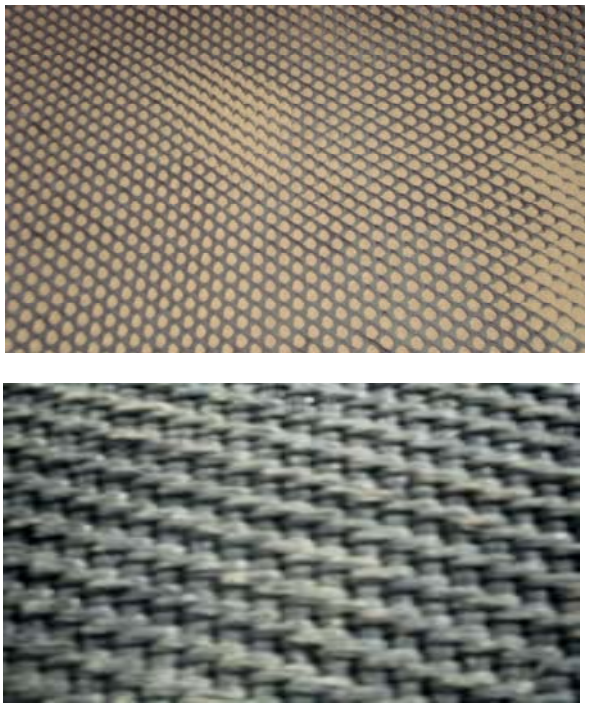

Figure (3) geogrid and geotextile used

Table (7) results of collapse settlement under different inundation stress

inundation stress, (kpa)	100	150	200
collapse settlement ratio, $\frac{\Delta_h}{B}$	0.0786	0.2448	0.4635
collapse strain, $\Delta_h / h_\circ$	1.75%	5.44%	10.3%

Table (8) relation between depth of geogrid and collapse settlement ratio

depth of geogrid	**collapse settlement ratio,** $(\frac{\Delta_h}{B})$
0.3 b	0.1338
0.7 b	0.143
0.3band 0.7b (two layers)	0.128

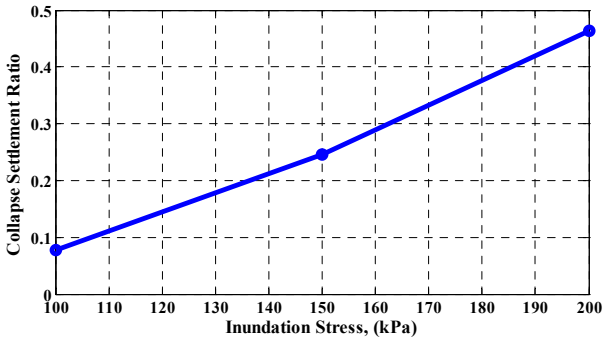

Figure (4) relationship between inundation stress and collapse settlement ratio

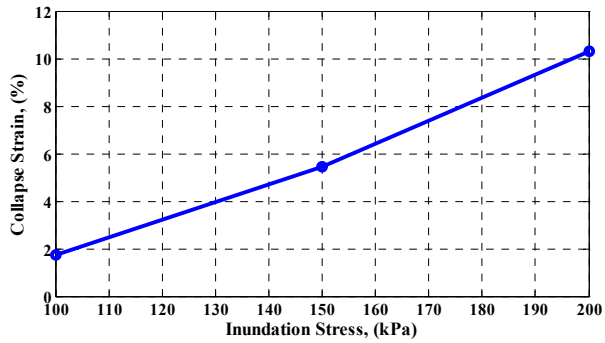

Figure (5) relationship between collapse strain and collapse settlement ratio

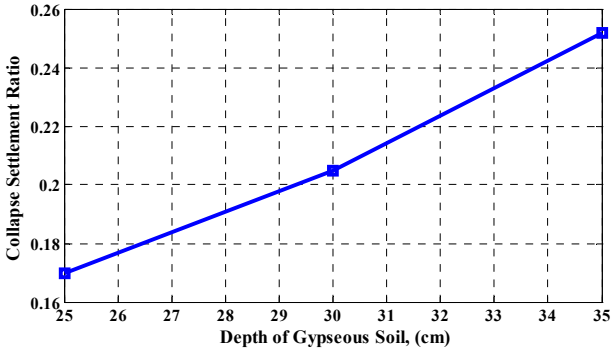

Figure (6) relationship between depth of gypseous soil and collapse settlement ratio

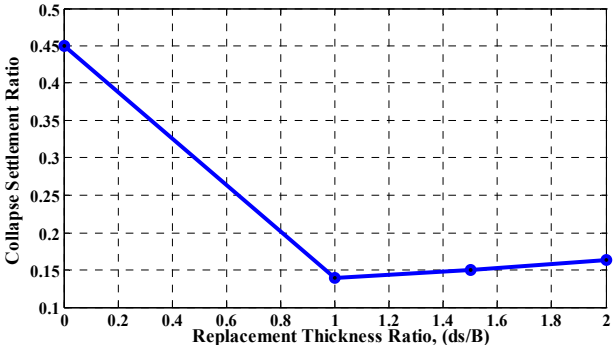

Figure (7) effect of replacement thickness ratio (ds /b) on the collapse settlement ratio within inclusion of geotextile

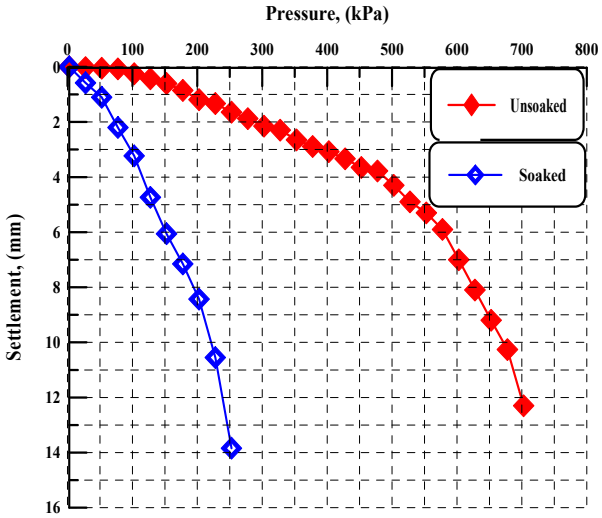

Figure (8) pressure - settlement relation for gypseous soil at dry and soaked state

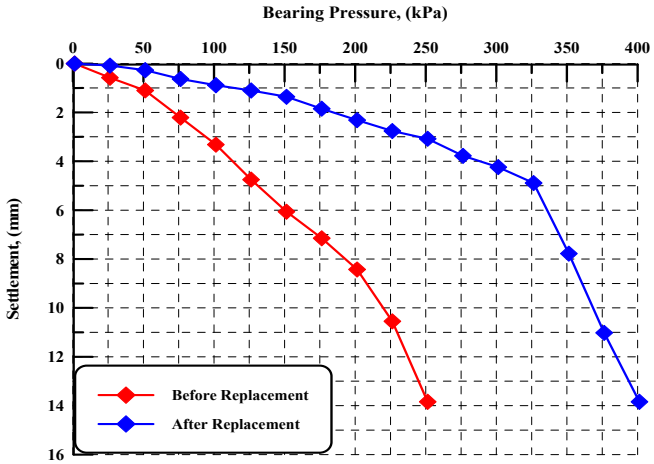

Figure (9) pressure - settlement relation of gypseous soil before and after replacement (soaked soil)

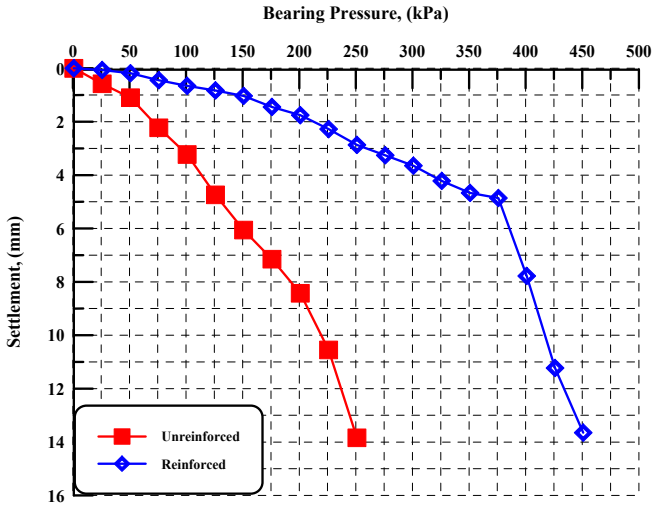

Figure (10) pressure - settlement relation of gypseous soil before and after reinforcement on replaced soaked soil

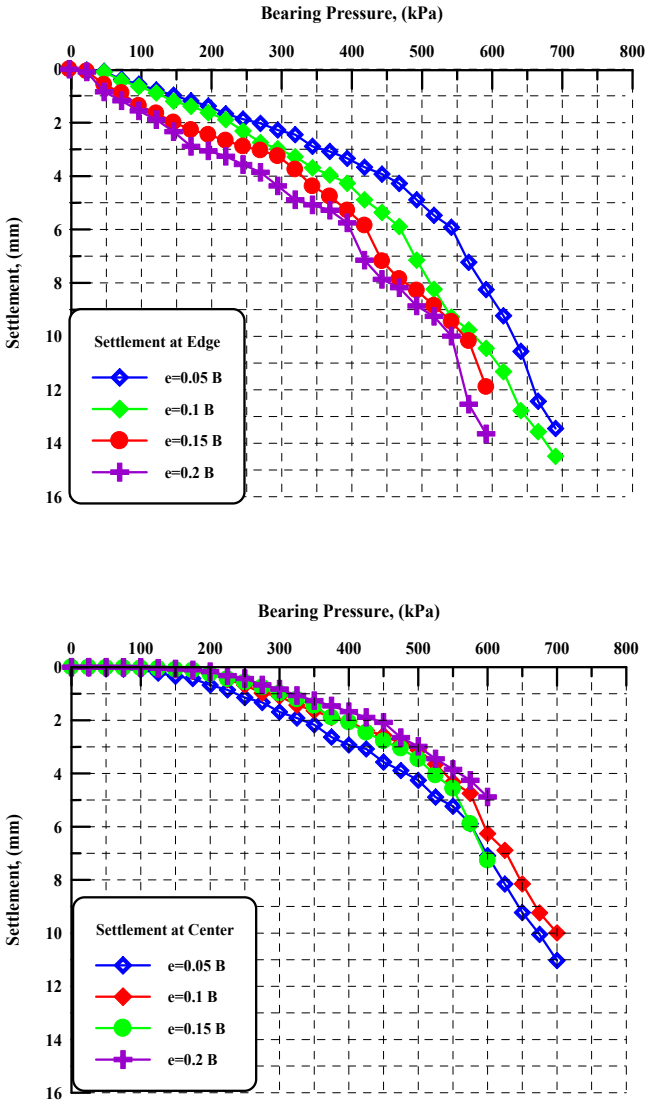

Figure (11) pressure - settlement curves at edge and center for gypseous soil at dry state

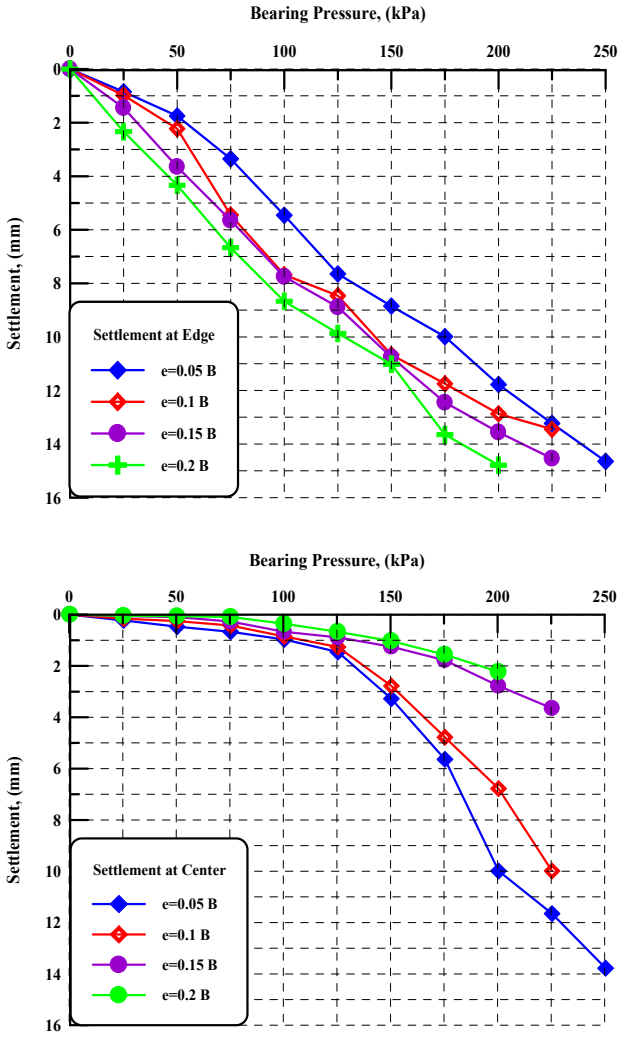

Figure (12) pressure - settlement at edge and center curves at center for gypseous soil at soaked state

Table (9) experimental and theoretical ultimate bearing capacity of (dry state)under different values of eccentricities

ultimate bearing capacity, (kpa)	theoretical	experimental results
bearing capacity at (e=0.05 b)	551.23	648
bearing capacity at (e=0.1 b)	540.63	635
bearing capacity at (e=0.15 b)	530	565
bearing capacity at (e=0.2 b)	519.40	540

Table (10) experimental and theoretical ultimate bearing capacity of (soaked state) under different values of eccentricities

ultimate bearing capacity, (kpa)	theoretical	experimental results
bearing capacity at (e=0.05)	134.85	187.5
bearing capacity at (e=0.1 b)	134.60	182
bearing capacity at (e=0.15 b)	134.36	140
bearing capacity at (e=0.2 b)	134.14	125

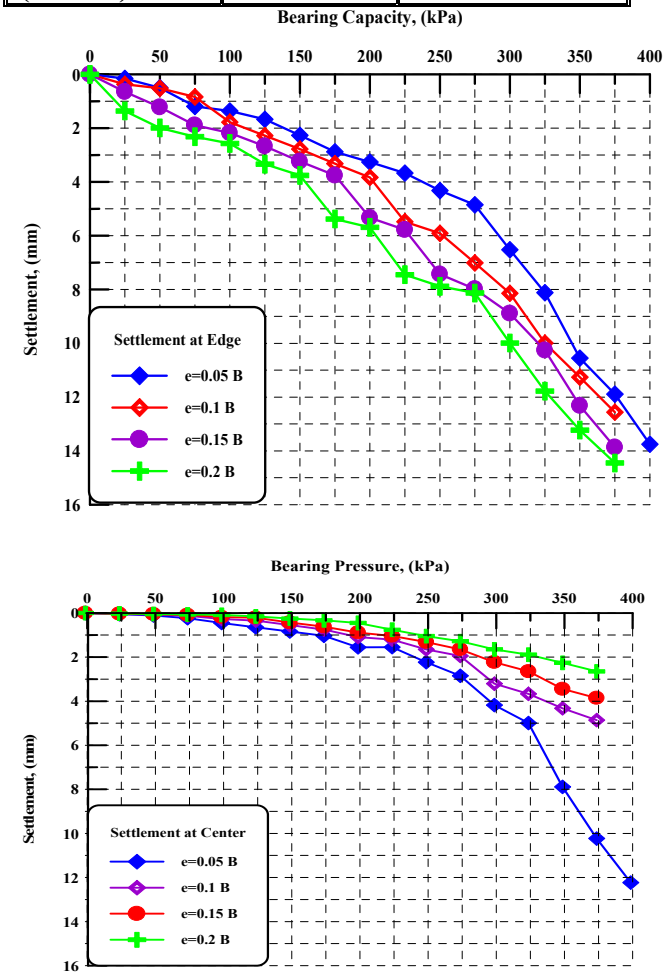

Figure (13) pressure - settlement at edge and center curves for gypseous soil after replacement

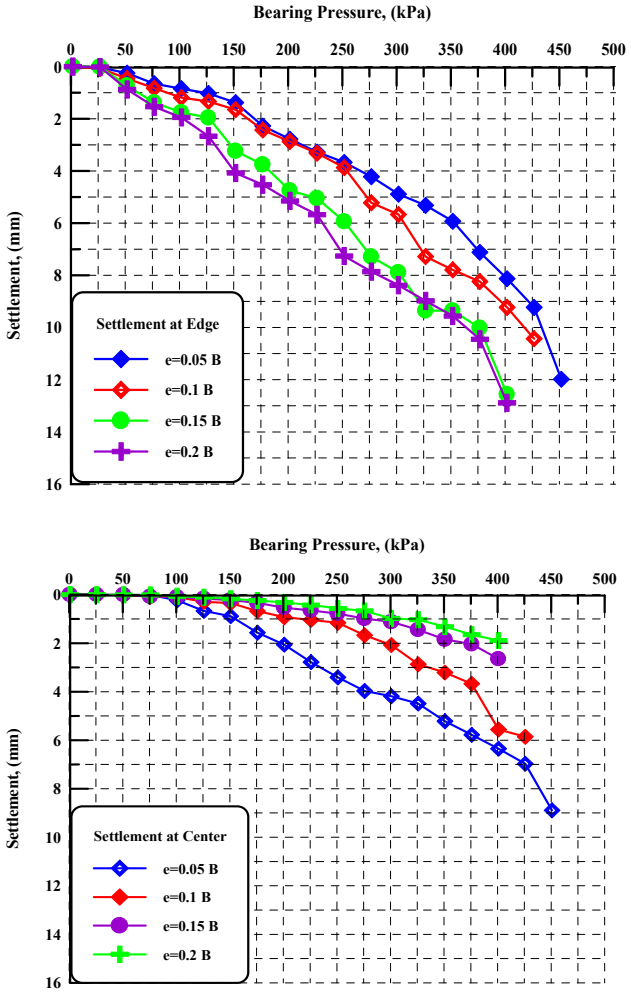

Figure (14) pressure - settlement at edge and center curves for gypseous soil after reinforcement on replaced soaked soil

Experimental and Numerical Analysis of Piled Raft Foundation with Different Length of Piles Under Static Loads

Prof. Dr. Mosa Jawad Al-mosawe Prof_mosa _2006@yahoo.com
Assist. Prof. Dr A'amal Abdul Ghani Al-Saidi dr_aamal@yahoo.com.
Dr. Faris Waleed Jawad civileng_faris@yahoo.com
Civil Engineering Department, College of Engineering, University of Baghdad

ABSTRACT:

In order to understand the effect of (**length of pile / diameter of pile**) ratio on the load carrying capacity and settlement reduction behavior of piled raft resting on loose sand, laboratory model tests were conducted on small-scale models. The parameters studied were the effect of pile length and the number of piles. The load settlement behavior obtained from the tests has been validated by using **3-D** finite element in **ABAQUS** program, was adopted to understand the load carrying response of piled raft and settlement reduction. The results of experimental work show that the increase in ($\mathbf{L_p/d_p}$) ratio led to increase in load carrying capacity by piled raft from (19.75 to 29.35%), (14.18 to 28.87%) and (0 to 16.49%) , the maximum load carried by piles decrease from (9.1 to 22.72%), (15.79 to 47.37%) and (44 to 81.05%) and the response of settlement piled raft decrease from (16.67 to 23.33%), (9.09 to 39.39%) and (30%) with increase the number of piles from 4 to (6 and 9) and (**length of pile / diameter of pile**) ratio increase to (14.14 and 21.2), respectively. The numerical and model test results are found to be in a good agreement.

KEYWORDS: Piled Raft; Different Length of Piles; Experimental and Numerical Static Work.

دراسة عملية وتحليلية للاسس الحصيرية المدعمة بالركائز مختلفة الاطوال تحت الاحمال الساكنة

موسى جواد الموسوي **امال عبد الغني حسين السعيدي** **فارس وليد جواد**
استاذ دكتور **استاذ مساعد دكتور** **دكتوراه**

الخلاصة

من اجل فهم تأثير نسبة (**طول الركيزة/ قطر الركيزة**) على مقدار التحمل والهطول للأساس حصيري مدعم بالركائز جالس على تربة رمليه مفككة تم بناء نموذج مختبري مصغر. العوامل التي تم دراستها هي تأثير طول الركيزة وزيادة عدد الركائز. النتائج التي تم الحصول عليها مختبريا سوف يتم تأكد منها ومقارنتها عدديا باستخدام العناصر المحددة المتاحة في برنامج (**ABAQUS**) لقد أظهرت النتائج أن زيادة في نسبة (**طول الركيزة/ قطر الركيزة**) يؤدي إلى زيادة في سعة تحمل الأساس الحصيري المدعم بالركائز من (19.75 الى 29.355)، (14.18 الى 28.87%) و (0 الى 16.49%))، نقصان في بمقدار سعة التحمل للركائز من (9.1 الى 22.72%)، (15.79 الى 47.37%) و (44 الى 81.05%) وان مقدار التقليل في الهطول الاساس الحصيري المدعم بالركائز بلغ (16.67 الى 23.33%)، (9.09 الى 39.39%) و (30%) مع زيادة عدد الركائز من (4) الى (6 و 9) وزيادة نسبة (**طول الركيزة/ قطر الركيزة**) من (21.2 الى 14.14) على التوالي . وان المقارنة النتائج العملية والعددية باستخدام العناصر المحددة أظهرت توافق جيد.

الكلمات الرئيسية:اساس حصيري مدعم بالركائز، ركائز مختلفة الاطوال، دراسة عملية وعددية تحت تأثير الاحمال الساكنة.

1. INTRODUCTION

One of the most important aspects of a civil engineering project is the foundation system. Designing the foundation system carefully and properly, will surely lead to a safe, efficient and economic project overall. In other words, foundation system design is one of the most critical and important step when a civil engineering project is considered. Until quite recently, there were some separately used systems like shallow foundations such as rafts and deep foundations such as piles. However, lately the foundation engineers tend to combine these two separate systems. By combining these two systems, the foundation engineer will provide the necessary values for the design obtain the required safety and also come out with a more economical solution. Several authors studied piled raft foundation in experimental and analytical work by different materials such as concrete model **Katzenbach et al**. (1997) and aluminum model, **Giretti** (2009).

In this paper, in order to examine the effect of pile length on the behavior of piled raft in loose sand, experimental work and three-dimensional finite element analyses were carried out using **ABAQUS/CAE 6.10.1** program. The parameters studies:

1) 4-piles raft at ($\mathbf{L_p/d_p}$=10.61, 14.14 and 21.2) where L_p and d_p are variable length and diameter of pile (dp=14.14mm), respectively.
2) 6-piles raft at ($\mathbf{L_p/d_p}$=10.61, 14.14 and 21.2)
3) 9- piles raft at ($\mathbf{L_p/d_p}$=10.61, 14.14 and 21.2).

2. EEXPERIMENTAL WORK:

A series of model loading tests were conducted inside a steel box of dimensions (600X600X700mm) depth, made of steel plate of 3mm thickness, stiffened with 3 lines of 25mm angle sections, provided with 280 *220mm hatch for sand refilling as shown in **Plate (1)**.

The internal faces of the box were covered with polyethylene sheets in order to reduce the slight friction which might be developed between the box surface and soil. Scaling laws were followed in the design of the model to eliminate the model stress error and boundary effects.

The square aluminum raft model was a 120mm in dimension and thickness (t_r=15mm). The square cross section aluminum model of piles employed in the tests (d_p=14.14mm) as shown in **Plate (2).**

2.1. Static Loading Measurment

A conventional compression machine with digital control system was used to apply the axial loading on footing model .The load on the footing was measured using proving ring of 3KN capacity. The settlement of pile raft model was measured by two dial gauges (0.001mm, division) fixed on the edges of the footing by two magnetic holders as shown in **Plate (3)**.

The static load of pile in group measured by strain gage was (50mm) gage length, (120Ω) resistance, (2.1) gage factor and it was bonded to the pile surface by using instance adhesive which was specially used for the strain gage type. Before bonding the strain gage, the pile surface was smoothed and cleaned by alcohol. The surface of pile was coated by epoxy resin to protect the strain gauges. Thus each model pile was tightly secured through openings in the raft using screws to create a fixed-head condition (see **Plate (4)**). The half Wheatstone bridge circuit was used for strain gages connection, **Dally et al**. (1965).

2.2. Soil Used

2.2.1 Sand Properties:

Poorly graded sand was used in the tests. The sand was placed in the test box at unit weight of approximately 15.3 kN/m^3 (relative density=30%). Some properties of sand are given in **Table (1)**.

2.2.2 Mechanical Behavior of Sand

The mechanical behavior of dry sand in loose state used at (Dr=30%, γ_d=15.3kN/m^3 and e=0.73) using triaxial test (UU test) and direct shear test are listed in **Table (1).**

2.3 Mechanical Properties of Aluminum Used

The aluminum specimen used to model raft and piles were tested in accordance to the **ASTM (B557–06)** specifications. Yield strength **(**fy**)**, tensile strength (fu), elongation (e) and Poisson's ratio (v). The results mechanical properties of aluminum used under tensile test can be listed in **Table (2).**

3. NUMERICAL WORK

All the numerical calculations were carried out with the finite element program **ABAQUS/CAE.** The 3D-models are developed to soil depth, pile dimensions and soil properties from the test are adopted into the models. Each separate part of the model, such as piles and soil, is given its material properties.

Piles are assumed to have linear elastic behavior and the material behavior of the soil was simulated using the modified Drucker-Prager elasto plastic material model. In **ABAQUS/CAE** program a mesh of model type C3D8R an 8-node linear hexahedral element used and the total number of element (22392) as shown in **Plate (5).**

The interactions between surfaces need to be assigned properties in order to determine the behavior of the interfaces. The relative motions between surfaces are set normally. Tangentially interaction has "rough" behavior which means that the relative velocity between the surfaces is zero i.e. no slip can occur. The interaction between the raft and the soil is assumed to be rough to represent the assumed full adhesion between the sand and the raft surface, but the interaction between pile surfaces and soil is assumed surface to surface contact (standard) tangentially behavior depend on interface angle.

4. RESULTS AND DISCUSION OF EXPERIMENTAL WORK

Figures (1 to 3) show the measured load-settlement curves for piled raft at (N=4, 6 and 9), s=3dp, tr=15mm and Dr =30% (where N is the number of piles, s: spacing between piles, tr: raft thickness and Dr: relative density of sand). In general the results show the increase L_p/d_p value led to increase in load carrying of piled raft and decrease in load carrying by piles in piled raft due

to increase in the interaction load with increase L_p/d_p ratio.

Figure (4) shows the computed maximum load versus the ratio L_p/d_p. It is clear that the maximum load carried by piled raft increase from (19.75 to 29.35%), (14.18 to 28.87%) and (0 to 16.49%) and the maximum load carried by piles decrease from (9.1 to 22.72%), (15.79 to 47.37%) and (44 to 81.05%) with increase the number of piles from N= 4 to (N = 6 and 9) and L_p/d_p ratio increase to (14.14 and 21.2), respectively.

Figure (5) shows the computed maximum settlement versus the ratio L_p/d_p. The response of settlement piled raft decrease from (16.67 to 23.33%), (9.09 to 39.39%) and (30%) with increase the number of piles from N= 4 to (N = 6 and 9) and L_p/d_p ratio increase to (14.14 and 21.2), respectively.

5. COMPARSION OF EXPERIMENTAL AND NUMERICAL WORKS

The results obtained from the 3D-finite element analysis are presented and compared with the experimental results. **Figures (6 and 7)** show the comparison results of max. load and max settlement plotted with L_p/d_p ratio, respectively. It can be seen from the figures that the finite element results are close to the experimental test results are in the ranges of (1.1-1.16). **Figures (8 and 9)** show the three dimensional full and half contour mapping of miss stress at max load of 6-Piled Raft**.**

6. CONCLUSION

- In general the increase in L_p/d_p ratio led to increase in maximum load carrying by piled raft and decrease in maximum settlement.
- The increase in L_p/d_p ratio led to decrease in load carrying by pile (axial load) due to increase in the load carrying by shaft of pile (interaction load).
- The increase in L_p/d_p ratio for piled raft has the number of piles (N=4 and 6) is more effective than piled raft at (N=9).
- 3-D finite element by using **ABAQUS** program shows good results are compared with the experimental test results.

7. REFRENCES

- ASTM (B557 – 06) **"Standard Test Methods for Tension Testing Wrought and Cast Aluminum- and Magnesium-Alloy Products".**
- ASTM D422-2001, **"Standard Test Method for Particle Size-Analysis of Soils"**.
- ASTM D4253-2000, **"Standard Test Method for Maximum Index Density and Unit Weight of Soils Using a Vibratory Table"**.
- ASTM D4254-2000, **"Standard Test Method for Minimum Index Density and Unit Weight of Soils and Calculation of Relative Density"**.
- ASTM D854-2005, **"Standard Test Method for Specific Gravity of Soil Solids by Water Pycnometer".**
- Dally, J.W., and Riley, W.F. (1965), **"Experimental Stress Analysis"** McGraw-Hill Book Company.
- Daniela Giretti (2009) **"Modeling of Piled Raft Foundations in Sand"** Ph. D. Thesis, University of degli Studi di Ferrara.
- Katzenbach, R. & Arslan, U. & Gutwald, J. & Holzhäuser, J. (1997). **"Soil-Structure-Interaction of the 300m High Commerzbank Tower in Frankfurt am Main, Measurements and Numerical Studies".** Proc. of the Fourteenth Intern. Conf. on Soil Mech. and Found. Eng., Hamburg, 6-12 September 1997: 1081-1084, Rotterdam.

Plate (1): Container of Sand Used.

Plate (2): Square Aluminum Raft Model, Piles and the Screwed Opening to Fix Piles.

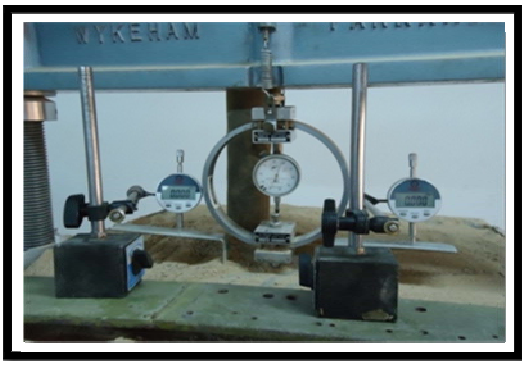

Plate (3): Instrumentation of Static Loading.

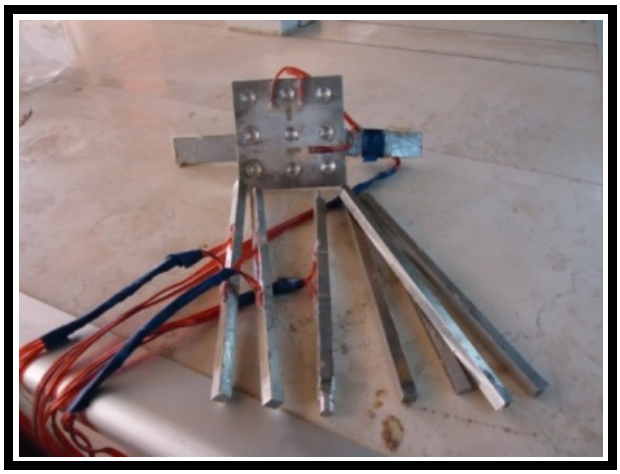

Plate (4): Aluminum Footing Model with Strain Gage.

Table (1): Properties for Sand Used.

Property		Values
***Specific Gravity*, Gs**		2.65
Dry Unit Weight (γ_d) of Sand	Maximum unit weight, γ_{dmax}	17.9kN/m^3
	Minimum unit weight, γ_{dmin}	14.4 kN/m^3
Void Ratio(e) of Sand	Maximum void ratio (e_{max})	0.81
	Minimum void ratio (e_{min})	0.45
Dry Unit Weight Used (γ_d)	Loose state, γ_{dused}	15.3
Void Ratio Used (e)	Loose state (e_{used})	0.73
Friction Angle (Φ^o)	Loose state	28.81°
Poissons Ratio (ν)	Loose state	0.30
Modulus of Deformation (E_s, kN/m^2)	Loose state	10000

Table (2): Mechanical Properties of The Used Aluminum Alloy.

Property	Value
Modulus of Elasticity (GPa)	70
Minimum % of Elongation (e)	10
Assume Poisson's Ratio (ν)	0.33

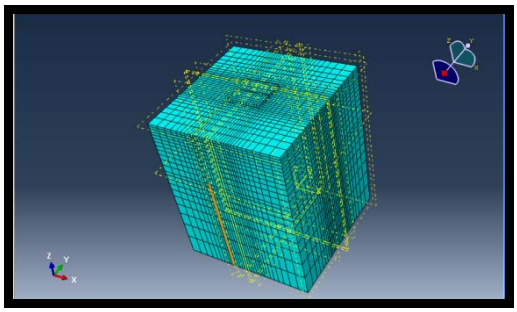

Plate (5): Meshing Model of Piled Raft.

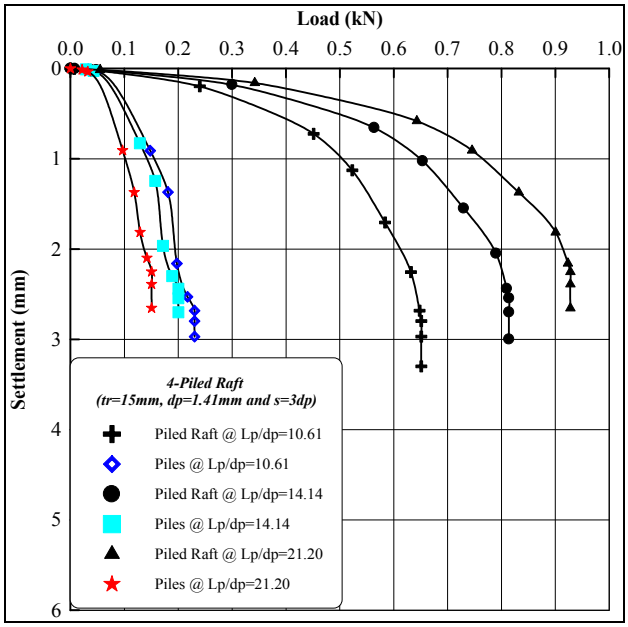

Figure (1): Load-Settlement curves for 4-Piled Raft.

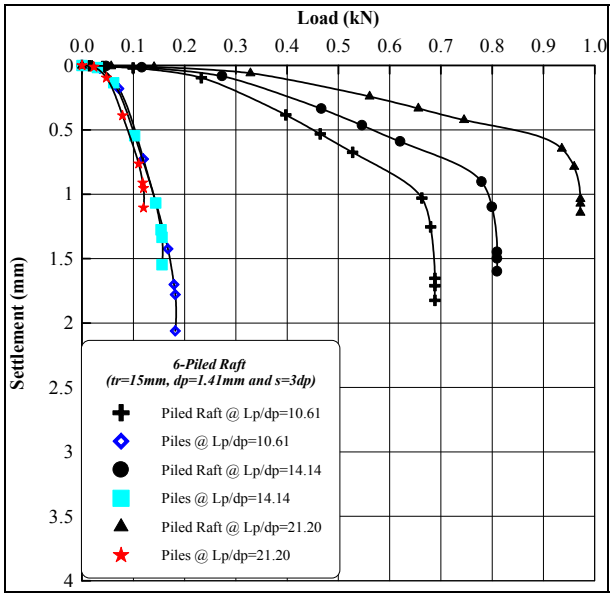

Figure (2): Load-Settlement curves for 6-Piled Raft.

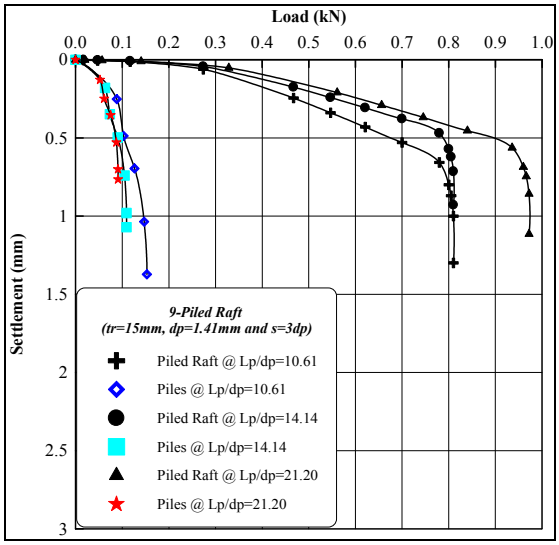

Figure (3): Load-Settlement curves.

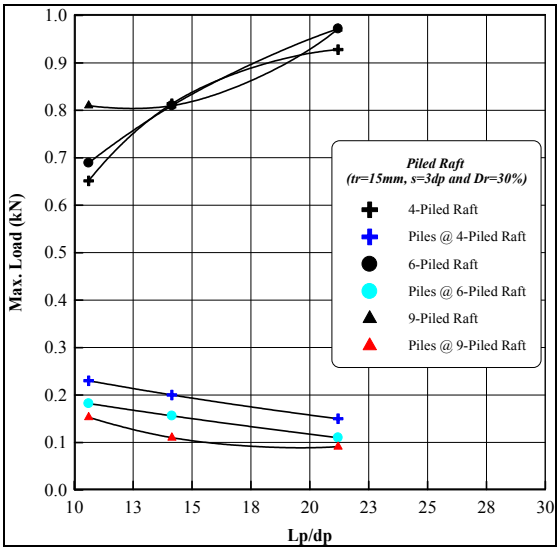

Figure (4): Max. Load- L_p/d_p Ratio Curves.

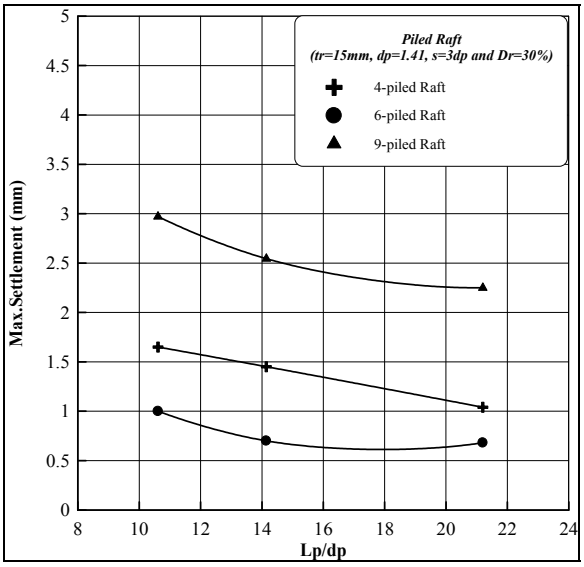

Figure (5): Max. Settlement L_p/d_p Ratio Curves

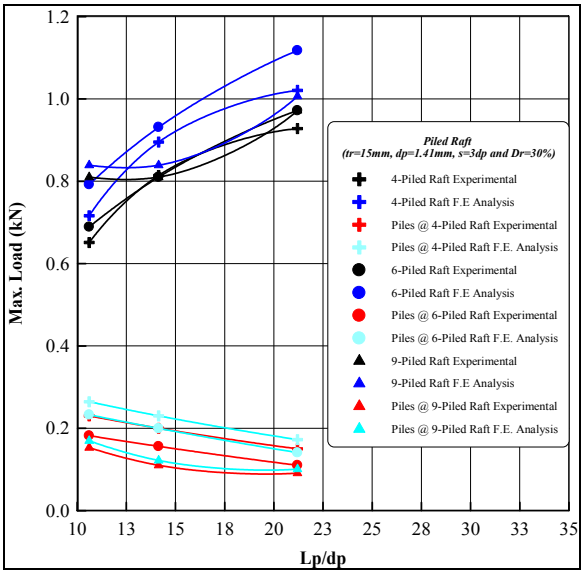

Figure (6): Comparison of Max. Load- L_p/d_p Ratio Curves.

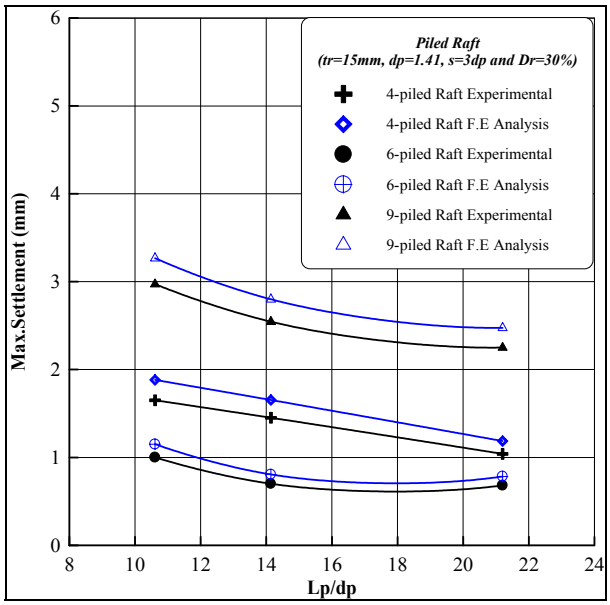

Figure (7): Comparison of Max. Settlement L_p/d_p Ratio Curves.

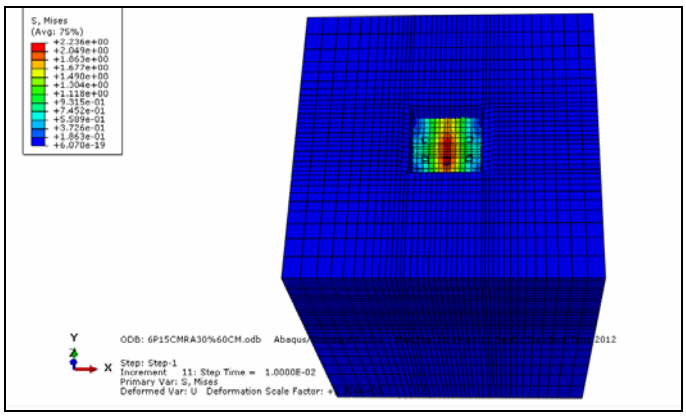

Figure (8): Three Dimensional Full Contours Mapping of Miss Stress

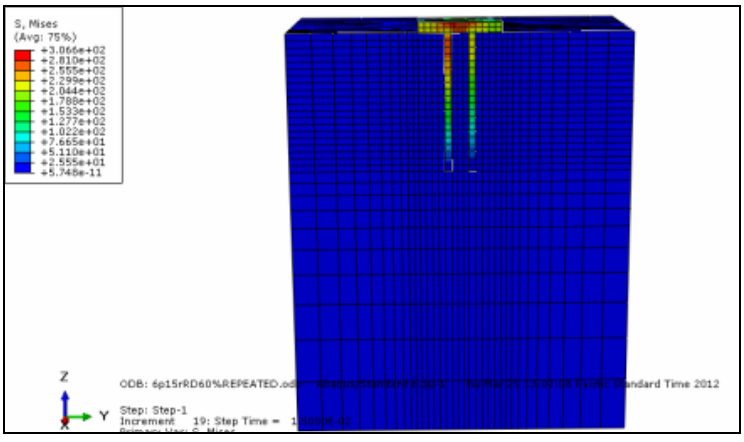

Figure (9): Three Dimensional Half

Contours Mapping of Miss Stress

Flotation Method for Selective Separation of Lead and Zinc from Simulated Wastewater

Ass. Prof. Dr. Ahmed Abed Mohammed **Saba Waleed kadhem**

sosa_wkd @ yahoo. com

Environmental Engineering Department-College of Engineering

University of Baghdad

ABSTRACT

In this paper flotation method experiments were performed to investigate the removal of lead and zinc. Various parameters such as pH, air flow rate, collector concentrations, collector type and initial metal concentrations were tested in a bubble column of 6 cm inside diameter. High recoveries of the two metals have been obtained by applying the foam flotation process, and at relatively short time 45 minutes . The results show that the best removal of lead about 95% was achieved at pH value of 8 and the best removal of zinc about 93% was achieved at pH value of 10 by using 100 mg/l of Sodium dodecylsulfate (SDS) as a collector and 1% ethanol as a frother. The results show that the removal efficiency increased with increasing initial metal concentrations in the alkaline conditions while it decreased in the acidic condition. Increasing air flow rate up to 1000 ml/min enhanced the separation efficiency. Selective flotation experiments were also conducted in the presence of metal ion mixture solutions. It was possible to separate lead and zinc under suitable condition, successful removals reached about 84% and 81% for lead and zinc respectively . It was observed that the first order equation fitted the data as good and better than any of the other equations.

KEY WORDS: - Flotation, heavy metals, wastewater

طريقة التعويم للفصل الانتقائي لعنصري الرصاص والخارصين من المياه الملوثه

ا. م. د. احمد عبد محمد و صبا وليد كاظم

قسم الهندسة البيئية _كلية الهندسة_ جامعة بغداد

الخلاصه

طريقه التعويم انجزت لتحقيق فصل عنصري الخارصين والرصاص من المياه الملوثه ولقد تم دراسه العوامل التي تؤثرعلى عمليه الازاله وبالتالي كفاءه الفصل هذه العوامل تتضمن الداله الحامضيه ،تصريف الهواء، تركيز الخارصين، تركيز الرصاص، تركيزالماده الخافضه للشد السطحي ونوعها وايضا تاثير اضافه ملح الطعام. ولقد تم الحصول على كفاءات عاليه في استرجاع العنصرين باستخدام طريقه التعويم وبوقت قصيرنسبيا 45 دقيقه. النتائج اعطت 95% استرجاع لعنصرالرصاص في داله حامضيه مقدارها8 و93% استرجاع لعنصرالخارصين تم في داله حامضيه مقدارها 10 باستعمال SDS كماده خافضه للشد السطحي واستخدام 1%ايثانول كعامل مساعد. النتائج بينت ان زياده التركيز الاولي للعناصر يزيد كفاءه الازاله في الوسط القاعدي ويقللها في الوسط الحامضي .وقد وجد ان زياده تصريف الهواء الى 1000 ml/min يزيد كفاءه الازاله .

تجارب التعويم للفصل الانتقائي ايضا تم مناقشتها بوجود محاليل خليط ايونات المعادن حيث من الممكن فصل الرصاص والخارصين تحت ظروف ملائمه بكفاءات 84% و81% للرصاص والزنك على التوالي .وقد وجد ان معدل ثابت الانتقال من الدرجه الاولى.

كلمات رئيسيه :- التعويم، العناصر الثقيله، المياه الملوثه

INTRODUCTION

Water pollution is nowadays a matter of deep apprehension. Many industrial wastewaters contain numerous toxic metals, such as chromium, zinc, cadmium, lead and copper which must be removed before reuse of the water or its discharge to the environment (Zhang and Jing, 2009). In order to reduce the pollution problem in environment that is caused by these heavy metals, their concentrations must be reduced before discharging to obey the wastewater standards So, an effective treatment process must be applied. Among the evaluated processes flotation method is proved to be one of the most effective method as a separation process due to its simplicity, rapidity, economy, good and high separation yields(R>95%), large possibility of application for species having different nature and structure and production of more concentrated sludge, occupying smaller volumes .It is believed that this process will be soon incorporated as a clean technology to treat water and wastewater (Ghazy et. al.,2008). Therefore, flotation technique was selected for this investigation. The technique of ion flotation provides a simple physical method for removing and concentrating the ions present in very dilute solutions. The method is classified as a foam separation process, which relies on the direct

Interaction between an ionic surfactant and an oppositely charged metal ion (either simple or complex). If the ions to be removed are not surface active, they can be made so through union with or adsorption of surface-active agents (Nicol et. al.,1992). With the aid of suitable surfactants the metal ions are rendered hydrophobic giving origin to metal-collector complexes known as "sublate". When rising bubbles are introduced into the system, the sublate adsorbs on the bubble-water interface and are carried upwards producing a foam layer at the top of the bulk solution. This layer can then be physically separated from the bulk solution (Scorzelli et. al.,1999). The size of the air bubbles in flotation cell should be fine in the order of a few hundred micrometers to present sufficient surface area for collection. The reagents which control the size of the bubbles by reducing the air/water interfacial tension are called frothers. As opposed to the classical flotation process where the valuable mineral species are floated and removed with the froth, ion flotation is selectively concentrating the metal ions in froth phase. A successful removal of metal ions should correspond to a large metal ion/water ratio in the froth phase (Polat and Erdogan, 2007). The scope of this study was to investigate the efficiency of bubble column for the removal of zinc and lead from waste water analyzing the flotation kinetics in term of pH, air flow rate, anionic and cationic surfactant, initial metals concentration and ionic strength.

EXPERIMENTAL WORK

Materials

two types of surfactants, Sodium dodecyl sulfate (SDS; MW=288 g/mol) and Hexadecyltrimethyl ammonium bromides (HTAB; MW=364.5 g/mol)

from Fisher Scientific were used as anionic and cationic collectors, respectively. The first type is a white powder material with a chemical structure of ($C_{12}H_{25}OSO_3Na$).The second type is a white powder material with a chemical structure of ($C_{12}H_{42}BrN$). Ethanol (C_2H_5OH) from Lancaster Synthesis was used as frother. Zinc nitrate hexahydrate ($Zn(NO_3)_2.6H_2o$, assay (complexometric)= 98.5-102% and MW=297.51 g/mole) made in the European Union and Lead nitrate ($Pb(NO_3)_2$; Minimum assay =99.5% and MW=331.21 g/mole) made by (BPH) chemical LTd poole England were used as the colligend. Sodium chloride (NaCl, purity=99.5% wt) from Fisher Scientific were used as the ionic strength adjuster. Nitric acid (HNO_3) and caustic soda (NaOH) were used for pH adjustments. Air was the gas used in the present study (compressed at 1 bar up to 7 bars) and supplied by a compressor.

Method

The foam flotation tests were carried out in a bubble column (acrylic) of 6 cm inside diameter and 120 cm in height. Air supplied by the compressor was fed to the column through a pre-calibrated rotameter. Air entered the column was dispersed as bubbles into liquid. Feed enter with different metal concentration (25 ,50 ,and 100 ppm) was poured gently at the top of the column. Perforated plate of the air distributor was used which has 25 holes with 0.05 cm diameter. The column was operated at batch mode as far as the liquid phase and continuous flow with respect to air. This column contains six taps of 0.2 cm inside diameter, arranged at interval of 15cm and used to draw samples from the column.

Preparation of Solution

Synthetic polluted water samples with desired concentration of Zinc and Lead were prepared by dissolving ($Zn(NO_3)_2.6H_2O$, and $Pb(NO_3)_2$) in distilled water. Surfactants and ethanol were added to the synthetic polluted water. Foam samples were taken at preset time intervals as 3, 5, 10, 15, 20, 25, 30, 40 and 55 minutes. A port 0.45 m above the base was used for periodic sampling. The required mass of $Zn(NO_3)_2.6H_2O$ or $Pb(NO_3)_2$ was calculated as follows:

$$W = V \times C_i \times \frac{M.wt}{At.wt} \quad (1)$$

Where W: Weight of $Zn(NO_3)_2.6H_2O$ or $Pb(NO_3)_2$ (mg); V: Volume of solution (l); C_i: Initial concentration of zinc or lead ions in solution (mg/l); MW: Molecular weight of $Zn(NO_3)_2.6H_2O$ or $Pb(NO_3)_2$ (g/mol); At.wt: Atomic weight of zinc or lead (g/mole).

RESULTS AND DISCUSSION

Effect of pH

Solution pH is a significant factor for determining the form and the charge of the metal present in solution, so, the initial flotation tests were conducted as a function of pH to observe the response of the zinc and lead towards the collectors used. The experiments with anionic SDS (100 mg/l) were carried out at pH values of 3, 6, 8, and 10 for lead and zinc and the results are presented in Figures 1 and 2. These Figures show that the concentration ratios decreases suddenly at the beginning of the run then the ratios began to decrease slowly with time due to consumption of surfactant with time. From the figure the highest removal of lead was a chieved when the pH of the

solution was 8. And the highest removal of zinc was achieved when the pH of the solution was 10. According to (Ghazy et. al.,2008) the dominant species for lead are positively charged Pb^{+}, $PbOH^{+}$ recovery for pH value of 8. The removal of lead ions at pH=8 was rapid and virtually complete within a relatively short time than the removal of lead at any other pH. Similar observations can also be made for Zn at pH value of 10. At pH 10 where zinc hydroxide precipitation take place the removal of zinc ions was more efficient (Zouboulis et. al., 2003).

Effect of initial metal concentration

The effect of initial metal concentration was also tested. The results were presented in Figures 3 and 4, when the initial metals concentrations was increased to 100 mg/l in the presence of 100 mg/l SDS and 1% ethanol at pH 8 for lead and pH 10 for zinc, the recovery decreased. According to (Shakir and Ahmed, 2010) the decreasing in removal rate due to large surfactant:metal ion ratio which cause competition for bubble surface, between the metal-collector product and free collector ions.

Effect of surfactant concentration

Similar flotation tests were also conducted as a function of SDS at pH value of 8 for lead and 10 for zinc, the results were presented in Figures 5 and 6. From these figures, it was found that surfactant concentrations have a much greater effect on removal efficiency at acidic conditions than basic conditions. This result was similar to (Lemlich, 1972) he suggested that the metal ions are completely soluble at low pH and the removal rates are strongly dependent on collector concentration requiring higher collector concentration for at pH values less than 8, and they are negatively charged $Pb(OH)^{-}_{3}$ and $Pb(OH)^{-}_{4}$ at pH values greater than 8. At pH value of 8, precipitation takes place that explain the higher complete removal and at high pH the metal ions are insoluble and the removal rates are considerably less affected by collecter concentration.

Effect of surfactant type

The removal rate of metals ions from water was studied at two different types of surfactant (sodium dodecyl sulfate and Hexadecyltrimethyl ammonium bromide) in order to show the effect of adding anionic and cationic surfactant on the removal rate of metals. The effect are shown in Figures 7 and 8. From these figures, it can be seen that the anionic surfactant (SDS) is more efficient than the cationic surfactant (HTAB), and at pH 8 for (lead, zinc) there is no significant removal rate was obtained by using (HTAB) and the removal rate increases for pH 10 for lead. This result was similar to Polat and Erdogan (2007) they suggested that the increasing removal rate for more alkaline pH solutions was explained by the appearance of negatively charged metal species.

Effect of air flow rate

The effect of air flow rate (250,500 and 1000 ml/min) at fixed SDS and ethanol concentration was also tested. The data presented in Figures 9 and 10 indicate that the removal efficiency of metals was highly affected by the gas flow rate. According to (Sulaymon and Mohammed, 2010) as gas flow rate increased, the removal efficiency increased, This is because increased gas flow rate causes early bubble detachment, large fluid activities (stress) at the bottom section and bubble coalescence and (mostly)

break up. However, higher gas flow rate of 1000 ml/min results in decreasing the removal efficiency from the maximum due to the redispersion of some of the metal collector–precipitate product back in to the bulk solution.

Selective flotation of metals

In the selective flotation of lead and zinc, metal ions were floated selectively when they are present together. The foregoing discussion implies that selective separation of ionic constituents in a solution can be achieved through pH adjustment (Lu et. al. 2005). Different flotation experiments were performed. The influence of the pH on the selectivity of metal ions were examined, for Lead-Zinc system, the best separation of lead was achieved at pH 8 where the lead in precipitate form $pb(OH)_2$ whereas zinc is in positive form.The results are presented in Figures 12 these results simply show that SDS has much more affinity towards the available lead species at this pH than it has towards the zinc species. And the best separation of zinc was achieved at pH 10 where the zinc in precipitate form $Zn(OH)_2$ whereas lead is in negative form.

The effect of adding NaCl to the (Zinc-Lead) system at pH value of 8 was shown in Figures 11 From this figure the removal rate decreases with NaCl concentration. This decrease can be explained by the competition between Na^+ ions with Zn^+ and Pb^+ ions so the metals cannot find enough sulfate molecules to attach to (Choi et. al.,1998).

CONCLUSIONS

1. High recoveries of metals from dilute aqueous solutions containing SDS have been obtained by applying the foam flotation process, and at relatively short time. The results show that the best removal of lead
2. about 95% was achieved at pH value of 8 when lead concentration 100 mg/l, SDS concentration 100mg/l, ethanol 1% and gas flow rate 500 ml/min and the best removal of zinc about 93% was achieved at pH value of 10 when zinc concentration 100 mg/l, SDS concentration 100mg/l, ethanol 1% and gas flow rate 500 ml/min.
3. Flotation studies were conducted to investigate the selectively removing metals, high recoveries from mixture solutions containing SDS have been obtained. The results show that for lead the best removal about 84% was achieved at pH value of 8 and for zinc the maximum removal efficiency about 82% was achieved at pH value of 10, when zinc concentration 100 mg/l, lead concentration 100 mg/l, SDS concentration 100 mg/l, ethanol 1% and gas flow rate 500 ml/min.

REFERENCES

Choi, S.J., and Kim, K.H., The improvement of the removal efficiency of foam flotation by synergistic effect of mixed surfactant solutions, Environment Technology, 19, 1151-1156(1998).

Ghazy, S. E., El-moray, S. M., and Ragab, A. H., Ion flotation of copper (II) and lead

(II) from environmental water samples, J. Ap pl. Sci. Environ. Manage, 12, 75 –82(2008).

Lemlich, R., Adsorptive bubble separation techniques, Academic Press ,New York and London (1972).

Lu, S., Pugh, R. J., and Forssberg, E., Interfacial separation of particles: Studies in interface science, Elsevier, 634-635(2005).

Nicol, S.K., Galvin, K.P., and Engel, M.D., Ion flotation—potential applications to mineral processing, Minerals Eng., 5, 1259–1275 (1992).

Polat, H., and Erdogan, D., Heavy metal removal from waste waters by ion flotation, Journal of Hazardous Materials, 148, 267-273 (2007).

Scorzelli, I.B., Fragomeni, A.l., and Torem, M.L., Removal of cadmium from a liquid effluent by ion flotation, Minerals Eng., 12, 905–917 (1999).

Shakir, K., and Ahmed, F. , Removal of rhodamine (a basic dye) and thoron (An acidic dye) from dilute aqueous solutions and wastewater stimulants by ion flotation, Water Research, 44, 1449– 1461(2010).

Sulaymon, A., and Mohammed, A., Separation and hydrodynamic performance of air –kerosene-water system by bubble column, International Journal of Chemical reactor engineering, 8, 1-15 (2010).

Zhang, J., and Jing, Y., Removal of trace Cu^{2+} from aqueous solution by foam fractionation, Desalination, 249, 503–506 (2009).

Zouboulis, A.I., Matis, K.A., and Stalidis, G.A., Parameters influencing flotation in removal of metal ions, International Journal of Environmental Studies, 35, 183-196 (1990).

l; SDS=100 mg/l; Q =500 ml/min;
Ethanol=1%)

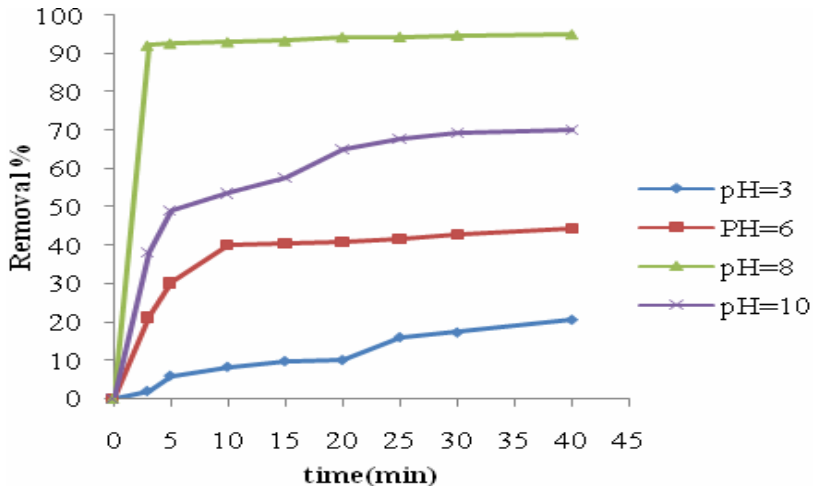

Fig. 1 Effect of pH on the removal efficiency of lead ions (C_o = 100 mg/l; SDS=100 mg/l; Q =500 ml/min; Ethano1=1%).

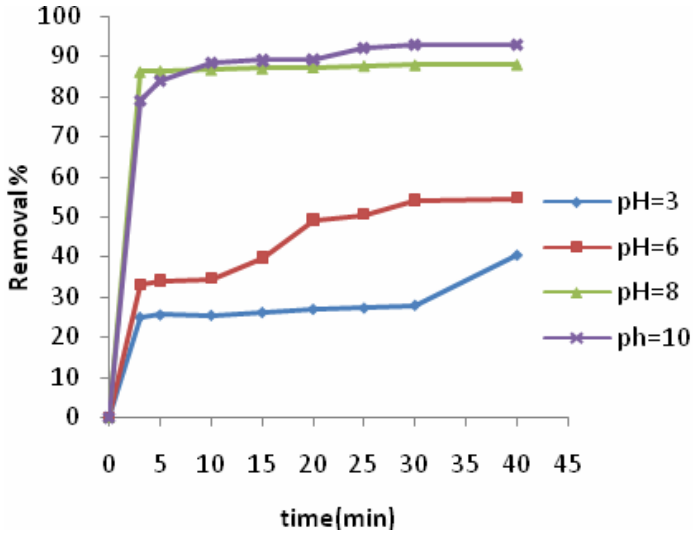

Fig. 2 Effect of pH on the removal efficiency of zinc ions (C_o = 100 mg/l; SDS=100 mg/l; Q =500 ml/min; Ethanol=1%).

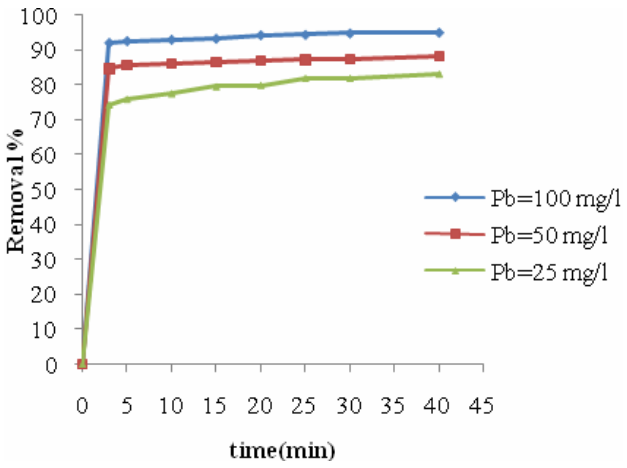

Fig. 3 Effect of lead concentration on the removal rate (pH=8; SDS= 100mg/l; Q=500 ml/min)

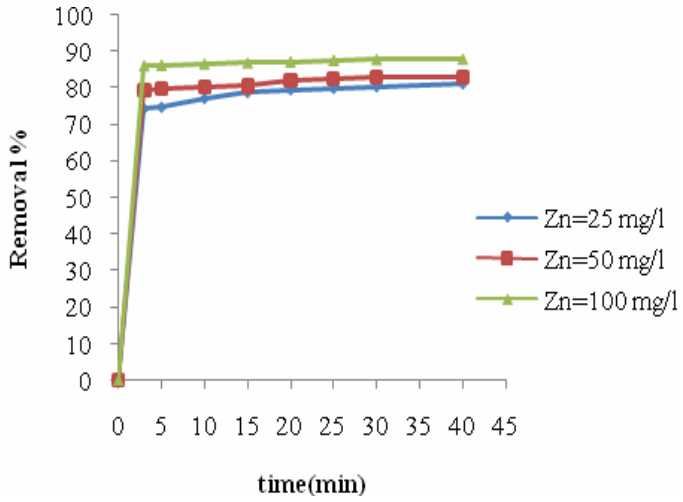

Fig. 4 Effect of zinc concentration on the removal rate (pH=8; SDS= 100 mg/l; Q =500 ml/min)

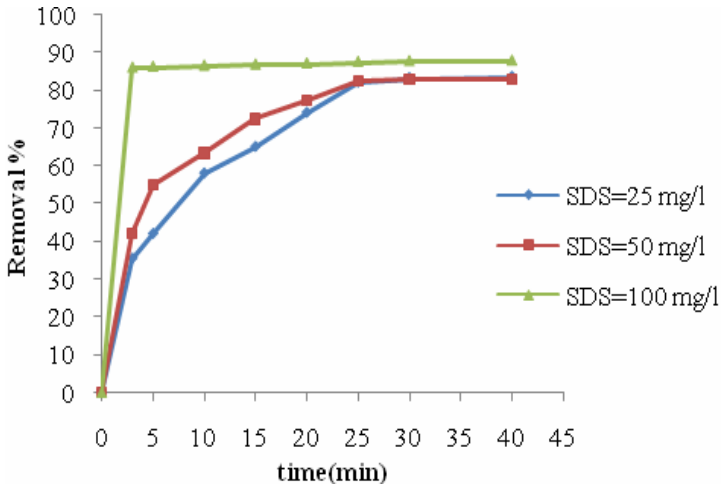

Fig.5 Effect of surfactant conc. on the removal of zinc that (pH = 8; Co = 100 mg/l; Q = 500ml/min)

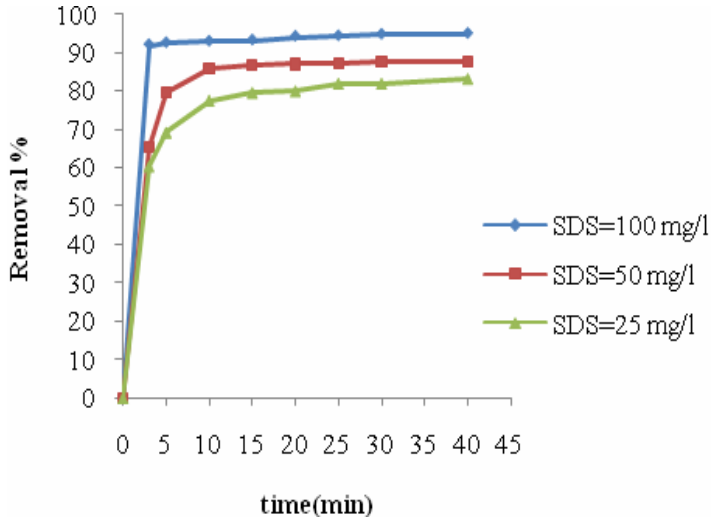

Fig. 6 Effect of surfactant conc. on the removal rate of lead (pH=8; Co=100mg/l; Q=500ml/min)

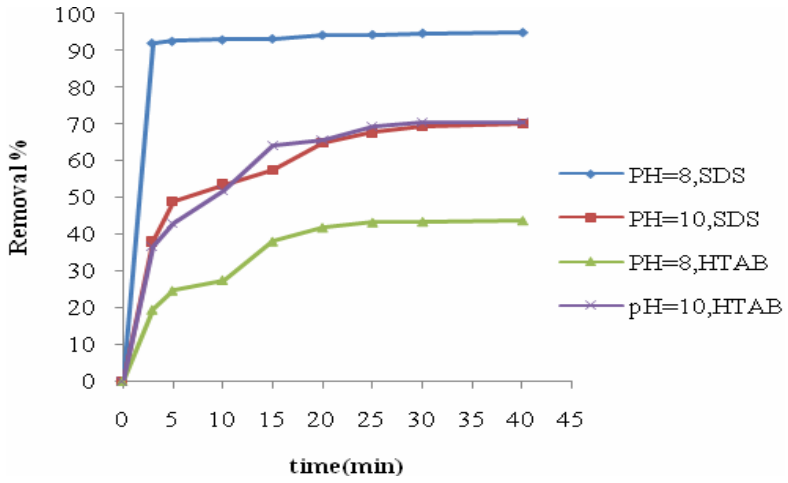

Fig.7 Effect of surfactant type on the removal rate of lead (SDS=100mg/l; HTAB=100mg/l; Pb=100 mg/l; Q=500ml/min)

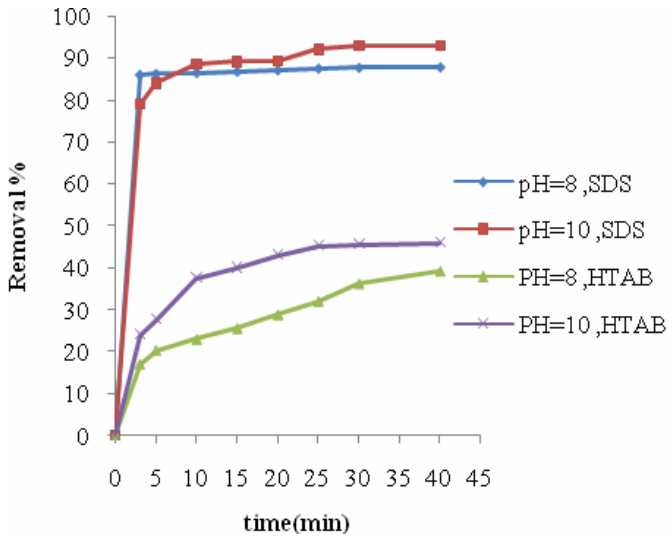

Fig. 8 Effect of surfactant type on the removal rate of zinc (SDS=100mg/l; HTAB=100mg/l; Zn=100mg/l; Q=500ml/min)

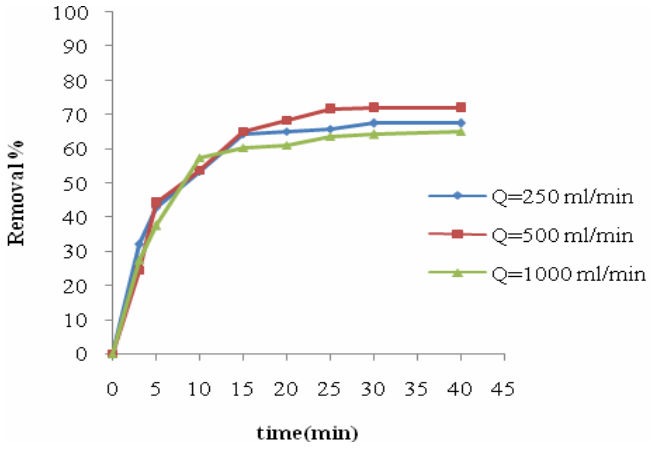

Fig. 9 Effect of gas flow rate on the removal of lead (pH=8; Pb=100 mg/l; SDS=100 mg/l;Ethanol=1%)

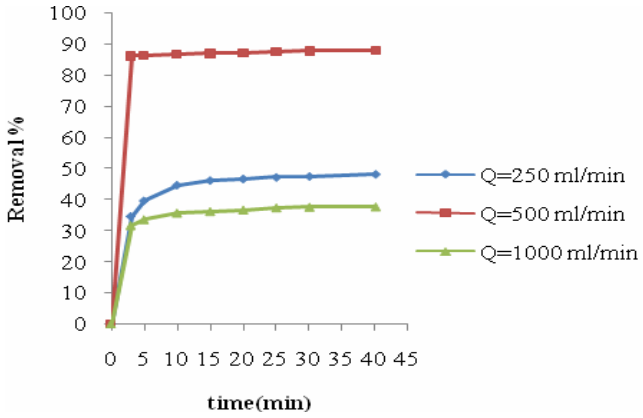

Fig. 10 Effect of gas flow rate on the removal of Zinc (pH=8;Zn=100mg/l; SDS=100mg/l;Ethanol =1%)

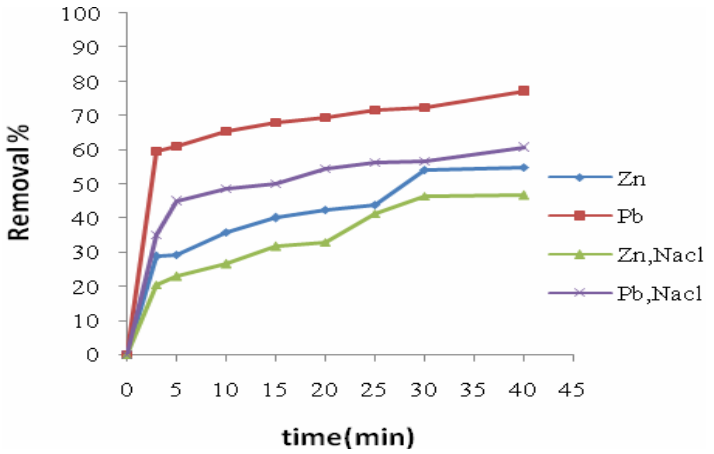

Fig.11 Effect of NaCl on the removal rate of metals(pH=8;SDS=100mg/l; NaCl=50mg/l Zn=100mg/l; Pb=100mg/l; Q=500 ml/min)

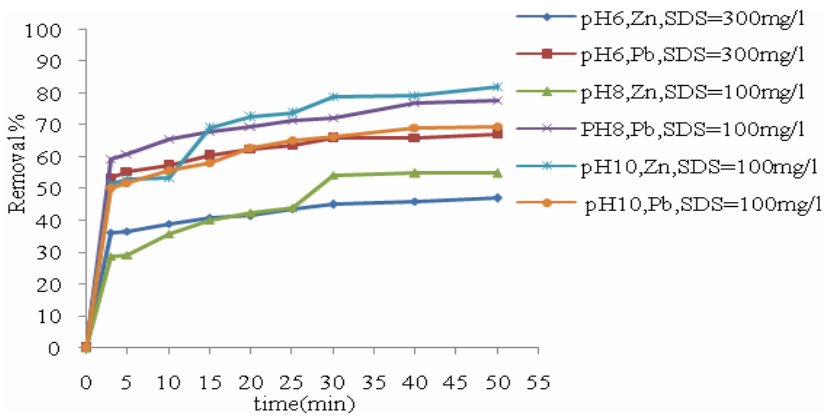

Fig. 12 Effect of pH on the removal of zinc and Lead (Zn=100 mg/l; Pb=100 mg/l; SDS=100mg/l; Q=500 ml/min)

Design and Analysis of Electro-Hydraulic Servo System for Speed Control of Hydraulic Motor

Dr. Ali Abdul Mohsin Hassan AL-Assady
Asst. prof. Dept. of Mech. Eng.
Email: dralicit@yahoo.com
Baghdad University

Mohammad Talib. Jassim AL-Khafaji
Dept. of Mech. Eng.
Email: mohammad_t.jassim @yahoo.com
Baghdad University

ABSTRACT

In this study, the electro-hydraulic servo system for speed control of fixed displacement hydraulic motor using proportional valve and (PID) controller is investigated theoretically ,experimentally and simulation . The theoretical part includes the derivation of the nonlinear mathematical model equation of (valve – motor) combination system and the derivation of the transfer function for the complete hydraulic system , the stability test of the system during the operation through the transfer function using MATLAB package V7.1 have been done. An experimental part includes design and built hydraulic test rig and simple PID controller .The best PID gains have been calculated experimentally and simulation, speed control performance tests for the system at different thermal conditions for hydraulic oil have been done , Simulation analysis for (EHSS) using Automation Studio package V5.2 have been done . Comparison was made between experimental work and simulation work .The experimental results show good performance for (EHSS) using simple (PID) controller at hydraulic oil temperature around (60 – 70 °C) and good speed response and performance for hydraulic motor with constant rotation speed (700) rpm with different load disturbance applied on the hydraulic motor .

KEYWORDS: **Servo, PID controller, Proportional valve, Hydraulic motor, Automation Studio (AS)**

تصميم وتحليل منظومة الكترو- هيدروليكية مغلقة للسيطرة والتحكم في سرعة محرك هيدروليكي

أ.م.د علي عبد المحسن حسن الاسدي **جاسم الخفاجي طالب محمد**

الخلاصة

يتناول هذا البحث دراسة نظرية وعملية وبطريقة المحاكاة لمنظومة الكترو-هيدروليكية للتحكم في سرعة دوران محرك هيدروليكي ثابت السعة باتجاة واحد بأستخدام صمام تناسبي .الجانب النظري يتضمن أستقاق المعادلات اللا خطية للنموذج الرياضي لنظام مجموعة (الصمام – محرك) واشتقاق معادلة دالة الانتقال (transfer function) للنظام الهيدروليكي الكامل .تم أجراء فحص الاسقرارية اثناء التشغيل بواسطة معادلة دالة الانتقال وبستخدام برنامج (MATLAB package V7.1) .الجانب العملي يتضمن تصميم وبناء جهاز الاختبارالهيدروليكي وتصميم وبناء دائرة التحكم بسيطة (PID controller) . تم ايجاد افضل قيم للثوابت دائرة التحكم عمليا وبأستخدام برنامج المحاكاة .تم اجراء فحص أداء التحكم بالسرعة للمنظومة في ظروف حرارية مختلفة لزيت الهيدروليك .جانب الدراسة الخاص بالمحاكات التشبيهية للمنظومة الهيدروليكية تم بستخدام برنامج المحاكاة الخاص بالمنظومات الهيدروليكية المسمى (Automation Studio package V5.2) .المقارنة تمت بين النتائج العملية ونتائج المحاكات للبرنامج .النتائج العملية اظهرت اداء جيد للمنظومة بأستخدام زيت الهيدروليك عند درجة حرارة تتراوح بين 60 الى 70 درجة سيليزية واستخدام دائرة تحكم بسيطة (PID controller).تم الحصول على نتائج متقاربة للنتائج العملية بأستخدام المحاكاة للمنظومة .استجابة واداء جيد للتحكم بسرعة الموتور الهيدروليكي واستقرارها عند سرعة دورانية ثابتة (700) (دورة / دقيقة) تحت تسليط احمال مختلفة على المحرك الهيدروليكي.

الكلمات الرئيسية :- النظام المغلق ، منظم تناسبي تكاملي اشتقاقي ،صمام تناسبي ،محرك هيدروليكي ،برنامج المحاكات الدوائر الهيدروليكية

INTRODUCTION

Electro-hydraulic servo system (EHSS) is widely used in many industrial applications and mobile systems because of their high power-to-weight ratio, high stiffness, fast response, self cooling, good positioning capabilities, etc. Either of two basic methods is used for electro hydraulic servo system for speed control of a hydraulic motor.

First, a variable displacement pump controls flow to the motor. Second, a servo or proportional valves Second method is a closed loop speed control system the actuating error signal which is the difference between the input signal and the feedback signal which is fed to the controlled so as to reduce the error and bring the output of the system to a desired value .This work is focused on study fixed displacement pump-Fixed displacement motor by using proportional valve PV and PID controller. The closed- loop of speed control as shown in **fig. 1** Vladimir (2006).

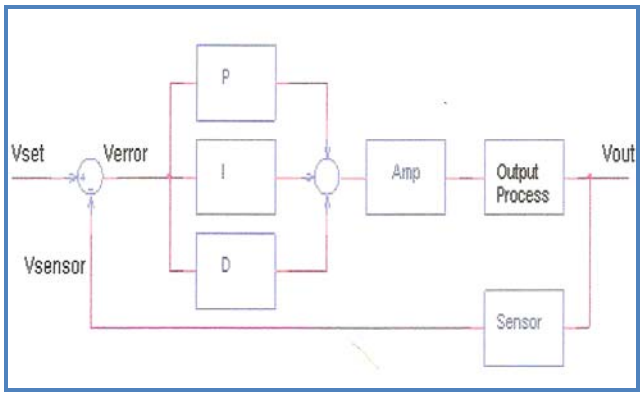

Fig (1): Schematic diagram of the Servo control system with PID controller

The error signal is control signal which controlled using (PID) controller (proportional integral derivative) controller .this type of controller is still the most popular ones in the processing industries for speed control.

There are several circuits for speed control system like meter – in flow controls, meter – out flow controls, bleed – out flow controls and variable volume pump .the meter – in/out flow controls as shown in **fig. 2** (Web site 1).

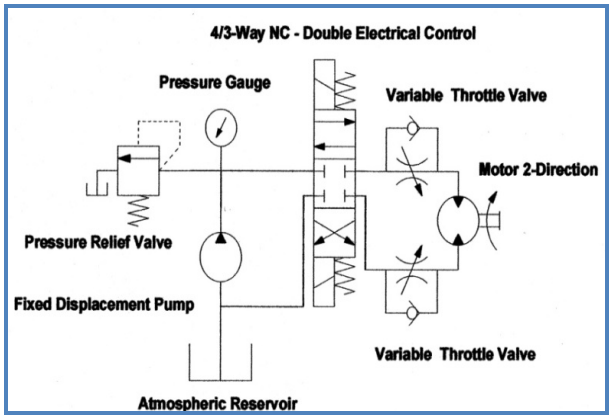

Fig (2): Motor circuit with meter – in / out flow controls

Much research work have been accomplished in the area of the performance investigation of(EHSS) for speed control with various combinations of pumps and motors.

Ambuel (1993) introduced an experimental and analytical study dealt fuzzy – PI control applied to speed control of fixed displacement hydraulic motor. They found that the performance characteristics of a hydraulic motor under conventional (PI) control could be improved by implementing a fuzzy– PI controller design.

Yasukazu (2000) **,** introduced simulations and experimental study dealt with new type for rotational speed control of hydraulic motor with large inertia loud by using sliding mode control**.** the result of theoretical and experimental study of sliding mode control show many benefits such as setting time and low sensitivity to disturbances and system parameter variations in the (HS).

Aichao et al (2008) introduced simulation and analytical study dealt with the speed regulation fundamental principle of complete system fixed displacement pump- variable displacement motor. and use integral control . The AME Sim simulation model of the system was Built, analyzing the influences of relevant factors on constant speed output control, The simulation results provides theoretical basis for designing the constant speed output of the hydraulic motor under change of many factors and give good response of the system output .

Dasgupta et al (2011) introduced modeling and simulation study dealt with comprehensive model of closed- loop servo valve controlled

hydro motor drive system has been made using (Bond graph simulation technique) . The dynamic performance of the complete system has been studied with respect to the variation of the parameters of the (PI) controller that drives the servo valve, They have also studied the effects of the variation of torque motor parameters on the servo valve performance using MATLAB simulik environment.

Hossam et al(2011) introduced an experimental and theoretical study of (EHSS) of speed control of hydraulic motor .The performance of the model-based control system depends strongly on the accuracy of the process model used. Least squares support vector machines method (LS-SVM) is powerful method for modeling nonlinear system results show good performance over wide range of operating conditions and load disturbances.

In the present work, the objective is to investigate experimentally speed control system for the hydraulic motor using fixed displacement pump and proportional valve with a simple (PID) controller under different range of hydraulic temperature and simulation analysis for the system with Automation Studio (AS) package V5.2.

THEORETICAL ANALYSIS

The modeling of the system has been performed depend on assumptions (Vladimir 2006):-

- A constant pressure source
- Fluid inertia is neglected.
- No flow reversal or cavitations
- Return line pressure (P_o) is neglected
- Orifices are matched and symmetrical

MATHEMATICAL DESCRIPTION OF THE PV AND HYDRAULIC MOTOR

The nonlinear dynamic model of (EHSS) shown in **Fig. 3**, which consists of a hydraulic motor controlled with proportional valve**.** **(**Merritt1967**)**

Equations of flow through the PV are derived from the application of flow continuity through the orifices of proportional valve and defined by the following terms**:-**

$$Q_1 = C_d A \sqrt{\frac{2}{\rho}(P_s - P_1)} \quad (1)$$

$$Q_1 = C_d A \sqrt{\frac{2}{\rho}(P_s - P_2)} \quad (2)$$

$$Q_2 = C_d A \sqrt{\frac{2}{\rho}(P_2 - P_o)} \quad (3)$$

$$Q_2 = C_d A \sqrt{\frac{2}{\rho}(P_1 - P_o)} \quad (4)$$

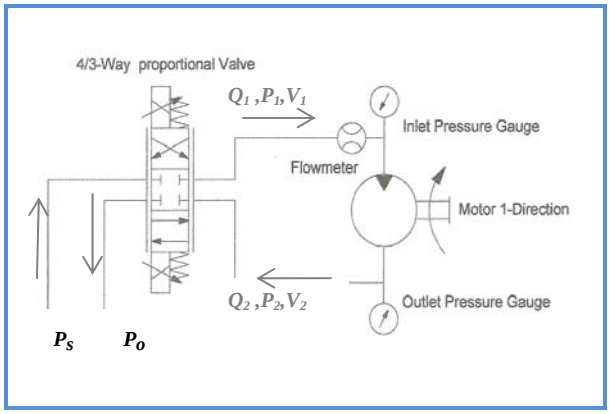

Fig (3): Schematic diagram of (valve – motor) combination system

If internal and external leakages are neglected, hydraulic pressure behavior for a compressible fluid volumes is given by the differential equations (1,2,3,4) :-

$$Q_L = C_d |A| \frac{x_v}{|x_v|} \sqrt{\frac{1}{\rho}\left(P_s - \frac{x_v}{|x_v|} P_L\right)} \quad (5)$$

Where Q_L is the load flow threw the motor and P_L is the loud pressure. Linearized flow equation, which describes dynamic behavior of the proportional valve and around an operating point, is as follows:-

$$\Delta Q_L = K_q \Delta X_v - K_c \Delta P_L \quad (6)$$

Where Kq is the flow gain of the PV and K_c is the pressure flow gain of the valve. K_q and K_c are given by:-

$$K_q = C_d \pi d_{spool} \sqrt{\frac{1}{\rho}(P_s - P_L)} \quad (7)$$

$$K_c = \frac{C_d \pi d_{spool} X_v}{2\sqrt{\frac{1}{\rho}(P_s - P_L)}} \quad (8)$$

By assuming:-

$$Q_L = \frac{Q_1 + Q_2}{2} \quad (9)$$

$$P_L = P_1 - P_2 \quad (10)$$

The continuity equations for each motor chamber same equations. (Merritt 1967):-

$$Q_1 - C_{im}(P_1 - P_2) - C_{em} P_1 = D_m \omega_m + \frac{V_1}{\beta}\frac{dP_1}{dt} \quad (11)$$

$$C_{im}(P_1 - P_2) - C_{em} P_2 - Q_{mo} = -D_m \omega_m + \frac{V_2}{\beta}\frac{dP_2}{dt} \quad (12)$$

From equations 9,10,11,12

$$Q_L = D_m \omega_m + C_{tm} P_L + \frac{V_t}{2\beta} P_L s \quad (13)$$

Where $V_1 + V_2 = V_t$

The torque equation for motor is given by :-

$$T_g = (P_1 - P_2) D_m = J_m \omega_m s + B_m \omega_m + T_{fm} + T_m + T_s \quad (14)$$

From equations 6, 13 and 14, over all TF for the system is given by :-

$$\omega_m = \frac{\frac{K_q}{D_m} X_v - \frac{TK_{ce}}{D_m^2}\left(1 + \frac{V_t}{2\beta K_{ce}} s\right)}{\frac{J_m V_t}{2\beta D_m^2} s^2 + \left(\frac{J_m K_{ce}}{D_m^2} + \frac{B_m V_t}{2\beta D_m^2}\right) s + \frac{B_m K_{ce}}{D_m^2} + 1} \quad (15)$$

Or two TF for the system (no load speed) and and (speed drop due to load) respectively:-

$$\frac{\omega_m}{X_v} = \frac{\frac{K_q}{D_m}}{\left(\frac{s^2}{\omega_h^2} + \frac{2\delta_h}{\omega_h} s + 1\right)} \quad (16)$$

$$\frac{\omega_m}{T} = \frac{-\frac{K_{ce}}{D_m^2}\left(1 + \frac{V_t}{2\beta K_{ce}} s\right)}{\left(\frac{s^2}{\omega_h^2} + \frac{2\delta_h}{\omega_h} s + 1\right)} \quad (17)$$

Where national frequency and damping ratio are given by:-

$$\omega_h = \sqrt{\frac{2\beta D_m^2}{V_t J_m}} \quad (18)$$

$$\frac{B_m}{2D_m}\sqrt{\frac{V_t}{\beta J_m}} + \delta_h = \frac{K_{ce}}{D_m}\sqrt{\frac{\beta J_m}{V_t}} \quad (19)$$

ANALYSIS OF (PID) CONTROLLER SYSTEM

(PID) controllers are simple controller for servo system, as shown in **fig. 4:-**

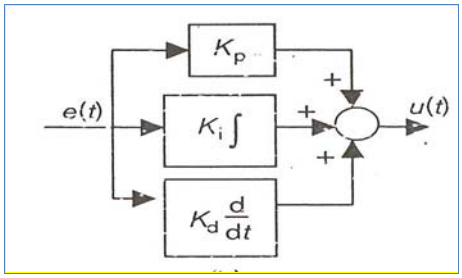

Fig (4): (PID) controller block diagram

A typical (PID) controller has following transfer function form is:-

$$u(t) = K_p e(t) + K_i \int_0^t e(t)dt + K_d \frac{de(t)}{dt} \quad (20)$$

(PID) controller could be determined by many methods which lead to regulate the (PID) controller for example trial and error method or Ziegler and Nichols Jacqueline (2008)

Stability Test Using MATLAB Package V7.1

This analysis include the system stability analysis in accordance to the TF . The equations 19,20 .**fig. 5** is block diagram using MATLAB package V 7.1 .

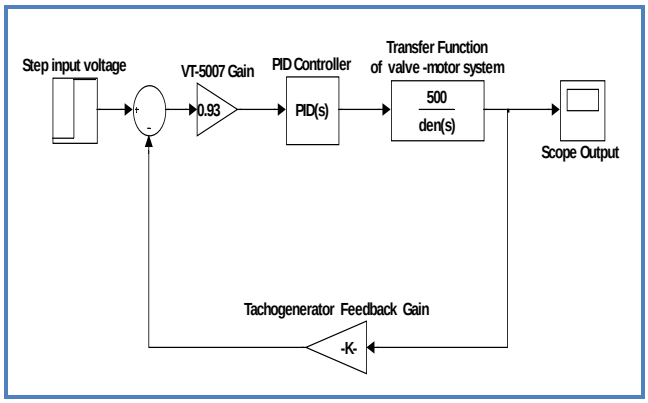

Fig (5): Block diagram of hydraulic control system with (PID) controller.

EXPERIMENTAL WORK

Design and Build the Test Rig

The test rig for this work is shown schematically in **fig. 6** and photographically in **fig. 7.**

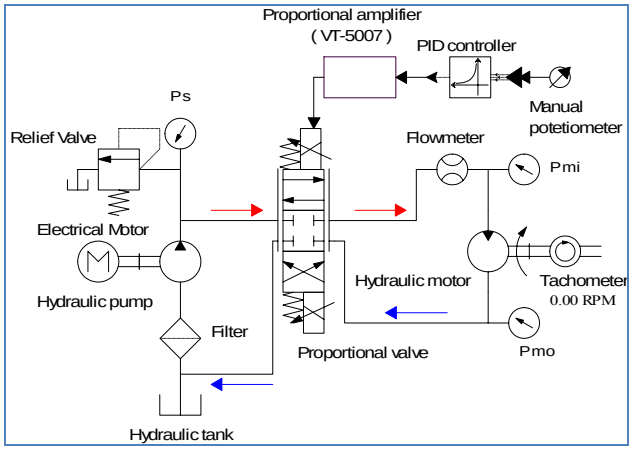

Fig (6): Schematic diagram of (EHSS) for speed control

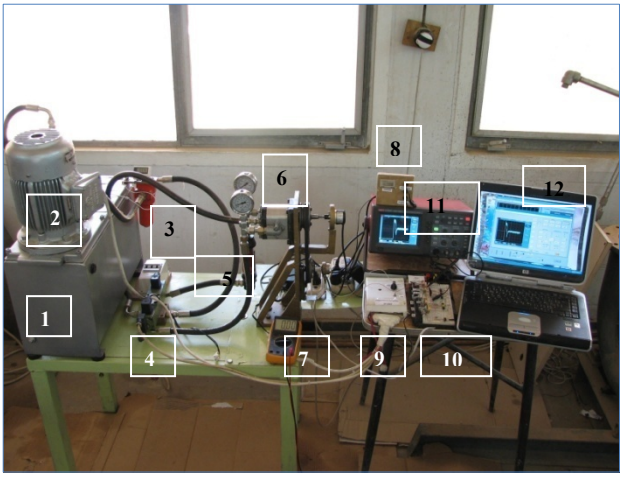

Fig (7): (EHSS) for speed control test rig

This test rig structure have many parts according to **fig. 6** , The hydraulic power unit (1) utilizes a gear pump (Duplomatic -11 cm^3/rev) to deliver the fluid to the system at a maximum rate of 14 l/min and maximum nominal pressure of 75 bar. The oil pump is driven by an electrical motor (2) (1.5 kW at 1400 rpm). high pressure filter (3) is used to protected the hydraulic system. The electro-hydraulic proportional valve manufactured by Bosch Rexroth (4WRAE 6 E16-10/24Z4/M) (4) directly controlled by proportional amplifier (VT-5007) (9) threw simple (PID) controller (10) ,the hydraulic motor (6) is fixed displacement external gear motor (Cassapa -11 cm^3/rev) with tow direction of rotation and leakage port, the rotation speed of the hydraulic motor transmitting to the sliding pulley which coupling with feedback tachogenerator sensor (7)using (V-belt), two pressure gauges (new –Tec) have been used in the hydraulic system and flow meter ,using digital tachometer (Autonics) (8) to record the rotation speed of hydraulic motor ,the output speed response of hydraulic motor is recorded by using digital oscilloscope (11) and save data on PC (12).

DESIGN AND BUILD (PID) CONTROLLER

This simple (PID) controller designed and built experimentally and as shown schematically in **fig. 8** and photographically in **fig. 9**, this controller is design and build experimentally by using 7 omp. amplifier type LM 741 , 5 potentiometers 250,100 KΩ , Capacitors 1 ,10 µF, -12 to 12 DC Power supply , Breadboard and jumper wire .(Thrower . et al 1998).

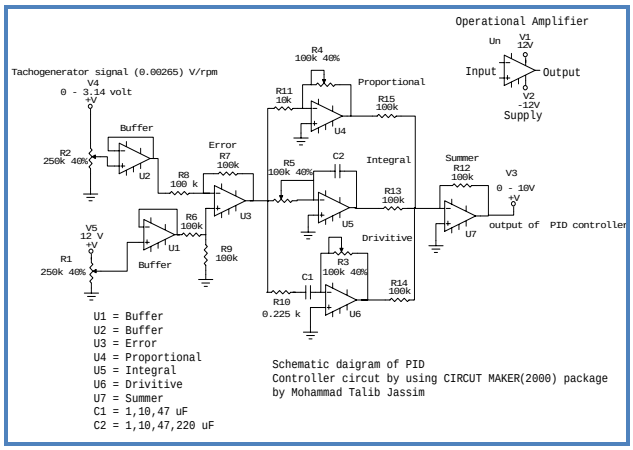

Fig (8): Schematic diagram of (PID) Controller

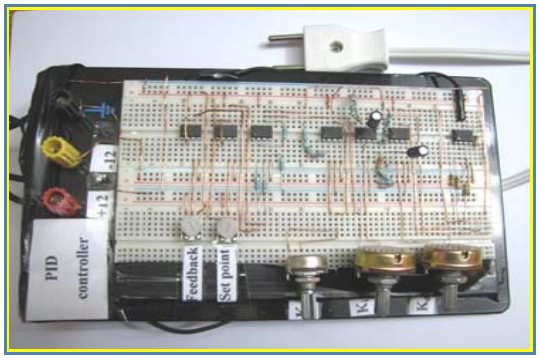

Fig (9) : Simple (PID) controller circuit

EXPERIMENTAL TESTING

Several comprehensive tests have been conducted on the (EHSS) for speed control test rig to investigate the hydraulic system and controller design performance and compare it against several studies. The first test was to calculate the total friction torque of the hydraulic motor and transmission system with V-belt . Second test was to verify the (PV) and hydraulic motor characteristic input voltage with rotation speed and flow rate and calculate the gain of the proportional amplifier experimentally. third test was open - loop system test by disconnected feedback signal of tachogenerator to check the stability and the response of the system .forth test was closed- loop system by connecting feedback signal of tachogenerator and (PID) controller test to evaluated the best (PID) gains for this system .last test was the speed control test at **(45 ± 5)** $^{\circ}C$ and (**65 ± 5**) $^{\circ}C$ temperature of hydraulic oil and using throttle valve working as variable load applied on the hydraulic motor by change the outlet flow rat of the hydraulic motor and with using set speed is (700) rpm.

SIMULATION ANALYSIS WITH AUTOMATION STUDIO V.52

(EHSS) for speed control of hydraulic motor has been built and simulated by using Automation Studio (AS) package V5.2 . This package was developed in (2003) by (FAMIC Technologies inc / Canada) to contain comprehensive libraries of hydraulic, pneumatic, ladder logic, and digital electronic symbols . This package is completely integrated software package that allows the user to design, simulate and animate circuits consisting of various automation technologies. After complete the design of (EHSS) for speed control, simulation process can be done. The simulation process is shown in **fig. 10**

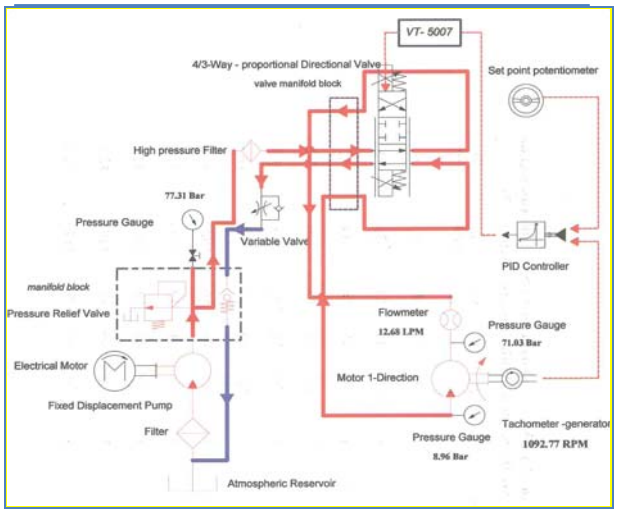

Fig (10): Simulation process of (EHSS) using (AS)

Fig. 11 shows the plotter window of this simulation process. (Automation Studio 2008)

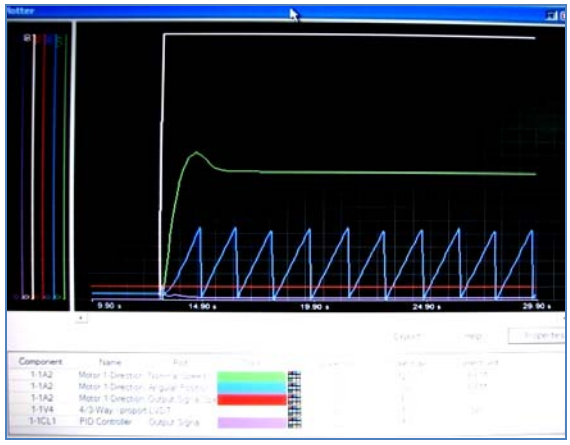

Fig (11): The plotter window for (AS)

RESULTS AND DISCUSSION

The torque required to overcome the friction when the hydraulic motor started from the rest from first test . **Fig. 12** represent pressure drop with motor rotational speed using the conversion ($T = P\ D_m$) .The static friction is (1.92) N.m . The coulomb friction is (0.96) N.m . Viscous coefficients is (0.0051) N.m.sec/rad. The characteristic tests of the (Valve – motor) system has been done with two cases of supply pressure (70 , 40) bar. **Fig. 13** and **Fig. 14** show the relation between the input signal with rotation speed and flow rate .When the input signal value increases, the hydraulic motor velocity increases because increasing the input signal leads to increased

volumetric flow rates and the hydraulic velocity as long as the increases. The difference between experimental and theoretical results due to losses in pressure in the system and friction effect and nonlinearity in system. if the supply pressure increased ; volumetric flow rate increased as well as the hydraulic motor speed. And plotting experimentally the variation of output voltage with input voltage to the proportional amplifier VT-5007. The slop of this curve is the gain $K_{amp.}$ of VT - 5007 and equal to (0.93) .

Fig. 15 shows the velocity - form of hydraulic motor under open loop system from third test of EHSS as a oscilloscope window represented the relation between the output voltage (mille V) of tachogenerator and the time (sec.).this figure show the rise time and steady state and transient region .

Figs. 16 shows the velocity - form of hydraulic motor under close - loop system from third test of (EHSS) as a oscilloscope window .with best (PID) gains using two methods, trail and error methods and Ziegler and Nichols methods. **Table 1** shows the difference in PID gain between experimental and simulation analysis.

Fig.17 and **Fig. 18** show the speed control tests results of the oscilloscope windows of (EHSS) under 65 ± 5 and 45 ± 5 C° of hydraulic oil temperature under load disturbance applied of the hydraulic shift ,experimentally the performance of (EHSS) of speed control is best at 65 ± 5 C° and give smooth response under load disturbance and short time to return to set speed . **Table 2** and **Table 3** show the speed control parameters test with hydraulic temperature at 65 ± 5 and 45 ± 5 C° respectively. Generally it is clear that this system has good response as it reaches the final value smoothly without any overshoot.

Fig. 19 represented comparison between the PID controller methods to calculate the gains at simulation process by (AS) package V5.2 , and the best (PID) gains for speed controller of EHSS clear that the simulation gains are approximately same the experimental work.

Fig. 20 shows the simulation process of (EHSS) of speed control using AS package V5.2 under same experimental applied load toque on hydraulic shift, it is clear that using simulation analysis is agree with experimental work expected small delay , the experimental results are represented the real behavior of the system under many nonlinearity factors like frictions and compressibility while the simulation results represented the simulation process for the system depended on input data for all components in the simulation program.

Figs. 21 show the step response of (EHSS) for speed control by using MATLAB package V7.1 simulation analysis. It is clear that step response is agree with experimental and simulation analysis. **Table 4** shows Self - turn parameters for (EHSS) by MATLAB package V7.1 ,and show the stability of (EHSS) , approximately, all the gains of the (PID) controller form these methods are same value.

Figs. 22 shows the bode diagram of (EHSS) ,from the bode diagram, the peak gain margin is 1.76 db at phase margin is 145°, all meet system stabilizing requirements and good dynamic quality can be secured.

Table (1): (PID) controller gains methods for (EHSS)

(PID) gains calculated methods	K_p	K_i	K_d
Trial and error method (experimentally)	3	1-10	0-0.5
Ziegler and Nichols method (experimentally)	2.04	5.1	0.2
Trial and error method (simulation analysis)	3	5	0.2
Ziegler and Nichols method (simulation analysis)	2.1	4.2	0.26
Self- turn parameters by MATLAB package V7.1	2.6	6.3	0.1

Table (2): Speed control parameter test with Hydraulic oil temperature 65 ± 5°C

Torque N.m	Set ω_m rpm	Min. ω_m rpm	Max. ω_m rpm	Time required sec.
0.38	700	690	715	1 0.8
0.74	703	686	724	1.3 1
1.5	702	652	780	1.5 1
2.8	705	632	855	1.8 1.2

Table (3): Speed control parameters test with Hydraulic oil temperature 45 ±5°C

Torque N.m	Set ω_m rpm	Min. ω_m rpm	Max. ω_m rpm	Time required sec.
0.38	702	685	720	1.5 1
0.74	708	674	733	2 1.3
1.5	705	645	805	2.2 1.5
2.8	708	622	864	2.5 1.8

Table (4) : Self turn parameters for (EHSS) using MATLAB package V7.1

Performance and Controller parameter	Turned value from MATLAB
Proportional gain (P)	2.6
Integral gain (I)	6.3
Derivative gain(D)	0.1
Rise time (sec.)	0.16
Gain margin (db at rad/sec.)	92 at 2.45e+003
Phase margin (deg at rad/sec.)	60.6 at 8.21
Closed - loop stability	Stable system

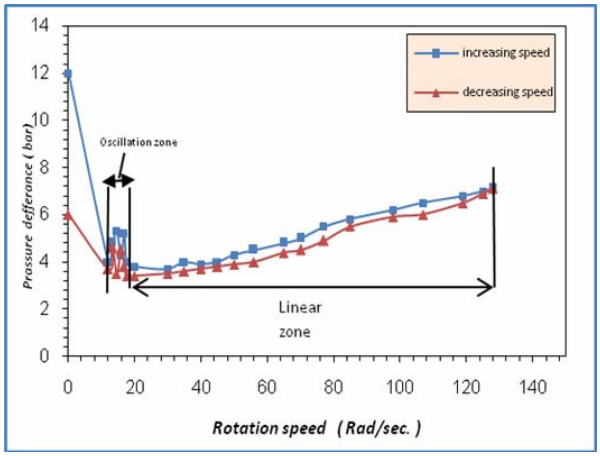

Fig (12)：Variation of rotation speed with pressure difference across the hydraulic motor

Table (5): Source of parameters of (EHSS) for speed control

Sym.	Description	Value	Unit	Source of Information
K_v	Proportional valve gain	$53*10^{-5}$	m/V	Manufacturer data
x_v	Spool stroke	$4.5*10^{-3}$	m	Manufacturer data
K_q	Valve flow gain	1.7	m^2/sec.	Calculated
K_c	Valve pressure gain	$2*10^{-9}$	m^3/sec. Pa	Calculated
d_{spool}	Spool diameter	$12*10^{-3}$	m	Manufacturer data
P_T	Return tank Pressure	$3*10^5$	N/m^2	From experimental
P_s	Supply pressure	$70*10^5$ $40*10^5$	N/m^2	From experimental
T_{fm}	Motor friction torque	2.92	N.m	Calculated experimentally
J_m	Inertia of motor and load	$32 * 10^{-5}$	$Kg.m^2$	Calculated
V_t	Total fluid volume in pipes	$24*10^{-5}$	m^3	Calculated
C_{tm}	leakage coefficient of motor	$1.5*10^{-13}$	m^3/sec. pa	Calculated experimentally
B_m	Viscous damping coefficient of motor	0.0051	N.m.sec./rad	Calculated experimentally
D_m	motor displacement	$16*10^{-7}$	m^3 /rad	Manufacturer data
β	Effective bulk modulus	$108*10^8$	N/m^2	Manufacturer data
ρ	Density of the Hydraulic oil	885	Kg/m^3	Manufacturer data
C_d	Discharge coefficient	0.65	---	Constant
D_p	Pump displacement	$16*10^{-7}$	m^3/ rad	Manufacturer data
ω_p	Pump rotational speed	146.5	rad/sec.	Manufacturer data
$K_{tach,}$	Tachogenerator gain	0.00264	V/rpm	Calculated experimentally

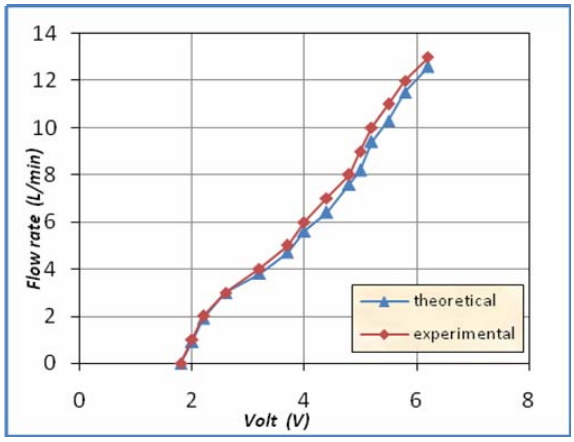

Fig (13) : Variation of hydraulic motor input flow rate with valve input signal (70 bar supply pressure)

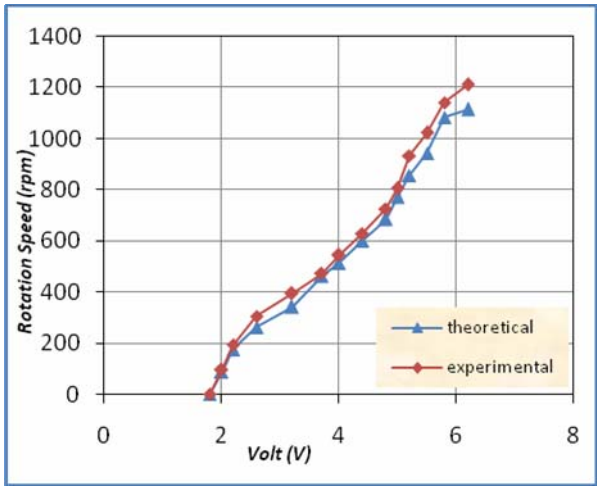

Fig (14): Variation of hydraulic motor rotation speed with valve input signal (70 bar supply pressure)

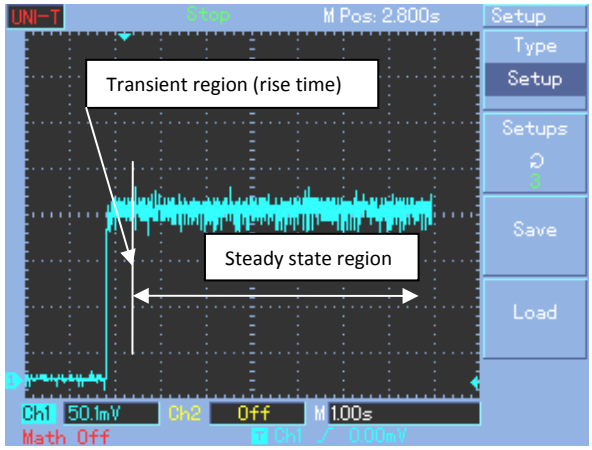

Fig (15) : Velocity of the hydraulic motor under open – loop system (70) bar

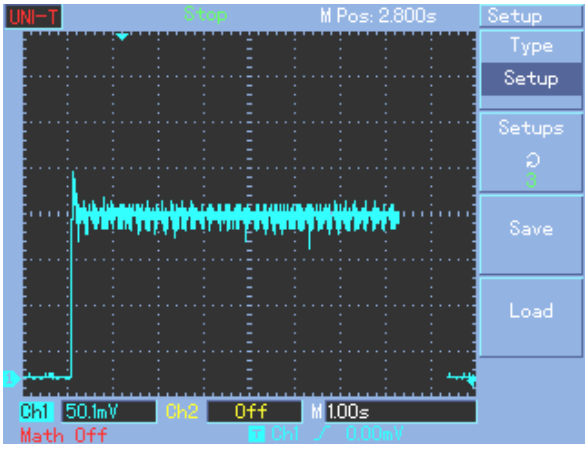

Fig (16): Velocity of the hydraulic motor under (PID) controller by Ziegler and Nichols method.

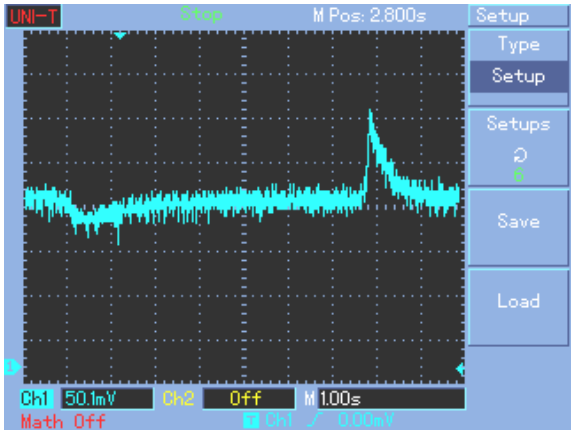

Fig (17) : Velocity of the hydraulic motor under (PID) controller with 2.8 N .m torque applied at 45 ±5 C° hydraulic oil temperature

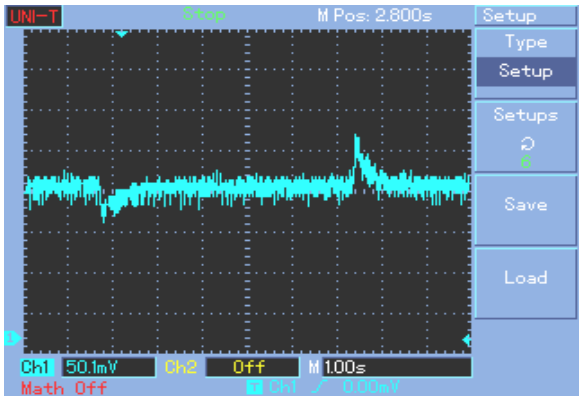

Fig (18) : Velocity of the hydraulic motor under (PID) controller with 2.8 N .m torque applied at 65 ±5 C° hydraulic oil temperature

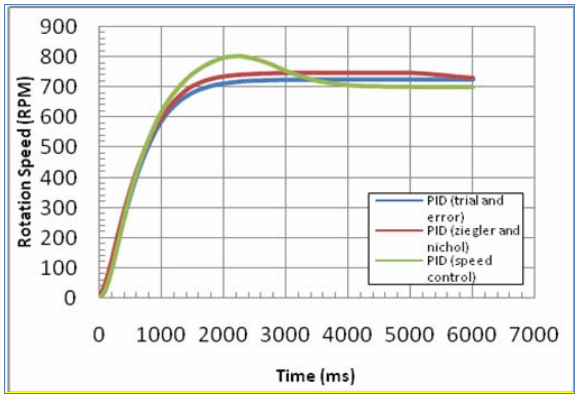

Fig (19): Simulation velocity of the hydraulic motor under (PID) controller by different methods

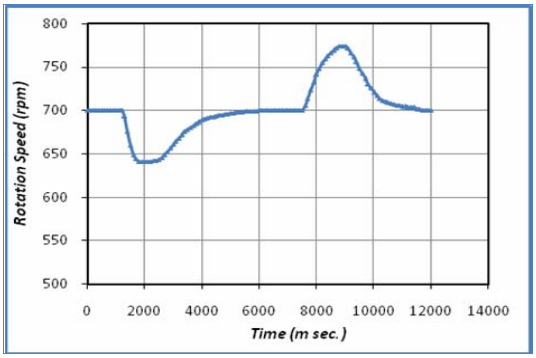

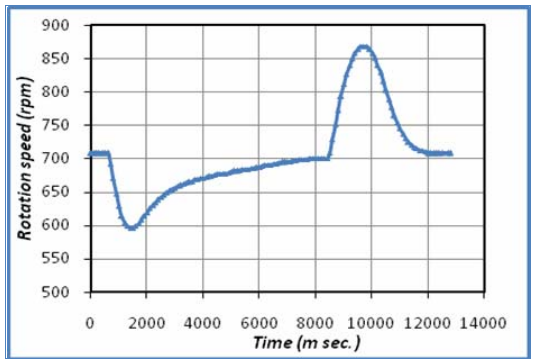

Fig (20) : Simulation velocity of hydraulic motor under (PID) controller with difference load

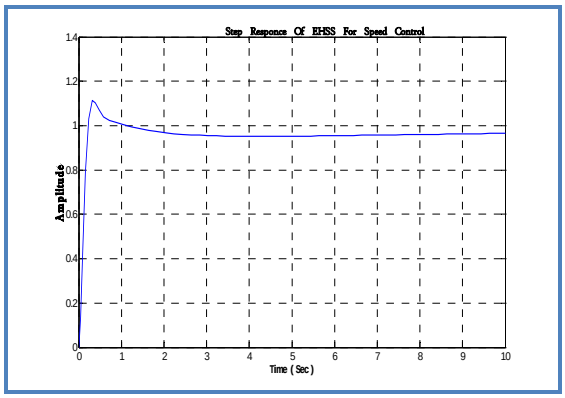

Fig (21): Step response of (EHSS) for speed control with MATLAB package V7.1

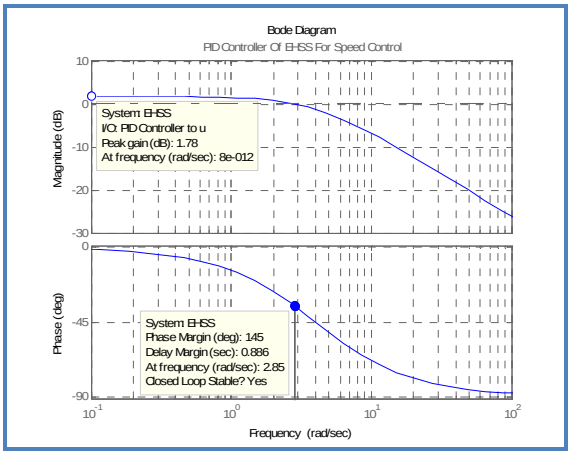

Fig (22) : Bode diagram for (no load speed TF) of (EHSS) for speed control

CONCLUSIONS

A model equations for (proportional valve – gear motor) combination system has been derived and verification, speed control system for hydraulic motor using simple low cost (PID) controller to get constant speed range of hydraulic motor under applied load .The range of speed control of the hydraulic motor depended on the system design like size of the hydraulic motor and the servo or proportional valve used, (flow rate) ,and reference speed.

Experimental tests showed that the performance and response of (EHSS) for speed control is best when the temperature of the hydraulic oil is **65** $\pm$**5°C** compared with low oil temperature oil **45** $\pm$**5°C**. Experimental and simulation results when using (AS) program shows a convergence in the results and .This leads us to the possibility of using this program for testing and analysis and design of any hydraulic system and deal with two types of users (professional or beginner).

ACNOWLEDGMENT

We would like to thank very much to all the staff of mechanical engineering department of the Baghdad University for them cooperation and help.

REFERENCES

Aichao ; Xiangdong Z.; Gang L. .(2008)" Simulation Study on Constant Speed Output Control of Fixed Displacement Pump-Variable Displacement Motor Hydraulic System" Fluid Power and Mechatronics, IEEE Xplore. .PP 276 - 281.

Automation Studio (AS) user manual 2008, "Automation Studio circuit design simulation software", Fluid Power and Automation Technologies" , http://www. automation studio .com

Ambuel, J., Steenhoek, L., Smith, R., and Colvin, T.(1993) "Control of hydrostatic transmission output speed Development and comparison of PI and hybrid fuzzy-PI controllers", Transactions of the ASAE, Vol. 36, PP 1057 -1064.

Hossam. ,Mohammad El- Bardini (2011)"Implementation of speed controller for rotary hydraulic motor based on LS-SVM" journal of Expert system with applications . Vol.(38) PP.14249-14256.

Jacqueline ,Michael J.,Reza K. (2008) ," control engineering an introductory course " Palgrave ,New work ,USA.

Dasgupta, J. Watton ,S. Pan (2005) "Open-loop dynamic performance of a servo-valve controlled motor transmission system with pump loading using steady-state characteristics" journal of Mechanism and Machine Theory, Elsevier Ltd, Vol. (41) PP. 262-282.

Thrower , Kiefer S., Kelmer K., and Silverberg L. (1998) " Basic Experiments in PID Control for Non-electrical Engineers" Retrieved from http://www.mae.ncsu.edu/silverberg/piddocs.pdf.

Merritt , H. (1967) ," Hydraulic control systems", John Wiley and Sons Inc, New York ,US ,first edition.

Vladimir . (2006) "Design and modeling of a new electro hydraulic actuator " National Library of Canada, M.Sc thesis ,Mechanical engineering ,Toronto ,Canada.

Web site 1 "speed control for hydraulic motor" from http://www.hydraulicspneumatics.com.

Yasukazu, (2000)"Rotational speed control of hydraulic motort using sliding mode control" Journal of Japan society of mechanical engineering, No. (00-1579) , PP.2559-2564.

NOTATION

Sym.	Description	unit
A	Orifice area gradient	m^2
B_m	Viscous damping coefficient of hydraulic motor	N.m.sec/rad
C_{tm}	leakage coefficient of hydraulic motor	m^3/sec.Pa
d_{spool}	Spool diameter	m
D_m	Volume displacement rate of the hydraulic motor	m^3 /rad
J_m	Total Inertia of motor and load	$Kg.m^2$
K_p	Proportional gain	dimensionless
K_i	Integral gain	dimensionless
K_d	Derivative gain	dimensionless
K_c	Valve pressure gain	m^3/sec. Pa
K_v	Proportional valve gain	m/V
K_q	Valve flow gain	m^2/sec.
$K_{tach,}$	Tachogenerator gain	V/rpm
Δ	difference	
P_1 , P_2	Inlet and outlet pressure of the hydraulic motor	Pa
P_L	Load pressure	Pa
P_s	Supply pressure	Pa
P_o , P_T	Tank pressure	Pa
Q_1, Q_2	Input and output flow rate of the hydraulic motor	m^3/sec.
t	Time	sec.
T_s	Static friction torque	N.m
T	Total friction torque on the hydraulic motor	N.m
T_{fm}	Coulomb friction torque of the hydraulic motor	N.m
T_g	Torque generated by motor	N.m
T_m	External load torque on the hydraulic motor	N.m
$e(t)$	Input error signal of (PID)	V
u (t)	Output of (PID) signal	V
V_t	Total fluid volume in pipes	m^3
x_v	Spool valve position	m
ρ	Density of the Hydraulic oil	Kg/m^3
ν	Kinematic viscosity	mm^2/sec.
ω_h	Hydraulic natural frequency	rad /sec.
ω_m	Angular speed of the hydraulic motor shaft	rad /sec.
β	Effective bulk modulus	N/m^2
δ_h	Hydraulic damping coefficient	dimensionless

ABBREVIATION	MENE
AS	Automation studio
EHSS	Electro- hydraulic servo system
Sym.	Symbol
TF	Transfer function
PID	Proportional integral derivative
PV	Proportional valve

Effect of Cryogenic Trteatment on the Tensile Properties of Carbon Dual Phase Steel

Ph.D.Abbas Abdul Hussein abid
University of Baghdad, Mech. Eng. Dept
abbasaltaee@yahoo.com

Hussein Burhan Muhammad
Ms.C, Diala University, Mech. Eng. Dept

ABSTRACT

The aim of this study was to evaluate tensile properties of low and medium carbon ferrite -martensite dual phase steel, and the effect cryogenic treatment at liquid nitrogen temperature (-196 ºC) on its properties. Low carbon steel (C12D) and medium carbon steels (C32D & C42D) were used in this work. For each steel grade, five groups of specimens were prepared according to the type of heat treatment. The first group was normalized, the second group was normalized and subsequently subjected to cryogenic treatment then tempered at (200 ºC) for one hour, the third group was quenched from intercritical annealing temperature of (760 ºC) to obtain dual phase (DP) steel, the fourth and fifth groups were both quenched from (760 ºC), but the forth group was subjected to cryogenic treatment and the fifth group was subjected to cryogenic then tempered at (200 ºC) for one hour. Mechanical tests were carried out which includes, tensile, hardness, as well as microscopic examination. Yield strength, ultimate tensile strength and ductility for DP were correlated to martensite volume fraction. The yield and tensile strength (σy, σu) of (DP) for the three steels, were higher than those of normalized condition, and increased after cryogenic treatment. These values, for the three steel grades, decreased after tempering at temperature 200 ºC. Tempering of (DP) steel at 200ºC for one hour, after cryogenic treatment, causes the reappearance of yielding point for steels (C12D) and (C32D) while no such a change noticed in (C42D) steel. The results have shown that hardness of (DP) increased after cryogenic treatment for the three steel grades.

KEY WORDS: Cryogenic treatment، dual phase steel ،tensile properties، hardness ،steel

تأثير المعاملة الزمهريرية على خواص الشد للصلب الكربوني ثنائي الطور

الخلاصة

الهدف من هذه الدراسة هو تقييم خواص الشد للصلب الثنائي الطور المنخفض و المتوسط الكربون ، وتأثير المعاملة الزمهريرية عند درجة حرارة النتروجين السائل (196 ºC-) فى هذه الخواص. استعمل الصلب منخفض الكربون (C12D) و متوسط الكربون (C32D) و (C42D) في هذه الدراسة.قسمت عينات الاختبار لكل صنف من أصناف الصلب على خمس مجاميع وفق المعاملة الحرارية. المجموعة الأولى أخضعت إلى معاملة التطبيع، المجموعة الثانية أخضعت إلى التطبيع ثم المعاملة الزمهريرية ثم المراجعة عند درجة حرارة (200 ºC) مدة ساعة واحدة، المجموعة الثالثة قسيت من درجة حرارة (760 ºC) للحصول على الصلب ثنائي الطور(DPS). المجموعة الرابعة و الخامسة كلاهما قسيتا عند (760 ºC) ،لكن المجموعة الرابعة أخضعت إلى المعاملة الزمهريرية و المجموعة الخامسة أخضعت للمعاملة الزمهريرية ثم المراجعة عند (200 ºC) مدة ساعة واحدة. تم إجراء فحص الشد والصلادة علاوة على الفحص المجهري. ان مقاومة الخضوع والشد و كذلك المطيلية مرتبطة بنسبة المارتنسايت. مقاومة الخضوع والشد للصلب ثنائي الطور(DP) لأنواع الصلب الثلاثة أعلى من الصلب المطبع، و لوحظ ارتفاعها بعد المعاملة الزمهريرية، وان هذه القيم انخفضت بعد المراجعة عند (200 ºC). المراجعة عند درجة حرارة (200 ºC) للصلب الثنائي الطور (DP) بعد المعاملة الزمهريرية أدت إلى عودة نقطة الخضوع لنوعي الصلب (C12D, C32D) بينما لم يلاحظ هكذا تغيير بالنسبة للصلب (C42D). كذلك لوحظ ان الصلادة للصلب الثنائي الطورازدادت بعد المعاملة الزمهريرية ولأنواع الصلب الثلاثة.

الكلمات الرئيسية: معاملة زمهريرية، صلب ثنائى الطور، خواص الشد، الصلادة، الصلب .

1. INTRODUCTION

Prior to dual-Phase steel developments, it have been focused primarily on applications involving cold-or hot-rolled sheet containing about 0.1% C. Carbon content was kept low because of the need for good spot weldability recent developments have been directed at producing dual-phase steels with high carbon contents (0.2 to 0.4) for use in forging or bar applications (S. Tasuhara et al, 1987). Medium carbon low alloy steel grades are widely utilized for the design of components and structural parts for moderate to high stress applications. Such applications require the selection of materials having an optimum combination of high strength, ductility, and toughness for effective service performance. Moreover, failure of stress bearing components can be catastrophic in nature, leading to grave economic and technical losses (Soboyejo W 2003, Brobergs KB. 1999). It is for these reasons there is a sustained interest in the development of steel microstructures with excellent high strength and toughness characteristics (Lozano JA, 2008, Salehi AR et al., 2006). The development of high strength - ductile microstructures in medium carbon low alloy steel has been explored with the adoption of intercritical treatment with encouraging results obtained (Alaneme KK and Kamma CM 2010), (Alaneme KK et al., 2010) .The tensile and fatigue properties of dual phase microstructures produced in medium carbon low alloy steels by intercritical treatment have been reported to be superior to that obtained from conventional heat-treatment processes (Alaneme KK, 2010). Ferrite martensite dual phase (DP) steels have microstructure containing hard martensite islands embedded in a soft and ductile ferrite matrix. this unique microstructure result in characteristic mechanical properties like absence of yield point phenomena, large ratio of tensile strength to yield strength, high rates of work hardening, high total and uniform elongation, excellent forming characteristic and high fracture toughness (M.S. Rashid, 1981, S. Hayami, 1975) . It has, thus become possible to employ DP steel widely in automobile components such as bodies, chassis, bumpers, wheel discs and rims (M.S. Rashid, 1981).

Dual phase steels have been designed to have low carbon with or without alloying elements and heat treated or hot rolled to have martensite volume fractions (MVF) rarely exceeding 15% because beyond this percentage, formability of DP steels is b**adly affected (M.S. Rashid, 1981).** The ensemble of the stronger phases, martensite, bainite and pearlite, is often referred to as "second phase ", retained austenite is also generally present in DP steels due to uncompleted austenite to martensite transformation. The amount of retained austenite varies from 2 to 9 % with composition, tending to be more prevalent in steels with high carbon content and other alloying elements **(G.R. Speich, 1981)**.

A cryogenic treatment is the process of treating work pieces to cryogenic temperatures (i.e. below -190 ºC) to remove residual stresses and improve wear resistance on steel. The process has a wide range of applications from industrial tooling to improvement of musical signal transmission. Some of the processes benefits include longer part life, less failure due to cracking, reduce coefficient of friction an less electrical resistance. This kind of treatment apart from identical effects as in the event of traditional cold treatment is also accompanied by crystallographic and microstuctural changes thanks to which as a result of tempering process carried out after cryogenic treatment in the steel microstructure very fine carbide precipitations occur. These precipitations affect both the material strength and its wear resistance (Collins D.N., 1996, Huang J.Y., 2003).
In the present work the (C12D, C32D &C42D) steels were intercritically heat treated and effect of martensite content on tensile properties and effect cryogenic treatment on its properties and microstructure was examined.

2. MATERIALS AND METHODS

2-1 Materials

The steels grades used in this research were selected from standard types of carbon steel, with different carbon content ranging from low to medium. This helps to understand the effect of carbon content and cryogenic treatment on the properties of dual phase steel. The tested steels, who is chemical compositions shown in table1, designated (C12D, C32DandC42D), according to the German standards specifications (DIN).

2-2Heat Treatments

The heat treatment included normalizing, intercritical annealing and tempering treatment as shown in Table 2. Intercritical annealing carried out at (760 ºC), and the holding time was (30 min), followed by quenching in Brine **solution**

(10% NaCl) to obtain (DP) steel. Tempering was carried at (200 ºC) for one hour, and was employed after cryogenic treatment. The research methodology is shown in Fig. 1.

2-3 Cryogenic Treatment

Liquid nitrogen was used as cooling media to carry out the cryogenic treatment. The specimens were encased in paraffin wax to act as insulator. This enables gradual change in the temperature of the specimen to prevent any thermal shock that may occur, thus causing undesirable deformation or cracking. When cryogenic treatment temperature (-196 ºC) is reached, the components then held at that temperature for a period of 24 hours, after that they were removed and left to warm at room temperature. The cryogenic treatment of the specimens was done in a chamber which is fully covered with multilayer super insulation and is filled by liquid nitrogen.

3-MECHANICAL PROPERTIES TESTS

3-1 Tensile Testing

The tests were performed using tensile testing machine type (United Hydraulic SHFM Series), in Specialized Institute for Engineering Industries\ Ministry of Industry. The test machine has a maximum capacity of (100KN) with a speed of 1 mm/min. Two specimens are used to perform each tensile test.

3-1-1 Specimen for Tensile Test

The tensile test specimens have been prepared in a accordance with the German standard for testing materials (DIN). They are of a cylindrical shape type, and are shown in fig. 2.

3-2 Microhardness Testing

In present work Vickers microhardness tester type (HVS-1000) was used, with pyramid indenter and load (500 g), in Ministry of Sciences & Technology. The specimens used for this test were cylindrical shape (ϕ15 mm x8 mm).

4- RESULTS AND DISCUSSION

4-1 Tensile Properties

The results of tensile propeties test i.e yield strength(σy), ultimate tensile strength(σu), and percentage elongation (El%) are presented in tables 3 and Fig. 3, 4 and 5, for (C12D), (C32D) and (C42D) steels respectively. The key factor which differentiates dual-phase steel from the variety of the ferritic steels (e.g. mild steels and conventional HSLA) with respect to the deformation characteristics, is the absence of yield point.The ferritic-martensitic steels exhibit continuous yielding. This feature together with the very high initial strain hardening rates account for the excellent formability properties of dual-phase steels. The continuous yielding of dual phase steel remains after cryogenic treatment ,but after tempering at temperature (200 ºC) for one hour, the yield point reappear for (C12D) and (C32D) steel, but it is less clear in the later steel. As for (C42D) steel, the tensile profile did not show such effect. For the three grades of steel , both tensile and yield strength (σu, σy) of dual phase steel are higher than those of normalized steel, this is due to the martensite presence in the structure of dual phase steel, whereas, normalized steel consist of the lower hardness pearlite. The improvement in tensile strength and yield strength follow a similar trend with increasing martensite content. These results are not surprising since martensite is a hard phase. As the martensite content increases, it is expected that the strength of dual phase steel increases but at the same time brings brittleness to the steel. But the benefit here, is the increase in the difference between (σu) and (σy) after (DP) treatment, because the greater the difference between the yield and ultimate tensile strength, and the further of the material can be stretched prior to necking (Richard Gendny, 2002).Table 4 represents these differences measured from tensile test profiles taking into account the approximate actual (σy) and not the 0.2% proof stress

The best documented cryogenic treatment mechanism affecting steel, other than causing the transformation austenite-to-martensit, is the precipitation of strengthening phases, in particular the carbide phase (Collins D. N., 1996).Therefore, the martensite content of dual phase steel has been increase after cryogenic treatment for this cycle and this result in both (σu) and (σy) increased after cryogenic treatment.

4-2 Microhardness Property

Microhardness tests after (DP) treatment. Shows an increase by (47.56%), (44.84%) and (9.02%) for the above steels respectively over those of normalized specimens. This increase in hardness is directly related to the nature of dual phase steel microstructure, which consist of a hard phase martensite and the soft phase ferrite,

whereas normalized steel consist of a less hard pearlite and ferrite. Also some of the carbon and other element, which remains in solution of the ferrite phase after quenching, contributes to a small increase in hardness. The differences in hardness between the (DP) of these steels, are due to the volume fraction of martensite, which increases as the carbon content of the steel increased, hence it is logical to expect an increase in hardness of dual phase steel with increasing martensite volume fraction at the expense of the ferrite phase.

After cryogenic treatment, the hardness increased by (71.33%), (58.00%) and (13.25%) respectively over those of normalized condition or by (16.11%), (9.08%) and (3.88%) over those of (DP) condition. The response of dual-phase (C12D) and (C32D) steel to cryogenic treatment is clear and showed positive increase in hardness while (C42D) steel shows only moderate increase, which means that (DP) steel of a high martensite volume fraction due to higher carbon content, have moderate response to cryogenic treatment concerning hardness. This could lead to a conclusion that changes in the ferrite phase structure after cryogenic treatment have a major contribution to the increase in the hardness of (C12D) and (C32D) steel. The microstructure presented in Fig. 9 shows the ferrite phase after cryogenic treatment contains finely distributed precipitates.

4- MICROSTRUCTURE TEST

4-1 Microstructure of C12D Steel

The microstructure of (DP) steel, before and after cryogenic treatment is shown in Fig. 8and 9. By using point counting method, it was found that martensite content approximately (21%).For (DP) after cryogenic treatment and dual phase after (cryogenic + tempering) treatment, it was found that martensite content for both conditions approximately (25%). This small increase in martensite content may attribute to the transformation of retained austenite to martensite after cryogenic treatment. Also it can be noticed that the ferrite in (DP) steel after cryogenic treatment contains finely distribution precipitates as shown in fig. 9.

4-2 Microstructure of (C32D) steel

Fig. 10, 11 are microstructure of (DP) steel before and after cryogenic treatment. The martensite content of dual phase steel is approximately (37%), and after cryogenic treatments, the amount of martensite was found to be the same. After tempering, the structure showing some changes in which the martensite areas contains fine precipitates and the boundaries between martinsite and the ferrite is no longer sharp.

4-3 Microstructure of (C42D) steel

Fig. 12, 13 are microstructure of (DP) steel before and after cryogenic treatment, The martensite content of dual phase steel is approximately (78%), and after cryogenic treatments, the amount of martensite was found to be the same. However after (cryogenic + tempering) treatment there are clear changes, the microstructure contain fine precipitates throughout the microstructure.

5- CONCLUSIONS

- Quenching from temperature of (760 ºC) (Intercritical Annealing) produces a mixture of ferrite and martensite, i.e. (dual phase steel). The volume fractions of martensite were 21%, 37% and 78% for (C12D, C32D & C42D) steels respectively, and cause continuous yielding (no yield point) for the three steel grades.
- Cryogenic treatment carried out on dual phase steels did not cause the reappearance of the yielding point.
- Tempering treatment at temperature (200 ºC) for one hour causes the reappearance of the yielding point for steels (C12D & C32D), while no such a change was noticed in (C42D) steel.

- 4-A further small increase in σy and σu can be achieved by cryogenic treatment.

- 5-The response of carbon dual phase steels to cryogenic treatment largely influenced by the carbon content. Lower carbon steels (C12D) and (C32D) generally has higher response than (C42D) of higher carbon content.

6-REFERENCES

Alaneme KK and Kamma CM. Phase Transformation Studies of a low alloy steel in the ($\alpha + \gamma$) Phase Region. *Materials Research*. 13(1), 2010, 119 -123.

Alaneme K K, Ranganathan S and Mojisola T. Mechanical Behaviour of Duplex Phase Structures

in Medium Carbon Low Alloy Steel. *Journal of Minerals, Materials Characterization and Engineering*. 9(7), 2010, 621-633.

ASM Handbook, Vol. 4 "Heat Treating "ASMthird printing (1995).

ASM, Handbook, Vol. 8, Mechanical Testing and Evaluation, 2000.

Brobergs KB. *Cracks and Fracture*. 1999,Academic Press; London, p. 1-771. doi:10.1016/B978-012134130-5/50001-5

Collins D. N., Deep Cryogenic Treatment of Tool Steel: a review, Heat Treatment of Metals, No. 2, 1996, PP. 40-42.

G.R. Speich, Physical Metallurgy of Dual Phase Steels. *Fundamental of Dual-Phase Steels. Conference and Proceedings*. Chicago, February 1981, p. 3-45.

Huang J.Y., Zhu Y. T., Liao X. Z., Beyerlein I. J.,Bourke M. A., Mittchell T. E., Microstructure of cryogenic treated M2 tool steel, materials science and engineering, vil.A339, 2003,PP. 241-244.

Lozano JA and Panta-Mesones JT. Evaluation of the Heat-treatment Response of a Multiphase Hot-Rolled Steel Processed by Controlled Rolling and Accelerated Cooling. *Materials and Manufacturing Processes*. 23, 2008, 357-362. Doi: .10. 1080/10426910801937850

M.S. Rashid, "Dual Phase Steel " Ann. Rev. Mater. SCI. Vol.11, 1981, p. 245-266

Richard Gedney, "SHEET METAL FORMABILITY " *Advanced materials & Processes*. August 2002.

Salehi AR, Serajzadeh S, and Taheri AK. A Study on the Microstructural changes in Hot Rolling of Dual-Phase steels. *Journal of Materials Science.* 41(7) 2006, 1917-1925. doi: 10.1007/s10853-006-4486-6

Soboyejo W. Mechanical properties of Engineering Materials ,2003. Marcel Dekker Inc, New York, p. 1-583.

S. Hayami and T. Furukawa, A family of high strength, Cold-rolled steel. In Microalloying 75, proceedings of the Conference, pages 78-87, Vantiec, London, 1975

S. Tasuhara, M. Osamu, H. Takechi, Y. Ishii, and M. Usada, "Influence of Retained Austenite on the Bending Formability of Steel Sheet Containing Retained Austenite " paper presented at the 114th Iron and Steel Institute of Japan Meeting, Tokyo, 1987.

Table 1: Showing chemical composition of the investigated steels.

Steels / % Elements	C12D	C32D	C42D
C	0.12	0.33	0.43
Si	0.25	0.276	0.209
Mn	0.58	0.527	0.673
P	0.012	0.023	0.018
S	0.035	0.045	0.010
Cr	0.087	0.142	0.132
Mo	0.015	0.016	0.017
Ni	0.073	0.057	0.070
Cu	0.174	0.011	0.118

Table 2: Showing details of the heat treatments used in the present work.

steel	Heat treatment	Tempe-rature (°C)	Holding time (min)	Cooling medium
C12D	N	900	30	Air
	IA	760	30	Brine
	T	200	60	water
C32D	N	860	30	Air
	IQ	760	30	Brine
	T	200	60	water
C42D	N	850	30	Air
	IQ	760	30	Brine
	T	200	60	water

Table 3: Results of the tensile tests .

Steels	Parameters	Type of treatment				
		N	N+CT+T	DP	DP+CT	DP+CT+T
C12D	σy(MPa)	355.28	367.84	467.71	479.31	435.52
	σu(MPa)	494.6	497.24	669.68	704.01	572.57
	El%	33.61	35.25	22.05	18.01	24.60
C32D	σy(MPa)	364.16	393.73	473.3	526.61	386.85
	σu(MPa)	591.13	589.66	692.74	736.64	594.67
	El%	27.03	29.45	19.87	17.12	23.58
C42D	σy(MPa)	488.48	488.6	551.75	563.62	525.57
	σu(MPa)	700.01	696.1	742.79	755.17	715.43
	El%	24.22	26.11	19.16	17.86	20.46

Table 4: The difference between σu and the actual σy for normalizing condition and (DP) of the tested steels.

Steel grade	(σu-σy) MPa Normalized	(σu - σy) MPa Dual phase	Increase (MPa)
C12D	139.32	273.68	134.36
C32D	226.97	271.74	44.77
C42D	211.53	240.79	29.26

d_o	d_1	L_O	L_c	L_t	h	R
8	10	40	48	115	30	4

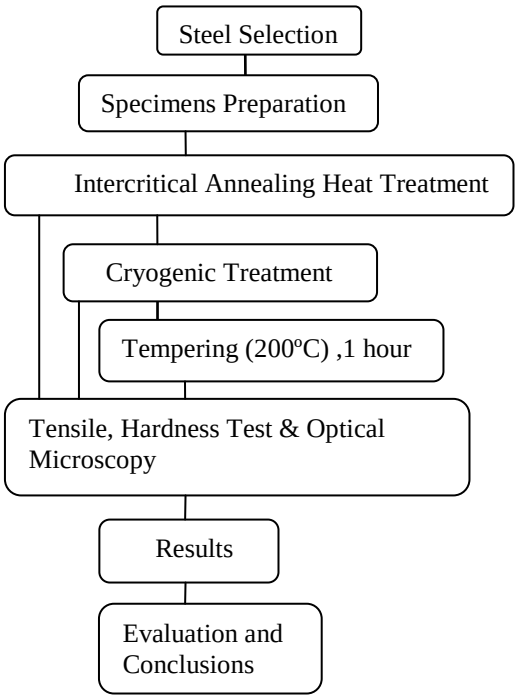

Fig. (1) Research Methodology

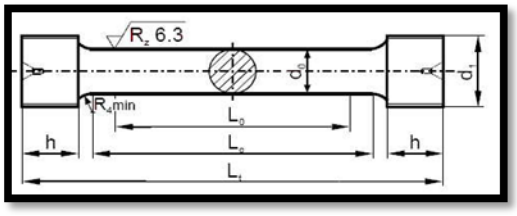

Fig. (2) Schematic of the tensile test specimen (all dimensions are in mm)

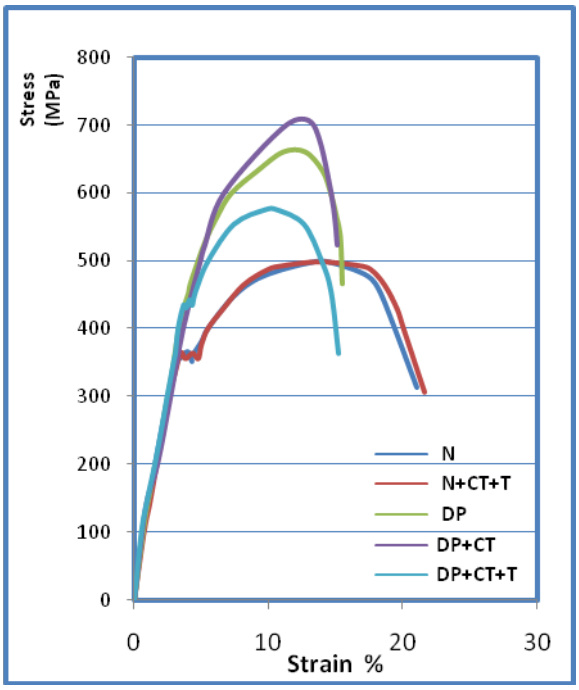

Fig. (3) Tensile test curves for C12D steel.

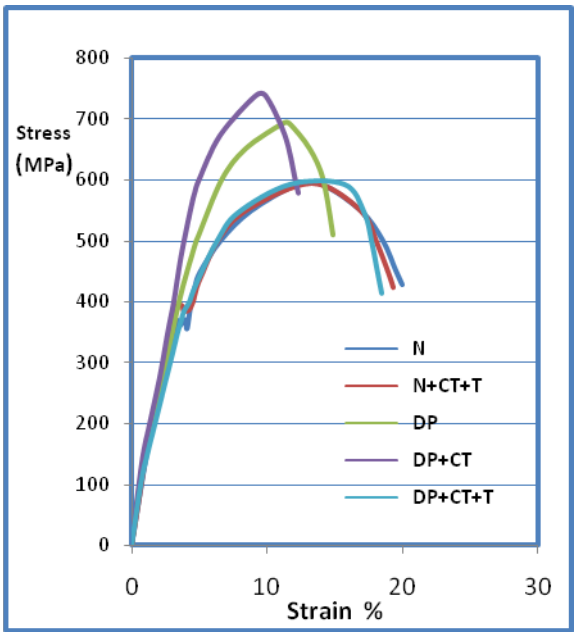

Fig. (4) Tensile test curves for (C32D) steel.

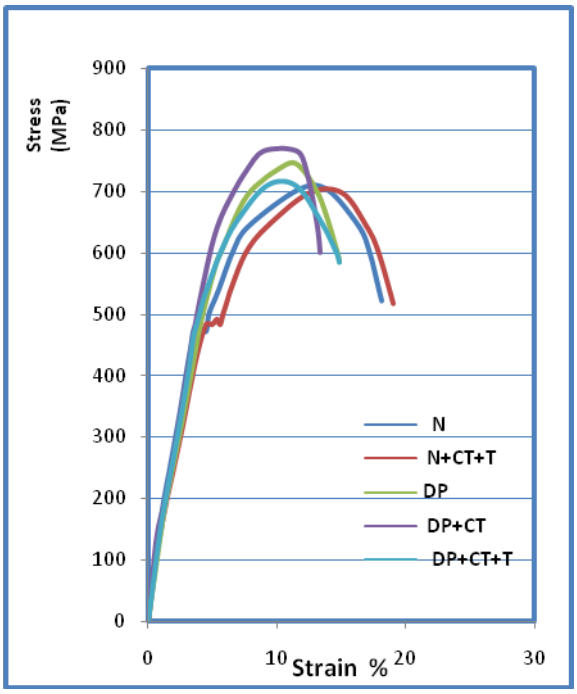

Fig. (5) Tensile test curves for C42D steel.

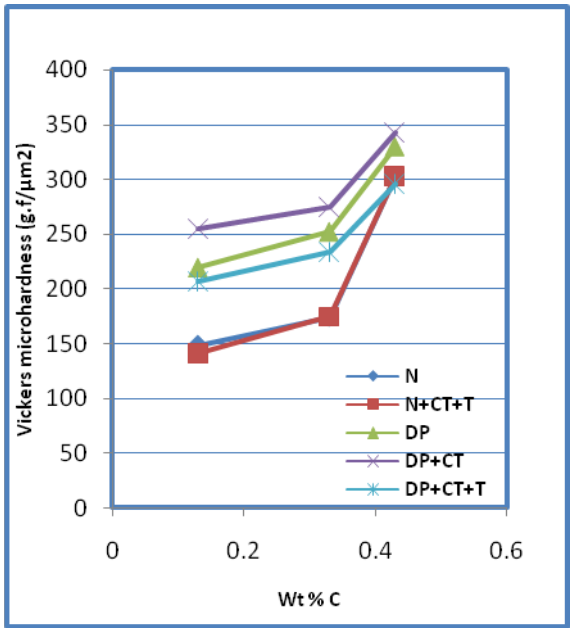

Fig. (7) Effect of carbon content on the response of dual phase steel to cryogenic treatment.

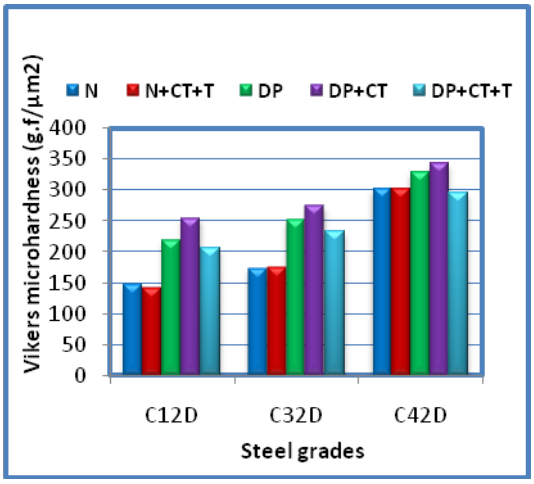

Fig.(6) Hardness level and the response of each steel to cryogenic treatment.

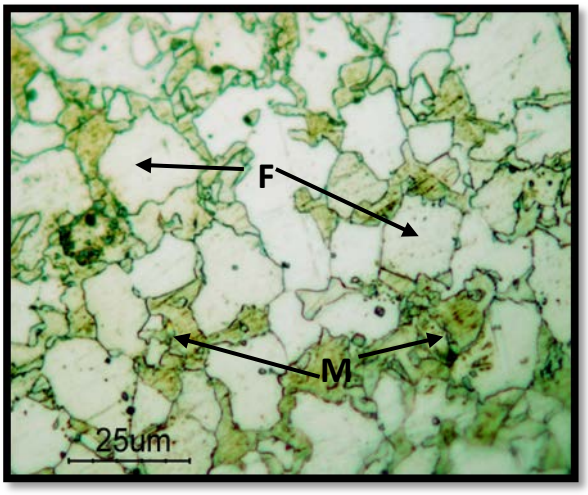

Fig. (8) Microstructure of dual phase for (C12D) steel. Ferrite (F), Martesit (M).

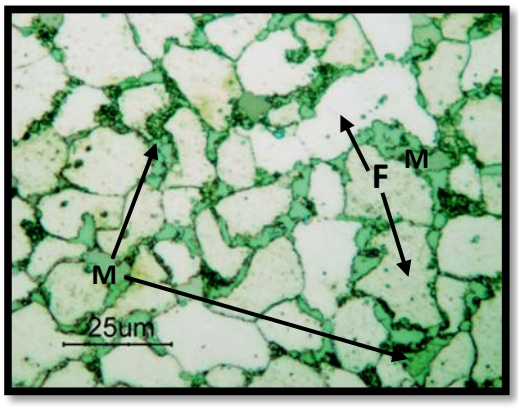

Fig.(9) Microstructure of dual phase after cryogenic treatment for (C12D) steel sowing fine precipitates within Ferrite grains.

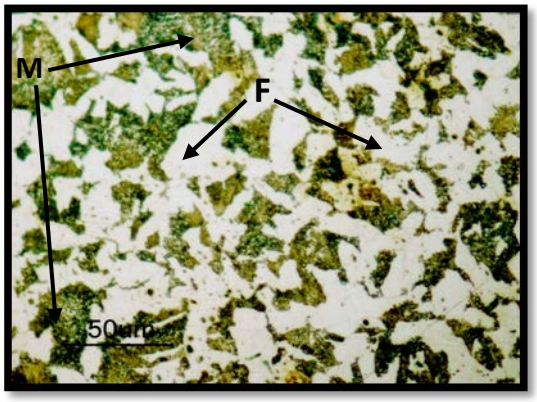

Fig. (10) Microstructure of dual phase for (C32D) steel. Ferrite(light), martesite(dark).

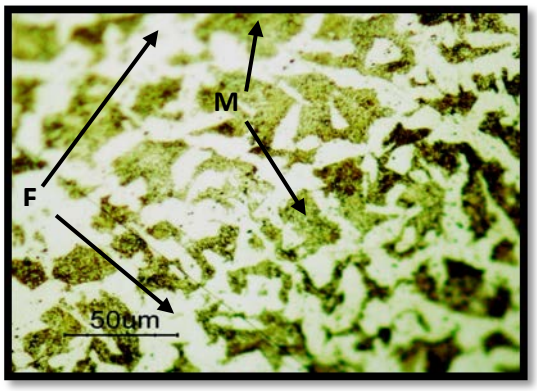

Fig. (11) Microstructure of dual phase after cryogenic treatment for (C32D) steel.

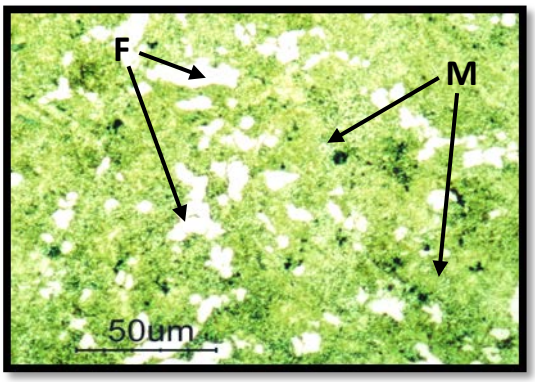

Fig.(12) Microstructure of dual phase (C42D) steel.

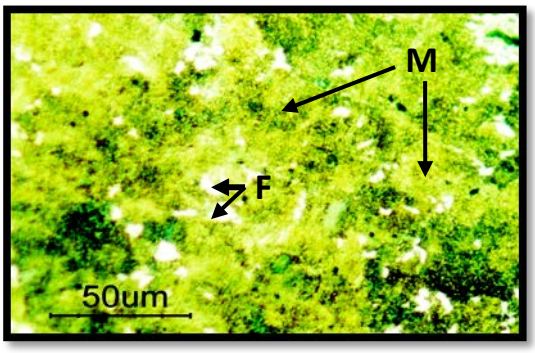

Fig. (13) Microstructure of dual phase (C42D) steel after cryogenic treatment.

Abbreviation	The meaning
σy	Yield stress
σu	Tensile stress
DP steel	Dual phase steel
MVF	Martensite volume fraction
El%	Percentage elongation
N	Normalizing treatment
CT	Cryogenic treatment
T	Tempering treatment
0.2 PF	Proof stress
IA	Intercritical annealing
HSLA	High strength low alloy steel
M	Martensite
F	Ferrite

Number 5 Volume 19 may 2013 Journal of Engineering

Experimental Study of Power Increase Transient in Heat Generation Systems Simulated By Immersed Heat Source

Dr. Akram W. Ahmed Ezzat
Asst. prof. Dept. of Mech. Eng.
Baghdad University
Email: akram whabi@yahoo.com

Sarmad A. Abdul Hussain
Dept. of Mech. Eng.
Baghdad University
Email: akram whabi@yahoo.com

ABSTRACT

Theoretical and experimental investigations of the transient heat transfer parameters of constant heat flux source subjected to water flowing in the downward direction in closed channel are conducted. The power increase transient is ensured by step change increase in the heat source power. The theoretical investigation involved a mathematical modeling for axially symmetric, simultaneously developing laminar water flow in a vertical annulus. The mathematical model is based on one dimensional downward flow. The boundary conditions of the studied case are based on adiabatic outer wall, while the inner wall is subjected to a constant heat flux. The heat & mass balance equation derived for specified element of bulk water within the annulus and solved by using Laplace method to determine the variation of bulk water temperature. The experimental investigation included a set of experiments carried out to investigate the temperature variation along the heat source for power increase transient of (5%, 10%, 15% and 20%) of its nominal value during and after reaching the steady state condition. Estimation of the boiling safety factor is predicted and compared with the theoretical values. Reliable agreement between experimental and theoretical approaches is reached. The later showed that the elapsed time required for the clad surface temperature to reach its steady state values after each transient is less than that related to bulk water temperature. New correlation for prediction of critical heat flux, CHF based on inlet water temperature and water mass flux are investigated and compared with CHF correlations obtained from previous researches. Specific recommendations concerned with preventive measured required to eliminate the effect of boiling crisis are concluded based on theoretical and experimental results related to transients setting times obtained from each case study.

KEYWORDS: CHFprediction, Sub-cooled flow boiling, Heat transfer parameters, Nucleate boiling, Concentric annular channel.

.

دراسة تجريبية للحالة العابرة لزيادة الطاقة في انظمة التوليد الحرارية من خلال تمثيله بمصدر حراري مغمور

سرمد عزيز عبد الحسين
قسم الهندسة الميكانيكية
جامعة بغداد

أ.م.د. أكرم وهبي احمد عزت
قسم الهندسة الميكانيكية
جامعة بغداد

تم أجراء بحث نظري وتجريبي للعناصر الاستدلالية على أنتقال الحراره العابرة لمصدر حراري ثابت الفيض خاضع لجريان الماء نحو الاسفل في قناة مغلقة. تم زيادة الطاقة العابرة من خلال زيادة درجية في الفيض الحراري للمصدر. البحث النظري تضمن نموذج رياضي لتجويف حلقي عمودي متناظر محوريا يكون فيه جريان الماء فيه طباقي متطور. الشروط الحديه لهذه الدراسه كانت تعتمد على أساس جدار خارجي معزول حراريا في حين يتعرض الجدار الداخلي لتدفق حراري ثابت. تم اشتقاق معادلة التوازن الحراري والكتلي لعنصر محدد داخل مجرى الجريان وذلك بأستخدام طريقة لابلاس لتحديد التباين في درجة حرارة الماء. شمل البحث العملي مجموعة من التجارب التي اجريت للبحث في قيم درجة حرارة السطح على طول المصدر الحراري لزيادة طاقة عابرة بنسبة مئوية (5٪، 10٪، 15٪ و 20٪) من القيمة الفعلية خلال وبعد الوصول الى حالة الأستقرار. كذلك

تضمن البحث العملي حساب عامل الأمان للغليان من خلال التنبأ بقيمته ومقارنته مع القيم التي تم الحصول عليها من الجانب النظري. المقارنة جيدة بين النتائج العملية والنظرية فقد تبين أن الزمن اللازم درجة حرارة سطح المصدر الحراري لوصول الى الحالة المستقرة هي أقل من تلك اللازمة

لوصول درجة حرارة الماء الى حالة الأستقرار، وتم وضع معادلات مناسبة لكل منهما. تم التنبأ بقيمة التدفق الحراري الحرج ووضع معادلات خاصة بذلك ومقارنته مع العلاقات الرياضية الخاصة بالابحاث السابقه ضد الفرق في درجة حرارة الدخول والخروج وكذلك التدفق الكتلي للماء. أظهرت نتائج المقارنة مطابقة مقبولة تم وضع أستنتاجات ذات علاقة بالخطوات اللازمة للتقليل من أثار أزمة الغليان أستنادا الى النتائج النظرية والعملية المتعلقة بتحديد الأوقات اللازمة للوصول الى الحالات المستقرة بعد كل حالة عابرة

الكلمات الرئيسية: تنبأ معدل التدفق الحراري، ظاهرة الغليان لجريان مائع، خواص انتقال الحرارة، غليان النوى، قناة حلقية متماثلة

INTRODUCTION

During safety analysis of any heat generation system it is necessary to demonstrate how far are the limits and conditions established to prevent anticipated transients and ensure plant integrity. The effect of heat power increase transients (HPIT) in power generated system is studied thoroughly to explain its practical significance in flow boiling systems**.** The study becomes very important because it represents an engineering foundation to ensure the safety of the heat generation systems from the initialing events that may take place and lead to rapid temperature build up during the transient course. One of these main consequences that possibly take place is the critical heat flux phenomenon **(CHF**) or also called the "boiling crisis". **CHF** is a phenomenon that denotes the sudden drop of the boiling heat transfer coefficient which results from the replacement of liquid by vapor near the boiling surface. The transient boiling heat transfer is of great importance in analyzing thermo hydrodynamic characteristics of many thermal engineering systems such as petrochemical and nuclear power plants. The transient boiling phenomenon sometimes occurs in the steps of started-up and shut-down of the boiling systems. Power transient occurs when the heat generation rate or heat input varies with time. Generally, an increasing power transient is potentially disastrous and chaotic and is thus more important than a decreasing power transient. Figure (1) shows the heat transfer characteristics during sub-cooled flow boiling of a pure liquid. The onset nucleate boiling (**ONB)** location was identified by visual observations as well as temperature and heat flux data. For the given set of flow conditions (hysteresis delays nucleation to D in some cases). Following the **ONB** condition, heat transfer is by combined nucleation and convection modes in the region C-E (Partial Boiling). Finally, beyond E, Fully Developed Boiling (FDB) is established in the region E-G, and heat transfer is entirely by nucleate boiling mode. Nucleate boiling in which bubbles are formed by nucleation at the solid surface. In highly sub-cooled boiling these bubbles rapidly collapse, transferring their latent heat to the liquid phase and thus heating it dawn towards the saturation temperature. Therefore, it required to know the boiling safety factor (**K**) to avoid sub-cooled nucleate boiling at clad surface. As the maximum clad temperature at the hot spot shall be lower than boiling temperature, K should be higher than unity.

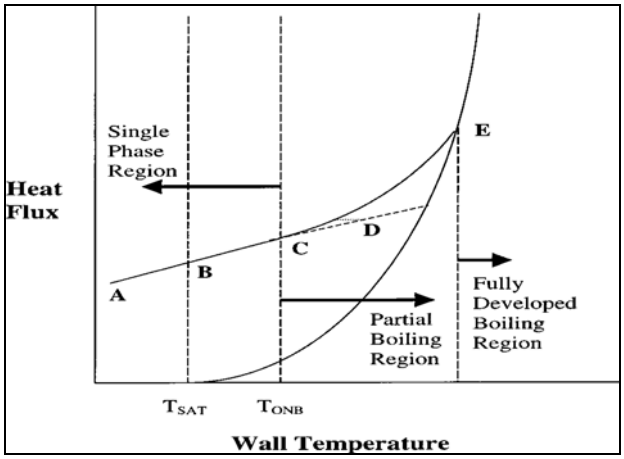

Fig (1): Heat flux dependence on wall superheat during sub-cooled flow boiling, (Kandlikar, 2003).

Young (1994) investigated experimentally in his study the critical heat flux (CHF) in transient boiling systems with vertical thin rectangular parallel plates

channel. One of the transient boiling systems is power transients. Power transient occurs when the heat generation rate or heat input varies with time. Generally, an increasing power transient is potentially disastrous and chaotic and is thus more important than a decreasing power transient. In the experiments related to forced convective boiling study, the primary parameters under investigation were transient modes, channel gap distances (3, 5 and 8 mm), inlet sub-cooling temperature (7.5 - 20.3) ^{o}C, mass flow rate (738 – 2162) kg/m2 sec and flow directions (Upward and downward). It is proved that as power is applied to the section as a function of time, the temperature and heat flux increase slowly at first and then very rapidly.

David and Issam (1996) predicted CHF correlations applicable to sub-cooled flow boiling in a uniformly heated vertical tube. They published in handbooks as well as the most recent correlations analyzed with the PU- BTPFL CHF database, which contains 29718 CHF data points. The parametric ranges of the CHF database are diameters from (0.3 to 45) mm, length-to-diameter ratios from (2 to 2484), mass velocities from (0.01x 10^3 to 138 x 10^3) kg/m^2.sec, inlet sub-under change of many factors and give good response of the system output. Cooling from (0 to 347) °C, inlet qualities from (2.63 to 0.00), outlet sub-cooling from (0 to 305) °C, out let qualities from (-2.13 to 1.00), and CHF from (0.05 x 10^6 to 276 x 10^6) W/m^2. A correlation published elsewhere is the most accurate in both low and high mass velocity regions. In general, CHF correlations developed from data covering a limited range of flow conditions cannot extended to other flow conditions without much uncertainty.

$$CHF = \frac{GD}{4L} C_{p,ave} (T_{out} - T_{in}) \quad (1)$$

Braz (2000) studied the thermal hydraulic behavior of electrically heated rod during a critical heat flux transient. He analyzed the front propagation velocity for the drying out and rewetting processes during the occurrence of CHF in electrically heated rod. The electrically heated element simulates nuclear fuel rods model's during the transient by applying an electrical power step from steady state condition. He made heated rod (16 cm diameter and 100 cm length) from a Ni-Cr wire. He found the linear power density is increased by 10% from its steady state to reach the CHF at 4 sec then the electric power is cut off. He showed the effect of the pressure, mass flow rate, inlet temperature on the behavior of electrically heating rod and that this variable has more influence on the drying front velocity than on the rewetting one.

Tomio Okawa et al. (2003) predicted the critical heat flux in annular flow regime accurately through new set correlations for the film flow analysis. All the correlations adopted on experimental data. The (4375) data of CHF in forced flow of water in vertical uniformly heated round tubes were used to test the basic performance of the model. He compared between the calculated and measured critical heat fluxes and he showed that the predicated results by the present model agree with the experimental data fairly if the flow pattern at the onset of CHF condition is considered annular flow.

Wu et al. (2010) conducted experiments which used the water as working fluid with pressure ranging from 1 to 4 MPa, mass flow velocity from 56 to 145 kg/m^2 s and wall heat flux from (9 to 58) KW/m^2 to study the onset of nucleate boiling (ONB) in heated vertical narrow annuli with annular gap sizes (0.95, 1.5 and 2) mm. They found that the ONB sometimes occurs only on outer annulus surface, sometimes occurs only on inner annulus surface and sometimes occurs on both annulus surfaces. The heat flux of the other side has great influence on the heat flux of the ONB and the latter will decrease with the increase of the heat flux of the other side. It is also found that the heat flux of the ONB increases with the increase of the pressure, the mass flux and wall superheat. However, the heat flux of the ONB will decrease as the gap size increases in narrow annuli. They predicted the heat flux of the ONB in narrow annuli through a new correlation, which has good agreement with the experimental data.

THEORETICAL ANALYSIS

Flowing water in a vertical annulus subjected to transient forced convection effect in radial direction is presented for modeling. A one-dimensional model can be used to describe the transient forced convection heat transfer in vertical annuals, with inner radius r_i and outer radius r_o which has a configuration shown in figure (2). Water flow direction is assumed to be in the downward direction according to the experimental setup.

The following assumptions are used in the modeling

- Incompressible fluid.
- One dimensional in (z-axis) flow. There is only one non zero velocity component, namely that in the direction of flow, v_z thus, $v_r = v_\theta = 0$.
- The axial velocity is independent of the angular location; that is, $\frac{\partial v_z}{\partial \theta} 0$.
- Simultaneously developing hydrodynamic.

- No internal heat generation and heat dissipation.
- Neglecting viscous dissipation.

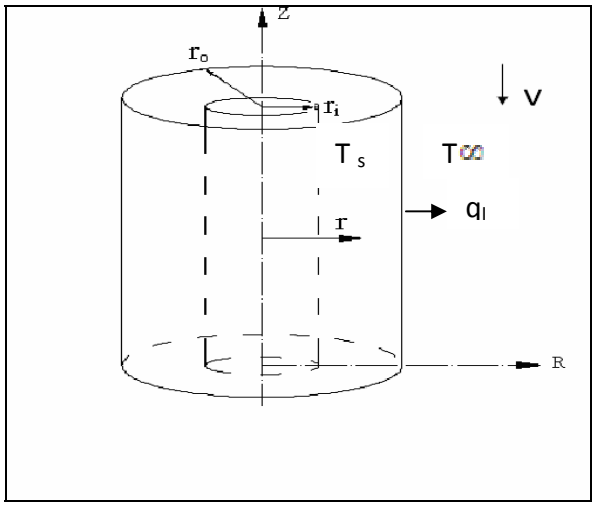

Fig (2): Axial annular geometry

FURTHER CALCULATIONS

To analyze the heat transfer process by forced convection from the heat source surface to the water flowing along it through annular section adjacent to the heat source surface simplified steps were used by conducting mass and heat balance at specified cross sectional area in the channel. The heat transfer coefficient is one of the affective parameters that should be estimated using the proper equations, Calculation procedure is conducted as follows:

- The total input power supplied to the wall can be calculated as;

$$q_t = V * I \quad (2)$$

- The heat loss (q_l) from the annular channel to the surrounding can be found from the following relation:

$$q_l = \frac{T_s - T_\infty}{\frac{1}{hA} + \frac{\ln(\frac{r_o}{r_i})}{2\pi k_g} + \frac{1}{h_{ins} A_o}} \quad (3)$$

The outer heat transfer coefficient of insulated cylinder (h_{ins}) is found using the following equation, **(Harlan and Bengtson, 2010)**. The correlation for Nu adopted for laminar flow at $(Ra \leq 10^9)$ is:

$$Nu = 0.68 + \frac{0.67 \cdot Ra^{.25}}{[1+(\frac{.492}{Pr})^{9/16}]^{4/9}} \quad (4)$$

$$Gr = g\beta L^3 \Delta T/\vartheta^2 \quad (5)$$

$$Pr = (\frac{\mu C_p}{k})_\infty \quad (6)$$

$$Ra = Gr * Pr \quad (7)$$

$$h_{ins} = (Nu * k_\infty)/(z) \quad (8)$$

- Heat transferred to the flowing water by convection is calculated by the following relation;

$$q_c = q_t - q_l \quad (9)$$

- Convective heat flux is calculated by using the following relation;

$$q'' = q_c/A_s \quad (10)$$

$$A_s = \pi D_i L \quad (11)$$

The Input parameters related to the total power of the heat source, hydraulic diameter, water volumetric flow rate, channel geometry and inlet water temperature are based on the experimental data that are used during the experimental part of the study. The target from theoretical study is to ensure certain model that predicts the measured parameters during experiments that uses power ranges higher the heater capacity. This insurance is validated by comparing the experimental and theoretical results to calculate the differences between them.

BULK WATER TEMPERATURE

To determine the bulk water temperature at the six points and compare them with the six thermocouple read out fixed along heater tube wall during study state condition, the following calculations are conducted;

$$T_{i+1,st} = T_{i,st} + \left(\frac{q'' \pi D_i z}{\dot{m} cp}\right) \quad (12)$$

The bulk water temperature during transient condition at any section of the annular gap at any time

could be derived from the following heat balance and as shown in figure (3):

Heat balance:

Inlet heat rate – outlet heat rate = accumulated heat

$$q_{i,tr}(t) - q_{l,tr}(t) + \dot{m}C_p T_{i,tr}(t) - \dot{m}C_p[2$$

$$T_{ave,tr}(t) - T_{i,tr}(t)] = MC_{p,ave}\frac{\partial T_{ave,tr}(t)}{\partial t} \quad (13)$$

$$T_{ave,tr}(t) = \frac{[T_i(t) + T_{i+1,tr}(t)]}{2} \rightarrow T_{i+1,tr}(t) = 2T_{ave,tr}(t) - T_i(t) \quad (14)$$

$$T_{ave}(t) = T_{ave,tr}(t) + T_{ave,st} \quad (15)$$

$$T_i(t) = T_{i,tr}(t) + T_{i,st} \quad (16)$$

$$T_{i+1}(t) = T_{i+1,tr}(t) + T_{i+1,st} \quad (17)$$

$$q_i(t) = q_{i,tr}(t) + q_{i,st} \quad (18)$$

$$q_l(t) = q_{l,tr}(t) + q_{l,st} \quad (19)$$

The equation [13] derived for specified element of bulk water within the annulus and solved by using Laplace method by using the transient part of the above equations [14, 15, 16, 17, 18 & 19] to investigate the transient part at node

$$T_{ave,tr}(s) = \frac{\Delta q}{s(\tau s + 1)(c1 + 2\dot{m}C_p)} + \frac{c1c2}{(\tau s + 1)(c1 + 2\dot{m}C_p)} + \frac{2\dot{m}C_p T_{i,tr}(s)}{(\tau s + 1)(c1 + 2\dot{m}C_p)} \quad (20)$$

Where:

$$\Delta q = \frac{q_t * \%\text{power increase} * c(z_{i+1} - z_i)}{L}$$

$$c1 = \frac{1}{[R_{the} + R_{the,con} + R_{the,ins}]} \qquad c2 = T_\infty$$

$$R_{the} = \frac{1}{hA}, \quad R_{the,con} = \frac{\ln\left(\frac{r_o}{r_i}\right)}{2\pi k_g}, \quad R_{the,ins} = \frac{1}{h_{ins}A_c}$$

$$\tau = \frac{MC_p}{c1 + 2\dot{m}C_p}, \quad M = \rho_{ave}a(z_{i+1} - z_i)$$

The eq. [20] derived to find the transient accumulated heat;

$$T_{ave,tr}(t) = \frac{\Delta q}{(c1 + 2\dot{m}C_p)}\left[1 - e^{-\frac{t}{\tau}}\right] + \frac{c1c2}{\tau(c1 + 2\dot{m}C_p)}e^{-\frac{t}{\tau}} + \frac{2\dot{m}C_p e^{-\frac{t}{\tau}}}{\tau(c1 + 2\dot{m}C_p)}T_{i,tr}(t) \quad (21)$$

$T_{ave,tr}(t)$ Substituent in eq. [14] to find $T_{i+1,tr}(t)$

$T_{i+1,tr}(t)$ Substituent in eq. [17] to find $T_{i+1}(t)$.

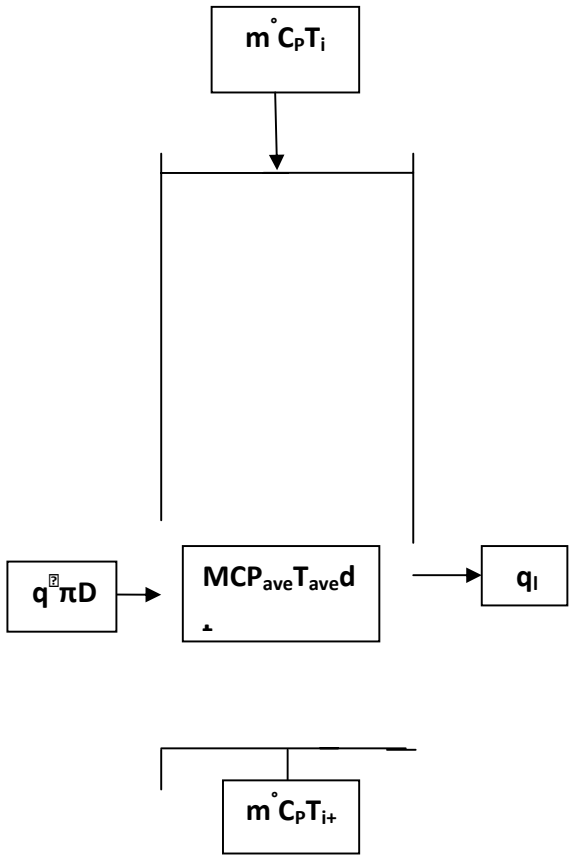

Fig (3): Heat balance mass transfer

LOCAL HEAT TRANSFER COEFFICIENT:

In order to investigate if the flow in the test section is fully developed or developing flow, it is necessary to estimate the thermal entrance length, The thermal entrance length (Z_{et}) given by the following expression; **(Ebadian and Dong 2006).**

$$\frac{Z_{et}}{D_h} = 0.034\,Re\,Pr \quad (22)$$

The following equation is used to calculate the heat transfer coefficient as shown below, **(EL-Wakil, 1962).**

$$h = \frac{0.021 C_{p,b} G (1+\frac{2.3 D_h}{L})}{(\frac{D_h G}{\mu_f})^{.2} Pr_f^{.66} (\frac{\mu_s}{\mu_b})^{.14}} \quad (23)$$

The thermal properties $(C_{p,b}, Pr_f, \mu_f, \mu_b \& \mu_s)$ in the eq. [27] is calculated from the heat transfer tables at film, bulk and clad surface temperatures $(T_f, T_{i-1}(t) \& T_s)$;

Where:

$$T_f = \frac{T_s + T_{i-1}(t)}{2} \quad (24)$$

$$T_s = T_{i-1}(t) + \frac{q''}{h} \quad (25)$$

To avoid sub-cooled nucleate boiling at clad surface, the maximum clad temperature at the hot spot shall be lower than boiling temperature. A safety factor (K) given by the following equation. **K** used to estimate this temperature; **(Ezzat and Taki, 1988).**

$$K = (T_B - T_{in})/(T_s - T_{in}) \quad (26)$$

Sub-cooled nucleate boiling of the coolant starts the heat source clad surface temperature reach to the boiling temperature at that position; T_B the following correlation is used for T_B estimation;

$$T_B = T_{sat} + 2.03 * q''^{0.35} * P^{-0.23} \quad (27)$$

$$P = P_i + \rho g z + (f \frac{z}{D_h}) . (\frac{v^2}{2g}) \quad (28)$$

EXPERIMENTAL WORK

The experimental work was conducted in the Heat Lab in the Mechanical Engineering department at Baghdad University. The design of the heat source simulates IRT-5000 research reactor by utilizing an electrical heater inside the heating element. The heating element is subjected to step power increase higher than its steady state value by around (5%- 20%) of its nominal power rate. The estimated heat flux based on 5 MW power of the research reactor was out of the capability of the heater used for simulation during the experimental part of the study. Therefore only 20% of this power is used during the experiments to ensure the integrity of the heat source. The water volumetric flow rate is fixed during the experiments at certain value that ensures the same temperature distribution along the heat source during steady state condition. While the inlet water temperature and other operational parameters are fixed as used in IRT 5000 reactor. The geometry of the heat source which is used during the experiments was cylindrical shape which is different from plate shape used in IRT-5000 reactor, due to fabrication difficulties. It consists of heat source consists of a nickel-chrome wire, wounded as (U) shape coil inside solid stainless steel cylinder and the stainless steel tube is fitted with thermal cement to isolate this coil from the stainless steel cylinder. The length of the heater is (70 cm), but the active heating length is (66cm), the diameter is (2 cm), the maximum total power is (2500 W), resistance of heat source (19.2Ω) and the maximum applied voltage (220-240) Volt. The flowing channel is made of Perspex glass to minimize the heat lost to the surrounding air due to its low thermal conductivity in addition to its transparency to enable visualization the flow patterns during water phase change. The cylindrical channel thickness is (1 cm), its length is (70 cm), with inner diameter equals (2.5 cm) and outer diameter equals (4.5 cm). To ensure the gap between two concentric cylinders equal to (0.25cm), proper flanges made from Teflon are fitted in the both ends of the cylindrical channel to resistant the high temperature caused by the effect of the heat source in the top and bottom of the annular channel. The temperature of the outside surface of the inner cylinder heat source is measured by using sixth asbestos sheath alumel-chromel (type T) thermocouples installed in six spaces (6.5, 19.5, 32.5, 45.5, 58.5 and 66) cm arranged along the heated wall. The digital thermometer type (12 channel temperature recorder with SD Card Data Logger) was used. The supplied water to the annular test section is heated up to 45^{o}C in a rectangular cross section tank. The tank dimensions are (120×60×40) cm which is used to heat up the water in the circulation loop to the inlet temperature of the annular test section channel. The tank is constructed of (0.4 cm) thick AISI stainless steel. It is open from the top and consists of six orifices. The purpose of the orifices is to control the hydraulic behavior of the water which is used for cooling the heat source passing through the channel. See figure 4. The tank is equipped with a gate of (40×40) cm dimensions fixed at (10 cm) height from the bottom of the tank. The gate could be dismantled easily using proper bolts and gasket. The purpose of this gate is to facilitate the accessibility to the annular test section channel during experiments. The power of electrical heater 3000 W, (13Amp and

220 Volt) located at (10 cm) from the bottom of the tank to heat the water to its inlet temperature (45°C), see plate 1. The tank is connected to the cold water inlet which is supplied from cold water tank fixed at level higher than original tank level. The dimensions of the cold water tank are (40 cm) diameter and (100 cm) length, see plate 2. The water in the main tank is mixed with the cold water added to it before the circulation of the water in the annular test section channel to ensure the (45°C). The temperature of the water in the inlet of the annular test section channel is fixed at (45°C), while the inlet pressure is fixed at (1.05 bar) ensured by adjusting the control valve in the inlet of the annular test section channel. Heat exchange in the channel is ensured by forced convection between circulating water and the heat source of (2500 W). The water is circulated through the closed loop, where, the water is withdrawn from the suction pipe fixed at (10 cm) from the bottom of the tank at temperature (45°C). The water that exits from the pump is divided between the test section and the bypass pipe. The purpose of the bypass pipe is to control water flow rate and pressure in the channel through a control valve. The feed pipe consists of a flow meter (1-7 l/min) to read water flow rate in the test section channel. A pressure gage whose range is (0-100 kPa) is used to measure the inlet pressure of the water. The manometer used to read the pressure across different locations in the test section. Additional thermocouples are installed inside the channel to measure water temperature in the inlet and the outlet of the channel. To predicate the CHF phenomena during transient conditions it is planned to either decrease water velocity in the annular test section channel or increase the temperature of water at the inlet of the test section, as power increase is limited to the capability of the heat source to withstand the input current. Different water flow rates ranging (0.5 – 1) l/min are used during the experiments, while the inlet water temperature to the annular test section is ranged (55 – 75) °C. Water flow pressure at distances (45.5, 58.5 and 65) cm from the heated wall inlet are measured by the water manometer during the power increase transient course at each water flow rate and water inlet temperature. When the pressure at any of these points starts to fluctuate sharply it predicts the transition of boiling configuration from nucleate boiling to film boiling at distance located upper from the pressure fluctuation point. The heat source power that initiates this fluctuation together with the related pressure measurements at the 3 above mentioned points, surface temperature and water temperature at these points are recorded versus the water inlet temperature and water flow rate.

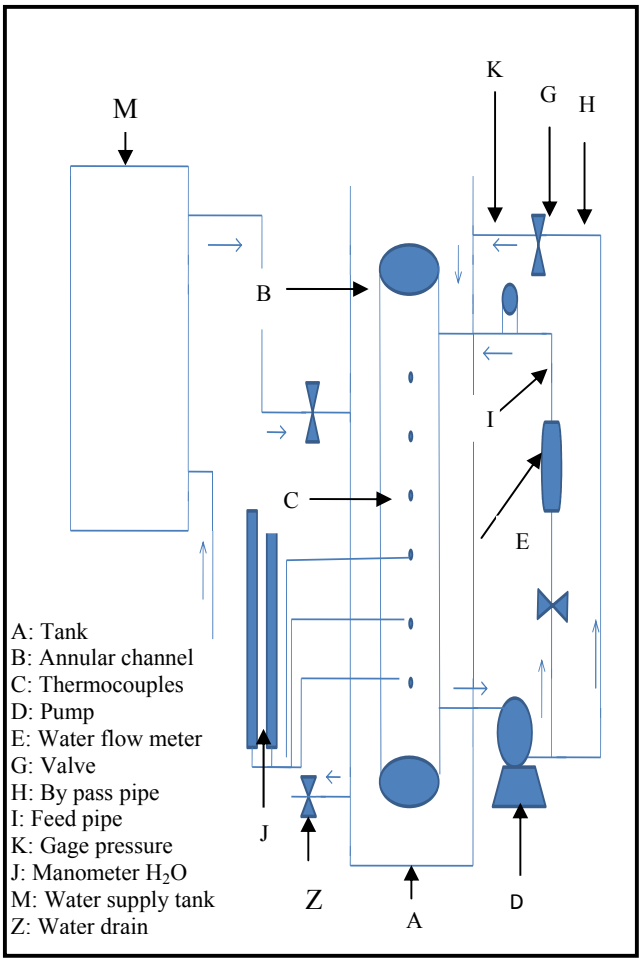

Fig (4): Diagram of annular test rig

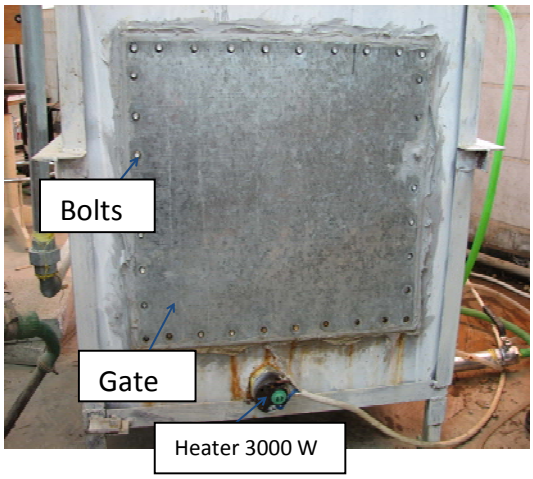

Plate (1): Test rig -back view

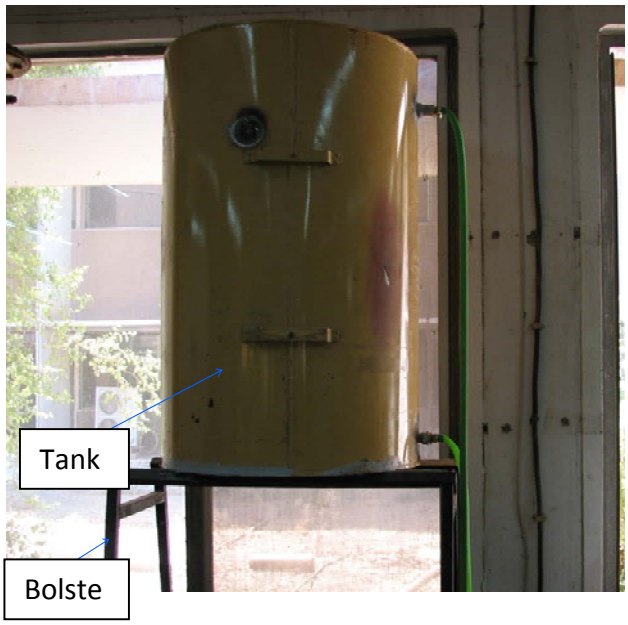

Plate (2): cold supply water tank

RESULT AND DISCUSSION

The adopted values of the total electrical power during the experiments are ranged (1920-2300) W which ensured heat flux values range (46.4-55.6) KW/m^2. The selection of heat flux range is limited to the above mentioned upper limit due to the limitation of the maximum available electrical power supplied to the heat source and the limitation of the material used to fabricate both the electrical source and its outer channel including the capability of the adhesive materials used to fix the thermocouples which starts to melt at temperatures exceed 120°C. Therefore the maximum value of heat flux didn't exceed 55.6 KW/m^2. The temperature variation along the heat source clad surface is plotted in figure 5. The figure shows the experimental and theoretical distribution of the surface temperature along electrical heat source at heat flux equal 1920 W during steady state condition. This figure reveals that the surface temperature increases starting from the annulus entrance and attains a maximum value at the end of the channel, point (65 cm). The rate of surface temperature increase is linearly proportional to the distance. Figure 6 shows the effect of 20% power increase transient respectively on the heat source clad surface temperature at the end of the electrical heat source, (65 cm). The figure shows that the maximum surface temperature is measured and calculated in the end of the heat source due to the effect of the increasing water bulk temperature affected by the accumulated heat added to the channel. The experimental and theoretical results related to the heat source clad surface temperature versus the elapsed time required to reach these temperatures to their steady state values at the end of the heat source, 65 cm are plotted. Figure 7 represents the curves plotted for power increase transient conditions (5%, 10%, 15% and 20%) of the nominal steady state power. It is clear that the clad surface temperature after reaching to their steady state values are proportional to power increase percentages, as these temperatures are directly proportional to the constant heat flux. Figure 8 shows the experimental and theoretical distribution of the bulk water temperature along heat source at power equal 1920 W during steady state condition. The bulk temperature is proportional directly with the distances (6.5 to 65) cm at constant heat flux (q''= 46376.8 W/m^2). The water bulk temperature reaches its maximum value at the end of the heat source, 65 cm due to the proportionality of the accumulated heat addition versus the channel distance. The figure shows that all bulk water temperatures are far from 100°C, water saturation temperature, while the degree of sub-cooling decreases along the heat source due to the continuous power addition. Figure 9 shows the experimental and theoretical bulk water temperature versus elapsed time required to reach the steady state condition at the end of the heat source, (65 cm) at 20% power increase transient. The figure shows that the maximum bulk water temperature measured and

calculated at the end of the heat source is proportional to the power increase rate due to the effect of the accumulated heat added to the channel. Figure 10 shows the experimental and theoretical values of the heat transfer coefficient versus the elapsed time required to reach the steady state condition at the end of the heat source, (65 cm) during 20% power increase transient. Comparison between heat transfer coefficient values after reaching to their steady state values demonstrates that these values are proportional to power increase percentages due to the effect of average bulk water velocity increase along the channel affected by water density decease to ensure continuity provision. The results reveal also that heat transfer coefficient increase the rate versus time is proportional also to the power increase percentages which justify the reason for the positive effect of power increase on the enhancement of the heat transfer process during nucleate boiling up to the point of departure from nucleate boiling, DNB. Figure 11 shows the boiling safety factor, K versus the elapsed time to reach steady state condition at the end of the heat source, (65 cm) after 20% power increase transients. It is clear that the decrease in K values versus elapsed time is due to the increase of the clad surface temperature versus power increase. The figure illustrates that power increase transient up to 15% of the nominal power during the recent experiments keeps **K** values above 1 till the end of the channel which excludes any possibility for nucleate boiling during these transients, while at 20% power increase transient K value goes below 1 which means ensuring of nucleate boiling at the end of the channel. To investigate the effect of higher power increase transients on the boiling safety factor and their related parameters, the heat source is assumed to be exposed to (30%, 40% and 50%) power increase percentages of its nominal power and the related parameters are studied theoretically only due to the limitation of the heat source to 20% power increase which bounded the experimental range. Figure 12 shows the comparison among curves related to theoretical results of the heat source clad surface temperature and bulk water temperature. These curves are plotted versus different power increase percentages (5% to 50%). It is clear that the elapsed time required for the bulk temperature to reach their steady state values are higher than those related to clad surface temperature and the slop of their curves are smoother which means that the response of any safety system to such power transients are more effective when their temperature sensors are linked to surface clad rather than bulk water. Figure 13 show the boiling safety factor at the end of the heat source surface (65 cm) at different percentage power increase (20%, 30%, 40% and 50%), respectively. It means that the elapsed times are proportional to the power increase percentages. This proportionality may leave linearity due to effect of the nucleate boiling phenomenon. There are several experimental methods to predict the critical heat fluxes. The first method depends on clad temperature observations during power increase transients. During applying this method, the heat flux is nominated as critical heat flux when its existence leads to sharp increase in clad temperature due to the poor heat transfer mechanism between the bulk fluid and clad surface affected by the progress of the nucleate boiling phase to film boiling phase. The second experimental method depends on the observation of the local water temperature along the heat source length. The position at which this pressure oscillates sharply will refer to the position of the DNB and the heat flux that leads to this oscillation will be nominated as critical heat flux. During the present experiments the second methodology is applied for prediction of critical heat flux. Figures 14 &15 show the experimental investigation of the effect of the water flow rate and the degree of water sub-cooled temperature respectively, on the critical heat flux **CHF** at which water starts to leave nucleate boiling at the clad surface hot spot temperature and pass to film boiling phase. Keeping each of the above two parameters constant during studying the effect of the other parameters on **CHF**, both curves show that critical heat flux is proportional directly with the water flow rate and with the sub-cooled water temperature. Figure 16 shows the pressure differences along the heat source water channel between their values during nominal power operation and those measured when the film boiling occures at departure from nucleate boiling, **DNB** postions during different water flow rates. These values obtained at water inlet temperature equals 60 °C. As discussed before as the water flow rate decreases the critical heat flux decreases at constant water inlet temperature and the position at which the film boiling initiates decreases. Accordingly, and as shown from the relevant figure, the slope of the pressure differences curve decreases also which means that the response time of any pressure sensor is proportional to water flow rates but however the sensitivity of this response is

inversely proportional to them. Figure 17&18 show the comparison between the experimental results obtained from the relevant experiments with those obtained using the correlation investigated by (David and Mudawar, 1996). Both figures investigate respectively the effect of the difference between inlet and outlet bulk water temperature and the water mass flux on the CHF. Keeping each of the above two parameters constant during studying the effect of the other parameter on CHF, both curves show that critical heat flux is proportional directly with the water mass flux and with the difference inlet and outlet bulk water temperature. The figures show some sensible differences with the relevant experimental results due to the differences in the applied operational pressure in the channels used during experiments.

CONCLUSIONS:

Heat transfer process improve versus power increase percentage transient due to the effect of nucleate boiling which depends on the nominal power rate, power increase percentage , coolant mass flow rate and channel geometry. The heat source is affected by the action of the hydraulic behavior of the water coolant (bulk water temperature, drop of the water pressure) where, the bulk water temperature and drop in the pressure due to the friction reaches their maximum values versus distance.

1. The nucleate boiling phenomena occurred only in case 20% power increase transient as the boiling safety factor was reached to equal (1) at the end of the heat source, .65 m at (10 sec), which means that power protection sensor should use the power increase percentage as threshold for its activation.
2. As the power source is constant heat flux, clad surface temperature reaches its maximum value at the end of the heat source, (0.65 m) in power increase transient which means that any power transient prediction should be fixed at the end of the channel.
3. The surface temperature response is faster than that related to bulk water temperature affected by power increase transient which means that any safety system response to such power transients are more effective when their temperature sensors are linked to surface clad rather than bulk water.
4. The critical heat flux, CHF is proportional to the mass flow rate of the coolant, while it is inversely proportional to channel inlet water temperature. There are more factors which affect the value of CHF as, channel length, diameter and water pressure inside the channel.

NOMENCLATURE

A_o	Surface area of channel
A_s	Surface area of heat source
c	Circumference of heat source **($c=\pi D_i$)**
c1&c2	Constants
C_p	Specific heat of constant pressure
D_i	Inner diameter of heat source
D_o	Outer diameter of channel
D_h	Hydraulic diameter= (D_o-D_i)
f	Friction factor (f= 64/ Re)
g	Gravity acceleration
G	Mass velocity of water
Gr	Grashof number
h	Heat transfer coefficient
I	Current
k_g	Thermal conductivity of the insulated channel
K	Boiling safety factor
L	Length of heat source
m°	Mass flow rate of water
M	Mass of water
P	Pressure
P_i	Inlet pressure at the top of the channel
pr	Prandtl number
q_c	Convective heat to the water
q_l	Heat lost to the surrounding air
q_t	Total heat power
q''	Heat flux
Ra	Rayligh number
r_i	Inner radius of the insulated channel
r_o	Outer radius of the insulated channel
Re	Reynolds number
Q	Flow rate of water
t	Time
T	Temperature
τ	Time Constant
v	Axial velocity
V	Voltage
z	Axial distance along heat source
z_{et}	Thermal entrance length

GREEK LETTERS

β	Coefficient of volume expansion
ϑ	Kinematic viscosity
ρ	Density

SUBSCRIPT

∞	Surrounding air around channel
ave	Average
b	Bulk
in	Inlet water
ins	Insulator
out	outlet water
sat.	Saturated
st	Steady state condition
tr	Transient
the.con	Theoretical conduction heat transfer

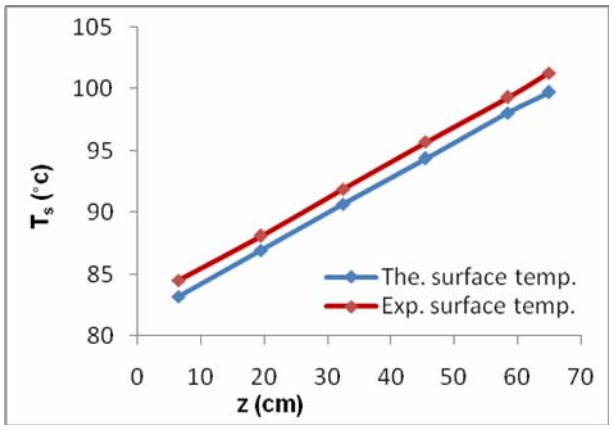

Fig 5: Experimental and theoretical clad surface temperature versus distance during steady state condition.

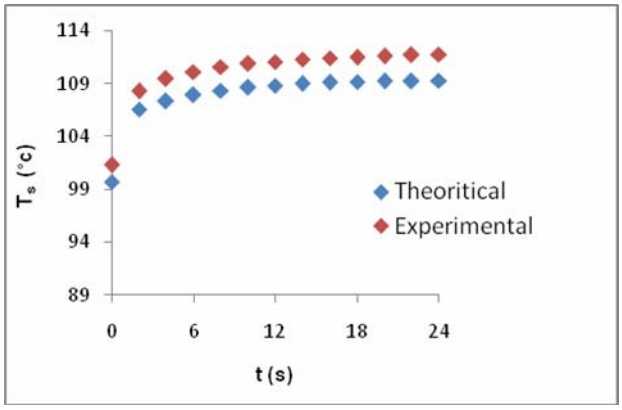

Fig 6: Theoretical and experimental clad surface temperature versus time at the end of the heat source, (65 cm) during 20% power increase transient.

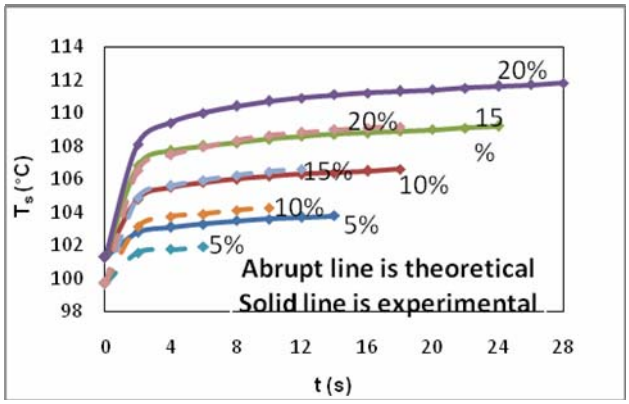

Fig 7: Experimental and theoretical surface temperature versus time at the end of the heat source, (65 cm) during (5%, 10%, 15 and 20%) power increase transient.

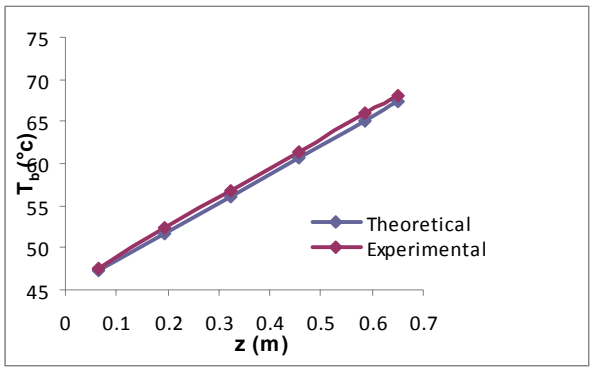

Fig 8: Experimental and theoretical bulk water temperature versus distance during steady state condition.

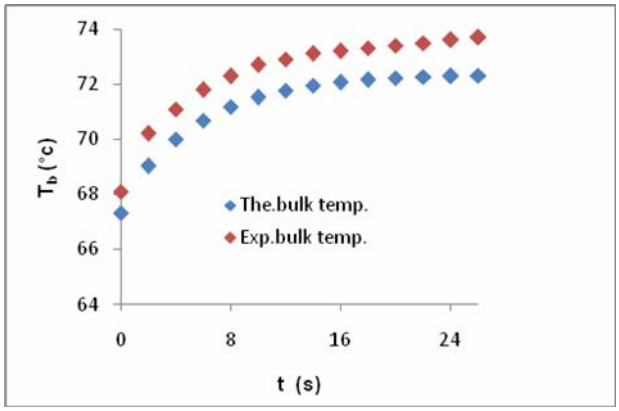

Fig 9.Theoretical and experimental bulk water temperature versus time at the end of the heat source (65cm) during 20% power increase transient

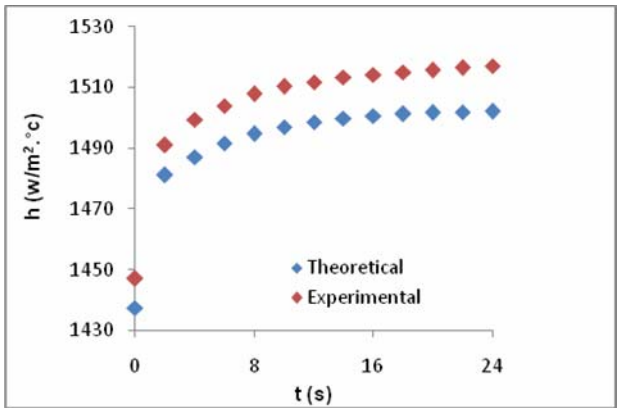

Fig 10: Theoretical and experimental heat transfer coefficient versus time at the end of the heat source, (65 cm) during 20% power increase transient.

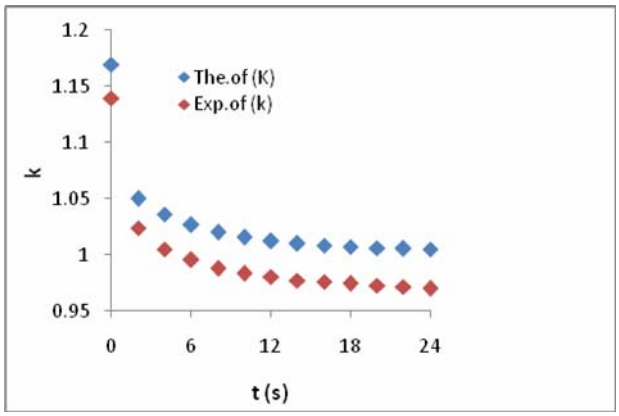

Fig 11: Theoretical and experimental boiling safety factor versus time at the end of the heat source, (65 cm) during 20% power increase transient.

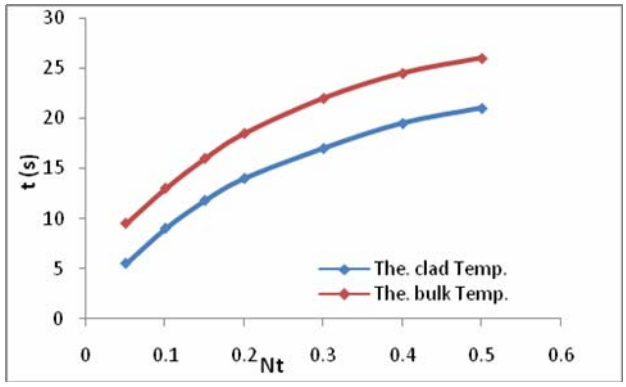

Fig 12: Theoretically measured elapsed time required to reach steady state surface clad and water bulk temperature at the end of the heat source, (65 cm) versus (5%, to 50%) percentage power increase transient.

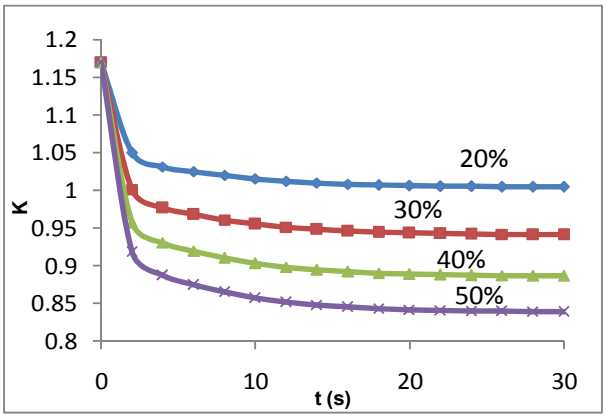

Fig 13: Theoretical boiling safety factor, K versus time at the end of the heat source, (65 cm) during 20%, 30%, 40% and 50% power increase transient.

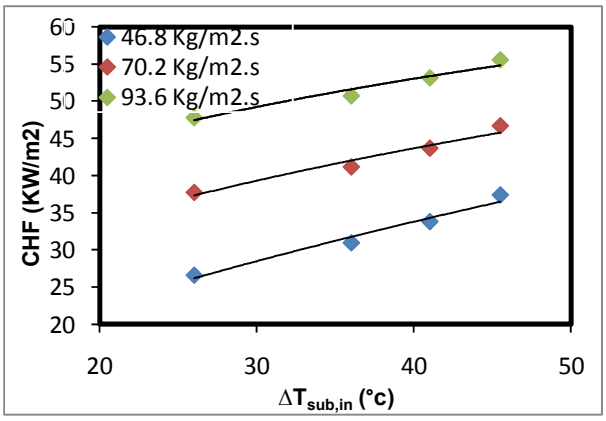

Fig 14: Experimental CHF versus inlet sub-cooled water temperature at different inlet water flow rate

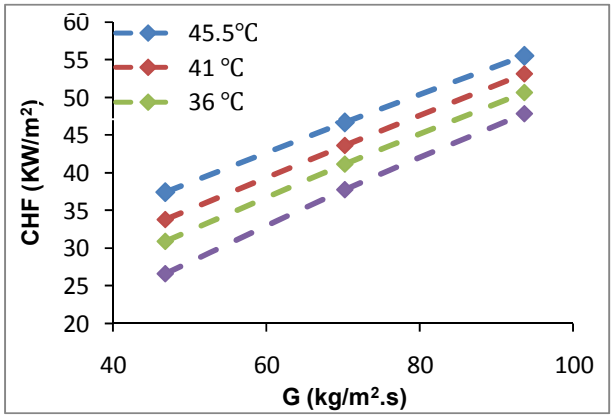

Fig 15: Experimental CHF versus mass flux of water at different sub-cooled water temperature.

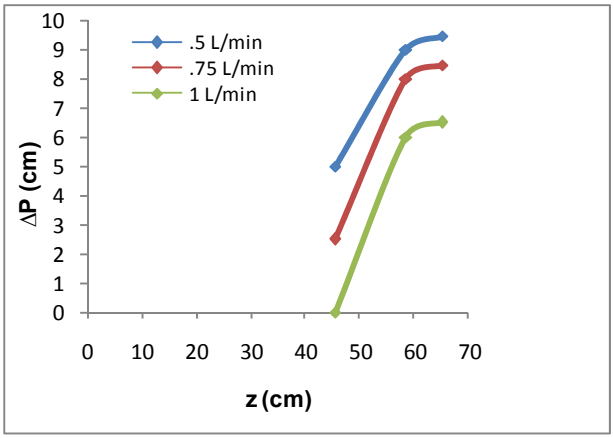

Fig 16: Pressure difference versus distance (45.5, 58.5 and 65) cm at inlet water temperature (60°C) in the steady state condition

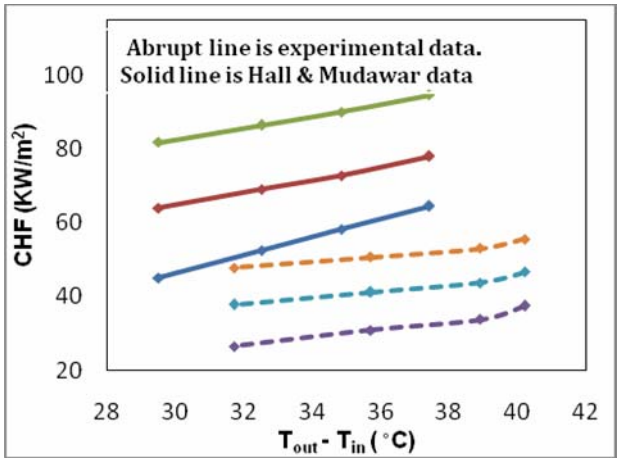

Fig 17: Comparison of experimental data with existing correlation (critical heat flux versus difference between inlet and outlet bulk water temperature for different mass flux).

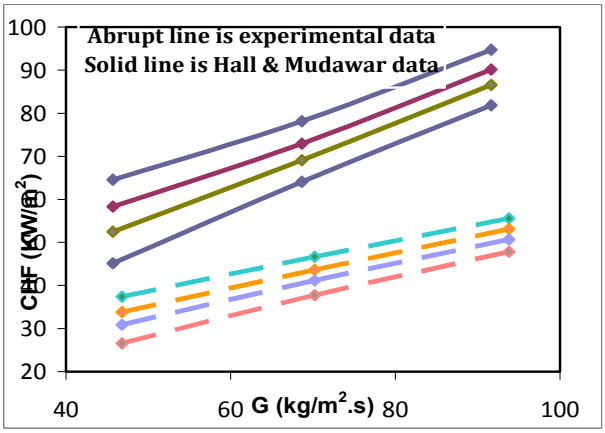

Fig 18: Comparison of experimental data with existing correlation (critical heat flux versus mass flux for different difference between inlet and outlet bulk water temperature ($T_{out} - T_{in}$)).

REFERENCES

A.W.Ezzat and H.M.Taki. (1988) Final safety report for 14th Tammuz 5000 KW reactor, INC, Iraq nuclear commission under the supervision of IAEA, paragraph 5.4.

David D.Hall and Issam Mudawar. (1996) "Evaluation of subcooled critical heat flux correlations using the PU-BTPFL CHF database for vertical up flow of water in a uniformly heated round tube", Boiling and Two-Phase Flow Laboratory, School of Mechanical Engineering, Indiana 47907-1288.

Dr.Harlan H.Bengtson, P.E. (2010) "Convection heat transfer coefficient estimation" www.SunCam.com, PP. 2-40.

J. Braz. (2000) " Thermal hydraulic behavior of electrically heated rod during a critical heat flux transient"Journal of Brazilian Society of Mechanical Sciences and Engineering, Vol. 22 No.4, ISS 0100-7386.

M.A.Ebadian and Z.F.Dong, (2006) "Forced convection, internal flow in ducts "Chapter 5, Florida International University.

M.M.El.Wakil. (1962) "Nuclear Power Engineering " McGraw-Hill Book Company, New York.

Tomio Okawa, Akio Kotani, Isao Kataoka and Masanori Naito, (2003), "Prediction of critical heat flux in annular flow using a film flow model" Journal of Nuclear Science and Technology, Vol.40, No.6, PP. 388-396.

Yong Tae Kang, B.S., M.S. (1994) "Experimental investigation of critical heat flux transient boiling systems with vertical thin rectangular parallel plate channels" Ph.Sc.Thesis, School of the Ohio State University.

Y.W.Wu, G.H.Su, B.X.Hu and S.Z.Qiu, (2010) "Study on onset of nucleate boiling in bilaterally heated narrow annuli" International journal of Thermal Sciences, Vol.49, PP. 741-748.

Field Study of Novel Storage Tank of Solar Water Heating System

Asst. Prof. Dr.Karima Esmail. Amori drkarimaa@yahoo.com

Jinan Shaker Sherza Jenan_sherza@yahoo.com

Univ. of Baghdad/ Mech. Eng. Dept. , Baghdad-Iraq

ABSTRACT

In this paper thermo-hydrodynamic characteristics were investigated experimentally for a new type shell-helical coiled tube heat exchanger used as a storage tank of closed loop solar water heater system. Triple concentric helical coils were made of copper tubes of (12.5mm OD and 10mm ID) with coils diameter of (207, 152.2, 97mm) for outer, middle and inner coils respectively. The experiments were carried out during a clear sky days of (March and April 2012). The parameters studied in this work are: history of average temperature of shell side of the storage tank, collector heat gain, heat rejected from coils to shell side of the storage tank, collector efficiency, thermal effectiveness of the heat exchanger (storage tank), and pressure drop. These parameters were studied at four different circulating mass flow rates of (1.8, 3, 6, 9 l/min) and for two consuming modes of supply water namely no withdrawal, and continuous withdrawal of (1 l/min). The results show that stratification temperature in the storage tank is increased for no withdrawal compared with water withdrawal, also the shell side average temperature increases with increased solar time. Collector efficiency is increased with increasing circulation flow rates, also increases with water withdrawn from storage tank. The pressure drop decreases with the increase of solar radiation .

KEYWORDS: solar hot water system; storage tank; heat exchanger; helical coil tube; pressure drop; effectiveness.

دراسة ميدانية لخزان جديد مستخدم في منظومة شمسية لتسخين الماء

أ.م.د. كريمة أسماعيل عموري جنان شاكر شيرزة

الخلاصة

في هذا البحث تم التحقق من المواصفات الحرارية والهيدروديناميكية عمليا لمبادل حراري جديد نوع قشرة-أنبوب ملتف حلزونيا مستخدم كخزان لمنظومة شمسية لتسخين الماء. صنعت ثلاثة ملفات حلزونية متمركزة من أنبوب نحاس ذو قطر خارجي =12.5 ملم وقطر داخلي=10ملم وبقطر ملف خارجي، وسطي، وداخلي (207، 152.2، و 97ملم) على التوالي. أجريت التجارب في أيام صحوة خلال شهري آذار ونيسان من سنة 2012. درست المتغيرات التالية: توزيع معدل درجة الحرارة في ماء قشرة الخزان، الكسب الحراري للمجمع الشمسي، الحرارة المنتقلة من ماء الملف الى ماء القشرة، كفاءة المجمع، الفعالية الحرارية للمبادل الحراري، وهبوط الضغط. تم دراسة هذه المتغيرات عند اربع قيم لمعدل جريان ماء التدوير (1.8، 3، 6، و 9 لتر/دقيقة) ولنموذجي صرف من ماء التجهيز للمستهلك وهما نموذج عدم سحب الماء، والآخر صرف الماء بمعدل 1لتر/دقيقة وبصورة مستمرة. بينت النتائج وجود تراصف حراري أقوى في الخزان في حالة عدم السحب مقارنة بحالة السحب، وان معدل درجة حرارة ماء

الخزان تتزايد مع تقدم ساعات النهار. تتزايد كفاءة المجمع الشمسي مع زيادة معدل جريان ماء التدوير، وتزداد في حالة سحب الماء من الخزان عما هو عليه في حالة عدم السحب. يقل هبوط ضغط ماء التدوير مع زيادة قيمة الأشعاع الشمسي عمليا ونظريا".

الكلمات الرئيسية: منظومة شمسية لتسخين الماء، خزان،مبادل حراري،أنبوب ملتف حلزونيا، هبوط الضغط، فعالية.

INTRODUCTION:

Heat exchangers are used in a wide engineering applications including power plants, nuclear reactors, refrigeration and air conditioning systems, automotive industries, heat recovery systems, chemical processing, and food industries. Heat transfer enhancement enables the size of the heat exchanger to be considerably decreased. The previously used enhancement techniques can be divided into two groups: active and passive techniques. The active techniques require external forces like fluid vibration, electric field, and surface vibration. The passive techniques require special surface geometries or fluid additives like various tube inserts. Several studies have indicated that helically coiled tubes are superior to straight tubes when employed in heat transfer applications. The centrifugal force due to the curvature of the tube results in the secondary flow development which enhances the heat transfer rate.

Seban and Mclaughlin (1962) presented friction and heat transfer results for the laminar flow of oil and the turbulent flow of water in tube coils having ratios of coil diameter to tube diameter of 17 and 104, for Reynolds number ranged from 12 to 65000.**Rogers and Mayhew (1964)** reported and compared experimental results for forced convection heat transfer and friction factors, obtained for water flowing through steam heated coils. Existing equations for isothermal friction factors in smooth coils are deemed satisfactory. Non-isothermal friction factors and heat-transfer coefficients can be estimated from proposed equations for design purposes, but results cannot yet claim the same validity as those for straight pipes..**Ali (1994)** obtained average outside heat transfer coefficients for turbulent heat transfer from vertical helical coils submersed in water. Water was pumped through the coil and the inside heat transfer coefficients were calculated based on the Nusselt number correlation of **Rogers and Mayhew**. Outside heat transfer coefficients were calculated based on the thermal resistance method for cylindrical tubes. **Kharat, et.al. (2009)** developed a correlation for heat transfer coefficient for flow between concentric helical coils. A Correlation is found to result in large discrepancies with the increase in gap between the concentric coils when compared with the experimental results. They are used experimental data and CFD simulations using Fluent 6.3.26 to develop improved heat transfer coefficient correlation for the flue gas side of heat exchanger. **Salimpour (2009)** investigated experimentally the heat transfer coefficients of shell and helically coiled tube heat exchangers. Three heat exchangers are tested with different coil pitches for both parallel and counter-flow configurations. The inlet and outlet temperatures of tube side and shell-side fluids, flow rate are measured. It was found that the shell side heat transfer coefficients of the coils with the larger pitches are higher than those for smaller pitches. Empirical correlations were proposed for shell-side and tube-side. His results were compared with previously existing correlations for other boundary conditions and a reasonable agreement was observed. **Jayakumar et. al. (2010)** adopted CFD simulation package FLUENT version 6.3 for vertically oriented helical coils by varying coil parameters such

as (i) pitch circle diameter, (ii) tube pitch and (iii) pipe diameter and their influence on heat transfer. Correlations are developed of local Nusselt number as a function of angular location of the point. **Ghorbani et.al. (2010)** investigated experimentally the mixed convection heat transfer in a coil-shell heat exchanger for various Reynolds number, Rayleigh numbers, various tube-to-coil diameter ratios and dimensionless coil pitch.

The objective of this work is to investigate experimentally the thermal and hydrodynamic characteristics of a new type of shell-helical coiled tube heat exchanger used as a storage tank of forced closed loop solar water heater system for Baghdad climate conditions. The outdoor tests are performed under different circulation flow rates to establish the, thermal stratification within the shell side of the storage tank, collector efficiency, storage tank effectiveness, and pressure drop of the helical coiled tubes. Up to our knowledge there is no previous reported study dealing with this type of work.

EXPERIMENTAL SETUP

Fig.(1) shows a schematic diagram of the experimental set-up. A closed loop forced circulation solar hot water system is formed of two flat plate solar collectors, of single glass cover, south oriented, (each of dimensions 1.92m*0.85m) are used to provide hot water stream to a storage tank formed of shell-triple concentric helical coiled tubes. A cold supply water stream (flowing in the shell-side of the storage tank of 120 liter capacity) cools the hot circulating water flowing inside the helical coiled tube. The heat exchanger includes a copper coiled tube and an insulated shell. The specifications of the heat exchanger are depicted in Table (1). This design has been adopted based on the capacity of the storage tank. A centrifugal water pump type Vicounte PKM60 of (0.5HP) power, is used to circulate water within the closed cycle. Five valves are used to control the flow rate of hot water and supply coolant water. The experimental set-up is a well instrumented, fourteen calibrated thermocouples (type K) are located at different positions of the test rig as shown in Fig.(1). All thermocouples are connected to two 12-Channels thermometers (type k temperature reader with SD Card Data-Logger - Model BTM-4208SD-Lutron Company). A flow meter type Z-4002 float type of range (1.8 to 18 l/min) is used of (0.3 l/min) resolution. The pressure drop of water flowing in the helical coiled tubes is measured by using a Borden gage of range (0 to 160 mbar) and 5 mbar resolutions. The global solar radiation has been taken from the Ministry of Science and Technology in Baghdad city 33.3^{o} north.

THEORY

The thermo-physical properties of the hot water for the coil side or for the shell side are taken at the water bulk temperature of that side for each reading (the experimental readings were taken every 30 minutes). Heat rejected from the coil Q_c to the shell side is calculated as:

$$Q_c = \dot{m} c_p (T_{ci} - T_{co}) \quad (1)$$

where Q_c is the heat rejected from the coils (W), is the flow rate (kg/s) ,T_{ci} is the coil inlet temperature (K),T_{co} is the coil outlet temperature (K), and c_p is water specific heat (J/kg.K).

The hot water mass flow rate $\dot{m}$ is obtained from flow-meter reading $\dot{V}$ as:

$$\dot{m} = \rho * \dot{V} \quad (2)$$

The collector heat gain can be calculated from

$$Q_{coll.} = \dot{m} c_p (T_{coll.o} - T_{coll.i}) \quad (3)$$

The effectiveness of the storage tank can be expressed as:
for no withdrawal

$$\varepsilon = \frac{(T_{c,i}-T_{c,o})}{(T_{c,i}-T_{tank\,avg.})} \quad (4)$$

for water withdrawal **Ghorbani (2010)**

$$\dot{\varepsilon} = \frac{(T_{C,i}-T_{C,O})}{(T_{C,i}-T_{S,i})} \quad (5)$$

The collector efficiency is calculated as:

$$\eta = \frac{\dot{m}C_p\Delta T}{AI} \quad (6)$$

where
$\dot{m}$ is circulating mass flow rate of water (kg/s)
ΔT is collector outlet and inlet temperature difference (K)
A is area of collectors (m^2)
I is incident solar radiation (W/m^2)

RESULTS AND DISCUSSION

Figure (2) illustrates the incident solar radiation on the collector plane, the ambient temperature and wind speed on 19-3-2012 (clear sky day). The ambient temperature rises as the solar radiation rise, the maximum values indicated after solar noon was 20.6°C at 3:00PM with no considerable variation in wind speed. The global solar radiation was 230 W/m^2 and 615 W/m^2 at 8:00, 12:00 respectively.

The collector inlet and outlet temperature for different circulation flow rates are shown in Fig.s (3.a-b-c-d) and (4 a-b-c-d) for no water withdrawn and water withdrawn of 1 l/min respectively. Water drawn modes are selected according to **Agbo(2006)**. The temperature difference decreases as circulating flow rate increases. When solar radiation increases with time the temperature difference increases with time also. It is clear that higher temperature difference is obtained when the storage tank is under water withdrawal. Quantitatively at the solar noon the temperature differences were (13.65 °C at 1.8 l/min and 3.65 °C at 9 l/min) for water withdrawal, while for no water withdrawn they were (10.3 °C at 1.8 l/min and 2.85 °C at 9 l/min).

Figures (5a-b-c-d) and Fig (6 a-b-c-d) show the stratification phenomena in the storage tank for no withdrawal and water withdrawal of (1 l/min) respectively. It is clear that the temperature of the storage tank increases with increasing solar radiation. Fig.(5) shows inconsiderable variation in the temperature along the storage tank height for different circulating flow rates when no water withdrawn from the tank. The water temperature within the storage tank decreases when supply water is withdrawn compared with that of no water withdrawn as shown in Fig.(6). It is clear that a considerable variation in water temperature along storage tank height for different circulating flow rates.

Figures (7 a-b-c-d) and Figure (8 a-b-c-d) illustrate the influence of circulation flow rate on useful heat gain by the collector (Q_{gain}) and the heat rejected from the helical coil side to the shell side of the storage tank (Q_{coil}). Both of (Q_{gain}) and (Q_{coil}) increases with the increase of the circulation flow rate in a similar behavior, knotting that the useful heat gain is higher than coil heat rejected to the shell side since part of the heat is lost to the ambient. For case I the values of (Q_{gain}) and (Q_{coil}) are (1276, 1376, 1509, and 1770 W) and (1251, 1325, 1447, and 1739 W) respectively at 12:00AM for circulating flow rates of (1.8, 3, 6, and 9) respectively. The effect of circulation flow rate on (Q_{gain}) and (Q_{coil}) is found higher fo case II than that for case I (no withdrawal).

Figures (9 and 10) demonstrate the collector efficiency for different circulation flow rates and for no withdrawal and withdrawal of (1 l/min) respectively. The increase of the circulation mass flow rate leads to increase Reynolds No. which

increases Nusselt No. and heat transfer coefficient so higher heat gain can be obtained. The collector efficiency reaches (52.7%, 55.3%, 69%, and 71.6%) at 12:00 PM for mass flow rates of (1.8, 3, 6, and 9 l/min) respectively for no water withdrawal. Higher collector efficiencies are found for water withdrawal namely (93.3%, 91.5%, 87.8% and 74.5%) at 12:00 PM for mass flow rates of (1.8, 3, 6, 9 l/min) respectively, since colder water enters the shell side and the distribution of the triple helical coils within the shell assist to reject more heat to it so colder circulating water will return to the collector. The triple concentric helical coil used in this work enhances the flat plate collector efficiency especially at 9 l/min and for water drawn off from the storage tank. the collector efficiency reaches 93% during the day hours as noticed from Fig. (10). This is because the good thermal performance of this coil in transforming heat from coil side to shell side. The compact size of the storage tank used in this work is another advantage of this design of heat exchanger.

The storage tank effectiveness follows the incident solar radiation as shown in Fig.(11) when there is no withdrawal, while it is decreased with time when there is water withdrawal as presented in Fig.(12). It clear that the effectiveness rises with decreasing the circulation flow rate, since an increase of circulating flow rate decreases its' temperature difference across the storage tank thence decreases its' effectiveness. Also as solar radiation increases, the temperature difference $(T_{c,i} - T_{st,i})$ is increases which causes a decrease in effectiveness with time. The effectiveness was (0.8, 0.56, 0.35, and 0.23) at (9:00A.M) and (0.38, 0.25, 0.14, and 0.1) at (14:00PM) for circulation flow rates of (1.8, 3, 6, and 9 l/min) respectively.

The hourly pressure drop decreases as indicated in Fig.s (13 and 14) since the properties of water (density and viscosity) are reduced with the increase of its temperature. It is clear that increasing circulating flow rate increases the pressure drop. Pressure drop reaches (1, 2.2, 5.3, and 9.2kPa) at (12:00 PM) for circulation flow rates of (1.8, 3, 6, 9 l/min) respectively. A tiny deviation of the measured pressure drop is observed between with and with no water withdrawal, especially for circulating flow rates of (1.8, and 3 l/min). Since there is a rare work matches the parameters studied in this study, the heat gain to heat input ratio at (3 l/min) circulating flow rate of the present work is compared with the results of Mondol et al. for single coil-shell storage tank (119.6 liter) at (2.4 l/min) circulating flow rate as shown in Fig. 15., the triple concentric coiled tube is more efficient than the single coil tube.

CONCLUSIONS

The following conclusions can be extracted from the previous discussion of the results obtained through this work:

1. A weak variation of temperature difference between collector inlet and outlet temperature during the test day for higher values of circulating flow rates.
2. The circulation rate is a significant parametric effect on the useful heat gain of the collector. Higher values of collector heat gain can be obtained when there is water withdrawal from storage tank
3. The efficiency of the collector increases with the increase of circulation mass flow rate. Higher values of collector efficiency are obtained when water is withdrawn from the storage tank.
4. Effectiveness of heat exchanger is increased when circulation

flow rate is decreased. The heat exchanger effectiveness follows the solar radiation for no water withdrawal while it is decreased with time for water withdrawal .

5. The hourly pressure drop is decreased When Dean number increases.

REFERENCES

Agbo S.N., "Effect of Hot Water Withdrawal Rate on the Mean Temperature of a Themosyphon Solar Water Heater", The Pacific J. of Sci. and Techn., V.7, No.2, pp.199-203,2006

ALI M.E., "Experimental investigation of natural convection from vertical helical coiled tubes" ,Int. J. Heat Mass Transfer. V.37,No.4,pp.665 - 671, 1994.

Jayakumar J.S., Mahajani S.M., Mandal J.C., Iyer K.N. , VijayanP.K.," CFD analysis of single-phase flows inside helically coiled tubes" , Computers and Chemical Engineering V.34, pp.430–446 , 2010.

Ghorbani N., Taherian H., MofidGorji , HessamMirgolbabaei, "An experimental study of thermal performance of shell-and-coil heat exchangers" , International Communications in Heat and Mass Transfer, V.37 pp.775–781 , 2010.

Kharat R., Bhardwaj N., Jha R.S. , "Development of heat transfer coefficient correlation for concentric helical coil heat exchanger" , International Journal of Thermal Sciences, V.48, pp. 2300–2308, 2009.

Mondol JD, Smyth M, Zacharopoulos A., "Experimental characterization of a novel heat exchanger for a solar hot water application under indoor and outdoor conditions", Renewable Energy V.36, pp.1766-1779, 2011.

Rogers G.F.C., Mayhew Y.R., "Heat transfer and pressure loss in helically coiled tubes with turbulent flow", Int. J. Heat Muss Transfer V. 7, pp. 1207-1216. 1964.

SalimpourM.R., "Heat transfer coefficients of shell and coiled tube heat exchangers", Experimental Thermal and Fluid Science, V.33 pp.203–207, 2009.

Seban R.A., Mclauchlin E.F., "Heat transfer in tube coils with laminar and turbulent flow", Heat mass transfer, V.6, pp.387-395, 1962.

NOMENCLATURE

symbol	Description	symbol	Description
A	surface area (m^2)	$\dot{m}$	mass flow rate (kg/s)
C_p	specific heat (KJ/kg K)	N	number of coil turns
D_c	helical coil diameter (m)	P	coil pitch (m)
d	outside tube diameter (m)	Q	heat transfer (W)
I	solar radiation (W/m^2)	T	temperature (^oC)
L_c	coil length (m)	$\dot{V}$	volumetric flow rate, m^3/s
Greek symbols			
ε	effectiveness	ρ	mass density (kg/m^3)
η	collector efficiency	ΔT	temperature difference (^oC)
Subscript			
c,	coil	o	outlet
coll.	collector	s,i	inlet of supply water
i	inlet	tank,avg.	tank average

Table (1): Geometrical characteristics of the triple concentric coils

Item	Outer Coil	Middle Coil	Inner
Coil diameter, tube-center-to-tube-center D_c, (mm)	207	152.5	97
tube outside diameter d, (mm)	12.5	12.5	12.5
tube inside diameter di , (mm)	10	10	10
Axial length of helical coil L_c , (m)	14.95	14.85	14.04
Number of turns in helical coil, N	23	31	46
Curvature ratio , d_i/D_c	0.048	0.066	0.1031
Coil pitch p, (mm)	20	15	10
Coil height (mm)	460	465	460

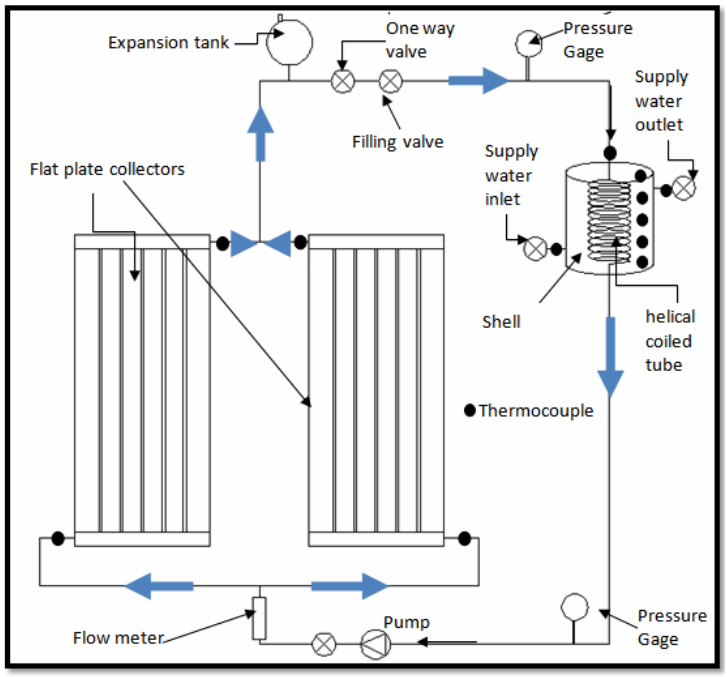

Fig.(1): Schematic Diagram of the Experimental rig (Solar Water Heating System)

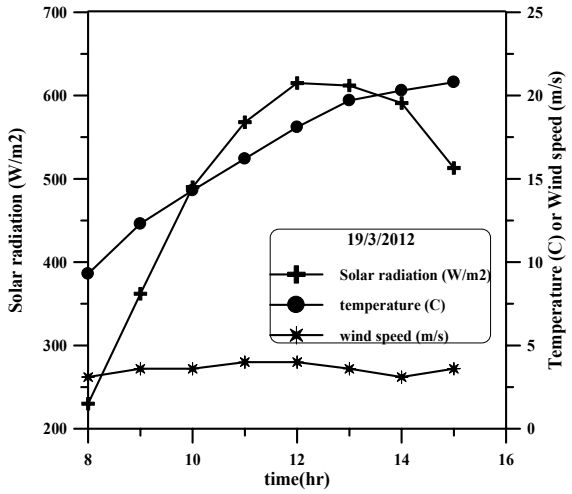

Fig.(2): Hourly Variation of Solar Radiation , Ambient Temperature, and Wind Speed.

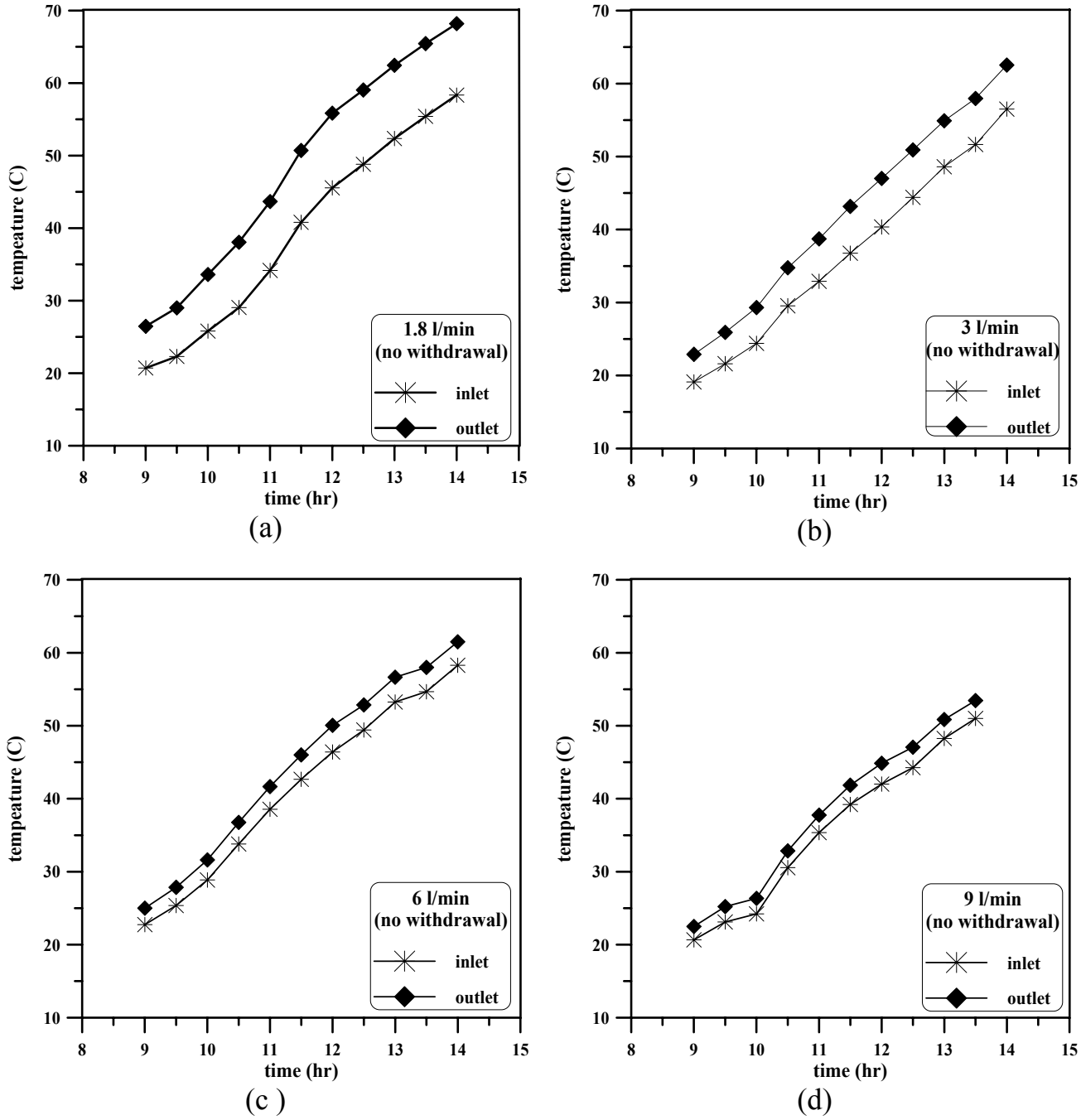

Fig.(3): Hourly Variation of Collector Inlet and Outlet Temperature for no Withdrawal. a)1.8 l/min, b)3 l/min, c)6 l/min, d)9 l/min

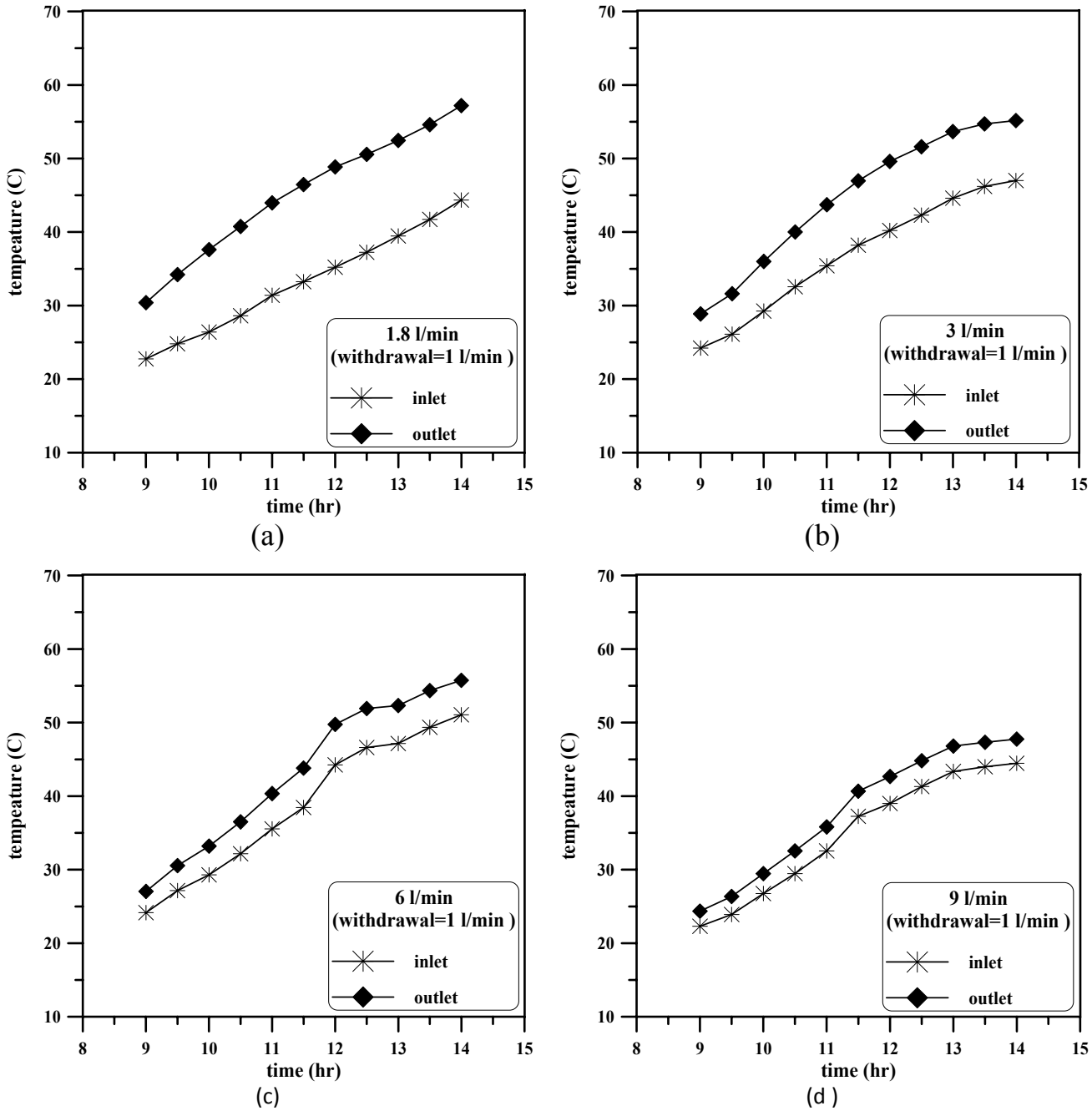

Fig.(4): Hourly Variation of Collector Inlet and Outlet Temperature for Water Withdrawal of (1 liter/min). a)1.8 l/min, b)3 l/min, c)6 l/min, d)9 l/min

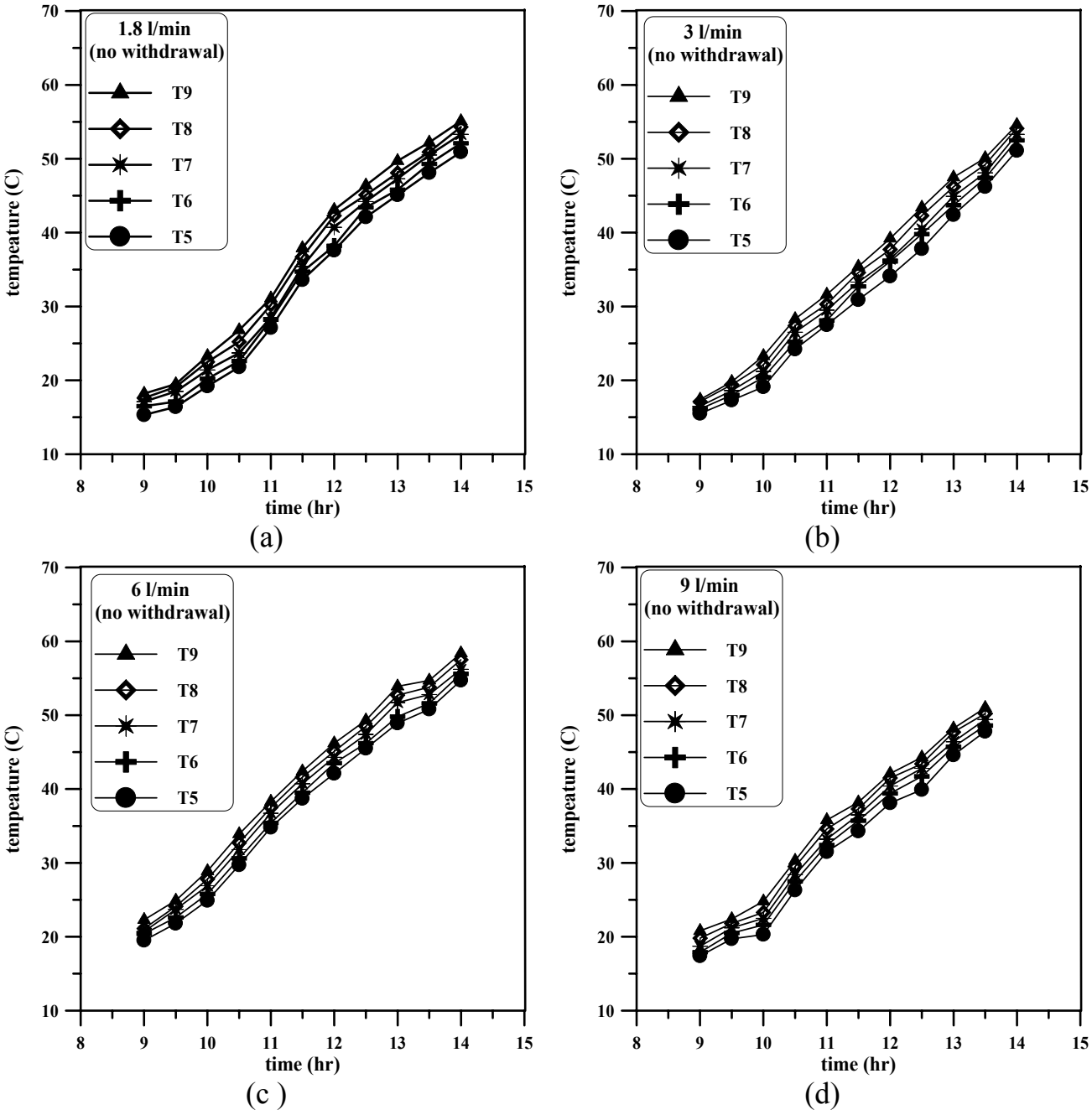

Fig.(5): Variation of Hourly Stratification in the Storage Tank with no Withdrawal.
a)1.8 l/min, b)3 l/min, c)6 l/min, d)9 l/min

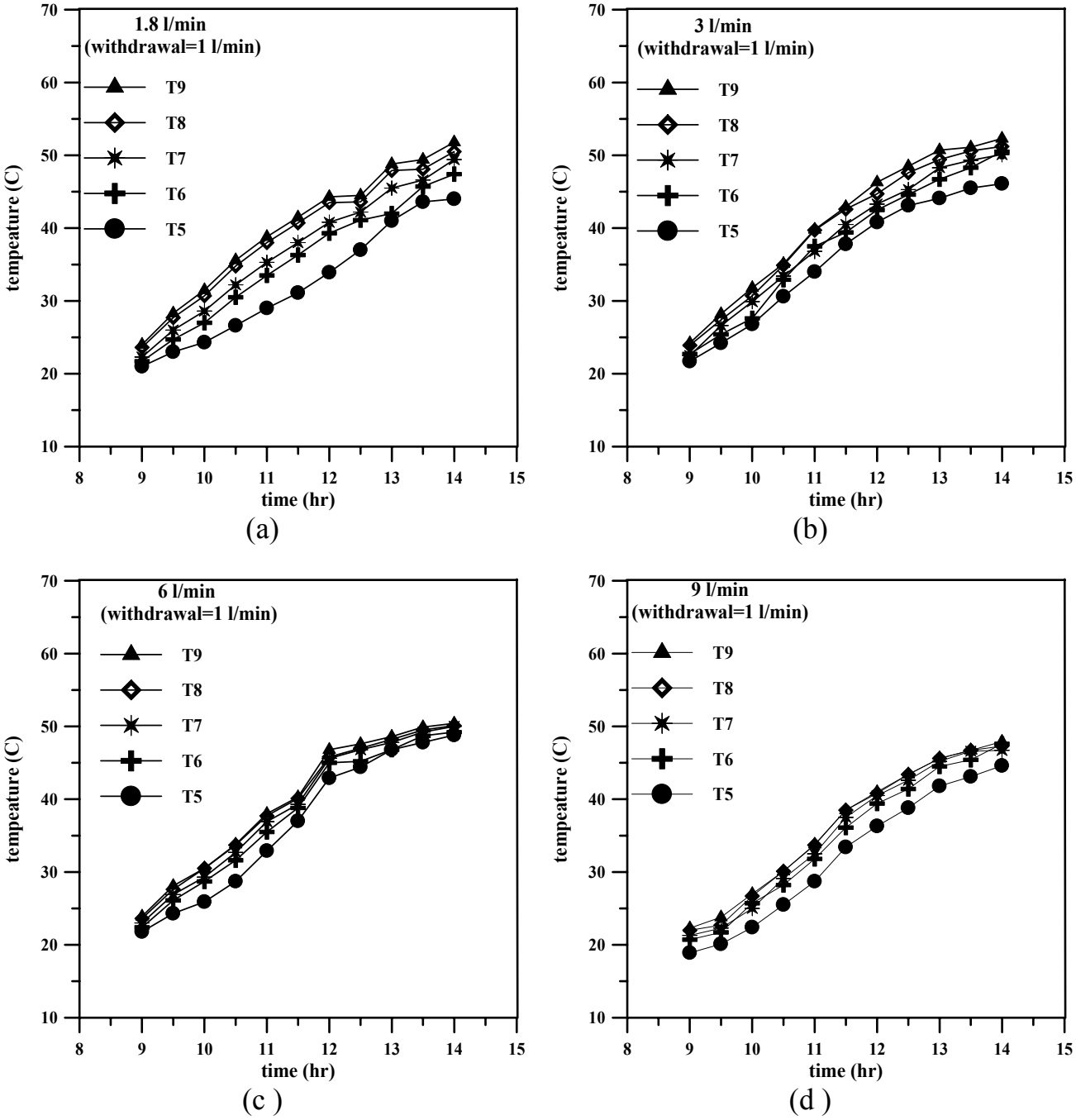

Fig.(6): Hourly Variation of Thermal Stratification in the Storage Tank for Withdrawal = 1 l/min. a)1.8 l/min, b)3 l/min, c)6 l/min, d)9 l/min

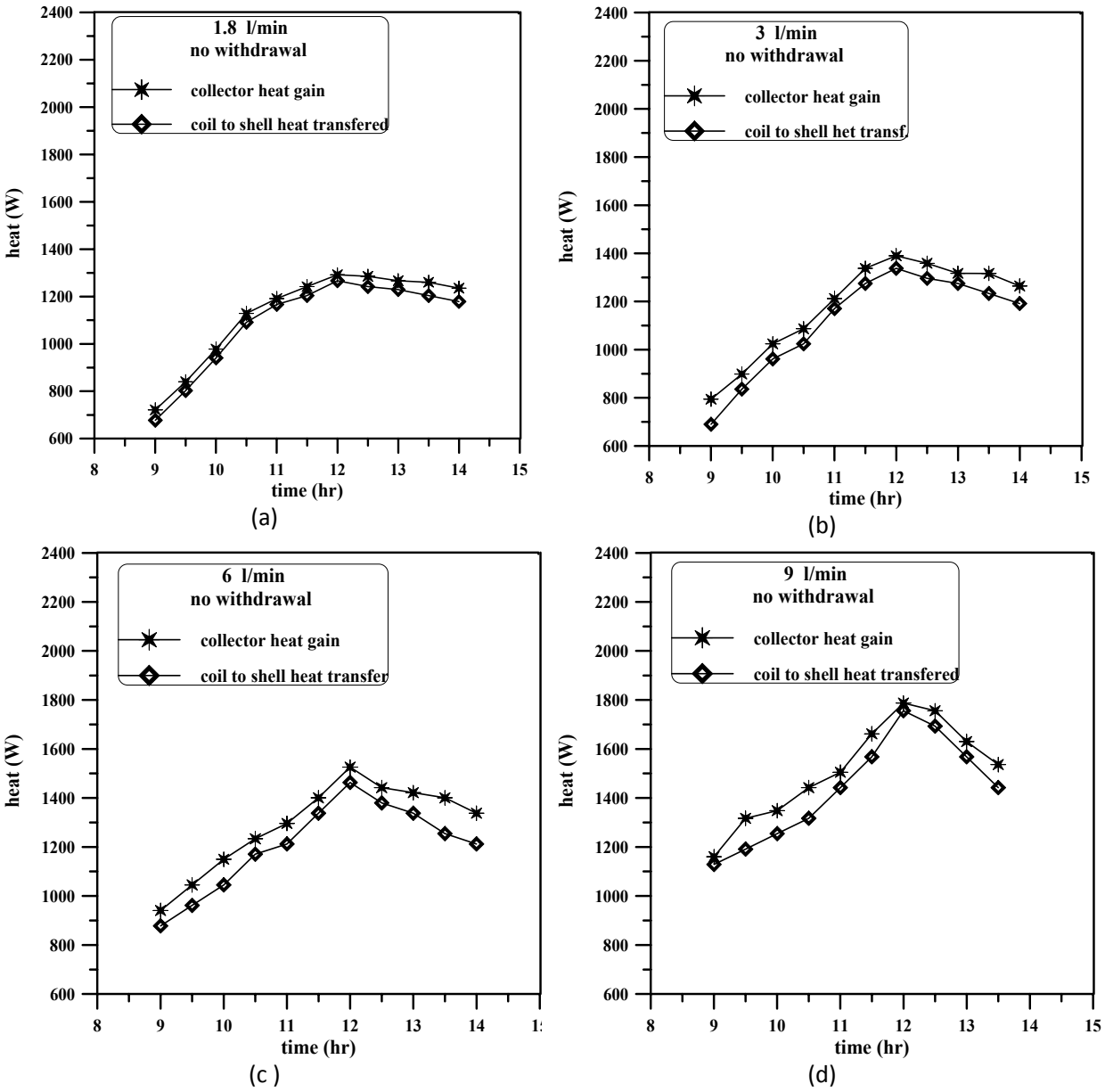

Fig.(7): Variation of Hourly Collector Heat Gain and Coil Heat Rejected for no Withdrawal. a)1.8 l/min, b)3 l/min, c)6 l/min, d)9 l/min

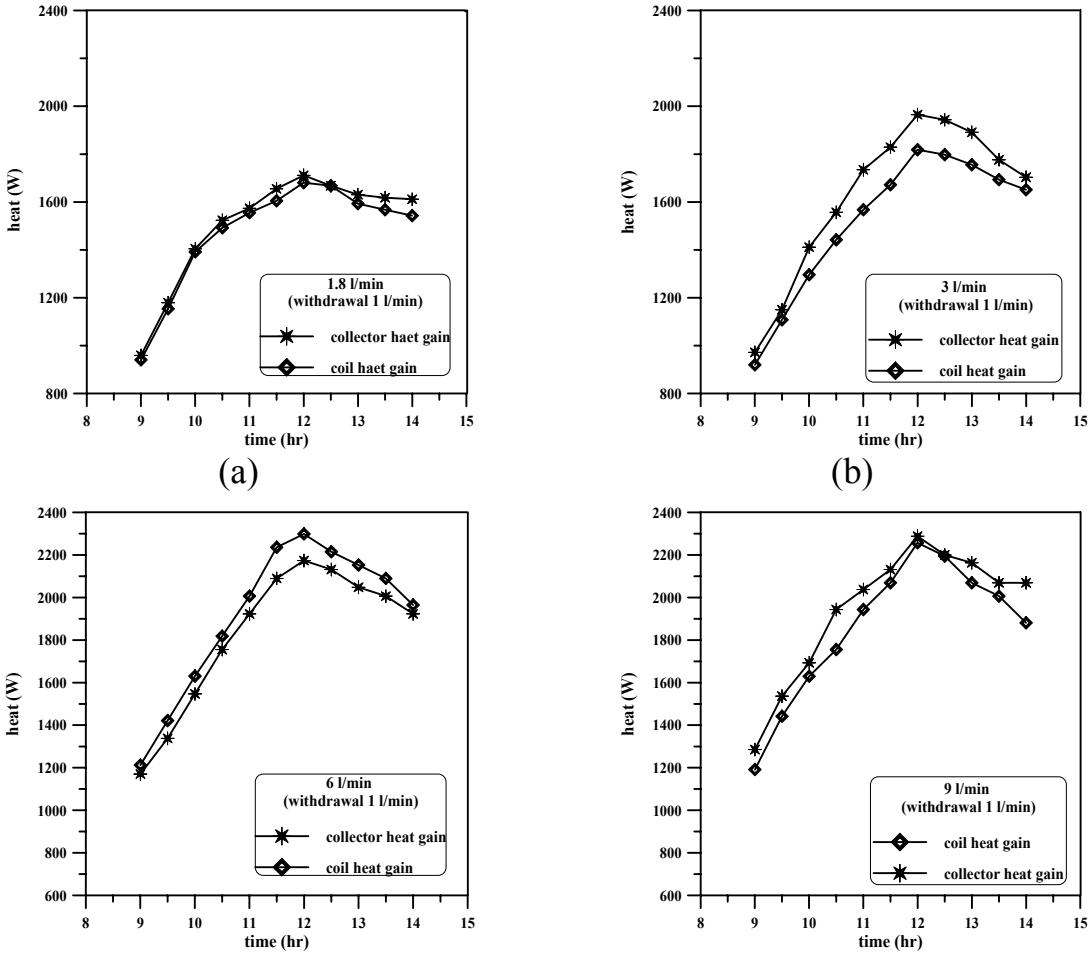

Fig.(8): Variation of Hourly Collector Heat Gain and Coil Heat Rejected for supply water Withdrawal=1 l/min. a)1.8 l/min, b)3 l/min, c)6 l/min, d)9 l/min

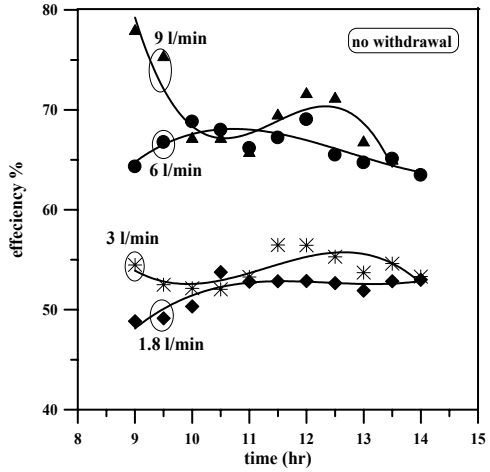

Fig.(9): Hourly Variation of Collector Efficiency for Different Circulation Flow Rates for no withdrawal

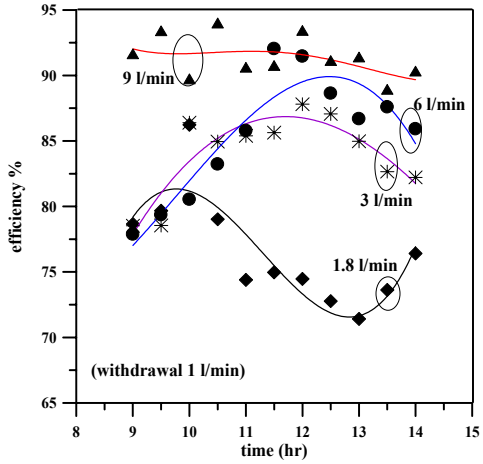

Fig.(10): Hourly Variation of Collector Efficiency for Different Circulation Flow Rates for withdrawal=1 l/min

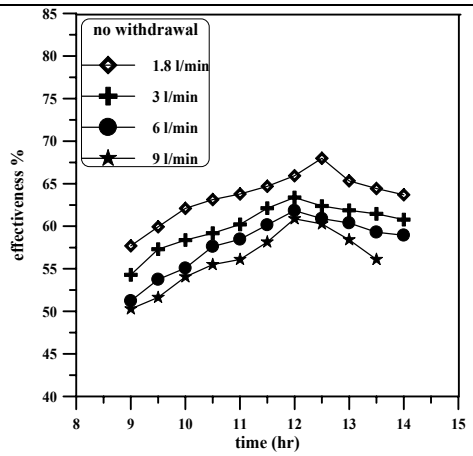

Fig.(11): Hourly Variation of Storage Tank Effectiveness for Different Circulation Flow Rates for no Withdrawal

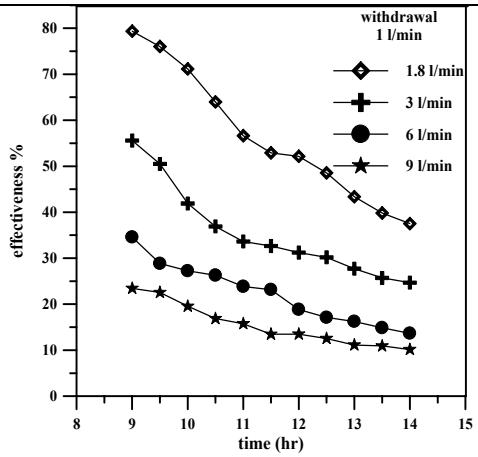

Fig.(12): Hourly Variation of Storage T Effectiveness for Different Circulation Rates for withdrawal=1 l/min

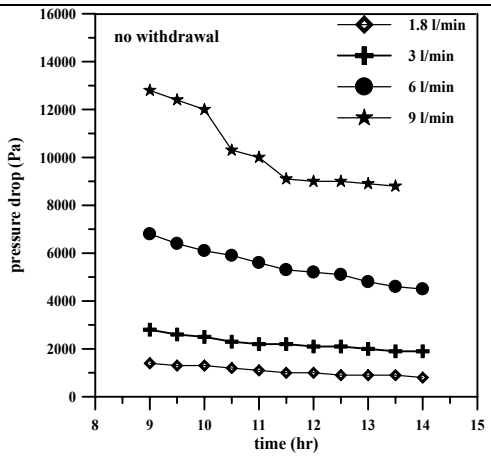

Fig.(13): Hourly Variation of Measured Pressure Drop Across Helical Coiled Tube. for no Withdrawal

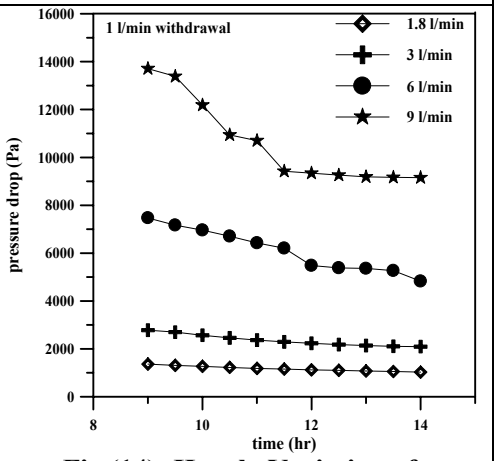

Fig.(14): Hourly Variation of Measured Pressure Drop Across Helical Coiled Tube. for Withdrawal =1 l/min

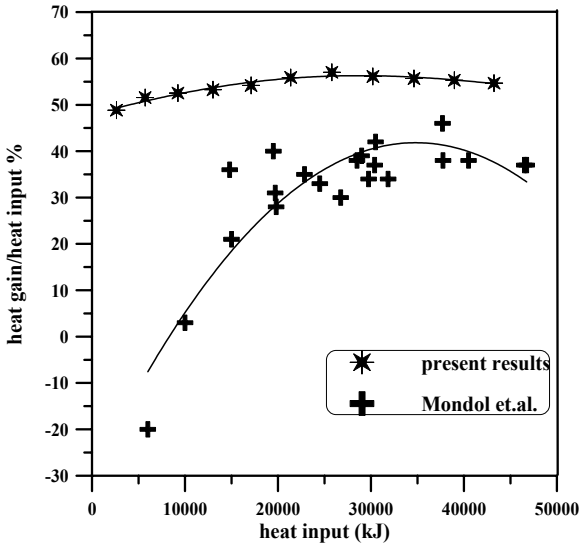

Fig. 15. Comparison of the percentage heat transfer of the present work with previously reported results.

Evaluation of Convective Heat Transfer and Natural Circulation in an Evacuated Tube Solar Collector

Asst. Prof. Dr. Saad M. Saleh Al-Mashat
Department of Mechanical Engineering
University of Baghdad
E-mail: almashatsaad@yahoo.com

Abbas Ahmed Hasan
Department of Mechanical Engineering
University of Baghdad
E-mail: abbas_ahmed_1985@yahoo.com

ABSTRACT

The evacuated tube solar collector ETC is studied intensively and extensively by experimental and theoretical works, in order to investigate its performance and enhancement of heat transfer, for Baghdad climate from April 2011 till the end of March 2012. Experimental work is carried out on a well instrumented collector consists of 16 evacuated tubes of aspect ratio 38.6 and thermally insulated tank of volume 112L. The relation between convective heat transfer and natural circulation inside the tube is estimated, collector efficiency, effect of tube tilt angles, incidence angle modifier, The solar heating system is investigated under different loads pattern (i.e closed and open flow) to evaluate the heat loss coefficient from tank and tubes, test the collector with various aspect ratios (32.9 and 27.2). The enhancement in collector performance is studied by using two reflectors (Flat Plate and Curved Plate) and nanofluid (Water-AL_2O_3).Theoretical work is run by software (Fluent 6.3), to compute the velocity and temperature profiles within the tube, for different tube diameters, effect of tube junction angle and stagnant region in the bottom of the evacuated tube. The experimental results shows that the heat loss coefficient for tube is 0.742 W/m^2.K and for tank is 1.153W/m^2.K, the maximum collector temperature is 79°C in winter and 99°C in summer, while that belong to nanofluid collector is 99°C in winter. The best tilted angle (optimum) of evacuated tube is 41° annually. The collector efficiency increased when using nanofluid of (1, 0.6, 0.3)% volume fraction as(28.4, 6.8, 0.6)% respectively. The efficiency decreases as (33, 62)% when decreasing tube aspect ratio from 38.6% to 32.9% and 27.2% respectively. An increase of (16.9 and 7.08)% in collector efficiency is obtained when using curved and flat plate reflectors respectively. From simulation the best junction angle of the tank is 22.5°. The stagnant region is influenced with changing heat flux, tilted angle and aspect ratio.

KEY WORDS: Evacuated Tube, ETC, Solar energy, Natural convection, Nanofluid.Al_2O_3.

تقييم أنتقال الحرارة بالحمل الطبيعي و معدل التدفق لمجمع شمسي ذو أنابيب مفرغة

عباس احمد حسن
قسم الهندسة الميكانيكية
جامعة بغداد

أ.م.د. سعد محسن صالح المشاط
قسم الهندسة الميكانيكي
جامعة بغداد

الخلاصة

في هذا البحث تم دراسة المجمع الشمسي ذو الأنابيب المفرغة بشكل مكثف وموسع عمليا ونظريا، الغرض منها هو دراسة الأداء الحراري للأنبوب المفرغ و تحسين انتقال الحرارة ضمن مدينة بغداد من شهر نيسان ٢٠١١ الى شهر آذار ٢٠١٢. الجانب العملي تم على مجمع شمسي يحوي ١٦ انبوب مفرغ بنسبة الطول الى القطر ٣٨,٦ وبخزان ماء معزول حراريا بحجم ١١٢ لتر، تم حساب العلاقة بين انتقال الحرارة ومعدل الجريان داخل الأنبوب، والكفاءة الحرارية، وتأثير زاوية الميلان للأنبوب، وتم حساب مصحح زاوية الأشعاع الشمسي (IAM)، وكذلك تم فحص المجمع الشمسي لعدة احمال(على سبيل المثال جريان مغلق ومفتوح)، وتم تقييم معامل الفقد الحراري للخزان و للأنبوب، و فحص المجمع الشمسي لنسب اطوال الى اقطار (٣٢,٩ و ٢٧,٢) عمليا، وجانب التحسين الحراري تم بأستخدام نوعان من العاكسات الصفيحية (عاكس صفيحي مستوى وعاكس صفيحي منحني) وكذلك تم توضيف سائل النانو (ماء+اوكسيد الألمنيوم). الجانب النظري تم بأستخدام حزمة برامج (Fluent 3.6) لايجاد توزيع السرع ودرجات الحرارة ضمن الأنبوب لحالات مختلف الأقطار، ومعرفة مدى تأثير زاوية ارتباط الأنبوب

في الخزان وتأثير المنطقة الخاملة في الأنبوب.النتائج العملية بينت ان معدل معامل الفقد الحراري للأنبوب W/m2.K ٠,٧٤٢ وللخزان W/m2.K ١,١٥٣ وان اقصى درجة حرارة للمجمع في فصل الشتاء ٧٩ درجة مئوية وخلال فصل الصيف ٩٩ درجة مئوية، بينما في حالة استخدام مائع النانو وصلت الى ٩٩ درجة مئوية خلال فصل الشتاء، افضل زاوية ميلان للأنبوب تقديريا هي ٤١° سنويا، وتزداد كفائة المجمع الشمسي بنسبة (٢٨,٤ ـ ٦,٨ ـ ٠,٦)٪ بأستخدام مائع النانو بنسبة حجمية لأوكسيد الألمنيوم في الماء(٠,٣ ـ ٠,٦ ـ ١)٪ ، وتقل كفائة الأنبوب بنسبة (٦٢ ـ ٣٣)٪ عندما تقل نسبة الطول الى الحجم من ٣٨,٦٪ الى ٣٢,٩٪ و ٢٧,٢٪ بشكل متسلسل، وكذلك زيادة في الكفائة بمقدار (١٦,٩ ـ ٧,٠٧)٪ عند استخدام عاكس صفيحي منحني وعاكس صفيحي مستوى. ومن اهم نتائج النظري هي افضل زاوية ارتباط للأنبوب مع الخزان هي زاوية ٢٢,٥°، وبيت النتائج النظرية ايضا ان المنطقة الخاملة التي تتأثر بشكل ملحوض مع تغير الأشعاع الحراري و زاوية الميلان و نسبة طول الأنبوب الى القطر.

لكلمات الرئيسية: أنبوب مفرغ. طاقة شمسية. جريان حر. مائع النانو. اوكسيد الألمنيوم.

INTRODUCTION

ETC evacuated tube solar collector is device of using and utilizing solar energy as water heating system. ETC works with pure natural convection with constant solar heat flux, ETC is important in studying the enhancement of heat transfer and occurs in various industrial solar applications like domestic water heating, space heating, cooling, and solar refrigeration. ETC had been investigated by (Qaiser Muslim Al-asadi 1993) he was investigated ETC performance theoretically by using simple numerical method, (I.Budihardjo, G.L.Morrison and M.Behnia 2003), (John H. Lienhard IV. and John H. Lienhard V. 2008), (Michel Hayek 2009) they had been investigated the ETC experimentally and evaluated ETCs performance and heat enhancement. The whom were investigated The ETC under Baghdad climate experimentally are (Hamza Jabbar Hammad 2009), (Hassan Naji Salman AL- Joboory 2009).

The current work interests with evaluation of ETC performance by evaluating convective heat transfer and natural circulation, Moreover, an improvement have done on this performance by using nanofluid (AL_2O_3+water) 10nm in diameter of particle with concentrations (0.3%, 0.6% ,1%) of volume, and implementing different kinds of reflector plates (Flat, Curved), tests the ETC at wide range of angles experimentally. Velocity and temperature profiles were founded theoretically with temperature stratification in the tank with help of Fluent 3.6 software.

EXPERIMENTAL WORK

The experimental work was conducted under Baghdad climate using ETC, it consists of 16 tubes deflected at angle β=45° from horizontal, aspect ratio of 38.6, tank 112.1L, and auxiliary heating element, see figure 1. Thermocouples were distributed in ETC, 5 thermocouples are installed at the third top tube opening three of them are acquiring the hot outgoing water from the tube and two of them are acquiring cold in coming water to the tube, 8 thermocouples were installed vertically in the tank, two thermocouples installed at inlet and outlet of water in case of open flow test (Load Test), the ambient temperature was acquired also, see figure 2. Two kinds of reflector plates were used (flat and curved) to achieve more heat input to the system. Same manner of thermocouples distribution has made on nanofluid rig, see figure 3, except the tank has only three thermocouples because it is smaller. Experimental has carried out under Baghdad condition from April 2011 until end of March 2012, the metrological data took from Ministry of science and technology by their data logger.

Figure 1: ETC assemble

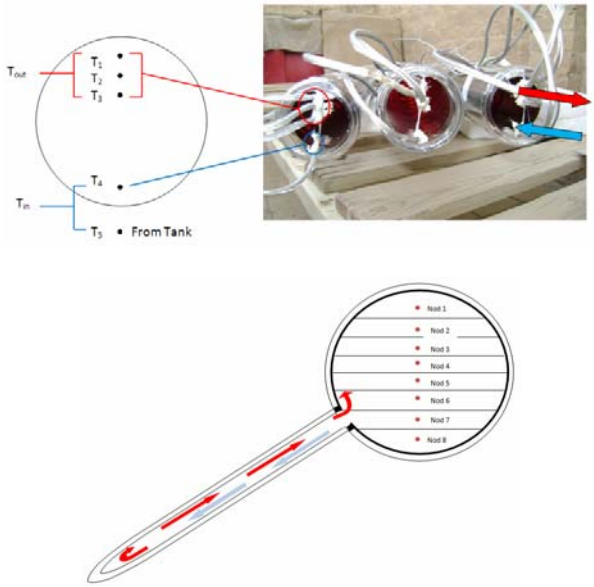

Figure 2: Thermocouples distribution.

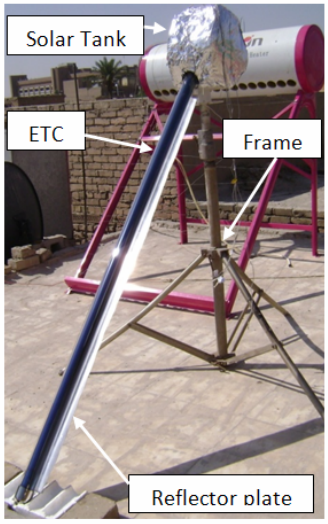

Figure 3: Nanofluid rig.

INSTRUMENTATIONS

Temperature was measured in various positions in the collector via thermocouple type K with numerical display and resolution 1˚C, the ambient temperature was measured by normal mercurial thermocouple. Solar radiation and wind speed has been measured from data logger which sat up on Ministry of Science and Technology building of acquisition rate 5 Sec. The flow rate has been measured during open test by measuring cylinder 2.5 L in volume.

PERFORMANCE EVALUATION TESTES.

The performance evaluated by collector parameters like U_{tube} evaluated by following equation [I. Budihardjo] . See figure 17.

$$U_{tube} = \frac{m_f C_f (T_i - T_f)}{\Delta t A_a (T_m - T_{atm})_{av}} \qquad (1)$$

while U_{Tank} wither tank of collector or nano rig evaluated from the following equation; in both cases cool down test is called.

$$U_{Tank} = \frac{\rho_f V_T C_f}{\Delta t} \ln\left[\frac{T_i - T_{atm(av)}}{T_f - T_{atm(av)}}\right] \quad (2)$$

Results are in table 1.

Relation between convective heat transfer and natural circulation in ETC was obtained by dimensionless numbers Ra^* (modified Rayleigh number) represents convective heat transfer and Re Reynolds represents natural circulation in ETC, this relation comes from regression the two variables evaluating the constants a and b in equation 3;

$$Re = a(R_a^*)^b \quad (3)$$

$$R_a^* = Nu\,Ra = \frac{(g\ cos\beta)\ B\, q_u\, d_a^4}{k\, v^2} Pr \quad (4)$$

$$Re = \frac{4\,\dot{m}}{\pi\, d_a\, \mu} \quad (5)$$

$$\dot{m} = \frac{Q_u}{C_f(T_{out} - T_{in})} \quad (6)$$

Test should run in plug flow test and results are listed in the table 2. See figures 18, 19 and 20.
ETC efficiency η is investigated also, the reading took during mid day (noon) because the sun will be perpendicular and heat flux maximum, the efficiency was extremely fluctuated due to dependency on temperature difference and precision, it can evaluate from the following equations.

$$\eta = \frac{Q_u}{G\, A_a} \quad (7)$$

$$Q_u = D_E + Q_{Tank} = m_{Tank}\, C_f(\bar{T}_f - T_i) + \int_{t_1}^{t_2} U_{Tank}(\bar{T}_T - T_{atm}) \quad (8)$$

$$\eta = \eta_{opt} - a_1 \frac{(\bar{T}_w - T_{atm})}{G} - a_2 \frac{(\bar{T}_w - T_{atm})^2}{G} \quad (9)$$

The results are listed in table 3 which represents the average approximated.

Incidence angle modifier (IAM) defines the ratio of the collector output at a given incidence angle $Q(\theta)$ and the collector output at normal incidence $Q(\theta = 0)$, see equation 10:

$$IAM(\theta) = \frac{Q(\theta)}{Q(\theta = 0)} \quad (10)$$

The test has carried out using six couples of ETCs each couple connected from top by manifold, three of them mounted on moved frame (sun trucker), see figure 4, and the rest of three pairs are seated on the ground and inclined at 45°, PRs were used in wither on sun tracking or tubes on the ground. All the manifolds receive constant flow rate 0.3 L/min during noon from 10:30 to 13:30. The IAM various during the day with incident angle changing and the behavior of evacuated tube as in equation 11 and fig. 23.

$$IAM(\theta) = 1 - C\left(\frac{1}{cos\,\theta} - 1\right) \quad (11)$$

Where C is constant calculated experimentally.

Figure 4: IAM test rig assemble.

The optimum tilted angle of solar collectors in general has been estimated by using equation 12, [Hamza J.] this equation is applicable on collector which does not affected by gravity or natural convection. The test of ETC at various tilted angles β, test has carried out on five couples of ETC tubes which inclined at various angles (3˚-5˚) between each couple of the other, see figure 5 ,and below and above the optimum tilted angle which has been estimate by equation 12, the test has done in certain time (mid days of the months) across the noon 11:15 till 12:45, the couples of tubes whose temperature is higher represent they are inclined at optimum angle at that month, results are showed the angles obtained by test is little pit than the optimum angle which obtained by equation 12, because we have consider the gravity effect on natural convection inside the tube. See figure 24.

$$\beta_{opt} = tan^{-1}\left[\frac{\sum_{i=1}^{12} H_b \tan(\varphi-\delta)}{\sum_{i=1}^{12} H_b}\right] \qquad (12)$$

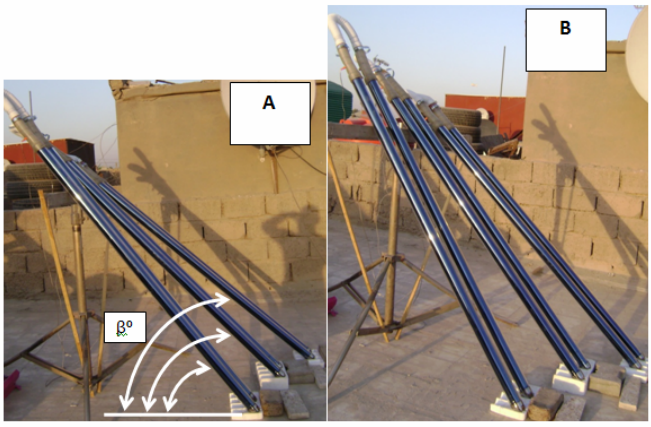

Figure 5: ETC couples of tubes at various inclinations.

ETC has been tested by open circuit flow (load test) with constant water flow rate (1.1215, 0.6, 0.48 L/min) with almost constant inlet temperature various slightly ± 1.5˚C for entire test, this test shows the ETC performance under loaded condition, and produced discharge temperature for specific application, see figures 6 and 22, equation 13 ,which is applicable to evaluate the heat gain.

$$Q_{gain} = \dot{m}\, C_f\, (T_{out} - T_{in}) \qquad (13)$$

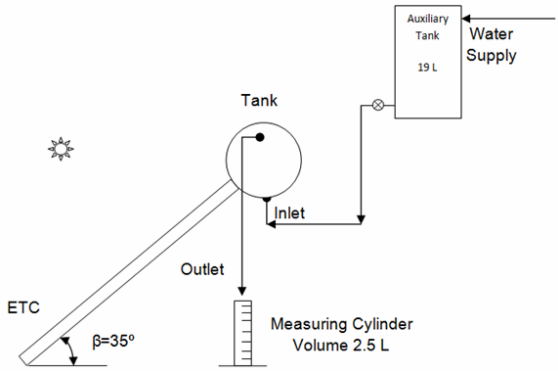

Figure 6: Loaded test of ETC.

ETC has been tested at different tube lengths in order to investigate more details on ETC aspect ratios changing, (170cm "standard length", 145cm ,125cm) by putting sand in the tube at limited length and putting a piece of corn above the sand to prevent mixing the sand with water, this have done on all tubes, see figure 7: see figures 19, 25 and 26.

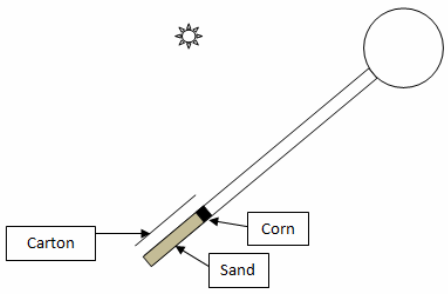

Figure 7: Test ETC at different lengths.

An enhancement on ETC has been performed by implementing nanofluid (Al_2O_3 + Water) instead of ordinary fluid Water at different concentrations of nano particles Aluminum

Oxide (alumina) Al_2O_3 99% (Gamma), (0, 0.3, 0.6, 1)% APS=10nm morphology, near spherical shape, the rig which used to ran the test as in figures 3 and 8:

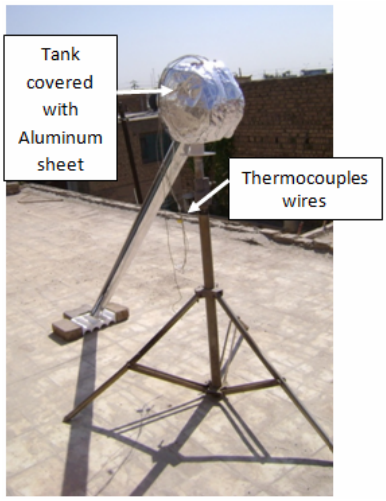

Figure 8: Nanofluid rig.

The ETC above consists one evacuated tube, tank volume is 4L, total volume including tube is 6.676L, the heat exchanges from nanofluid to fresh water which pumped by electric pump through copper coiled tube (Length = 1.9m, ID = 0.5cm, thickness = 1mm, K=365 W/k.m), see figure 9:

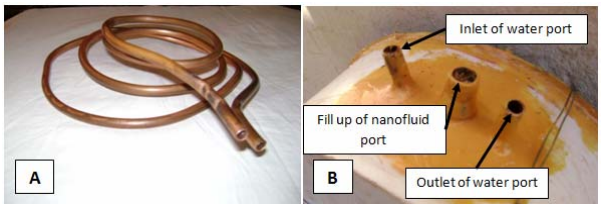

Figure 9: Copper coiled tube and tank ports.

Nanofluid has been prepared and mixed by (Ultrasonic Cleaner) for 17hrs, eventually no sediments in bottom of device's container were observed.

The tests by nanofluid are performed via using the both (plug and loaded test) for entire Al_2O_3 concentrations, see figure 10; fresh water rate is 1.2 L/min via electrical pump.

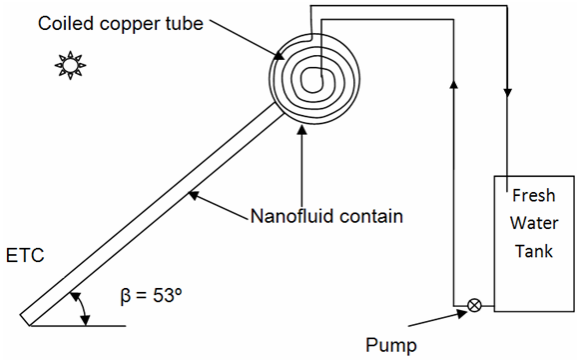

Figure 10: Nanofluid rig test sketch.

THEORETICAL WORK

Theoretical part has made to support the experimental work, especially the results that could not achieve practically. Although the results restricted with proper assumptions and error that come from simulation, theoretical work describes the ETC simulate using CFD package (FLUENT 6.3). see figure 11.

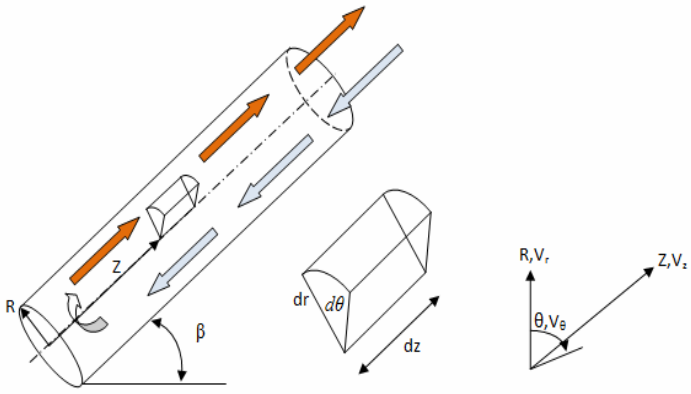

Figure 11: ETC with cylindrical coordinate.

ASSUMPTIONS

1- Perfect insulation at the bottom edge of the collector.

2- Density is comply to Boussinesq approximation.

3- the heat transferred by conduction in flow direction is neglected.

4- Neglect the temperature gradients inside the glass cover and the absorber.

5- Free convection inside the glass tube is not taken into account.

6- The absorber surface from below $\theta = \frac{\pi}{2}$ up to $\theta = \frac{3\pi}{2}$ has a constant temperature and equal tank temperature, only in case of there is no reflector.

7- Constant pressure condition at the open surface of the tube.

8- In this simulation the inflow and out flow from the tube domain are assumed to be normal to the surface in order to investigate heat distribution.

THE GOVERNING EQUATION.

$$\frac{1}{r}\frac{\partial}{\partial r}(rv_r)+\frac{1}{r}\frac{\partial}{\partial \theta}(v_\theta)+\frac{\partial v_z}{\partial z}=0$$

(14) Continuity

$$v_r\frac{\partial v_r}{\partial r}+\frac{v_\theta}{r}\frac{\partial v_r}{\partial \theta}-\frac{v_\theta^2}{r}+v_z\frac{\partial v_r}{\partial z}$$
$$=-\frac{1}{\rho}\frac{\partial P}{\partial r}+\frac{\mu}{\rho}\left\{\frac{\partial}{\partial r}\left(\frac{1}{r}\frac{\partial}{\partial r}(rv_r)\right)+\frac{1}{r^2}\frac{\partial^2 v_r}{\partial \theta^2}-\frac{2}{r^2}\frac{\partial v_\theta}{\partial \theta}+\frac{\partial^2 v_r}{\partial z^2}\right\}+g_r$$

(15) Momentum Equation r

$$v_r\frac{\partial v_\theta}{\partial r}+\frac{v_\theta}{r}\frac{\partial v_\theta}{\partial \theta}+\frac{v_r v_\theta}{r}+v_z\frac{\partial v_\theta}{\partial z}$$
$$=-\frac{1}{\rho}\frac{\partial P}{r\partial \theta}+\frac{\mu}{\rho}\left\{\frac{\partial}{\partial r}\left(\frac{1}{r}\frac{\partial}{\partial r}(rv_\theta)\right)+\frac{1}{r^2}\frac{\partial^2 v_\theta}{\partial \theta^2}+\frac{2}{r^2}\frac{\partial v_r}{\partial \theta}+\frac{\partial^2 v_\theta}{\partial z^2}\right\}$$

(16) Momentum Equation θ

$$v_r\frac{\partial v_z}{\partial r}+\frac{v_\theta}{r}\frac{\partial v_z}{\partial \theta}+v_z\frac{\partial v_z}{\partial z}$$
$$=-\frac{1}{\rho}\frac{\partial P}{\partial z}+\frac{\mu}{\rho}\left\{\frac{1}{r}\frac{\partial}{\partial r}\left(r\frac{\partial v_z}{\partial r}\right)+\frac{1}{r^2}\frac{\partial^2 v_z}{\partial \theta^2}+\frac{\partial^2 v_z}{\partial z^2}\right\}+g_z$$

(17) Momentum Equation Z

$$\frac{\partial T}{\partial t}+v_r\frac{\partial T}{\partial r}+\frac{v_\theta}{r}\frac{\partial T}{\partial \theta}+v_z\frac{\partial T}{\partial z}=\left(\frac{\kappa}{\rho c_p}\right)\left\{\frac{1}{r}\frac{\partial}{\partial r}\left(r\frac{\partial T}{\partial r}\right)+\frac{1}{r^2}\frac{\partial^2 T}{\partial \theta^2}\right.$$

(18) Energy Equation

The ETC modeling is ran on one tube and tank volume 121/16 L, a simplification has made (Symmetry condition) on both tank and ETC. see figure 12.

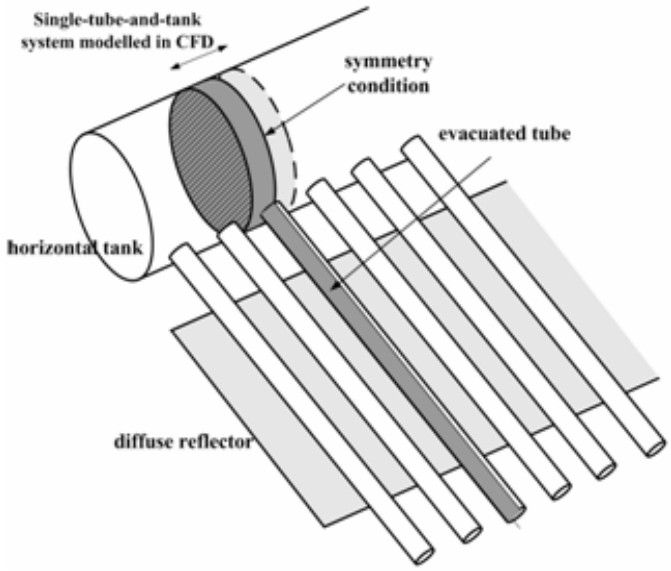

Figure 12: ETC modeling (Symmetry condition)

The modeling has carried out separately on ETC and tank, the condition in junction point between the tank and the tube is the same, the other boundary condition were taken from previous studies see figure 13.

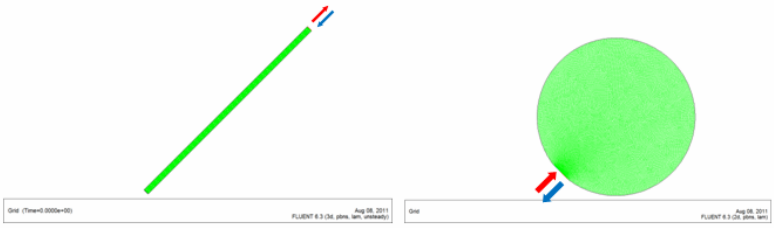

A constant heat flux and constant wall temperature boundary conditions were studied, moreover 2D and 3D were also studied, regarding the natural convection a Boussinesq

approximation which states that the density is constant in all governing equations terms except in gravity affect terms, the rest of parameters are taken from experimental work like ($G, U_{Tube}, U_{Tank}, T_{atm}, \ldots\ldots etc$).

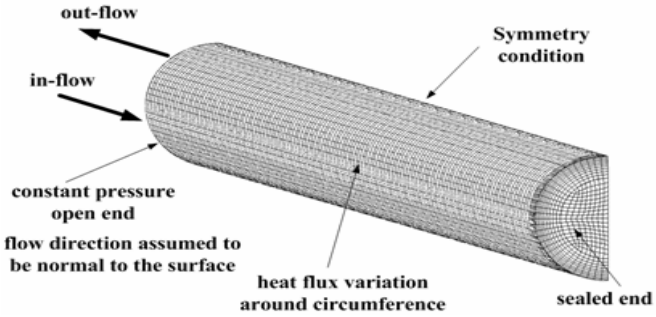

Figure 13: ETC modeling and boundary conditions.

Heat loss from ETC to the environment by various mode of heat transfer, see figure 14:

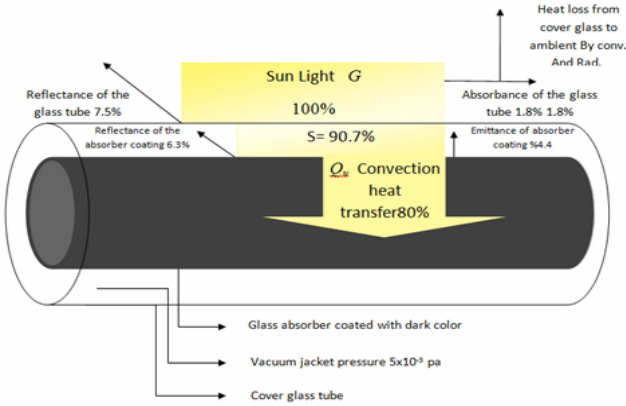

Figure 14: Schematic of heat transfer in ETC.(Hamza 2009).

During normal situation solar array incidences on ETC, most of it will utilize and transfer to the fluid, and the rest will be lost to ambient.

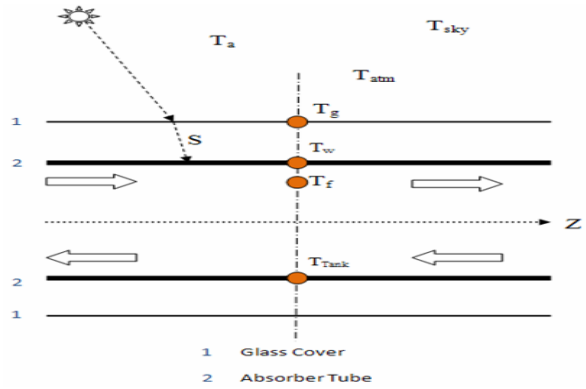

Figure 15: ETC temperatures section.

Figures 15 and16 indicates the ETC thermal net work and its equivalent, the outer glass receive the solar radiation then most of solar radiation passes through the outer glass (Transparent surface) and little reflects as a losses, the other heat loss by radiation and convection, the inner glass (Absorber) absorbs most of the fallen radiation which come from outer glass and transfer it to the liquid inside, as well as it exchanges the rest of heat as a loss with outer glass, the lower surface of absorber has a tank temperature been assumed.

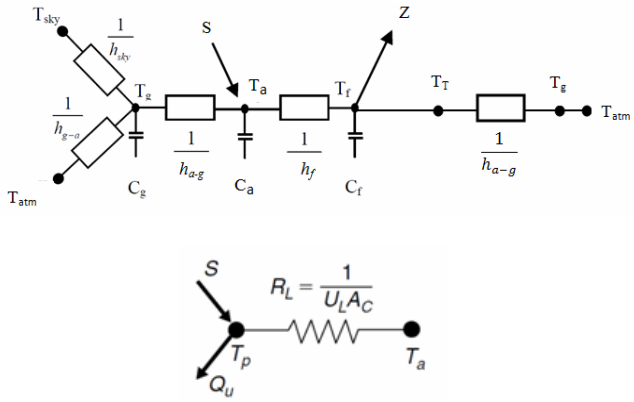

Figure 16: Thermal network of ETC.

EXPERIMENTAL RESULTS

Results were obtained experimentally are in following tables and graphs:

Heat loss coefficient is evaluated to different tanks, its value is influenced with type of thermal insulation, range of temperature difference and tank volume. See table 1 and figure 17:

Table 1: ETC's heat loss coefficients.

Heat loss coefficient	W/k
U_{tube}	0.1745/tube
U_{Tank}	1.523
$U_{nf-Tank}$	0.4205
$U_{Aux-Tank}$	1.1770

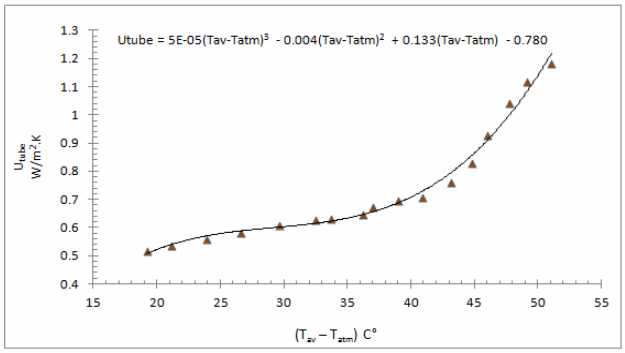

Figure 17: U_{tube} vs. temperature difference.

The relation between convective heat transfer and natural circulation has been estimated by merging a dimensionless numbers Ra* and Re, by regression the data to evaluate the constants a and b. The results showed that the relation become more proportional with using reflector plates, as well as with increasing the aspect ratio, and as long as the concentration of nanofluid is increased. See table 2 and figures 18, 19, 20:

Table 2: Relation between Ra^* vs. Re.

Case	a	b
ETC without RP	0.129	0.338
ETC with FRP	2E-5	0.759
ETC with CRP	2E-5	0.877
ETC aspect ratio =38.6	2E-5	0.850
ETC aspect ratio =32.9	2E-5	0.775
ETC aspect ratio = 27.2	2E-4	0.497
ETC with Al_2O_2 x=0%	2.1E-5	0.770
ETC with Al_2O_2 x=0.3%	2.1E-5	0.790
ETC with Al_2O_2 x=0.6%	2.1E-5	0.801
ETC with Al_2O_2 x=1%	2.15E-5	0.820

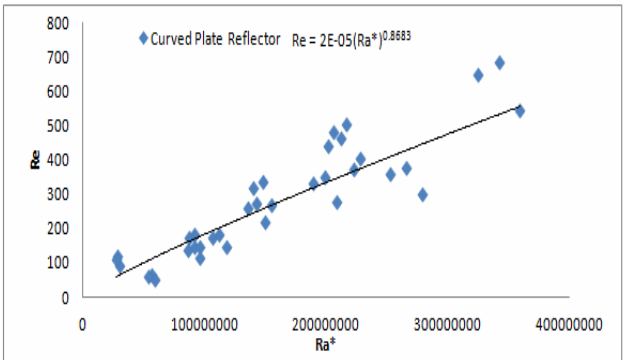

Figure 18: Re vs. Ra with curved reflector plate, β=45°.

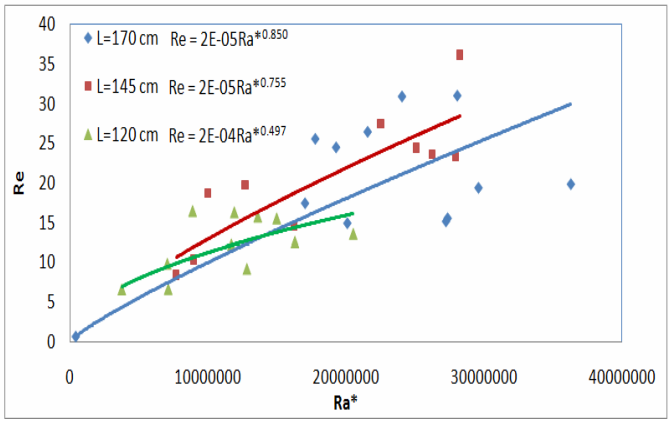

Figure 19: Re vs. Ra at different ETC lengths.

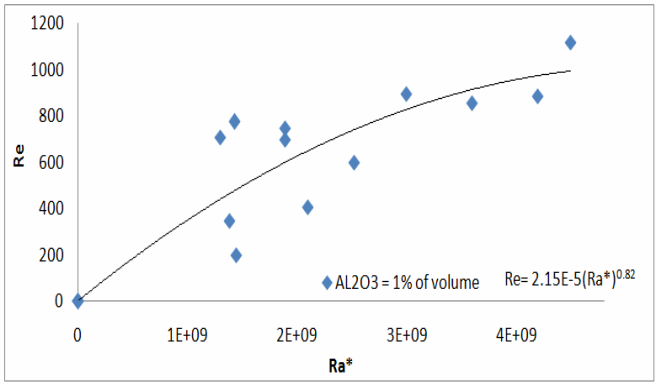

Figure 20: Re vs. Ra at X=1% Al_2O_3.

The efficiency of ETC is investigated with carious reflector plated with data extremely fluctuated, the results indicated the collector works without reflector is more efficient than with reflector due to the increment in amount of heat input and rising in average collector temperature therefore the amount of heat loss will increase. See table 3:

Table 3: ETC's efficiency.

Condition	η_{opt}	a_1	a_2
Without RP	0.725	0.85	0.0067
With FRP	0.676	0.82	0.0063
With CRP	0.642	0.76	0.0061

The experimental is indicated the ETC is producing non-uniform flow rate across the collector. See figure 21, depending on solar exposure and effect of heat loss such that the tubes at the edges are receiving more solar radiation once the sun in the horizon than the others, and the temperature of edge tubes (1 and 2) is relatively colder than the other (7 and 8) due to more heat loss, it is near by the tank surface.

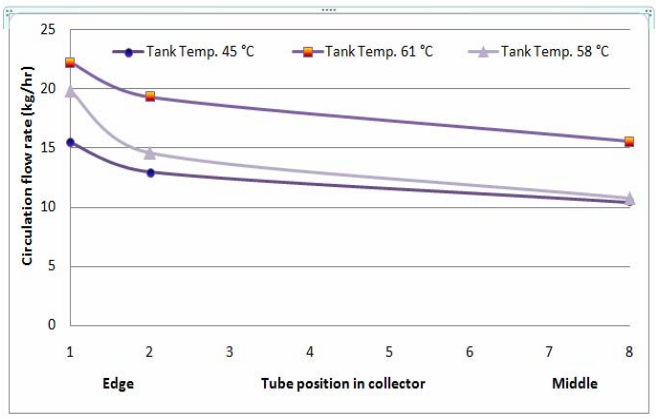

Figure 21: Circulation rate vs. Tube position.

Figure 22 shows the energy gain from collector discharge temperature during open flow test at different loads. Test showed the load with less mass flow rate produce higher discharge temperature due to maintaining the internal energy in the collector.

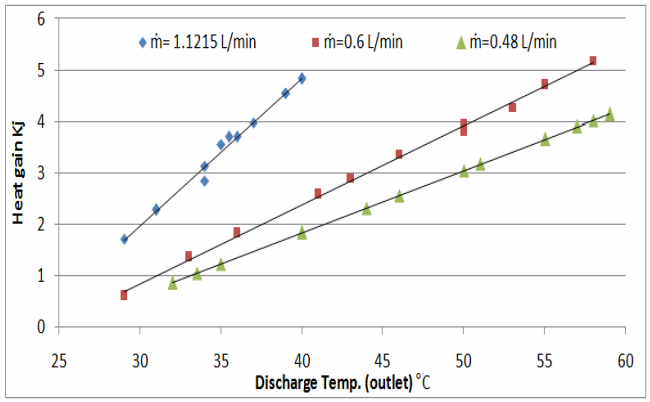

Figure 22: Energy gain vs. Discharge water Temp.

Incidence angle modifier (IAM) is evaluate at various reflector plates, figure 23 shows the effect of reflectors on (IAM) and the amount of constant C in equation 11 at various condition by regression the data.

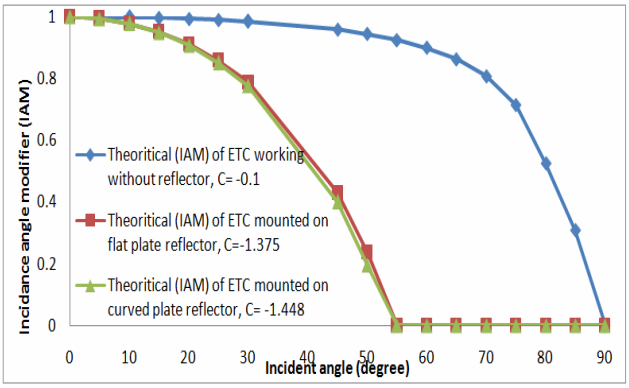

Figure 23: Theoretical (IAM) of ETC at different reflectors, β = 45˚.

The optimum tilted angle is approximately estimated for each individual month of Baghdad solar radiation. See figure 24, the results are showed the optimum tilted angle is bigger than the normal angle difference 5˚ to 12˚ and the average annual tilted angle is 41˚ and during the winter season is 53˚.

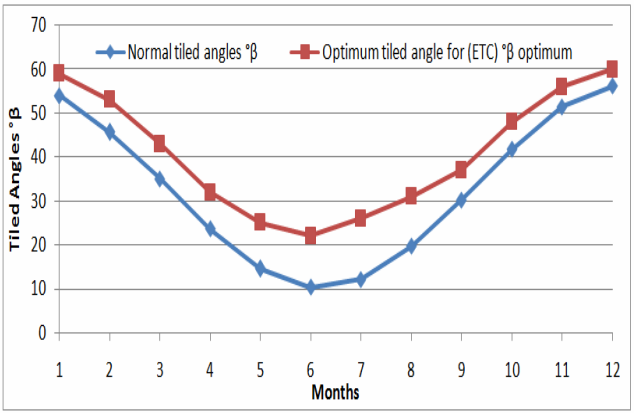

Figure 24: Normal tilted angle and Optimum tilted angle for ETC across year for Baghdad climate.

The results which gained from tests on ETC at different aspect ratios indicated the heat loss from bigger aspect ratio more than the others due to wider heat loss surface area, and circulation rate with bigger aspect ratio is more than the others due to the quantity of incidence solar radiation on the tube. See figures 25 and 26.

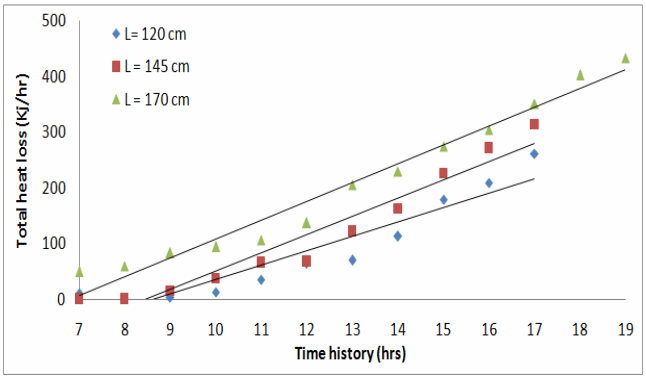

Figure 25: Heat loss from ETC at different lengths vs. time history.

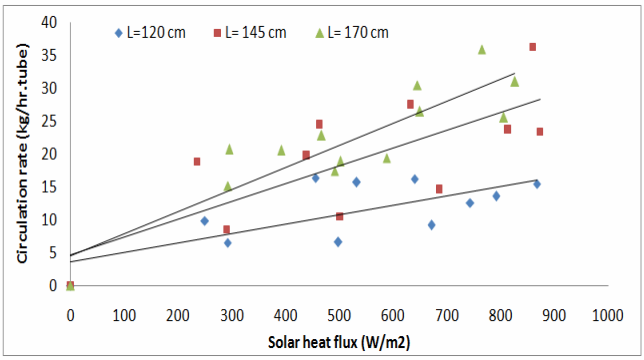

Figure 26: Circulation rate vs. solar radiation of ETC at different lengths.

THEORETICAL RESULTS

The main results were obtained by program (FLUENT 6.3) on ETC as following: figures 27, 28 and 29 are to evaluate heat loss coefficient of tube and tank respectively. Figures 28 and 29 are showing the temperature gradient elimination to two cases (With and without circulation pump).

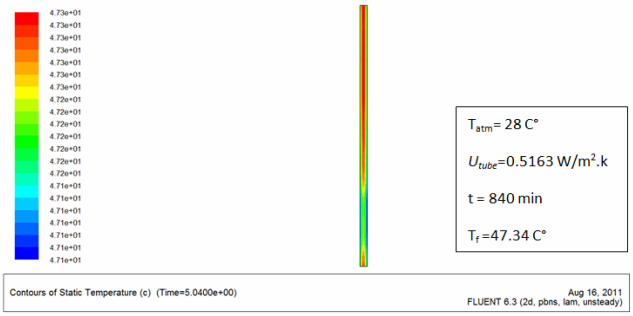

Figure 27: Evaluation the U_{tube} of ETC.

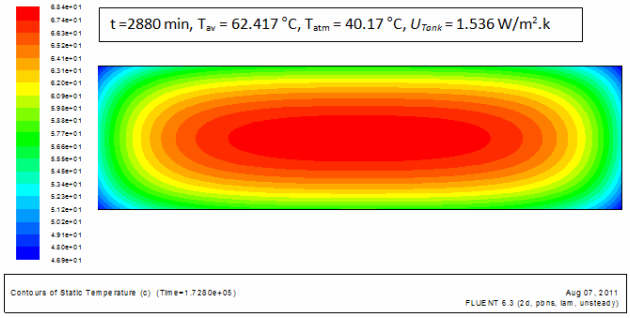

Figure 28: Evaluation the U_{Tank} of ETC First Method

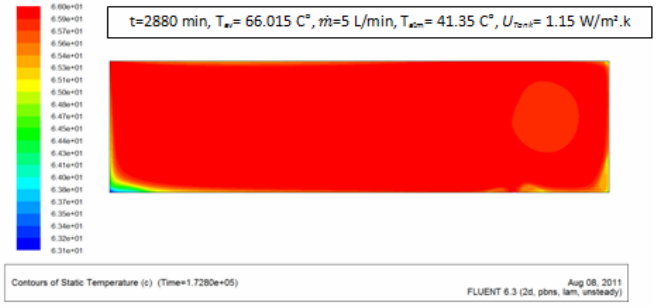

Figure 29: Evaluation the U_{Tank} of ETC (Second Method).

Figure 30 shows the best tube tank junction angle velocity contours, which is 22.5° from –y axis. This angle gives good temperature stratification in the tank for the current design theoretically.

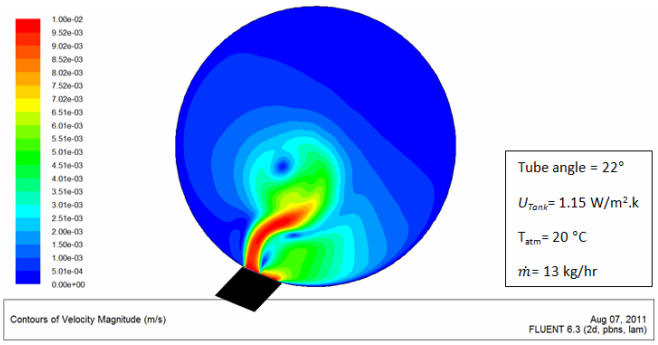

Figure 30: Tube junction angle effect on tank velocity profile.

Figure 31 showing the velocity contours of stagnant region, this region is influenced with ETC configuration, angle of inclination from the horizon and amount of solar radiation.

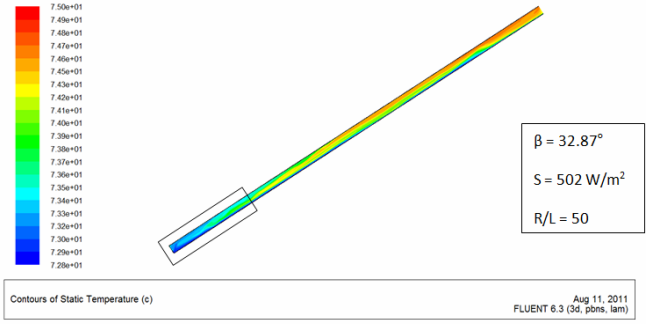

Figure 31: ETC stagnation region.

Figure 32 shows axial velocity profile at top of tube (junction with tank) with different inlet water temperature. The reason of increasing in velocity peck with increasing in temperature is come from more heat radiation fallen on the tube affecting on fluid particles disturbance, logically the amount of heat input is proportional with flow rate and fluid temperature.

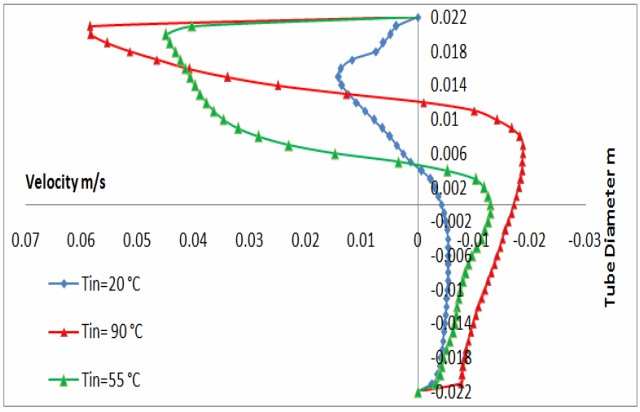

Figure 32: Velocity profiles of ETC at different back flow temperatures, β = 45°.

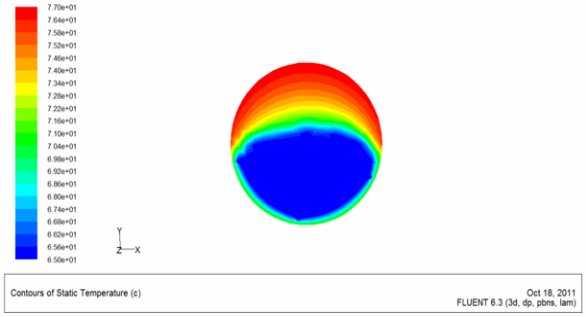

Figure 33: Temperature contour of ETC subjected to heat flux 502 W/m^{2}on top wall, β = 45°.

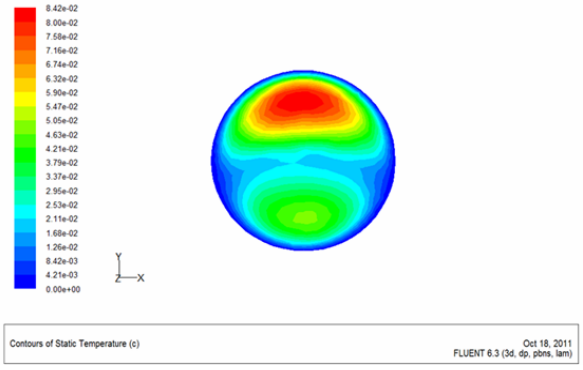

Figure 34: Velocity contour of ETC subjected to heat flux 502 W/m^{2}on top wall, β = 45°.

Figures 33 and 34 are temperature and velocity contours respectively for cross section aria of ETC at the opened end of the tube (junction with tank).

The average tank temperature of the tank affect on circulation rate if we consider same solar radiation on every case, the warmer average tank temperature produce more flow rate because the viscosity of fluid effects down with temperature increasing, therefore the fluid with higher temperature facing less prevention (less shear) with wall. See figure 35.

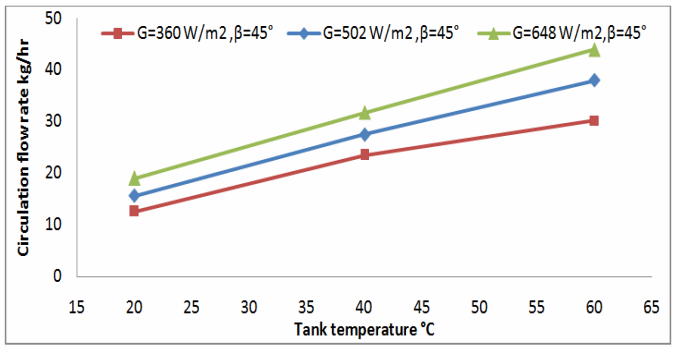

Figure 35: T_{tank} vs. Circulation rate.(Theoretical).

The simulation of ETC at various diameters is showing in figure 36, the effect of increasing in diameter will increase the heat transfer coefficient, it means there is more heat transfer in the tube.

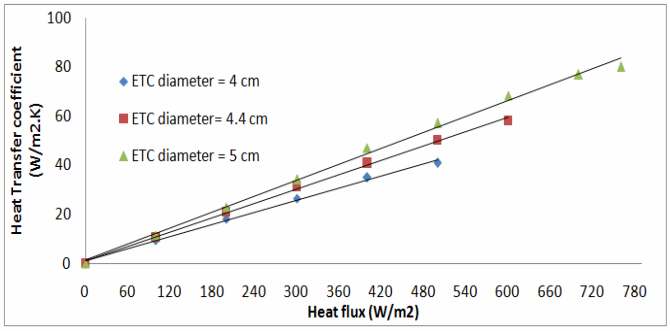

Figure 36: Heat flux vs. heat transfer coefficient of ETC at different diameters.

The effect of nanofluid concentration on circulation flow rate in two constant heat flux subjected on the upper half of ETC wall, figure 37 shows the simulation results, the increasing in

AL_2O_3 particle concentration in whole fluid at certain heat flux increase the circulation rate will take place due to the entire fluid properties enhancement.

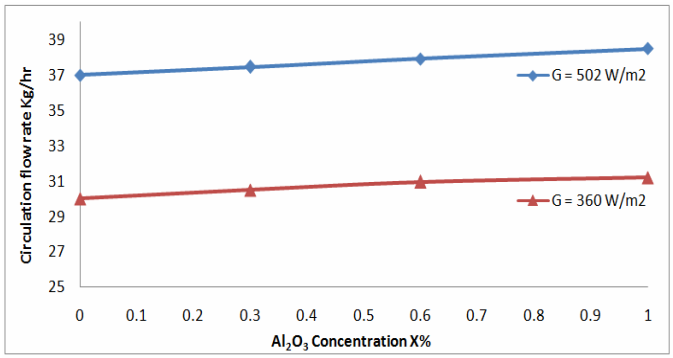

Figure 37: Circulation rate of ETC at different nanoparticle concentration and heat fluxes.

CONCLUSIONS

- The best method to evaluate U_{Tank} is the second method with 24%, because the eliminating of temperature gradient.
- The tilted angles of ETC for Baghdad climate have been investigated and showed the best tilted angles of ETC is relatively more than normal, annual angle is 41˚, during winter is 53˚, during summer is 28˚.
- The efficiency will increase 7.08% with using flat plate reflector, and 16.9% with using curved plate reflector.
- The volume concentration of Al_2O_3 is proportional to ETC performance, efficiency will enhance 28.4% with 1% of Al2O3, and 6.8% with 0.6% of Al2O3, for 0.3% of Al2O3 doesn't make sensible enhancement.
- An evaluation of heat and mass circulation rate (R_e and R_a^*) by non dimensional correlations for different conditions.
- (IAM) for different reflectors and shown that the ETC without reflector gives wide range of (IAMs).
- The effect of aspect ratio 27.2 the Re number will decrease to 62%, and aspect ratio 32.9 the Re number will decrease 33% from standard case which is 38.6 aspect ratio.
- The experimental work showed the tubes across collector provide different rates, the third tube in collector represents the equivalent tube across the 16 tube collector.

NOMENCLATURE

A	Area (m^2)
B	Coefficient of Volume Expansion (K^{-1})
C	Specific heat (j/Kg)
CPR	Curved Plate Reflector
d	Diameter (m)
ETC	Evacuated Tube Collector
FPR	Flat Plate Reflector
G	Solar energy (W/m^2)
S	Solar radiation on absorber (W/m^2)
g	Gravitational acceleration
IAM	Incidence Angle Modifier
K	Liquid thermal conductivity (W/m.K)
m	Mass of liquid (Kg)
$\dot{m}$	Circulation rate (Kg/Sec)

Nu	Nusselt number
PR	Plate Reflector
Pr	Prandtl Number
Q	Heat (W)
q	Specific heat (W/m^2)
Re	Reynolds number
Ra	Rayleigh Number
Ra^*	Modified Rayleigh Number
T	Temperature (˚C)
U	Heat loss coefficient ($W/ m^2.K$)
V	Volume (m^3)
L/R	length/radius (aspect ratio)

GREEK LETTERS

β	Tilted angle of ETC
Δt	Time interval (Sec)
ρ	Liquid density (Kg/m^3)
π	Constant = 3.14
ν	Kinematic viscosity (m^2/Sec)
μ	Dynamic viscosity (Kg.Sec/m)
η	Efficiency
θ	Incidence angle

SUPERSCRIPT

a	Absorber tube
atm	Atmosphere
av	Average
f	Final value
i	Initial value
in	Inlet
m	Mean value
out	Outlet
opt	Optimum
T	ETC tank
u	Useful energy
w	Wall
nf	Nanofluid

REFERENCES

AL-JobooryH. N. S., Experimental Investigation of Evacuated Tube Heat Pipe Solar Water Heating System, Ph.d. Thesis, University of Baghdad, Mechanical Engineering Department2009.

Al-asadi Q. M., Heat Transfer Numerical Analysis Of a Thermosyphon Solar Heating System, M.Sc. thesis, University of Basra, Chemical Department,1993.

Budihardjo I., Morrison G.L., Performance of Water-in-Glass Evacuated Tube Solar Water Heaters,Solar Energy, Vol. 83, Issue 1, pp. 49-56, 2009.

Duffi J. A., Beckman W., Solar Engineering of Thermal Processes, University Of Wisconsin-Madison, Solar Energy Laboratory.

Eiyad A.N.,Ziyad M., Hakan F. O., Antonio C.,Effect of Nanofluid Properties on Natural Convection enclosure,International Journal of Heat and Mass Transfer, Vol 49, pp. 479-491, 2009.

Eiyad A.N., Hakan F. O., Effect of Inclination Angle on Natural Convection in Enclosure Filled with Cu-water Nanofluid, International Journal of Heat and Fluid Flow, International Journal of Heat and Fluid Flow, Vol. 30, Issue 4, pp. 669-678, 2009.

G.L. Morrison, I.Budihardjo, M.Behnia, WATER-IN-GLASS EVACUATED TUBE SOLAR WATER HEATERS, Solar Energy, Vol. 76, No. 1, pp. 135-140, 2004.

Hamza J. H.,Thermal Performance of Evacuated Tube Solar Heating System, University of Baghdad, Mechanical Engineering Department, 2009.

I. Budihardjo, G.L. Morrison, M. Behnia, Development of TRNSYS Models for Predicting the Performance of Water-in-Glass Evacuated Tube Solar Water Heaters, University of New South Wales in Australia, School of Mechanical and Manufacturing Engineering, available at www.academicsearch.com , 2003.

I. Budihardjo, G. L. Morrison, M. Behnia, Performance of a Water-in-Glass Evacuated Tube Solar Water Heater,Solar Energy, Vol. 83, pp. 49-56, 2009.

I.Budihardjo, G. L. Morrison, M.Behnia Measurement and Simulation of Flowrate in a Water -In-Glass Evacuated Tube Solar Water Heater, Mina S., Amir H. M., Farhad T., Numerical Simulation of Steady Natural Convection Heat Transfer in a 3-Dimensional Single-EndedTube Subjected to a Nanofluid, Int. Comm.in Heat and Mass Transfer, Vol. 37,pp. 1535–1545,2010.

John H. L.IV, John H. L. V.,A Heat Transfer Text Book, Third edition. University Of Houston, Department of Mechanical Engineer, Department of Mechanical Engineer Massachusetts Institute of Technology, 2008.

Michel H., Investigation of Evacuated-Tube Solar CollectorsPerformanceUsing Computational Fluid Dynamics, IEEE Xplore, pp. 240-244, 2009.
Solar Energy , vol. 78, no. 2, pp. 257-267, 2005.

S. Yan, W. Yu, R. Tian, S. LI “Flow Structure in a Water-in-Glass Evacuated Tube Solar Water Heater, National Natural Science Foundation, pp. 4018-4021,IEEE, 2010.

The Effect of Tool Path Strategy on Mechanical Properties of Brass (65-35) in Single Point Incremental Sheet Metal Forming (SPIF)

Dr. Qasim Mohammed Doos Al-Attaby
kasim_daws@yahoo.com

Dr.Tahseen Fadhel Abaas
tfalani@yahoo.com

Aqeel Sabree Bedan
akeelsabree@yahoo.com

ABSTRACT:
In this paper, three tool paths strategies; iso-planar, helical and adaptive have been implemented to investigates their effect on the mechanical properties of Brass 65-35 formed by single point incremental sheet metal forming process. To response this task, a fully digital integrated system from CAD modeling to finished part (CAD/CAM) for SPIF process has been developed in this paper.
The photo-micrographs shows an identical grain formation due to the plastic deformation of the incremental forming process, change in the grain shape and size was observed. It's found that the adaptive tool path play a significant role to increase the hardness of the formed specimen from (48 to 90 HV) and the grain texture of the formed specimen found as round shape, while the hardness is increased in little amount from (48 to 74 HV) in the specimen formed using helical and it's grain texture was found as needle shape.

Keywords: Single Point Incremental Forming (SPIF), Tool path Strategy, Microstructure, Hardness test.

تأثير مسار العدة على الخواص الميكانيكية في التشكيل النقطي التزايدي لسبيكة البراص65-35

ا.د.قاسم محمد دوس ا.م.د.تحسين فاضل عباس عقيل صبري بدن

الخلاصة :
تم في هذا البحث اعتماد ثلاثة طرق لمسار العدة في دراسة تاثيرها على الخواص الميكانيكية لسبيكة البراص (65-35) عند تشكيلها بطريقة التشكيل النقطي التزايدي وباستخدام نظام تصميم وتصنيع متكامل تم تطويره لانجاز هذا البحث، تبين من خلال الفحص المجهري للعينات المنجزة بان البنية المجهرية قد تغيرت من ناحية الشكل والحجم نتيجة التشكيل اللدن من جراء التشكيل واستنتج بان مسارات العدة لها اثر كبير في تغير الخواص من ناحية الصلادة والبنية المجهرية حيث تبين بان مسار العدة المحسن (Adaptive) رفع من صلادة النماذج المشكلة (48-90) وحافظ على الشكل الدائري للبنية المجهرية للبراص في حين ان مساري العدة (Isoplaner and Helical) قد رفعا الصلادة بمقدار اقل من الاول(48-74) بينما تغيرت البنية المجهرية للنماذج المشكلة حيث تم الحصول على بنية مجهرية طولية الشكل.

الكلمات الرئيسية:-التشكيل النقطي التزايدي، ستراجية مسار العدة، الفحص المجهري، فحص الصلادة.

INTRODUCTION:

In most manufacturing industries, prototype manufacturing is an important step in the development or improvement of a product before proceeding to the manufacture of production. It allows a preliminary evaluation of the product during the design stage, and a reduction in the product development time (Rattanachan K.2009).

Incremental sheet forming technology (ISF) using CNC machine aims to reduce the investment costs and lead-time of tooling development in sheet metal forming. This technology has been investigated to become a pre-eminence process for low (or medium) production batches and rapid prototype manufacturing.

The ISF technology is a forming approach in which uses the numerically controlled (NC) technology to produce a part from the sheet materials. With this technology, the new product can be made in short time from CAD modeling to finished part (Chezhian B.S.2012).

Single Point Incremental Sheet Metal Forming (SPIF) distinguishes itself by the use of simple tools mounted on CNC machines with the aim of permanently deforming the sheet metal In order to form the sheet metal into the desired shape, a suited tool, mounted on the machine end, is moved accordingly to a predefined path (Jeswiet J.2007).

The main advantages of SPIF are best formability of sheets - reducing costs when prototypes or batches have to be manufactured while the drawbacks manufacture's times longer - sometimes poor geometry's respect and surface aspect Different steps of this process are shown in Fig. (1).

DEVELOPED SYSTEM

The developed system can recognize automatically the profile of CAD model of SPIF product. Then, it generates tool path based on machining data flow from CAD model to CNC code. For simplicity, a conical shape with varied degree forming angle along its profile as in figure(2) was formed during all the experiments of investigations, as maintained previously, three tool paths are employed to formed three specimens.

An integration of the tool path definition created by Matlab has also been developed then the data have been transferred to the CNC to control the tool.

The system is connected to CNC interface through Ethernet. All modules were integrated fully on Matlab software. The basic elements of ISF system are illustrated in Fig.(3).

TOOL PATH STRATEGIES:

The path followed by the tool is generated by CAM software, starting from the CAD model of the object. The tool deforms the sheet starting from the centre and moving towards the boundary, both outer-to-inner and inner-to-outer paths can be used.

The exact CAD model of final product is built in Matlab using Lagrange technique (Tahseen F,2011), this model is used as an input object to generate tool path. In commercial CAD/CAM system, there are two approaches for generating a tool-path that can be utilized for SIPF process, known as Iso-planar tool path and helical tool path.

In Iso-planar tool path the tool deform the sheet metals from the center and moving towards the boundary then it progress to the final depth of forming in circular movement with out changing the feed direction, The characterization of this tool path is only a continuous feed rate in X- and Y- direction of a deformed sheet plane, the feed rate in the Z-direction is done in the same angular position in the XY plane along a line down the side of the sheet (Syed A. R.2009). as illustrated in Fig.(4).

In helical tool path strategy, the tool progressively deforms the blank with a spiral movement from the top going towards the maximum depth (Hu Zhu 2011), the helical tool path gives a continuous feed in all three directions X, Y and Z depth (Fig. 5).

In this work, three tool path strategies Iso-planar , Helical and adaptive tool path was proposed and tested to investigates the effect of these tool paths on the mechanical properties of Brass 65-

35 in SPIF. In the adaptive tool path the tool is progressively moved downwards up to the bottom of the object progress in circular movement and the feed direction was changed for each successive layer, an example of tool path generated is shown to fig. (6).

EXPERIMENTAL WORK:

The experiments were carried out (State Company for Inspection and Engineering Rehabilitation activities (S.I.E.R)) using the Brass 65-35 sheet (Iso- Cu Zn 35 426/1), whose chemical composition is given in table (1).

A series of tensile tests were performed (University of Technology /Production Eng.) in order to determine the mechanical properties of blank material, the standard dimension of tensile test specimen cut of using CNC-milling machine and tool diameter 8mm (fig.7), mechanical properties given in table(2).

The primary microstructure of the yellow Brass65-35 (C26800) blank has a structure consisting of a single phase that labeled (α)(Mills Kathleen2004).Phases occupying such a position on an equilibrium diagram are solid solutions, as shown in Fig (8). Such solutions are invariably tough and ductile and this particular one is no exception, being the basis of one of the most malleable and ductile metallurgical materials in common use. Brasses containing between 10% and 35% zinc are widely used for deep drawing and general presswork.

A blank having the size of (225 mm × 225mm × 1mm) was tightly held at the periphery by a blank holder. A tool with the hemi-spherical end of 12 mm diameter shaped the part at the room temperature. The forming tool traveled along three different tool paths to formed three specimens. Fig.(3) illustrates the experimental set-up employed in this paper.

RESULTS AND DISCUSSION:

The results of hardness tests shown in Figure(9). The adaptive tool path(M2) specimen has the highest hardness specimen in group (92 HV) and its texture found round Fig (11). The hardness of iso-planer tool path(M1) specimen was increased to (76 HV) and it's texture found as a needle shape Fig.(10) , while the helical tool path(M3) specimen has the lowest increasing in hardness in the group (74 HV) and it's shape found as a needle shape also Fig.(12)

In adaptive tool path strategy grain-refinement occurred during the plastic deformation according to reflect the direction of the tool among the tool path in each successive deformed layer; on other hand a large amount of residual stresses within the structure due to tension and compression effect, so the hardness of the final product increased (48-92HV).

While in helical and iso planer tool path strategy the plastic deformation was occurred in one direction (isotropic) so the grains structure elongated in the direction of the tool path and this effect causing increasing the hardness of the final product (48-76HV).

CONCLUSIONS:

In this work, Brass 65-35 sheet was incremental formed under different-Tool path strategies and their effects studies, the following conclusions were drawn from the study:

1. The tool path strategy was found to effect on both hardness and microstructure of the specimen formed by SPIF.
2. The adaptive tool path was seen to be the most effective tool path over the variation in the tool path to increase the hardness of the formed specimen along it's profile depending on the slope angle
3. The microstructure of the formed specimen using adaptive tool path are found as a round shape and this according to the variation of the tool path in the direction of the feed , while the microstructure found as a needle shape in the formed specimen formed by both isoplanar , the same observation was prevalent by using helical tool path.

REFERENCES:

Chezhian Babu S., "Effect of Process Variables during Incremental Forming of Deep Drawing Steel Sheets", European Journal of Scientific Research, ISSN 1450-216X Vol.80 No.1, pp.50-56, 2012.

Hu Zhu, "Spiral tool-path generation with constant scallop height for sheet metal CNC incremental forming", Int J Adv Manuf Technol 54:911–919, 2011.

Tahseen F. Abbas, Aqeel S. Baden, "Statistical and Visual Analysis of Error In Interpolating Sculptured Surfaces", Eng.&Tech.Journal,Vol.29,No.12 ,2011.

Mills Kathleen and others, "ASM Metals handbook metallographic and microstructures" ,volume 9, 2004.

Rattanachan K., " Formability in Single Point Incremental Forming of Dome Geometry", AIJSTPME 2(4): 57-63, 2009.

Syed Asad Raza Gardezi, "Tool path Generation in SPIF, Single Point Incremental Forming Process",2009.

Silvaa M.B., Skjoedtb M. "Single point incremental forming of tailored blanks produced by friction stir welding" journal of materials processing technology 2 0 9 , 811–820, 2 0 0 9.

Jeswiet J., "Asymmetric Single Point Incremental Forming of Sheet Metal", Queen's University, Kingston, ON, Canada, 2007.

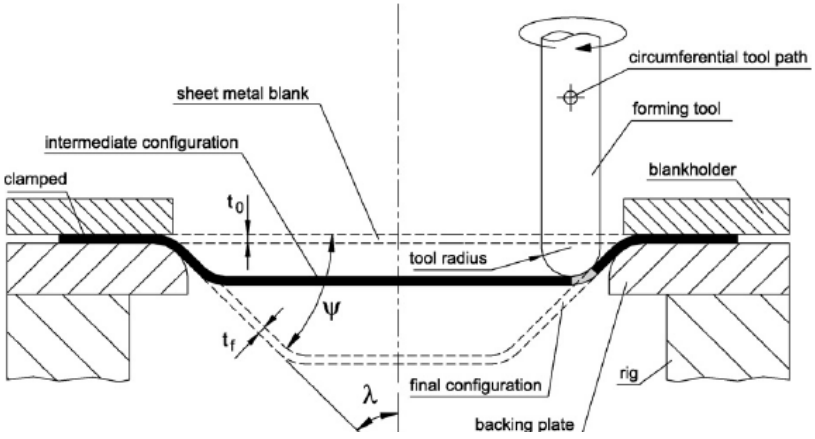

Figure (1) Single point incremental sheet metal forming process (Silvaa M.B.2009).

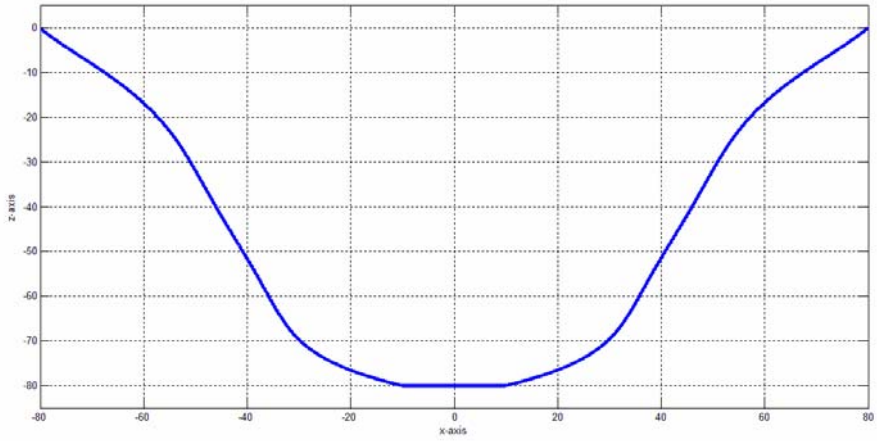

Figure (2) a conical shape profile

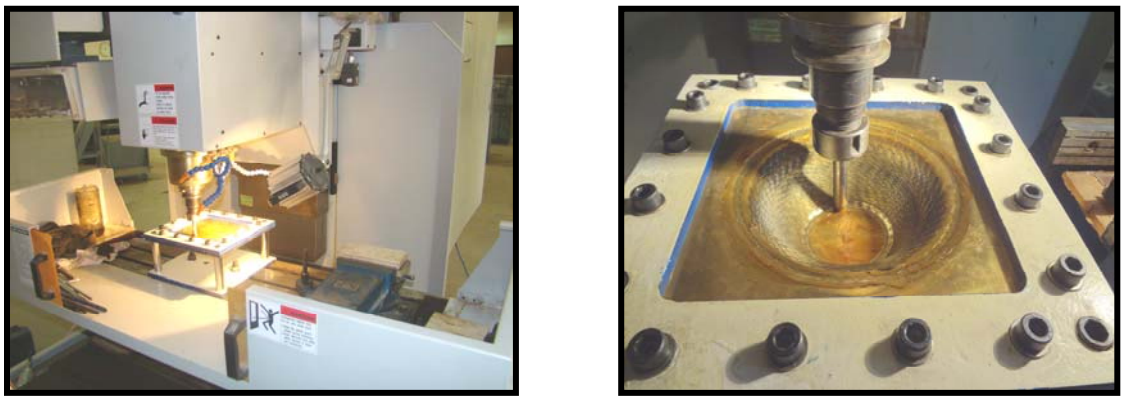

Figure (3) the experimental set-up

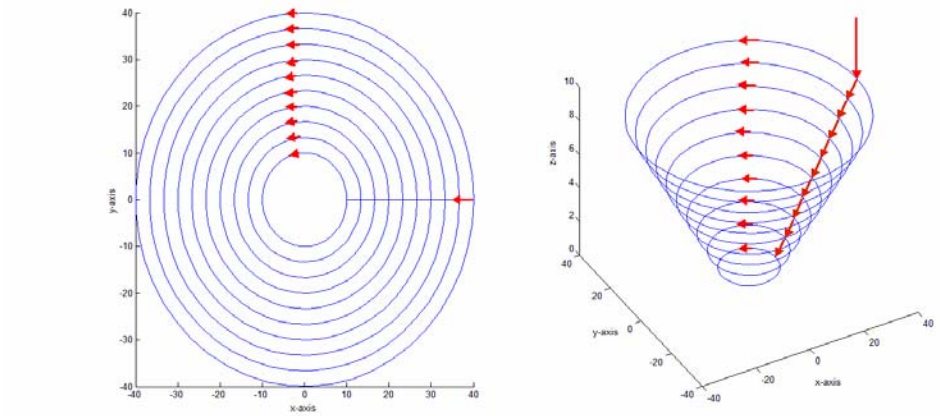

Figure (4) Isoplaner tool path.

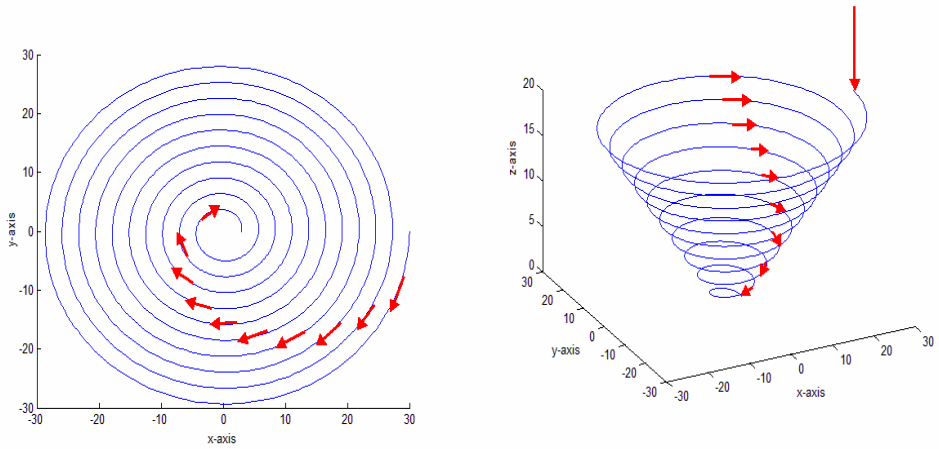

Figure (5)Helical tool path.

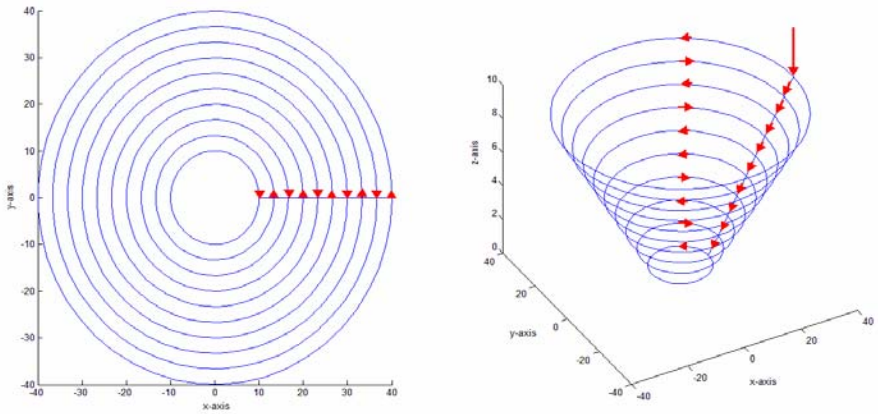

Figure (6) Adaptive tool path.

Table (1) Brass (65-35) chemical composition

Material		Zn%	Pb%	Sn%	P%	Mn%	Fe%	Ni%	Si%	Al%	Cu%
Brass	Exp.	35.23	0.007	0.001	0.007	0.000	0.021	0.001	0.001	0.002	64.7
	Iso	35.0	0.0	0.0	0.0	0.0	0.0	0.0	0.0	0.0	65.0

Table (2) Brass (65-35) mechanical properties of blank material

Material		Tensile Strength MPa	Modulus of Elasticity GPa	Poissons Ratio	Elongation % on 50 mm G.L.	Vickers Hardness HV	Iso
65/35 Brass 'O'	Exp.	248	110	0.33	56	≤ 92	Cu Zn 35 426/1
	Iso	260	110	0.375	50	≤ 100	

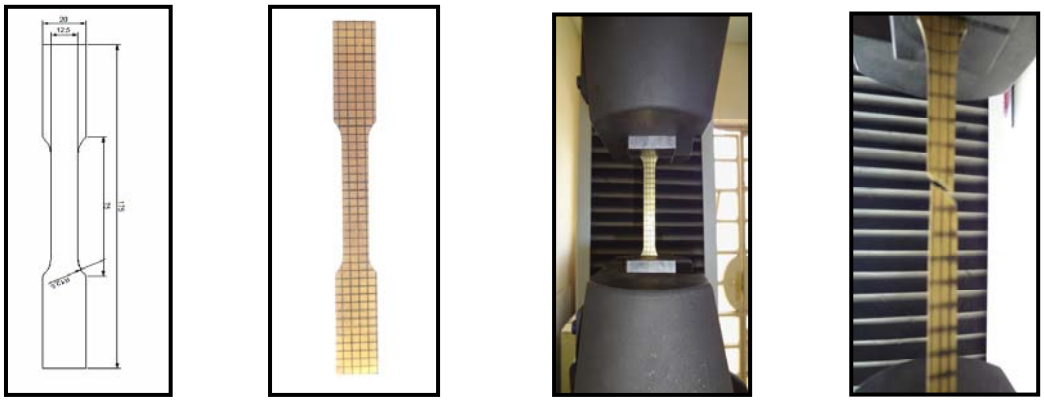

Figure (7) Tensile test of Brass (65-35) specimen.

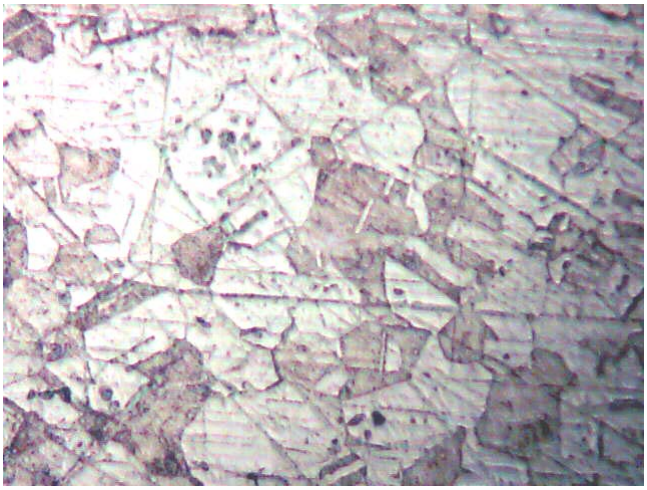

Figure (8) Primary Microstructure of the Brass 65-35 blank (x500).

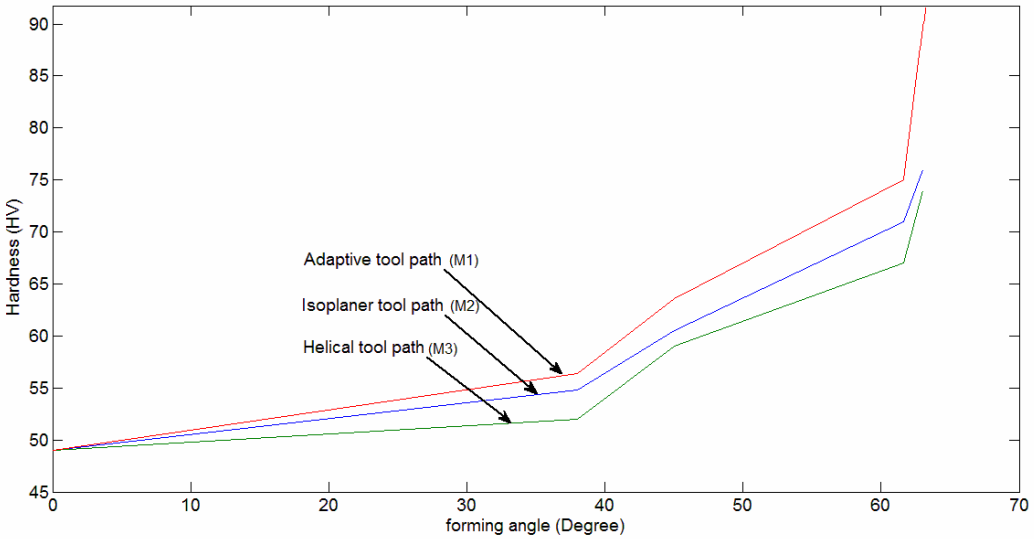

Fig. (9) Illustrates relation between hardness and forming angle of the three toolpath.

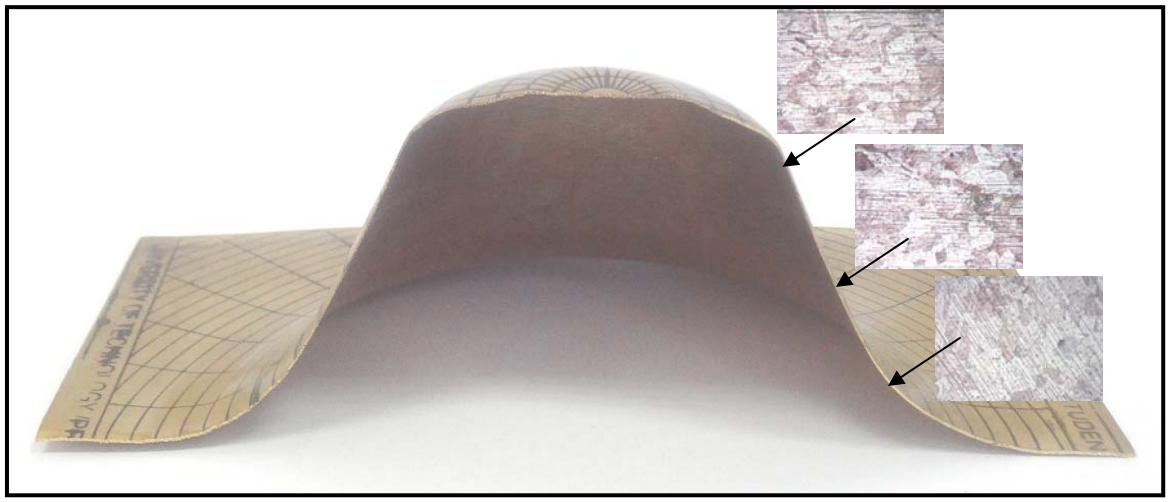

Fig. (10) Microstructure of brass in Isoplaner tool path (M1)

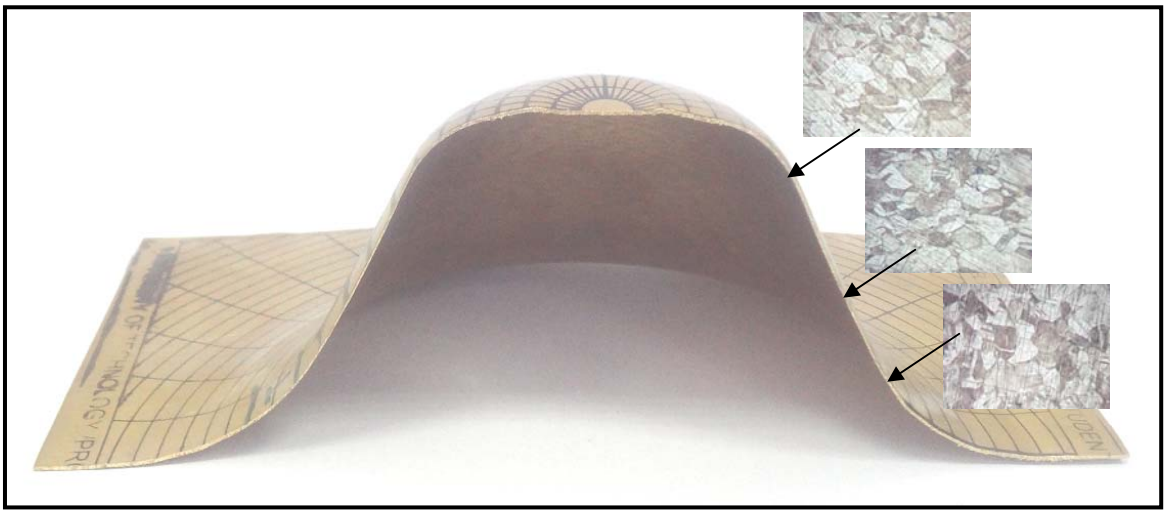

Fig. (11) Microstructure of brass in Adaptive tool path(M2)

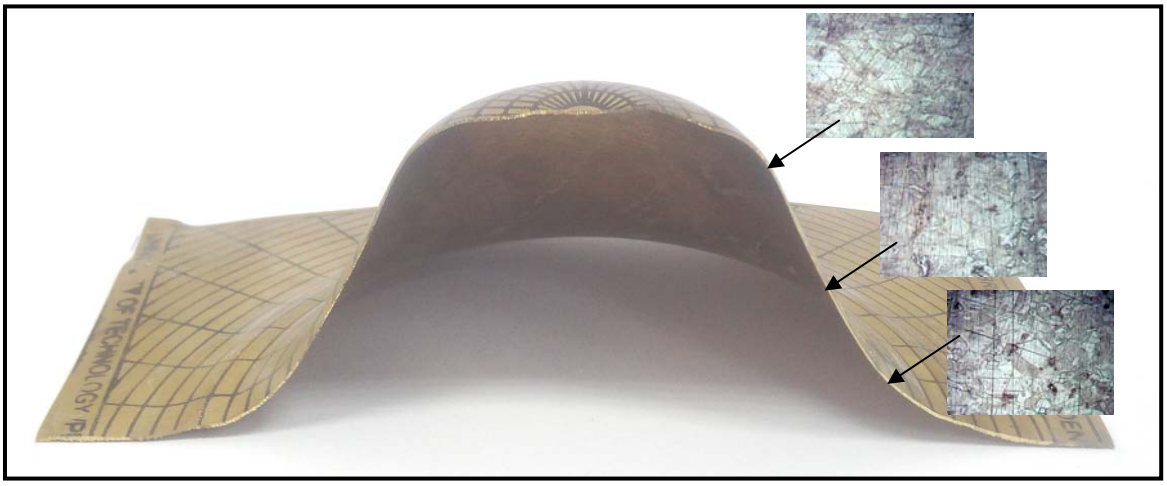

Fig. (12) Microstructure of brass in Helical tool path(M3)

Thermo-hydrodynamic Analysis of Misaligned Journal Bearing Considering Surface Roughness and Non-Newtonian Effects

Asst. Prof. Basim Ajeel Abass **Asst. Lec. Mustafa Mohammed Kadhim**
E-mail: *drbajab62@yahoo.com* *engmustafa_mo@yahoo.com*
Faculty member, *Mech. Eng. Department*, *University of Babylon*, *Babylon-Iraq*

ABSTRACT

This paper presents a numerical simulation for the combined effect of surface roughness and non-Newtonian behavior of the lubricant on the performance of misaligned journal bearing. The modified Reynolds equation to include the effect of non-Newtonian lubricant and bearing surface roughness has been formulated. The model accounts for the lubricant viscosity dependence on temperature and shear rate. In order to make a complete thermo-hydrodynamic analysis (THD) of rough surface misaligned journal bearing lubricated with non-Newtonian lubricant, the modified Reynolds equation coupled with the energy, heat conduction equations, the equation related the viscosity and temperature with appropriate boundary conditions have been solved simultaneously. The performance characteristics of the bearing were presented with different roughness parameter for the pressure, temperature, load carrying capacity, misalignment moment and friction force. The computer program prepared to solve the governing equations of the problem has been verified by comparing the results obtained through this work with that published by different workers. It has been found that the results are in a good agreement .The results obtained in the present work showed that the surface roughness characteristics of opposing surfaces and its orientation play an important role in affecting the performance parameters of the bearing. It has been shown that the load in rough aligned journal bearing is higher than that in rough misaligned journal bearing for all surface roughness patterns (γ). An increase in load has been calculated and found to be 29.5% for the bearing with moving roughness while it becomes 32% for the bearing with stationary roughness.

KEYWORDS: Thermo-Hydrodynamic Analysis, Surface Roughness, Journal Misalignment, Non-Newtonian Lubricant.

التحليل الثرموهيدروديناميكي للمسند المقعدي باعتبار تاثيرات المحاورالغير متحدة والتصرف اللانيوتوني

أ.م.د. باسم عجيل عباس **م.م. مصطفى محمد كاظم**
جامعة بابل / كلية الهندسة **جامعة بابل / كلية الهندسة**

الخلاصة:
يتضمن البحث تمثيلا عدديا للتاثير المشترك للخشونة السطحية والتصرف اللانيوتوني للزيت على اداء المساند المقعدية الغير متحدة المحاور. تم تهيئة معادلة رينولدز المحورة لتاخذ بنظر الاعتبار التاثير المشترك للخشونة السطحية والتصرف اللانيوتوني للزيت.ياخذ النموذج الرياضي الموضوع بنظر الاعتبار اعتماد لزوجة الزيت على درجة الحرارة ومعدل القص. لغرض اجراء تحليل حراري كامل للمساند المقعدية ذات السطوح الخشنة واللامتحدة المحاوروالمزيتة بالزيت اللانيوتوني التصرف فان معادلات رينولدز والطاقة ومعادلة انتقال الحرارة بالحمل اضافة الى معادلة اللزوجة والشروط الحدية

المناسبة حلت انيا. ان الصفات الادائية للمساند المقعدية مثل الضغط والحمل وعزم الانحراف وقوة الاحتكاك قد تم دراستها ولمعاملات خشونة سطحية مختلفة. تم اختبار البرنامج الحاسوبي المعد لحل المعادلات الحاكمة لهذه المسالة عن طريق مقارنة بعض النتائج المستحصلة في هذا البحث مع تلك المنشورة في الادبيات اللمتعلقة بالموضوع. اظهرت النتائج المستحصلة بان الخصائص السطحية للمساند المقعدية تلعب دورا مهما في اداء تلك المسا ند.

الكلمات الرئيسية: التحليل الحراري ، الخشونة السطحية، المحاور اللامتطابقة ،الزيوت ذات التصرف اللانيوتوني.

INTRODUCTION

Hydrodynamic bearings have been used in various ap- plications of mechanical industry since along time to support rotating shafts of heavy machines. They are con- sidered as a good choice due to their construction sim- plicity, reliability, efficiency and low cost. Hydrody- namic journal bearings are commonly found in internal combustion engines, for supporting the crank shaft, ce- ment mill and turbocharger applications. Any hydrody- namic lubrication process consists essentially of two surfaces (bearing and journal surfaces) in relative motion shearing a thin layer of viscous fluid between them. Oil film pressure and temperature inside the bearing affected by the applied conditions, operating parameters (such as, rotational speed), geometric factors (such as, radial clear- ance) and types of lubricant (Newtonian or non-Newto- nian lubricant). Oil viscosity as known varies substan- tially with the temperature leading to a large change in the bearing load capacity, consequently, thermal effect in hydrodynamic lubrication plays a crucial role in predict- tion of the bearing performance. Large number of re- searchers had been studied this subject using different methods of solutions as in **Pinkus and Bupara(1979), Majumder (1974), Mitsui et.al.(1983), Ferron et.al. (1983), Mitsui et.al.(1986), Mitsui (1987) , Oh et.al.(1998)**. Fluid film gap changes that occur in the axial direc- tion of the journal bearing are caused by a well known phenomenon called bearing misalignment which is defined as a non-parallelism between the axis of the bearing and that of the journal. This state has a considerable, and usually disadvantageous effect on the performance of the journal bearing. In engineering applications this misalignment can be identified with one, or combination of the following causes: each deflection of the journal or its support, thermal distortion of the shaft and bearing, error in manufacturing, or externally imposed misaligning moments. The above causes lead to two types of bearing misalignment namely, axial (vertical displacement) and twisting (horizontal displacement) or combination of them. Misalignment in hydrodynamic bearings has been recognized by several investigators as in **Oscar Pinkus et.al.(1979), P. H. Markhoet.al. (1979), Z. S. Safar (1984), M. O. A.Mokhtar et.al.(1985),D. Vijayraghavan et.al.(1998), S. M. Chun et.al.(2000), F. P. Brito et.al.(2007), L. Roy(2009).**

Journal bearing surfaces, in practice, are all rough. Surface roughness has a considerable effect on the functional characteristics of the bearing operating in hydrodynamic, and especially, in mixed lubrication regimes, this effect of surface roughness is greatly enhanced by increasing a common parameter of roughness called root mean square (RMS) or standard deviation (σ) of roughness. The operation parameters and geometric factors have also important role in enhancing the surface roughness effect. In recent years, a considerable amount of re- search activities have been devoted to the study of surface roughness effects on the performance of hydrodynamic journal bearing systems, and also the driving force behind these studies, is the frequent failure of tribological component due to metal to metal contact and the associated rise in the frictional heating in **Dyson(1976), Nadir Patir et.al.(1978), Safar (1988), Keith(1989), Banwait(2006), Yang et. al. (2008) , Sinha (2008).**

. Also the lubricant used in industrial applications seems to have non-Newtonian behavior rather than Newtonian because of the oil contamination. Many researchers dealt with this behavior using power law fluid model and another models as in **Nadir Patir et.al. (1979), Tripp (1983), Long Li(1998), Shi et. al. 1998, Wang, Shi et.al.(1998).**

The present work represents an attempt to study the effect of different parameters, namely, surface roughness, journal misalignment, non-Newtonian lubricant behavior and oil viscosity-temperature dependence on the per-

formance of the hydrodynamic bearings. This is important in order to predict a realistic and accurate solution of the bearing performance and to avoid the probability of asperity contact in the space between two rough surfaces of the journal bearing which leads to a considerable increase of the maximum oil film temperature and reduced the bearing life.

GOVERNING EQUATIONS

A schematic diagram for the journal bearing used in the present analysis with the suitable coordinate has been shown in **Fig.1**. It can be shown in this figure the effect of surface roughness of both journal bearing surfaces and the effect of the shaft misalignment on the oil film thickness. The following are the governing equations adopted through this work:

Reynolds Equation

In the present work a modified Reynolds equation to include the effect of surface roughness and viscosity variation along and across the fluid film has been derived following the same procedure of Feron et.al.(1983) using Patir and Chengs postulates(1978),(1979).

$$\frac{\partial}{\partial\theta}\left\{\phi_x\bar{h}^3\bar{F}\frac{\partial\bar{p}}{\partial\theta}\right\}+\left(\frac{R}{L}\right)^2\frac{\partial}{\partial\bar{z}}\left\{\phi_z\bar{h}^3\bar{F}\frac{\partial\bar{p}}{\partial\bar{z}}\right\} = \frac{\partial}{\partial\theta}\left\{\bar{G}\cdot\bar{h}_T\right\}+\frac{1}{\Lambda}\cdot\frac{\partial}{\partial\theta}\left\{\bar{G}\phi_s\right\} \quad (1)$$

where:

$$\bar{F}=\frac{\int_0^1\left\{\int_0^1\frac{\bar{y}}{\bar{\mu}}\mathrm{d}\bar{y}\cdot\int_0^{\bar{y}}\frac{1}{\bar{\mu}}\mathrm{d}\bar{y}-\int_0^{\bar{y}}\frac{\bar{y}}{\bar{\mu}}\mathrm{d}\bar{y}\cdot\int_0^1\frac{1}{\bar{\mu}}\mathrm{d}\bar{y}\right\}\mathrm{d}\bar{y}}{\int_0^1\frac{1}{\bar{\mu}}\mathrm{d}\bar{y}} \quad (2)$$

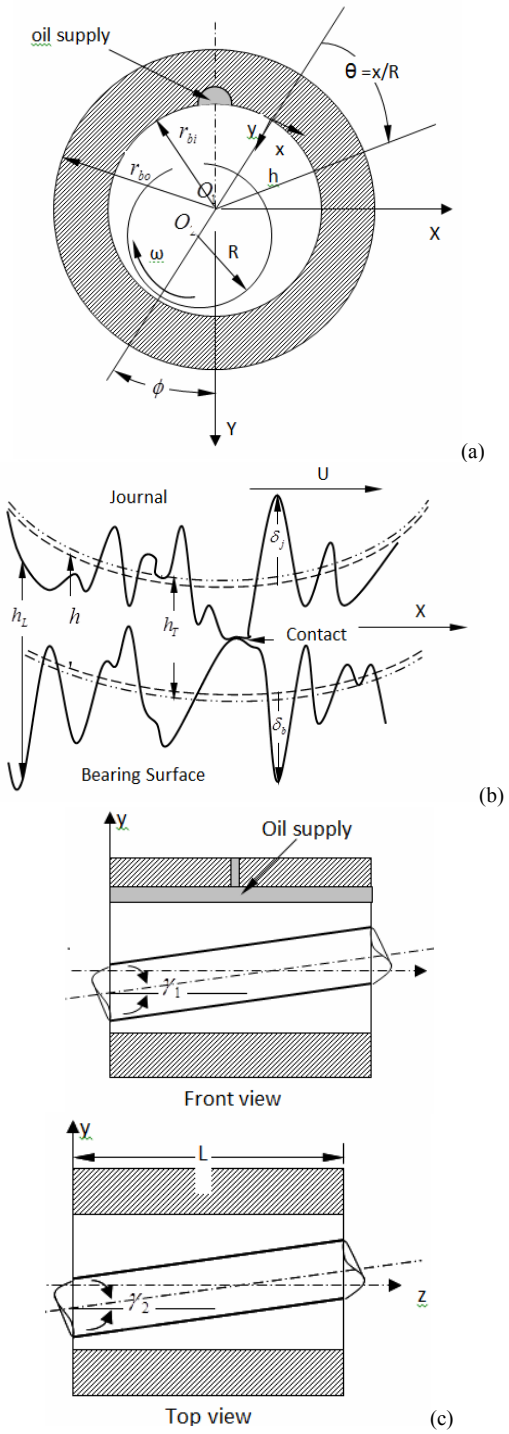

Fig.1 Geometrical Configuration of Grooved Misaligned Rough Journal Bearing System: (a) Journal Bearing Geometry and Coordinate System; (b) Oil Film Thickness and Surfaces Profile; (c) Bearing Misalignment.

$$\bar{G} = \frac{\int_0^1 \left\{ \int_0^{\bar{y}} \frac{1}{\bar{\mu}} \mathrm{d}\bar{y} \right\} \mathrm{d}\bar{y}}{\int_0^1 \frac{1}{\bar{\mu}} \mathrm{d}\bar{y}} \quad (3)$$

$$\bar{h} = \frac{h}{c},\ \bar{h}_T = \frac{h_T}{c},\ \theta = \frac{x}{R},\ \bar{y} = \frac{y}{h_T},\ \bar{z} = \frac{z}{L},\ \Lambda = \frac{c}{\sigma}$$

$\bar{h}_T$ is the average film thickness (separation) between the rough surfaces as shown in **Fig.1(b)**, (ϕ_x, ϕ_z) are pressure flow factors, and ϕ_s is a shear flow factor.

The second term in the right side of average Reynolds equation represents the additional flow transport due to sliding in a rough bearing.

Oil Film Thickness

The local film thickness h_L is defined as shown in figure 1(b):

$$h_L = h + \delta_j + \delta_b \quad (4)$$

where *h* is the nominal film thickness (compliance) defined as the distance between the mean levels of the two surfaces. δ_j and δ_b are the random roughness amplitudes of the two surfaces (journal and bearing roughness amplitudes) measured from their mean levels, δ_j and δ_b assumed to have Gaussian distribution of heights with zero mean and standard deviations σ_j and σ_b respectively as was used in Patir and Chengs (1978),(1979). The combined roughness $\delta = \delta_j + \delta_b$ has a variance $\sigma = \sqrt{\sigma_j^2 + \sigma_b^2}$.

For the journal bearing system having Gaussian distribution of surface heights the expression for average fluid – film thickness ($\bar{h}_T$) in fully lubricated ($\Lambda\bar{h} \geq 3$) and partially lubricated ($\Lambda\bar{h} < 3$) regions of misaligned journal bearings can be expressed as follows.

$$\bar{h}_T = \bar{h}$$

for $\Lambda\bar{h} \geq 3$

$$\bar{h}_T = \frac{\bar{h}}{2}\left[1 + erf\left(\frac{\Lambda\bar{h}}{\sqrt{2}}\right)\right] + \frac{1}{\Lambda\sqrt{2\pi}} e^{\frac{-(\Lambda\bar{h})^2}{2}} \quad \text{for } \Lambda\bar{h} < 3 \quad (5)$$

where $\bar{h}$ is the nominal fluid-film thickness (the fluid- film thickness of smooth journal bearing system) which can be introduced as in Jang et.al.(1987):

$$\bar{h} = 1 + \varepsilon\cos\theta \quad (6a)$$

For aligned journal bearing system

$$\bar{h} = \left\{(1 + \varepsilon\cos\theta) - \bar{z}\sigma_1^* \cos\theta + \bar{z}\sigma_2^* \sin\theta\right\} \quad (6b)$$

For misaligned journal bearing system where:

$$\sigma_1^* = 2\left(\frac{R}{c}\right)\left(\frac{L}{D}\right)\tan\gamma_1 \quad (6c)$$

$$\sigma_2^* = 2\left(\frac{R}{c}\right)\left(\frac{L}{D}\right)\tan\gamma_2 \quad (6d)$$

γ_1 and γ_2 are the tilting angles of the journal center line in vertical and horizontal direction respectively, as shown in figure 1(c).

FLOW FACTORS

The pressure flow factors ϕ_x and ϕ_z have been derived through numerical simulation as in Patir and Cheng (1978), while shear flow factor ϕ_s calculated as in Patir and Cheng (1979). The flow factors are determined in a function of the local average film thickness and in a function of the surface *r. m. s.* roughness (σ) and orientation (γ).

VISCOSITY-TEMPERATURE EQUATION

Energy equation is coupled to Reynolds equation through a nonlinear temperature viscosity relationship, since the viscosity of the lubricant was assumed to be variable across the film and a round the circumference. The dependence of viscosity on the temperature is given by the following equation as described by Ferron et.al.(1983):

$$\bar{\mu} = k_o - k_1\bar{T} + k_2\bar{T}^2 \quad (7)$$

k_o, k_1 and k_2 are viscosity coefficients, and $\bar{T}$ is a non-dimensional fluid temperature in the gap between two rough surfaces of the journal bearing system.

ENERGY EQUATION

The temperature distribution in the circumferential and a cross fluid-film directions for incompressible, Newtonian and non – Newtonian lubricant can be determined from a steady-state energy equation. The following non-dimensional form of energy equation is

adopted through this work, Ferron et.al.(1983), Yang et.al.(2008):

$$\lambda_1\left\{\bar{u}\frac{\partial\bar{T}}{\partial\theta}\right\}+\lambda_1\left\{\frac{\bar{v}}{\bar{h}_T}-\bar{u}\frac{\bar{y}}{\bar{h}_T}\cdot\frac{\partial\bar{h}_T}{\partial\theta}-\left(\frac{R}{L}\right)\bar{w}\frac{\bar{y}}{\bar{h}_T}\cdot\frac{\partial\bar{h}_T}{\partial\bar{z}}\right\}\frac{\partial\bar{T}}{\partial\bar{y}}$$
$$=\lambda_2\frac{1}{\bar{h}_T^2}\frac{\partial^2\bar{T}}{\partial\bar{y}^2}+\lambda_3\frac{\bar{\mu}}{\bar{h}_T^2}\left\{\left(\frac{\partial\bar{u}}{\partial\bar{y}}\right)^2+\left(\frac{\partial\bar{w}}{\partial\bar{y}}\right)^2\right\} \quad (8)$$

where:

$$\lambda_1=\frac{\rho C_o U R}{K_{oil}},\quad \lambda_2=\left(\frac{R}{c}\right)^2,\quad \lambda_3=\left(\frac{R}{c}\right)^2\frac{\mu_{in}U^2}{K_{oil}T_{in}},$$

and $\bar{T}=\frac{T}{T_{in}}$

$\bar{u},\bar{v}$ and $\bar{w}$ are the non-dimensional form of a velocity components of the lubricant flow. The terms on the left-hand side represent the energy transported by convection. The first term on the right-hand side represents the heat transfer by conduction and the last term on the RHS represents the energy generated by internal friction known as the viscous dissipation term. The heat generated is due to viscous shear of the lubricant.

FLUID-FILM VELOCITY COMPONENTS

The flow of lubricant between two rough surfaces can be modeled by an equivalent flow model. The equivalent flow model is defined as two smooth surfaces separated by a clearance equal to the average gap ($\bar{h}_T$). Based on this model, a new group of pressure flow factors (φ_x',φ_z') and a shear flow factor (φ_s') are defined as follows:

$$\phi_x'=\frac{\bar{h}^3}{\bar{h}_T^3}\phi_x;\quad \phi_z'=\frac{\bar{h}^3}{\bar{h}_T^3}\phi_z \quad\text{and}\quad \phi_s'=\phi_s \quad (9)$$

The non-dimensional velocity components in circumferential and axial directions are expressed as [Nagaraju et.al. 2007]:

$$\bar{u}=\frac{u}{U}$$
$$=\phi_x'\bar{h}_T^2\frac{\partial\bar{p}}{\partial\theta}\left\{\int_0^{\bar{y}}\frac{\bar{y}}{\bar{\mu}}d\bar{y}-\frac{\int_0^1\frac{\bar{y}}{\bar{\mu}}d\bar{y}.\int_0^{\bar{y}}\frac{1}{\bar{\mu}}d\bar{y}}{\int_0^1\frac{1}{\bar{\mu}}d\bar{y}}\right\} \quad (10)$$
$$+\frac{\int_0^{\bar{y}}\frac{1}{\bar{\mu}}d\bar{y}}{\int_0^1\frac{1}{\bar{\mu}}d\bar{y}}+\frac{\phi_s'}{\Lambda\bar{h}_T}\frac{\int_0^{\bar{y}}\frac{1}{\bar{\mu}}d\bar{y}}{\int_0^1\frac{1}{\bar{\mu}}d\bar{y}}$$

$$\bar{w}=\frac{w}{U}=\phi_z'\bar{h}_T^2\frac{\partial\bar{p}}{\partial\bar{z}}\left(\frac{R}{L}\right)\left\{\int_0^{\bar{y}}\frac{\bar{y}}{\bar{\mu}}d\bar{y}-\frac{\int_0^1\frac{\bar{y}}{\bar{\mu}}d\bar{y}.\int_0^{\bar{y}}\frac{1}{\bar{\mu}}d\bar{y}}{\int_0^1\frac{1}{\bar{\mu}}d\bar{y}}\right\} \quad (11)$$

While the non-dimensional velocity component across the fluid-film is obtained from the continuity equation and is expressed as [Nagaraju et.al. 2007]:

$$\bar{v}=\frac{v}{U}\left(\frac{R}{c}\right)=-\bar{h}_T\int_0^{\bar{y}}\left\{\begin{array}{l}\frac{\partial\bar{u}}{\partial\theta}+\left(\frac{R}{L}\right)\frac{\partial\bar{w}}{\partial\bar{z}}\\ -\frac{\bar{y}}{\bar{h}_T}\cdot\frac{\partial\bar{h}_T}{\partial\theta}\frac{\partial\bar{u}}{\partial\bar{y}}\end{array}\right\}d\bar{y} \quad (12)$$

HEAT–CONDUCTION EQUATION

The temperature distribution through the solid bush can be evaluated by solving the heat-conduction equation. The steady state heat-conduction equation with no heat source in non-dimensional form can be expressed as in Ferron (1983), Shi (1998):

$$\frac{\partial^2\bar{T}_b}{\partial\bar{r}_b^2}+\frac{1}{\bar{r}_b}\frac{\partial\bar{T}_b}{\partial\bar{r}_b}+\frac{1}{\bar{r}_b^2}\frac{\partial^2\bar{T}_b}{\partial\theta^2}=0 \quad (13)$$

where:

$\bar{T}_b$ is non-dimensional bearing temperature, $(\theta,\bar{r}_b)$ are the coordinates in circumferential and radial directions respectively.

NON-Newtonian Model

The constitutive relation of the power—law fluid model in non-dimensional form is expressed as in Nagaraju et.al.(2007):

$$\bar{\tau}=\bar{\mu}\left(\dot{\beta}\right)^{n_1} \quad (14)$$

where n_1 and $\bar{\mu}$ are the power law index and consistency index (Newtonian lubricant viscosity). For an incompressible non-Newtonian fluid, the shear strain rate $(\dot{\beta})$ is independent of direction and by considering it as a function of the second strain invariant of shear strain rate I_2 it can be expressed in non – dimensional form as:

$$\dot{\beta} = \sqrt{I_2} = \left[\left(\frac{1}{\bar{h}} \frac{\partial \bar{u}}{\partial \bar{y}} \right)^2 + \left(\frac{1}{\bar{h}} \frac{\partial \bar{w}}{\partial \bar{y}} \right)^2 \right]^{1/2} \quad (15)$$

The viscosity of a non-Newtonian lubricant is described by an apparent viscosity $(\bar{\mu}_{non})$ which is defined as a function of shear strain rate $(\dot{\beta})$.

$$\bar{\mu}_{non} = \frac{\bar{\tau}}{\dot{\beta}} = \bar{\mu} \left(\dot{\beta} \right)^{n_1 - 1} \quad (16)$$

BEARING PERFORMANCE CHARACTERISTICS

For obtaining the steady state characteristics for single axial grooved misaligned journal bearing, the load components along and perpendicular to the line of centers are found out from:

$$\bar{W}_r = \int_0^1 \int_0^{2\pi} \bar{p} \cos\theta \cdot \mathrm{d}\theta \cdot \mathrm{d}\bar{z} \quad (17)$$

$$\bar{W}_t = \int_0^1 \int_0^{2\pi} \bar{p} \sin\theta \cdot \mathrm{d}\theta \cdot \mathrm{d}\bar{z} \quad (18)$$

Therefore the total load carrying capacity of the rough misaligned journal bearing can be evaluated as:

$$\bar{W} = \sqrt{\bar{W}_r^2 + \bar{W}_t^2} \quad (19)$$

The attitude angle (ϕ) between the load line and the line of centers can be expressed as Oscar Pinkus et.al.(1979):

$$\phi = \tan^{-1} \left(-\frac{\bar{W}_t}{\bar{W}_r} \right) \quad (20)$$

The Sommerfeled number (bearing number) can be expressed as:

$$So = \frac{\mu_{in} \omega L R}{\pi W} \left(\frac{R}{c} \right)^2 = \frac{2 \mu_{in} N L R}{60 W} \left(\frac{R}{c} \right)^2 \quad (21)$$

$\omega = \frac{2\pi N}{60} =$ angular velocity of the shaft (rad/sec)

$W = UL\mu_{in} (R/c)^2 \bar{W} =$ load carrying capacity(N).

The mean viscous friction force of grooved rough misaligned journal bearing in dimensional form is described by the following equation as in Nadir Patir and Cheng(1979):

$$fr = \int_0^L \int_0^{2\pi R} \tau \mathrm{d}x\mathrm{d}z = \int_0^L \int_0^{2\pi R} \left(\mu \frac{U}{h} \left(\phi_f - \phi_{fs} \right) + \varphi_{fP} \frac{h}{2} \frac{\partial p}{\partial x} \right) \mathrm{d}x\mathrm{d}z \quad (22)$$

The non-dimensional form of the above equation is:

$$\bar{fr} = \frac{fr}{\mu_{in} UL (R/c)} = \int_0^1 \int_0^{2\pi} \left(\frac{\bar{\mu}}{\bar{h}} \left(\phi_f - \phi_{fs} \right) + \varphi_{fP} \frac{\bar{h}}{2} \frac{\partial \bar{p}}{\partial \theta} \right) \mathrm{d}\theta \mathrm{d}\bar{z} \quad (23)$$

where $(\phi_f, \phi_{fs}, \phi_{fP})$ are empirical shear stress factors used to explain the effect of surface roughness on the friction force of journal bearing as in Nadir Patir and Cheng (1979).

The required moment for steady state operation is calculated directly from the fluid film pressure distribution. Two components of the moment vector are required to maintain the two assigned angles γ_1 and γ_2. The non- dimensional form of these components are expressed as in Buckholz et.al. (1986):

$$\bar{M}_r = \int_0^1 \int_0^{2\pi} \overline{pz} \cos\theta \cdot \mathrm{d}\theta \cdot \mathrm{d}\bar{z} \quad (24)$$

$$\bar{M}_t = \int_0^1 \int_0^{2\pi} \overline{pz} \sin\theta \cdot \mathrm{d}\theta \cdot \mathrm{d}\bar{z} \quad (25)$$

and the total moment in non-dimensional form can be calculated as follows:

$$\bar{M} = \sqrt{\bar{M}_r^2 + \bar{M}_t^2} \quad (26)$$

BOUNDARY CONDITIONS

The following boundary conditions are used to gather with the governing equations to analyze the problem of thermohydrodynamic performance of grooved misaligned journal bearing with surface roughness.

A) Lubricant flow field

1) at the oil supply groove: $\theta = 2\pi - \phi$; $\bar{p} = \bar{p}_{in}$

2) at the journal bearing edges: $\bar{z} = 0$ & $\bar{z} = 1$
$\bar{p} = \bar{p}_{atm} = 0$

3) at the cavitation zone: $\partial \bar{p} / \partial \theta = 0$ and

$\bar{p} = 0$

B) Thermal field

1) the temperature across the oil film in the groove zone known as mixed temperature $(\bar{T}_{mix})$ is assumed to be constant and can be estimated as in Banwait (2006):

$$\bar{T}_{mix} = \frac{Q_{rec}\bar{T}_r + Q_{in}\bar{T}_{in}}{Q_{rec} + Q_{in}} \quad (27)$$

where $\bar{T}_r$ = recirculation temperature;
$\bar{T}_{in}$ = inlet oil temperature;
Q_{in} = supply oil flow rate (m^3/sec); Q_{rec} = recirculation flow rate (m^3/sec) and is expressed as follow:

$$Q_{rec} = LUc\int_0^1 \bar{u}\bar{h}\,d\bar{y} \quad (28)$$

2) at the oil-bush interface and at the oil-shaft interface the matching temperatures are

$$\bar{T} = \bar{T}_b \text{ at } \bar{y} = 0 \text{ and } \bar{T} = \bar{T}_{sh} \text{ at } \bar{y} = 1$$

3) the heat flux continuity on the surface between the bush and the oil film interface which yield to the following as in Ferron et.al. (1983),Yang and Jeng(2008):

$$\left.\frac{\partial \bar{T}_b}{\partial \bar{r}_b}\right|_{\bar{r}_b=1} = -\frac{K_{oil}}{K_b}\frac{r_{bi}}{c}\frac{1}{\bar{h}_T}\left.\frac{\partial \bar{T}}{\partial \bar{y}}\right|_{\bar{y}=0} \quad (29)$$

where $\bar{r}_b = r_b/r_{bi}$ and K_{oil} is the thermal conductivity of the fluid which is constant.

4) The boundary condition which is referred to the loses heat by free convection [Ferron et.al. 1983]:

$$\left.\frac{\partial \bar{T}_b}{\partial \bar{r}_b}\right|_{\bar{r}_b=\bar{r}_{bo}} = -\frac{h_{conv}}{K_b} r_{bi}\left(\bar{T}_{bo} - \bar{T}_a\right) \quad (30)$$

COMPUTATIONAL TECHNIQUE

The governing equations, Reynolds, energy, heat conduction and the cross film viscosity incorporating non Newtonian effect equations are solved for pressure and temperature distribution satisfying appropriate boundary conditions. A computer program was developed to determine the performance characteristics of the bearing. The finite difference scheme was used. The solution field was discretized into rectangular meshs of (m-1) sections in ($\boldsymbol{\theta}$) direction and (n-1) sections in (Z) direction to give mesh size of (m*n). The following iterative procedure was used to calculate the bearing performance characteristics:

1- Input the bearing data and initial values of different variables to the computer program.
2- Calculate the initial value of the attitude angle.
3- Assume initial pressure distribution.
4- Calculate the oil film thickness with suitable misalignement and roughness models.
5- Calculate the pressure distribution by solving Reynolds equation.
6- Repeat steps (4) and (5) until convergance occur.
7-Calculate the temperature distrbutio through the oil film.
8-Repeat steps (4-7) until cpnvrgent solution is obtained.
9- Calculate the load components (W_r) and (W_t), hence calculate the attitude angle.
10- Compare the new value of attitude angle with old one. If there is no convergence, a new pressure field is computed until the difference between the last values of attitude angle reached less than one degree.
Calculate The performance parameters of the bearing.
It should be noted that negative pressure values are replaced by zero.

The iterations are repeated until the pressure satisfies the following convergence criterion:

$$\text{error}_{(p)} = \frac{\sum\sum\left|\bar{p}^{\,n}_{(i,k)} - \bar{p}^{\,n-1}_{(i,k)}\right|}{\sum\sum\left|\bar{p}^{\,n}_{(i,k)}\right|} \le 10^{-4}$$

And the oil film temperature satisfies the following convergence criterion:

$$\text{error}_{(\bar{T})} = \frac{\sum\sum\left|\bar{T}^{\,n}_{(i,k)} - \bar{T}^{\,n-1}_{(i,k)}\right|}{\sum\sum\left|\bar{T}^{\,n}_{(i,k)}\right|} < 10^{-6}$$

VALIDATION

To validate the present numerical scheme, the pressure distribution, temperature distribution, and the maximum load carrying capacity of the lubricant film compared with earlier experimental results for smooth, aligned bearing

lubricated with Newtonian lubricant as shown in **Fig.s 2 to 4** . The numerical results agree quite well with Ferron's experimental work (1983). Also the numerical results for the maximum oil film pressure and the load carrying capacity agrees quite well with Roy's experimental work (2009) as shown in **Fig. 5** and **6.**

RESULTS AND DISCUSSION

The following numerical results are found for the combined effect of bearing surface roughness and non-Newtonian effect. The journal bearing variables used in computer program are listed in **Table 1**. **Figure 7** shows the effect of bearing surface roughness on the load carrying capacity of the bearing lubricated with Newtonian and non- Newtonian lubricant for different values of (h/σ) .It is clear from this figure that the load carrying capacity of the bearing with moving surface roughness decreases with increasing values of (h/σ). For the bearing with longitudinal roughness, the load carrying capacity of such bearing is greater than that of the bearing with smooth surfaces. Since the bearing with longitudinally oriented asperities permits only a small amount of side flow which enhances the flow in the direction of flow.

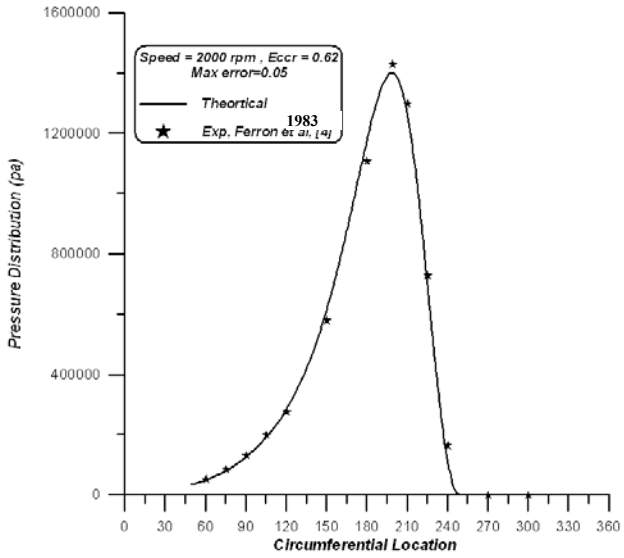

Fig.2 Oil film pressure distribution for smooth journal bearing

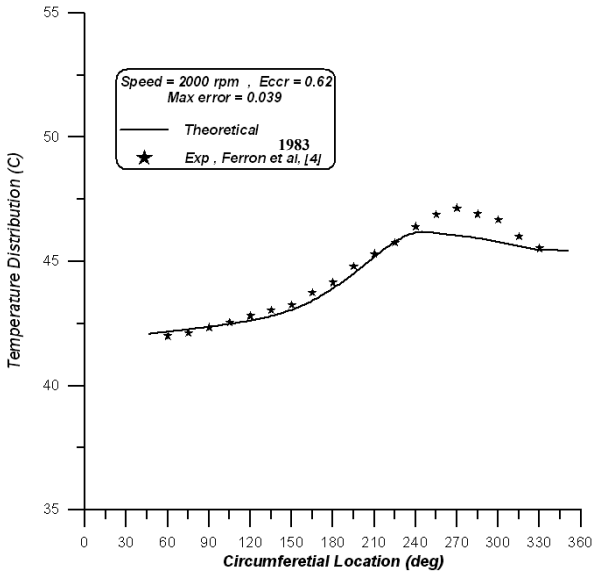

Fig.3 Oil Film temp. distribution for smooth journal bearing.

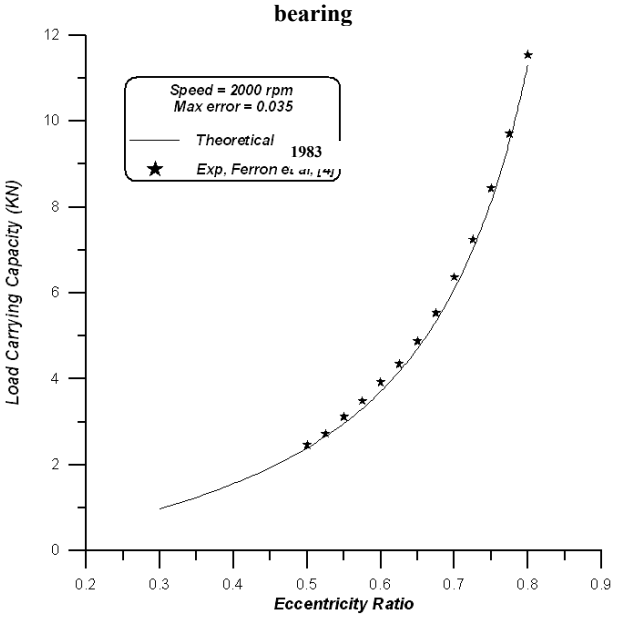

Fig. 4 Load Carrying Capacity versus Eccentricity Ratio for Smooth Journal Bearing

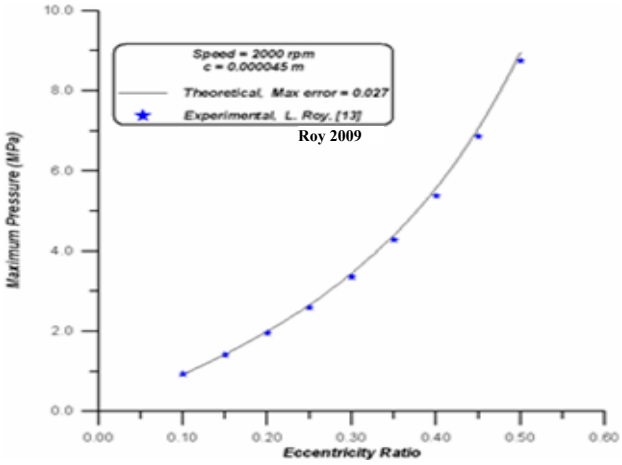

Fig.5 Maximum Pressure versus Eccentricity Ratio for Smooth Journal Bearing [Roy 2009].

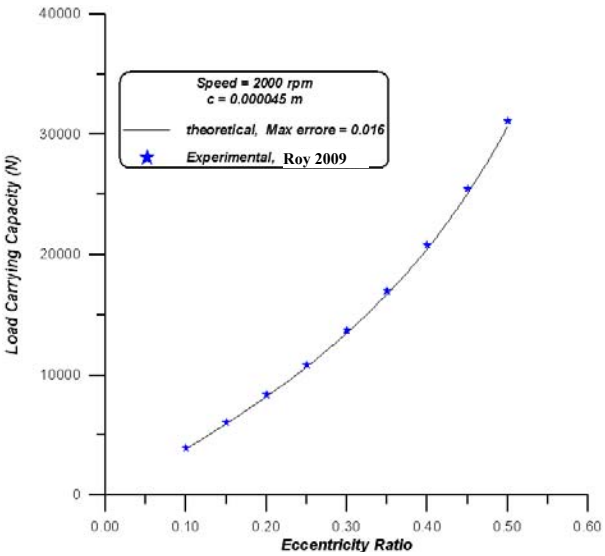

Fig.6 Load Carrying Capacity versus Eccentricity Ratio for Smooth Journal Bearing [Roy 2009].

different values of (h/σ) .It is clear from this figure that The bearing with isotropic and transverse roughness shows lower load carrying capacity than that of the bearing with smooth surfaces. This is expected since the decrease in (γ) results in small valley lengths which increased the side flow thereby decreasing the main flow which reduces the flow factors. The load carrying capacity of the bearing for all of the above cases become higher as the bearing lubricated with non- Newtonian lubricant of higher power index (n). The load carrying capacity of the bearing with stationary surface roughness shows different behavior than the bearing with moving surface roughness as can be seen from **Fig.**8.

Table 1. Geometric and operation parameters of the bearing.

Parameter	Symbol	Value and Unit
Bearing length	L	0.08 m
External bearing radius	r_{bo}	0.1 m
Journal radius	R	0.05 m
Radial clearance	C	0.000152 m
Eccentricity ratio	E	0.62
Misalignment angles in vertical and horizontal direction	γ_1, γ_2	(0.0002 and 0.00005 rad)
Surface roughness parameter	Λ	8 – 19
Surface pattern parameter for transverse, isotropic and longitudinal roughness pattern	Γ	1/6, 1.0, 6.0 respectively
Variance ratio	Vr_j	1.0, 0.0
Inlet lubricant temperature	T_m	40˚C
Ambient temperature	T_a	40˚C
Inlet lubricant pressure	p_m	70000 pa
Rotation speed	N	2000 rpm
Lubricant density at inlet temperature	ρ	860 Kg/m^3
Lubricant viscosity at inlet temperature	μ_{in}	0.0277 pa.sec
Viscosity coefficients	$(k_o, k_1, , k_2)$	3.287, 3.064 and 0.777

Lubricant specific heat	C_o	2000 J/Kg.˚C
Lubricant thermal conductivity	K_{oil}	0.13 W/m.˚C
Bush thermal conductivity	K_b	250 W/m.˚C
Bush convection heat transfer coefficient	h_{conv}	80 W/m^2.˚C
Air thermal conductivity	K_a	0.025 W/m.˚C
Groove angle	α_g	18 deg
Power law index of non-Newtonian Lubricant	N	1.2 and 0.8

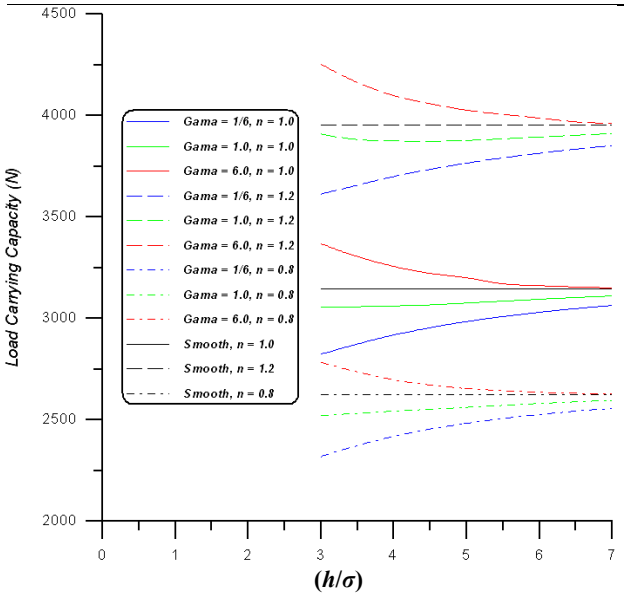

Fig.7 Hydrodynamic Load versus (h/σ) for Moving Surface Roughness in Misaligned Bearing using Newtonian (n = 1) and Non-Newtonian Lubricant (n = 1.2 and 0.8).

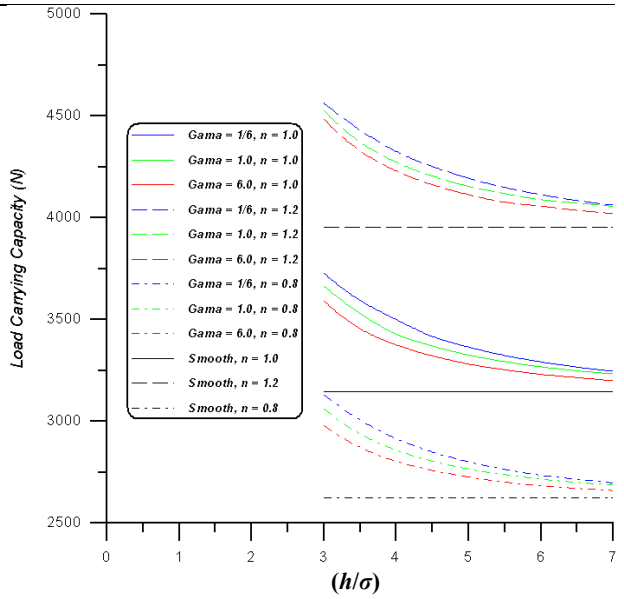

Fig.8 Hydrodynamic Load versus (h/σ) for Stationary Surface Roughness in Misaligned Bearing using Newtonian (n = 1) and Non-Newtonian Lubricant (n = 1.2 and 0.8).

The load carrying capacity increases with decreasing values of (h/σ), since decrease in (h/σ) is accompanied by a large increase in the mean gap, which enhances the flow factors. The bearing with transverse and isotropic roughness shows higher load carrying capacity than the bearing having longitudinally surface roughness. This is attributed to the fact that the asperities on the stationary rough surface acts a barriers in restricting the flow which results in a decreased mean flow as reveled by a negative shear flow factor. The load carrying capacity become higher when the bearing lubricated with a non Newtonian lubricant of higher index (n).

Figures 9 and 10 show the variation of maximum pressure against (h/σ) for the bearings with moving and stationary roughness. As expected the behavior of the maximum pressure is similar to that described for the bearing

load carrying capacity. **Fig.11** shows the variation of the maximum oil film temperature with (h/σ) for a bearing with moving surface roughness. It can be seen from this figure that the oil film temperature increases as (h/σ) decreases obtained for the bearing with transverse surface roughness. It can be deduced from this figure that lower maximum oil film temperature was obtained for the bearing with longitudinal surface rough- ness and it becomes higher for lower values of (γ). This can be attributed to the fact that the longitudinally oriented asperities permits only a lower values of shear flow factor while the transverse oriented asperities shows the highest value of shear flow factor. It is clear that the oil film temperature increases as the bearing lubricated with non –Newtonian lubricant of higher power index.

This is due to the higher viscosity in this case. The bearing with stationary surface roughness shows lower oil film temperature than that obtained for the bearing with smooth surfaces as shown in **Fig.12**.This is expected since it is well known that the asperities on the stationary rough surface act as a barriers in restricting the flow. This results in a decreased mean flow as reveled by a negative shear flow factor. It is clear that the oil film temperature decreases as (h/σ) decreases. The bearing with surfaces having transverse roughness shows lower temperature. This is attributed to the maximum

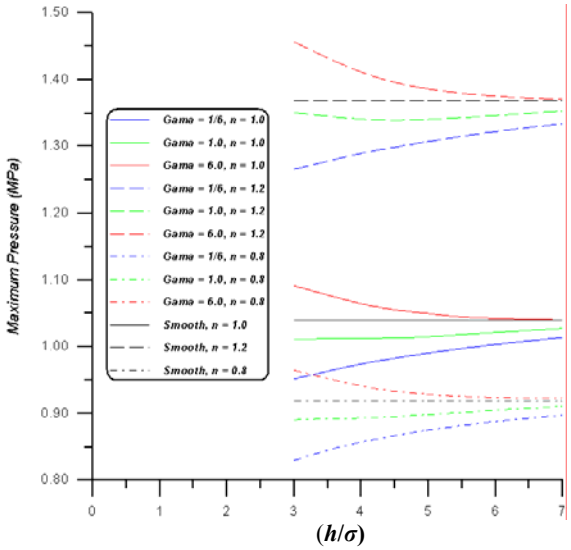

Fig.9 Hydrodynamic Maximum Pressure versus (h/σ) for Moving Surface Roughness in Misaligned Journal Bear- ing using Newtonian and Non-Newtonian Lubricant (n = 1.2 and 0.8).

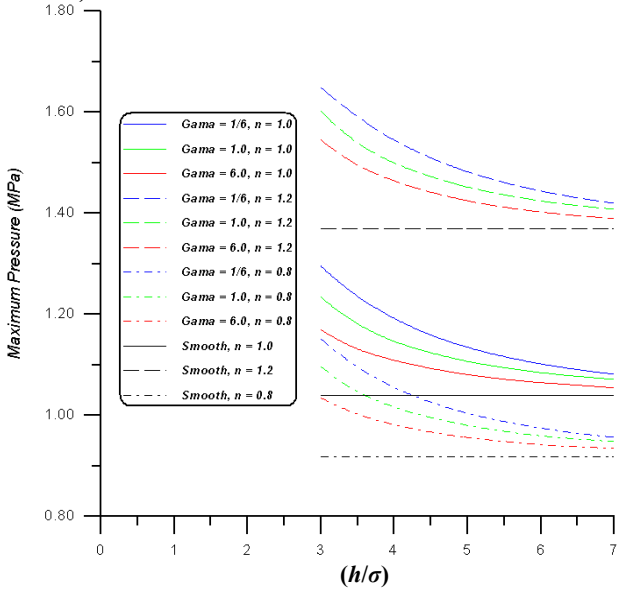

Fig.10 Hydrodynamic Maximum Pressure versus (h/σ) for Stationary Surface Roughness in Misaligned Journal Bearing using Newtonian and Non-Newtonian Lubricant.

resistance to the main flow offered by the transverse roughness thereby increasing the side flow, which reduces the flow factor ($\phi_x < 1$). Bearing lubricated with non –Newtonian lubricant of higher power law index shows a higher oil film temperature due to the higher viscosity and shearing effect.

Figures 13 and **14** show the variation of Sommerfeled number with roughness parame-

ter (h/σ). These Figures confirms the results have been previously discussed, related the load carrying capacity since Sommerfeled number proportional to the reciprocal of the load. The friction force produced in the bearing increased for the bearing lubricated with non-Newtonian lubricant with higher power law index as shown in **Fig.15**. This is due to the higher oil viscosity in this case. It can also be shown from this figure that the surface of moving roughness with transverse and isotropic roughness surfaces have a lower friction force than that in bearing with smooth surfaces with reducing the values of (h/σ). This is can be attributed to the positive shear stress factor and the correction factor of pressure (which always lower than 1) causes to decrease the friction force. The variation of friction force with roughness parameter (h/σ) for a bearing with stationary surface roughness can be shown in **Fig.16**. It is clear from this figure that the force increases with decreasing values of roughness parameter (h/σ). This can be explained by knowing that for the rough surface with stationary roughness , the valleys can be considered as stagnant pockets produce a large resistance to the fluid flow which leads to increase the shear stress and hence the friction force. The bearing with longitudinal, transverse and isotropic roughness surfaces shows higher friction force than that of smooth surface. Bearing with surfaces having transverse roughness shows higher friction force than that with isotropic or longitudinal roughness which indicates the increase of the shear stress factor in this case. The effect of non-Newtonian behavior of the oil on the moment of rough misaligned bearing with stationary and

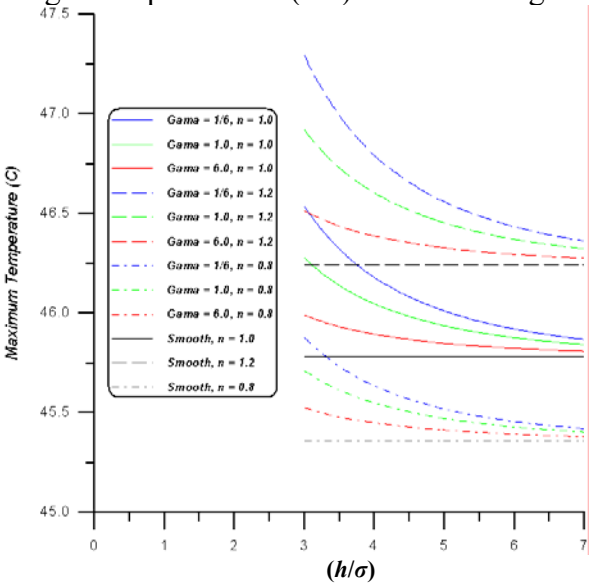

Fig.11 Hydrodynamic Maximum Temperature versus (h/σ) for Moving Surface Roughness in Misaligned Journal Bearing using Newtonian (n = 1) and Non-Newtonian

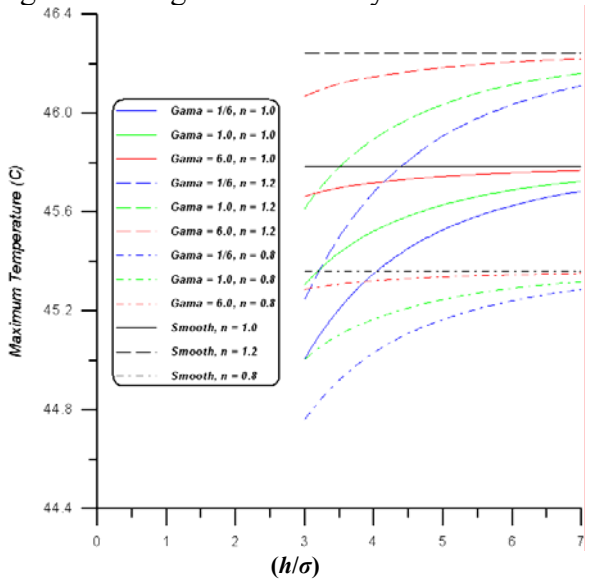

Fig.12 Hydrodynamic Maximum Temp. distribution for Stationary Surface Roughness in Misaligned Journal Bearing using Newtonian and Non-Newtonian Lubricant (n= 1.2 and 0.8)

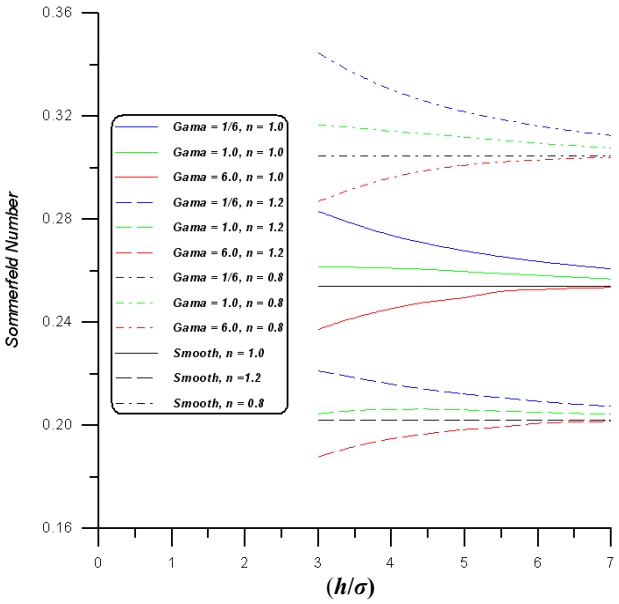

Fig.13 Sommerfeld Number versus (h/σ) for Moving surface roughness.

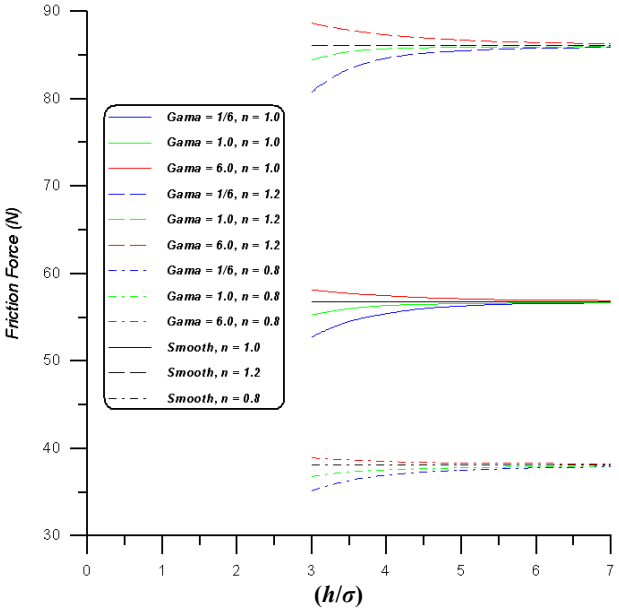

Fig.15 Friction Force versus (h/σ) for Moving Surface Roughness in Misaligned Journal Bearing using Newtonian and Non-Newtonian Lubricant.

moving roughness can be shown in **Fig.s(17) and (18)**. It can be shown from these figures that the bearing moment increases with bearing parameter for the bearing with moving surface roughness while it decreases for the bearing with stationary surface roughness.

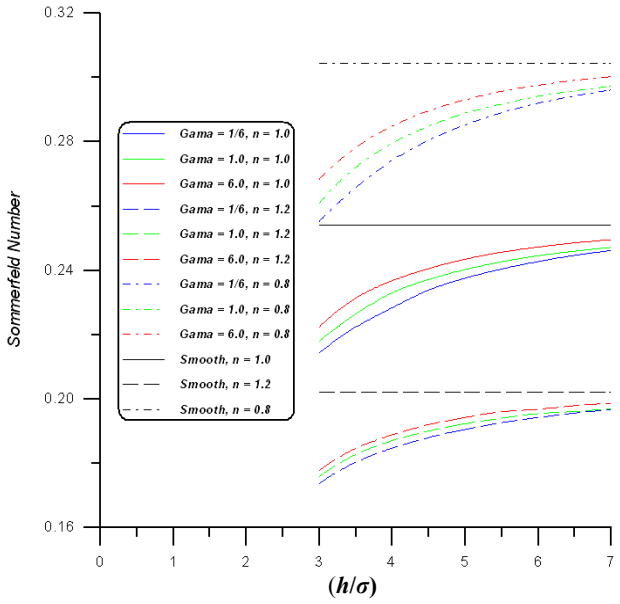

Fig.14 Sommerfeld Number versus (h/σ) for Stationary Surface Roughness in Misaligned Bearing using Newtonian (n = 1) and Non-Newtonian Lubricant (n = 1.2 and 0.8).

CONCLUSIONS

Thermohydrodynamic analysis of misaligned journal

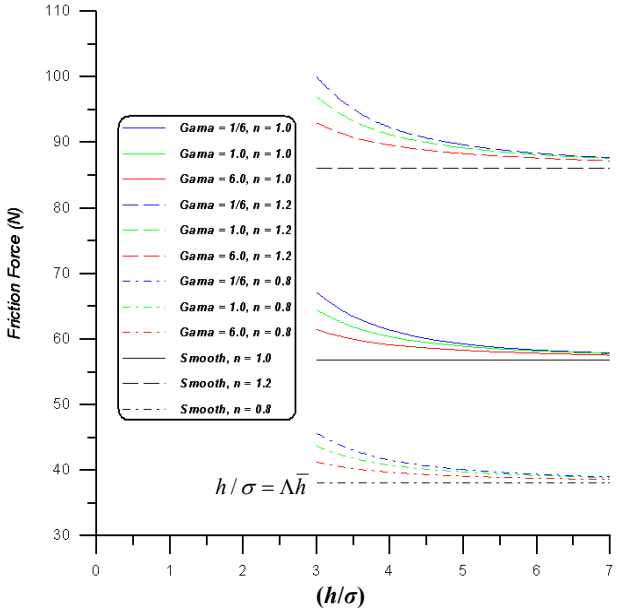

Fig.16 Friction Force versus (h/σ) for Stationary Surface Roughness in Misaligned Journal Bearing using Newtonian and Non-Newtonian Lubricant.

bearing with rough surface when lubricated with non-Newtonian lubricant has been implemented.The results obtained through this work

leads to the following conclusions can be remarked:

1) The surface roughness characteristics of opposing
surfaces (*i.e.*, variance ratio, Vr_j) and roughness orientations (γ) play an important role in reducing or increasing the performance parameters of the journal bearing.

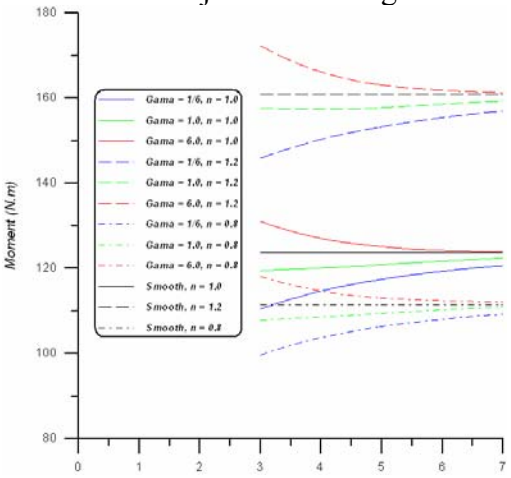

Fig.17 Moment versus (h / σ) for Moving Surface Roughness in Misaligned Journal Bearing using Newtonian ($n = 1$) and Non-Newtonian Lubricant ($n = 1.2$ and 0.8)

2) Combination of stationary roughness with a transverse surface roughness pattern provides maximum reduction in fluid – film temperature while it produces maximum increase in fluid – film pressure and load carrying capacity of the bearing. Contrary happens with moving surface roughness.

3) The combined effect of bearing misalignment and surface roughness in journal bearing leads to decrease each of load, pressure, temperature, friction force and mo- ment as compared with that of aligned journal bearing .

4) The non-Newtonian effect of lubricant has a significant effect on the thermohydrodynamic performance of journal bearing. Lubricant with higher values of power index ($n > 1.0$) causes to increase each of the values of bearing characteristics except of the sommerfeld number. These values decrease when the lower viscous lubricant index ($n < 1.0$) is used.

5) The effect of surface roughness on the performance parameters is more pronounce with decrease the value of roughness variable (h/σ). This effect is greatly affected by the rotational speed, non-Newtonian behavior and shaft misalignment.

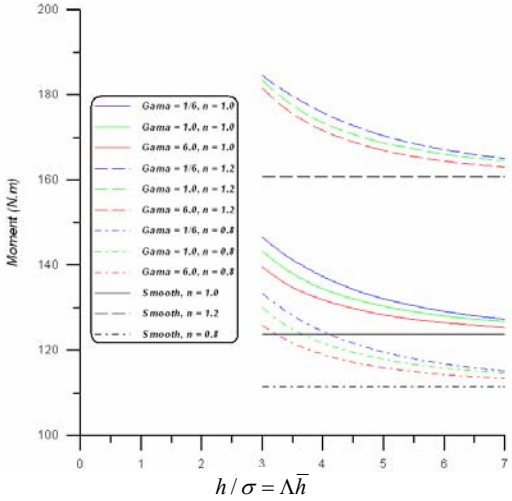

Fig.18 Moment versus (h / σ) for Stationary Surface Roughness in Misaligned Journal Bearing using Newtonian ($n = 1$) and Non-Newtonian Lubricant ($n = 1.2$ and 0.8)

6) There exists an interactive influence between surface roughness, thermal, journal is-alignment and non- Newtonian behavior of lubricant effects on thermohydrodynamic performance of the bearing, and hence, these effects should be studied to gather.

REFERENCES

A.Dyson, "The Failure of Elastohydrodynamic Lubrication of Circumferentially Ground Discs", Institution of Mechanical Engineers, 190, 699-711, 1976.

B. C. Majumdar, "The Thermohydrodynamic Solution of Oil Journal Bearings", Wear, 31, 287-294.

D. Vijayraghavan and D. E. Brewe, "Effect of Rate of Viscosity Variation on the Performance of Jour-nal Bearings", Journal of Tribology, 120,1-7, January 1998.

F. P. Brito, A. S. Miranda, J. Bouyer and M. Fillon, "Experimental Investigation of the In-

fluence of Supply Temperature and Supply Pressure on the Performance of a Two-Axial Groove Hydrodynamic Journal Bearings", Transaction of the ASME, 129, 98-105,January 2007.

F. Shi and Q. Wang, "A Mixed – TEHD Model for Journal Bearing Conformal Contacts – Part I: Model Formulation and Approximation of Heat Transfer Considering Asperity Contact", Transaction of the ASME, 120, 198-205, April 1998.

H. H. Oh and G. Parodissiadis, "Thermohydrody-namic Analysis of Journal Bearings Considering Cavita-tion and Revese Flow", Journal of Tribology,. 110, 439-447, July 1998

J. Mitsui, Y. Hori and M. Tanaka, "Thermohy-drody- namic Analysis of Cooling Effect of Supply Oil in Circular Journal Bearing", Transaction of the ASME, 105, 414-421, July 1983.

J. Ferron, J. Frene and R. Boncompain, "A Study of the Thermohydrodynamic Performance of a Plain Journal Bearing Comparison Between Theory and Experiments ", ASME J. Lubr. Technol., 105, 422-428, July 1983.

J. Mitsui, Y. Hori and M. Tanaka, "An Experimental Investigation on the Temperature Distribution in Circular Journal Bearings", Journal of Tribology, 108, 621-626, October 1986

J. Mitsui, "A Study of Thermohydrodynamic Lubrication in a Circular Journal Bearing", Tribology International, 331-341, 1987

J. H. Tripp, "Surface Roughness Effects in Hydrody- namic Lubrication: The Flow Factor Method", Trans-action or the ASME, 105, 458 – 465, July 1983.

J. Y. Jang and C. C. Chang, "Adiabatic Solution for A Misaligned Journal Bearing With Non-Newtonian Lubricants", Tribology International, 20, 267-275, October 1987.

L. Roy, "Thermo-hydrodynamic Performance of Grooved Oil Journal Bearing", Tribology International, 1187- 1198, March 2009.

M. O. A. Mokhtar, Z. S. Safar and M. A. M Abd-EI- Rahman, "An Adiabatic Solution of Misaligned Journal Bearings", Journal of Tribology, 107, 263-268, April 1985.

Nadir Patir and H. S. Cheng, "An Average Flow Model for Determining Effects of Three-Dimensional Roughness on Partial Hydrodynamic Lubrication", Transaction of the ASME. 100, 12-17, January 1978.

Nadir Patir and H. S. Cheng, "Application of Average Flow Model to Lubrication Between Rough Sliding Surfaces", Transaction of the ASME, 101, 220-230, April 1979.

Oscar Pinkus and S. S. Bupara, "Analysis of Misaligned Grooved Journal Bearings", Transaction of the ASME J. Lubr. Techno., 101, 503-508, October 1979

Pinkus and Bupara, "Adiabatic Solution for Finite Journal Bearing", Transaction of the ASME, 101, 492-496, October 1979.

P. H. Markho, S. S. Grewal and T. B. Stowell, "An Experimental Investigation of the Effect of Mis-alignment and Directionality on the Performance of an Externally – pressurized, Orifice- Compensated Air Journal Bearing", Transaction of the ASME, 101, January 1979.

P. Sinha and G. Adamu, "Thermohydrodynamic Analysis for Slider Bearing with Roughness: Special Reference to Load Generation in Parallel Sliders", Institution of Technology, 11-27, October 2008.

Q. Wang, F. Shi and Si C. Lee, "A Mixed – TEHD Model for Journal Bearing Conformal Contact – Part II: Contact, Film Thickness, and Performance Analyses", Transaction of the ASME, Vol. 120, pp.

R. H. Buckholz and J. F. Lin, "The Effect of Journal Bearing Misalignment on Load and Cavitation for Non- Newtonian Lubricants", Journal of Tribology, 108, 645-654, October 1986.

S. M. Chun and S. Jang, "Thermohydrodynamic Bubbly Lubrication Analysis of High Speed Journal Bearing", Kookmin University, 2000.

S. S. Banwait, "A Comparison Performance Analysis of Non-Circular Two-lobe and Three-lobe Journal Bearings", IE Journal, 86,

202-210, January 2006.

T. G. Keith. JR, "Effect of Cavitation on the Performance of A Grooved Misaligned Journal Bearing", Wear, 134, 377-397, April 1989.

T. Nagaraju, Satish C. Sharma and S. C. Jain, "Influence of Surface Roughness on Non-Newtonian Thermohydrodynamic Performance of a Hole-Entry Hybrid Journal Bearing", Journal of Tribology, 129, 595-602, July 2007.

W. Long Li, "Surface Roughness Effects in Hydro-dynamic Lubrication Involving the Mixture of Two Fluids", Transaction of the ASME, 120, 772-780, October 1998.

Y. K. Yang and M. C. Jeng, "Analysis of Viscos-ity Interaction and Heat Transfer on the Dual Conical Cylin- drical Bearing", Tribology Transaction, 77-85,February 2008.

Z. S. Safar, "Energy Loss Due to Misalignment of Journal Bearing", Tribology International, 17, 107-110, April 1984.

Z. S. Safar and M. S. M. Riad, "Prediction of the Coefficient of Friction of A Misaligned Turbulent Flow Journal Bearing", Tribology International, 21,15-19, February 1988.

NOMENCLATURE

D : Diameter of journal (m)

f_r : Friction force (N)

i, j, k: indexes along x,y,z axes respectively.

M :moment of the bearing. (N.m)

n : power law index.

P : oil film pressure (N/m^2)

$p = p/\mu_{in} U \cdot c^2/R$

S_O : Sommerfeld number

T : oil film temperature (C^o)

$\bar{T} = T/T_{in}$

T_s : Journal (shaft) temperature (C^o)

T_r : Recirculation oil temperature (C^o)

T_{mix}: Mixing oil temperature (C^o)

U : journal (shaft) speed (m/s)

Vr_J : journal rough surface variance ratio = $(\sigma_j/\sigma)^2$

Vr_b : bearing rough surface variance ratio $=(\sigma_b/\sigma)^2$

Vr : Combined variance ratio = $\left[\left(V_{r_J}\right)^2+\left(V_{r_b}\right)^2\right]^{0.5}$

GREEK SYMBOLS

γ : Surface roughness parameter = $\lambda_{0.5x}/\lambda_{0.5z}$

γ_j, γ_b : Surface roughness parameter for journal and bearing surfaces respectively.

δ_j, δ_b : Random roughness amplitude of the journal and the bearing surfaces respectively. (μm)

Δ : Combined roughness height (μm)

ε : eccentricity ratio.

$\lambda_{0.5x}, \lambda_{0.5z}$ = 0.5 correlation lengths of the x and z profile (μm).

μ : Lubricant viscosity (Pa.sec)

μ_{in} : Inlet viscosity (Pa.sec)

$\bar{\mu}$:Dimensionless lubricant viscosity = μ/μ_{in}

μ_{non} : Dimensionless viscosity of non-Newtonian lubricant.

σ_j, σ_b : Standard deviation of δ_j, δ_b for rough surfaces (μm).

σ : standard deviation of the combined roughness = $\sqrt{\sigma_j^2+\sigma_b^2}$

τ : Hydrodynamic shear stress N/m^2